

ADVANCED POWER ELECTRONICS AND ELECTRIC MACHINERY PROGRAM

VEHICLE TECHNOLOGIES PROGRAM

**Less dependence on foreign oil today,
and transition to a petroleum-free,
emissions-free vehicle tomorrow.**

2 0 0 7

annual progress report



U.S. Department of Energy
**Energy Efficiency
and Renewable Energy**

Bringing you a prosperous future where energy
is clean, abundant, reliable, and affordable

U.S. Department of Energy
Office of Vehicle Technologies, EE-2G
1000 Independence Avenue, S.W.
Washington, D.C. 20585-0121

FY 2007

**Annual Progress Report for the Advanced Power Electronics
and Electric Machinery Program**

Submitted to:

**Energy Efficiency and Renewable Energy
Office of Vehicle Technologies
Vehicle Systems Team**

Susan A. Rogers, Technology Development Manager

December 2007

Contents

Acronyms and Abbreviations	v
1. Introduction	1
2. Thermal Management and Systems.....	3
2.1 Thermal Control for Inverters and Motors.....	3
2.2 Thermal Buffer Heat Sink for Time-Averaged Operating Conditions	14
2.3 Low-Thermal-Resistance IGBT Structure.....	22
2.4 Plug-In Hybrid Electric Vehicle Impacts on Power Electronics and Electric Machines	33
2.5 Air Cooling Technology for Power Electronics Thermal Control.....	44
2.6 Jet and Spray Impingement Cooling for Power Electronics	56
2.7 Thermal Systems for Advanced Power Electronics and Electric Machines	68
2.8 Thermal Interface Materials for Power Electronics.....	79
3. Electric Machinery Research and Technology Development	91
3.1 Uncluttered Rotor PM Machine for CVT Design.....	91
3.2 16,000-rpm Interior Permanent Magnet Reluctance Machine with Brushless Field Excitation	96
3.3 IPM Drive Motor with Selectable Windings for HEVs.....	110
3.4 Control of Surface-Mounted Permanent Magnet Motors with Special Application to Motors with Fractional-Slot Concentrated Windings	123
3.5 Development of Improved Powder for Bonded Permanent Magnets	132
4. Power Electronics Research and Technology Development.....	147
4.1 Wide Bandgap Materials	147
4.2 dc/dc Converters for HEVs and FCVs.....	161
4.3 Cascade Multilevel Inverter for Fuel-Cell-Based HEV	174
4.4 Advanced Converter Systems for High-Temperature HEV Environments	186
4.5 Current Source Inverter	198
4.6 Utilizing the Traction Drive Power Electronics System to Provide Plug-in Capability for HEVs	212
4.7 dc/dc Converter for Fuel Cell and Hybrid Vehicle.....	221
4.8 High Performance Embedded Capacitors for (P)HEV Power Electronic Systems	231
4.9 Glass Ceramic Dielectrics for DC Bus Capacitors	239
5. Systems Research and Technology Development.....	245
5.1 Benchmarking of Competitive Technologies	245

Acronyms and Abbreviations

2-D	two-dimensional
3-D	three-dimensional
AC	air-conditioning
ac	alternating current
AIPM	automotive integrated power module
ANL	Argonne National Laboratory
BDCM	brushless direct current motor
BFE	brushless field excitation
BOM	bill of materials
CAN	controller area network
CFC	chlorofluorocarbon
COP	coefficient of performance
CPA	conventional phase advance
CPSR	constant power speed range
CSI	current-source inverter
DAC	data acquisition system
d-axis	direct-axis
dc	direct current
DMIC	dual-mode inverter control
DOE	U.S. Department of Energy
DSP	digital signal processor
EERE	Energy Efficiency and Renewable Energy
emf	electromotive force
EMI	electromagnetic interference
ESR	equivalent series resistance
EV	electric vehicle
FC	fuel cell
FCV	fuel cell vehicle
FEA	finite-element analysis
FVCT	FreedomCAR and Vehicle Technologies
GaN	gallium nitride
GT	Georgia Institute of Technology
GWP	global warming potential
HC	hydrocarbon
HCFC	hydrochlorofluorocarbon
HEV	hybrid electric vehicle
HFC	hydrofluorocarbon
HFE	hydrofluoroether
HSUPM	hybrid-secondary-uncluttered permanent magnet
HVAC	heating, ventilating, and air-conditioning
ICE	internal combustion engine
IGBT	insulated gate bipolar transistor
IM	induction motor
IPM	integrated power module
IPM	interior permanent magnet
I-source	current-source
ISR	Isothermal Systems Research
JFET	junction field-effect transistor

JIC	jet impingement cooling
mmf	magneto-motive
MOSFET	metal oxide semiconductor field-effect transistor
MS	methylsiloxane
MSU	Michigan State University
NASA	National Aeronautics and Space Administration
NTRC	National Transportation Research Center
ODP	ozone-depleting potential
OFCVTs	Office of FreedomCAR and Vehicle Technologies
ORNL	Oak Ridge National Laboratory
PCU	power converter unit
PEEM	Power Electronics and Electric Machines
PEEMRC	Power Electronics and Electric Machinery Research Center
PFC	perfluorocarbon
PMDC	permanent magnet direct current
PMSM	permanent magnet synchronous motor
PWM	pulse-width modulation
q-axis	quadrature-axis
R&D	research and development
rad/s	rotational speed
RFP	request for proposals
RIPM	reluctance interior permanent magnet
rms	root-mean-square
RSC	Rockwell Scientific Company
RTFC	real time flux control
SDPR	switching device power rating
Si	silicon
SiC	silicon carbide
SKAI	Semikron Advanced Integration
SMPM	surface mounted permanent magnet
SOC	state-of-charge
SPM	surface-mounted PM motor
THS II	Toyota hybrid system (2004)
toff	turn-off times
ton	turn-on
UWM	University of Wisconsin, Madison
VIBE	vibration-induced bubble ejection
V-source	voltage-source
VSI	voltage source inverter
WBG	wide bandgap
WEG	water-ethylene glycol
ZSC	zero-sequence circuit
ZVS	zero-voltage-switching

1. Introduction

The U.S. Department of Energy (DOE) and the U.S. Council for Automotive Research (composed of automakers Ford, General Motors, and Chrysler) announced in January 2002 a new cooperative research effort. Known as “FreedomCAR” (derived from “Freedom” and “Cooperative Automotive Research”), it represents DOE’s commitment to developing public/private partnerships to fund high-risk, high-payoff research into advanced automotive technologies. Efficient fuel cell technology, which uses hydrogen to power automobiles without air pollution, is a very promising pathway to achieving the ultimate vision. The new partnership replaces and builds upon the Partnership for a New Generation of Vehicles initiative that ran from 1993 through 2001.

The Advanced Power Electronics and Electric Machines (APEEM) subprogram within the FreedomCAR and Vehicle Technologies Program provides support and guidance for many cutting-edge automotive technologies now under development. Research is focused on understanding and improving the way the various new components of tomorrow’s automobiles will function as a unified system to improve fuel efficiency.

In supporting the development of hybrid propulsion systems, the APEEM effort has enabled the development of technologies that will significantly improve advanced vehicle efficiency, costs, and fuel economy.

The APEEM subprogram supports the efforts of the FreedomCAR and Fuel Partnership through a three-phase approach intended to

- identify overall propulsion and vehicle-related needs by analyzing programmatic goals and reviewing industry’s recommendations and requirements and then develop the appropriate technical targets for systems, subsystems, and component research and development activities;
- develop and validate individual subsystems and components, including electric motors and power electronics; and
- determine how well the components and subsystems work together in a vehicle environment or as a complete propulsion system and whether the efficiency and performance targets at the vehicle level have been achieved.

The research performed under this subprogram will help remove technical and cost barriers to enable the development of technology for use in such advanced vehicles as hybrid and fuel-cell-powered automobiles that meet the goals of the FreedomCAR and Vehicle Technologies Program.

A key element in making hybrid electric vehicles (HEVs) practical is providing an affordable electric traction drive system. This will require attaining weight, volume, and cost targets for the power electronics and electrical machines subsystems of the traction drive system. Areas of development include these:

- novel traction motor designs that result in increased power density and lower cost;
- inverter technologies involving new topologies to achieve higher efficiency and the ability to accommodate higher-temperature environments;
- converter concepts that employ means of reducing the component count and integrating functionality to decrease size, weight, and cost;
- more effective thermal control and packaging technologies; and
- integrated motor/inverter concepts.

2. Thermal Management and Systems

2.1 Thermal Control for Inverters and Motors

Principal Investigator: C. W. Ayers
Oak Ridge National Laboratory
National Transportation Research Center
2360 Cherahala Boulevard
Knoxville, TN 37932
Voice: 865-946-1342; Fax: 865-946-1400; E-mail: ayerscw@ornl.gov

DOE Technology Development Manager: Susan A. Rogers
Voice: 202-586-8997; Fax: 202-586-1600; E-mail: Susan.Rogers@ee.doe.gov

ORNL Program Manager: Mitch Olszewski
Voice: 865-946-1350; Fax: 865-946-1262; E-mail: olszewskim@ornl.gov

Objectives

- Refine physical design to capitalize on direct cooling/high dielectric environment.
- Design/develop a reliable hermetic power feedthrough for ac and dc power connections.
- Demonstrate high power density based on floating loop cooling.

Approach

- Produce a new physical design, iterating from the FY 2006 prototype, and incorporate feedthrough connector ideas.
- Design/Develop a reliable hermetic power feedthrough for ac and dc power connections.
- Perform capacitor ripple current testing to determine minimum acceptable capacitor size for the FY 2007 inverter.
- Evaluate die mounting techniques.
- Design and test final fully packaged one-third size inverter.
- Complete motor cooling tests in floating loop.

Major Accomplishments

- New reduced-volume design completed. Packaging design has been successful, based on SBE 350- μ F cylindrical polypropylene film capacitor and custom designed power/insulated gate bipolar transistor (IGBT) cards.
- Aluminum housing built at Oak Ridge National Laboratory (ORNL) and leak tested to 500 psi.
- Successfully produced a feedthrough design. A manufacturing technique was developed to produce a Cu-glass-Cu sealed fitting.
- Feedthrough pressure tested to 500 psi and load-tested to 400 amps with only 4°C rise.
- Motor cooling test to evaluate a plate heat.

Future Direction

- Funding is ending this fiscal year, but these are suggested areas of continued work in the future:
- Evaluate ribbon bonding of IGBTs in place of wire bonding.
 - Evaluate other promising die mounting and current carrying (bus bars) designs.
 - Evaluate single-phase direct contact cooling (such as high dielectric silicon-based oil, etc.).

Technical Discussion

This 3-year project has had the primary goal of developing a design for an inverter that would enable large reductions in size and weight. ORNL's cylindrical design, coupled with direct R134a refrigerant cooling and unique capacitor shaping, has provided a large reduction in volume and weight as compared to a baseline inverter.

The baseline inverter used for this comparison was a Semikron commercialized inverter product that exhibits a volumetric power density of about 9 kW/L. A major portion of the volume in the Semikron inverter is made up of the capacitor block which is about 1.6 L.

This component was a major target for the ORNL inverter design approach, leveraging better capacitor cooling to enable use of a smaller capacitor. An additional benefit derived from the capacitor change was a specific shape that fits well inside the cylindrical housing, and allows the power electronics to be packaged within the capacitor center. Figure 1 below shows the FY 2006 and FY 2007 inverter designs. The FY 2006 design (derived from a ProEngineer housing model) has a volume of about 3.1 L, and the new FY 2007 design exhibits a volume of 2.7 L.



Figure 1. Comparison of FY 2006 inverter model to completed FY 2007 inverter and housing.

A comparison of the baseline “brick” capacitor and the cylindrical style from SBE, Inc. that ORNL is using in the FY 2006 and FY 2007 designs is shown below in Figure 2. The long rectangular shape (seen in the upper left of Figure 2) fits well in a coldplate-cooled inverter that utilizes a two-dimensional architecture such as that used in the Semikron inverter and other similarly packaged inverters. The ORNL inverter is cooled in a pressurized housing, and a cylindrical shape is well-suited for handling pressure. The cylindrical capacitor fits well in this architecture, and the polypropylene capacitors are compatible with R134a and are cooled well with the submersion scheme of this design. The SBE, Inc. cylindrical capacitor is shown in the lower left of Figure 2. This ORNL cylindrical inverter architecture approaches

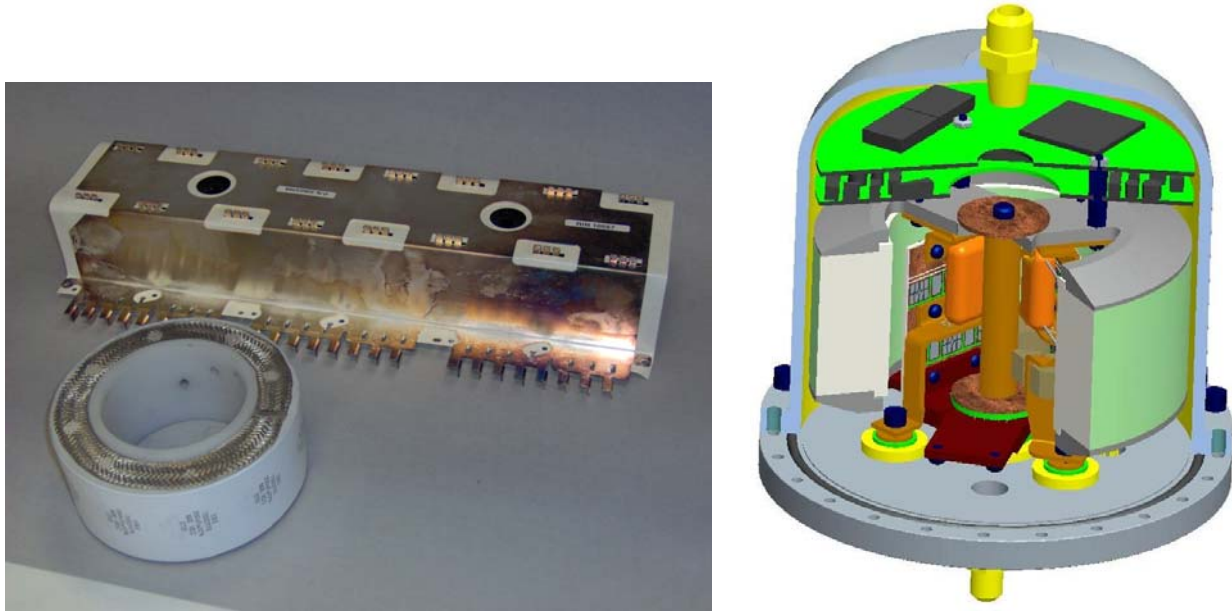


Figure 2. Comparison of baseline capacitor with ORNL capacitor. Upper capacitor is 1000 μF for use in the Semikron inverter, and the lower capacitor is the SBE 500 μF for the ORNL inverter. The cutaway model to the right shows how the capacitor and other components are packaged inside the cylindrical housing.

a spherical shape, which, while being most volumetrically efficient, also lends itself to a lightweight pressure vessel design. The power electronics cards (IGBTs and diodes) are mounted inside the center of the cylindrical capacitor, and this whole zone (slightly above the top of the capacitor) is submerged in liquid R134a refrigerant.

One task that needed to be completed before the final FY 2007 packaging design was finalized was to determine the ripple current capability of several capacitor models from SBE. The final capacitor chosen was an SBE 350- μF hollow cylindrical capacitor made with polypropylene film. This unit and several others were tested for ripple current capability, and all the units tested could handle 400 amps ripple current with no significant temperature rise. The 350- μF capacitor was the smallest unit that could adequately hold the power electronics that needed to be placed inside the cylinder.

Based on lessons learned from the FY 2006 design, build, and testing, we decided to redesign the gate driver card and the power cards to be better matched. It was also decided to put all the controls and gate drivers inside the inverter housing, with only command signals and power brought into the inverter. The model in Figure 2 shows how the gate driver and control cards are packaged on top of the inverter power core.

Power Feedthrough Development

An issue of interest came up late in FY 2006 regarding power feeds into and out of the inverter, where there was a requirement to contain a coolant under reasonable pressure, and concerns about reliability of that function. One of our tasks for the FY 2007 inverter development became to develop a reliable power feedthrough that was functional in an R134a pressurized vessel and could handle several hundred amps. A glass powder was found that was designed to bond to copper, Ferro EG3608. A feedthrough concept was developed based on this product, where the inverter core was designed to mount directly on top of the feedthroughs.

In Figure 3, our copper-glass bonded feedthrough prototype is shown on the left. This prototype replaces the center feedthrough shown in the bottom inverter flange on the right. The component is fabricated with matched tapered cylinders, where the annular spaces are filled with EG3608 powder, and



Figure 3. Left shows the two-conductor copper-glass-copper dc link feedthrough. Right shows the bottom flange of the FY 2007 inverter with epoxy-based ac and dc feedthroughs.

along with graphite jigs and an oven melting process, the three copper parts are bonded together in one procedure.

The copper-glass feedthrough prototypes were pressure tested successfully to 500 psi. They were subsequently tested in the glass test jars pressurized with R134a refrigerant. The test consisted of a short-circuit test to flow heavy current through the feedthrough while monitoring temperature inside the feedthrough using a thermocouple. The component was tested to 400 amps, as shown in Figure 4 below, with a temperature rise of only 4°C above the bulk liquid (R134a) temperature. The feedthrough enters through the bottom of the glass jar setup, and the copper links in the middle are the shorting bars that carry the load current from the center pin of the feedthrough to the tube conductor of the feedthrough. The meter in the background shows the thermocouple temperature that is measuring the core of the feedthrough at 34°C, while the bulk refrigerant fluid temperature was around 30°C.



Figure 4. Glass-sealed copper feedthrough testing in R134a at 400 amps.

This test setup was also used to mount and test the power cards for the subsequent dc load tests. No leaks were detected during any of these tests. The figure shows the O-rings on the outer copper shell of the feedthrough. These provide the seal between the feedthrough and the housing flange, where the feedthrough simply slides through the flange and is held in place with a snap ring. This sealing method is similar to techniques seen in commercially available R134a systems.

Power Card dc Load Testing

DC load testing of the power card subsections was performed to prequalify the cards for use in the finished inverter. These cards each comprise an upper and lower leg of the three-phase inverter circuit. The top and bottom conductor area on each card are the dc link terminals, and the center conductor area is the output phase terminal. They are made to have bus bars bolted to them inside the inverter. The card layouts can be seen in Figure 5. The load testing consists of mounting the card with the upper and lower terminals (dc links) connected to a power supply plus and common, with the gates of all IGBTs turned fully on, allowing current flow straight through the card. The power supply is operated in a current control mode, where the current is slowly graduated up to full current levels. Figure 6 below shows one of the power cards being tested at approximately 200 amps dc current. All of the cards being used in the inverter have undergone testing in the glass jar for full load current qualification.

Load testing results for these cards as delivered qualifies them for 250-amp operation. When they were built it was requested that they be wired with 0.015-in. wirebond diameter, but they were received with 0.008-in.-diameter wirebonds. The cards were expected to handle 300–400 amps in the dc load tests but are only able to handle about 270 amps before reaching a critical heat flux. It is believed that the wirebond conductor area reduction of 3 to 1 due to the wirebonding mistake is the cause of excessive heat at the wirebond locations, causing the additional heat flux. This error occurred too late in the year, and used up too large a percentage of our trench IGBT stock, to be able to recover and remake the power cards with proper size wirebonds. The inverter testing proceeded with a 250-amp limit, and conservative projections were made as to the maximum current and power capabilities based on a proper wirebond diameter.

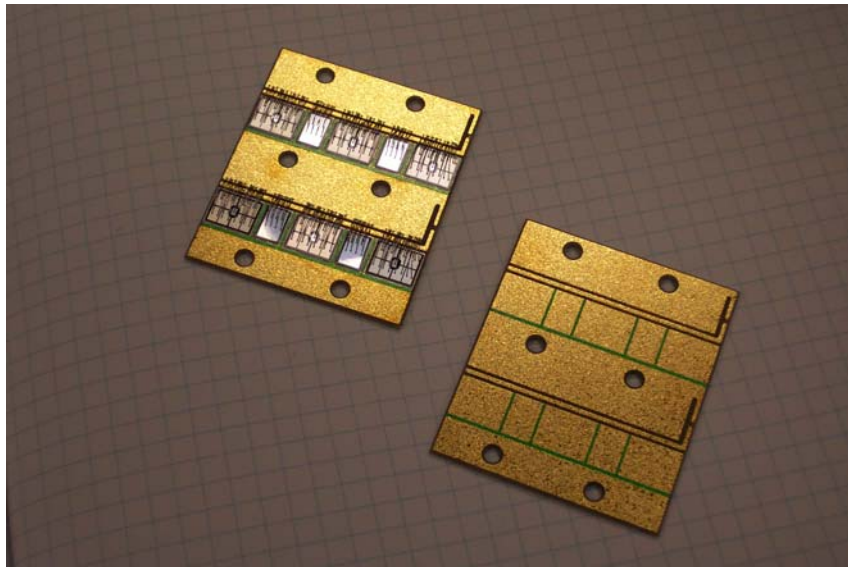


Figure 5. Empty and populated power cards DBCs using trench technology silicon-based IGBTs.

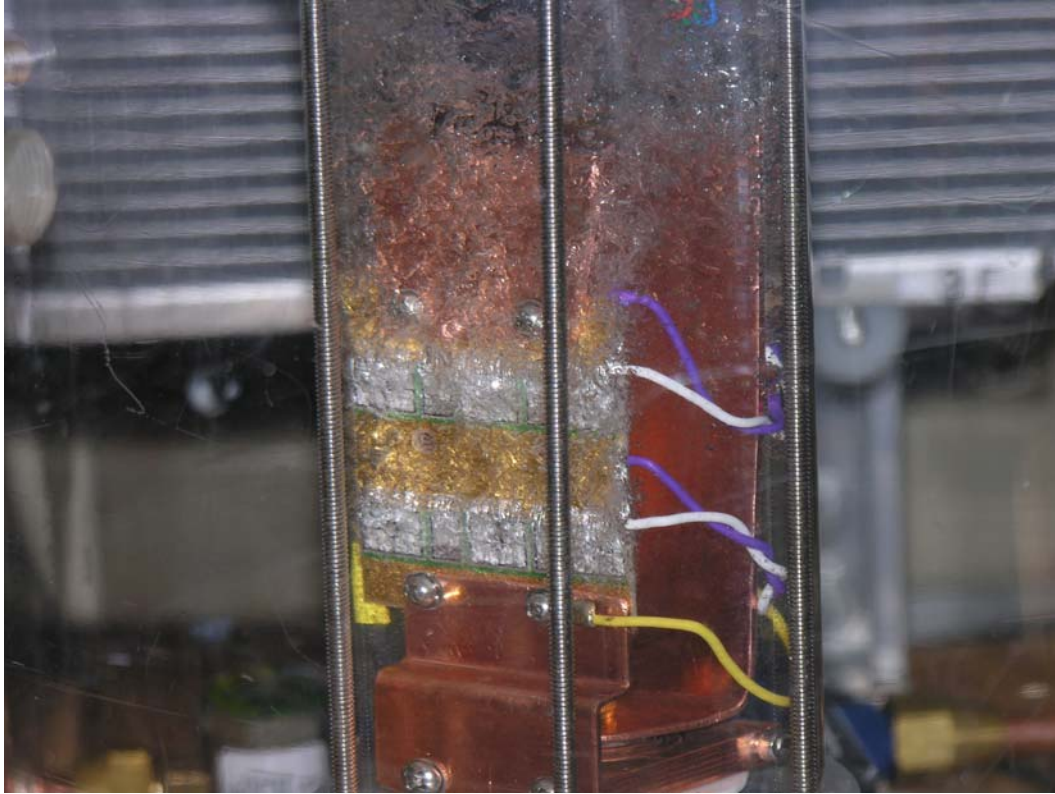


Figure 6. Single power card undergoing dc load testing in glass jar at about 200 amps.

Capacitor Testing

To determine the minimum capacitor size allowable, based on ripple current carrying capability, tests were performed on the SBE cylindrical capacitors to determine their ability to handle the proper ripple current for this application. Ripple current capability drops dramatically as the capacitor temperature is raised from 60°C up to 105°C, and capacitor volume has to be raised appropriately to handle a given amount of ripple current. The direct-cooled environment in the R134a cooled inverter allows the capacitor to operate at a much reduced temperature (around 60°C), so its size can be greatly reduced. These tests qualified the preferred capacitor design, SBE # 700D179 in Table 1, to 300 amps ripple current for this inverter application. This capacitor is a 350-μF polypropylene film capacitor, and the temperature rise in a direct-cooled environment was minimal (<10°C) (Table 2).

Table 1. Capacitor ripple current test results

Component description	Capacitance (μF)	Voltage rating (V_{dc})	Ambient temperature (°C)	Ripple current load (amps)	Temperature rise (°C)
Polypropylene film, SBE # 700D137	500	900	47	350	28
ORNL Tapered Metallization film, SBE # 700D161	500	700	53	350	4
Polypropylene film, SBE # 700D163	500	600	56	400	7
Polypropylene film, SBE # 700D179	350	600	53	300	10

Table 2. Capacitance measurements over time with heavy ripple current, SBE capacitor #700D163 at 400 amps

Test No.	Cumulative (h)	Capacitance (μF)
1	2.08	465
2	4.42	467
3	7.67	465
4	10.17	464
5	12.42	465
6	13.20	465
7	15.95	465
8	19.20	465
9	21.62	465
10	25.37	465
11	29.12	465
12		

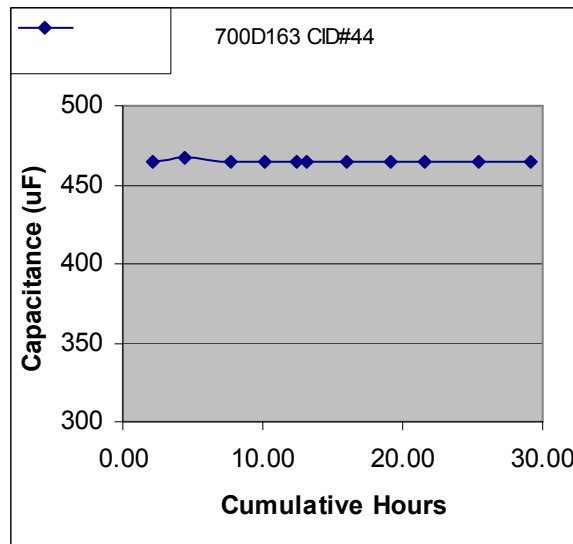


Figure 7. Capacitance response to 30 h of 400-amp ripple current stress.

FY 2007 Inverter Load Testing Results

After completing dc load tests on the individual cards, they were prepared for installation into the complete inverter package. This package includes the housing; circular dc links; cylindrical capacitor; A, B, and C phase power cards; gate driver card; and controller card. The system was put together and placed into operation and successfully tested with a three-phase ac output into a dummy R-L load in the Power Electronics and Electric Machinery Research Center (PEEMRC) laboratory. A dedicated R134a coolant loop was used for cooling the system, the same as was used for cooling the dc power card load tests in the glass jar setup.

Table 3 tabulates some of the highlights of our end-of-the-year testing on the FY 2007 cylindrical inverter.

Table 3. Inverter three-phase load testing results

dc link		ac output		Electric frequency (Hz)	Power input (kW)	Power output (kW)	pf λ	η (%)
V_{dc}	A_{rms}	V_{ac}	A_{rms}					
100.2	25.2	72.3	27.7	30	2.52	2.42	0.69	95.9
100.0	39.7	73.8	48.6	30	3.96	3.84	0.61	96.9
148.1	50.6	110	48.3	50	7.49	7.32	0.79	97.7
150.9	60.3	112.4	73.3	30	9.08	8.79	0.61	96.7

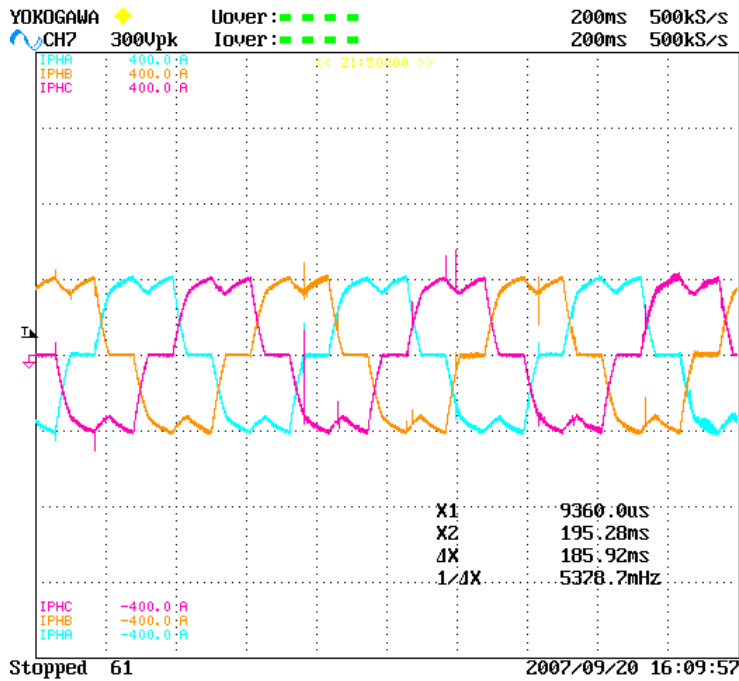


Figure 8. Example waveform from inverter three-phase load testing, output current at 75 A_{rms} , $V_{dc-link}$ at 150 V.

Projected Power Capabilities

DC load testing proved the cards up to a current load of 250 amps. This dc current is used for I_{peak} in the ac output power projection calculations.

The dc voltage V_{dc} uses a nominal battery voltage of 325 V_{dc} , and this is used to calculate an estimated $V_{line-line}$.

Output power is then estimated using the equation for “P” below:

$$I_{line} = I_{peak} / \sqrt{2}$$

$$V_{line-line} = 4\sqrt{3} (V_{dc}) / 2\pi\sqrt{2}$$

$$P = \sqrt{3} (V_{line-line}) I_{line} \cos \Phi, \text{ estimate } \Phi = 0.85$$

Tests to-date have conservatively demonstrated 250 amps for I_{peak} . Based on this number, power calculations and projections can be performed. The present capability calculated from the dc load tests is

$$P = 66 \text{ kW @ 250 amps (wirebond size 0.008 in.) .}$$

If the wirebond size were increased to only a 2 mils larger diameter, there would be a 60% increase in conductor area. A conservative estimate of current-carrying ability with this adjustment is 300 amps (only a 20% increase in current). The output power estimated from this number is

$$P = 80 \text{ kW @ 300 amps (wirebond size 0.010 in.) .}$$

AC load testing goals were to test the unit up to 250 amps peak, or a dc link current of 250 amps. This was the level that the 0.008-in. wirebonds were qualified to, so this would be used for the three-phase testing limits. Tests were terminated at 75 amps output (rms) due to problems that were causing failures in the power cards.

The source of these problems is still under debate, but some possibilities suggested are shoot-through failure due to random noise, voltage-related noise switching spikes, or short circuits on an IGBT edge due to foreign material inside the inverter.

The voltage waveforms that were recorded indicated very little switching noise, so it is difficult to settle on random noise causing shoot-through problems. A couple of the power cards that failed (separate events), after visual inspection, indicated that foreign material had shorted out across from the emitter to the collector of the chip and caused a small arc-flash. A third (separate) failed card appears to have more of a thermal failure, such as a shoot-through event on that phase's power card. In each of these failure cases, the other two phases remained in perfect condition, indicating that we did not experience overheating of the power cards due simply to load. One of the failures occurred at the highest voltage and current, but the last failure occurred at around 50 V and 50 amps, which argues against increasing voltage being the cause.

It is difficult to diagnose a closed inverter such as this design, so lack of time became the controlling factor on completing the ac load testing. The inverter can handle several hundred amps from a cooling standpoint, as indicated by the dc load testing. These spurious failures simply require more time to work out the root causes, as in any of our inverter developments, and this has unfortunately slowed down working within pressurized, closed inverter housing.

Motor Cooling Tests

As a continuation of FY 2006 motor cooling tests, the same ORNL motor was set up for motor coolant testing. The primary goal of this year's testing was to evaluate the viability of using a plate heat exchanger in the oil coolant loop where heat is rejected to R134a in the secondary side of the heat exchanger. Table 4 lists the data taken as the motor was electrically loaded to produce heat in the copper stator windings. The heat exchanger was connected into the floating loop system to provide two-phase cooling of the secondary side of the heat exchanger.

Initial indications from this data are that the two-phase heat exchanger does not perform as well as the liquid-liquid (i.e., oil to water) configuration that was tested in FY 2006. The temperature difference from the R134a coolant to the oil temperature under heavy loads is about 11°C, which is a reasonable delta temperature; but because of a missing oil cooler outlet temperature data point, there is not a comparable number with which to compare the delta temperature from the FY 2006 tests. This year's test data show a 45°C oil supply temperature and indicate a 62°C rise from that to the hottest winding location (T3) of 107°C. This temperature is not very high, but the system was not brought up to the full load of several kilowatts due to time constraints at the end of this fiscal year.

Table 4. Test data from R134a plate heat exchanger for motor spray-oil cooling

T1 (°C)	T2 (°C)	T3 (°C)	T4 (°C)	T5 (°C)	T6 (°C)	T7 (°C)	Volts (A, B, C)	Current (A, B, C)	Refrigerant pressure (psi)	Refrigerant temperature (°C)	Power level (W)
23	23	23	23	23	22	23	0 (A) 0 (B) 0 (C)	0 (A) 0 (B) 0 (C)	92	28	Start of three-phase power using step down transformer
48	54	80	37	41	64	54	47.8 (A) 48.2 (B) 48.1 (C)	77.9 (A) 78.3 (B) 77.2 (C)	103	32	1.575 kW
56	67	98	42	50	78	62	53.7 (A) 54.1 (B) 54.0 (C)	87.0 (A) 87.3 (B) 86.1 (C)	108	33	2.063 kW
60	72	107	45	55	85	66	55.9 (A) 56.3 (B) 56.2 (C)	90.4 (A) 90.8 (B) 89.5 (C)	110	34	2.267 kW

The test motor has been rewound since last year’s data, so the thermocouple locations are probably slightly different as well. Another factor that may be entering into the different performance results is that the liquid level in the R134a plate heat exchanger is not known. If the liquid level is too low, then proper two-phase cooling is not occurring inside the unit.

Further testing needs to be accomplished to allow these issues to be properly addressed. There needs to be some method established to properly charge the coolant in the secondary side of the heat exchanger, and the oil flow rate should be measured.

Conclusions

Compared to the FY 2005 baseline inverter, the ORNL goals of 50% and 67% reduction in volume have been met. The power density of the baseline unit was estimated at 9 kW/L, and the ORNL FY 2006 prototype inverter demonstrated about 18 kW/L. The ORNL final prototype cylindrical inverter for FY 2007 has demonstrated a 250-amp capability with the existing wirebonds and is projected to easily achieve above 300 amps with properly sized wirebonds. We are projecting a volumetric power density of nearly 27 kW/L based on the dc load testing, and more than 30 kW/L with the projected currents. These numbers exceed the FreedomCAR goals through the year 2020.

ORNL has successfully developed and demonstrated a floating-loop cooling system that utilizes the R134a refrigerant (a fluid system already available on the average vehicle) as a basis for a system that shares some of the auto ac system components. We have demonstrated a coefficient of performance as high as 40 for the floating-loop system.

The direct-contact cooling system has been shown to successfully operate in conjunction with an auto ac system, during all modes of operation. This cooling concept can also operate as a separate loop over a range of pressures. The heat flux demonstrated this year with R134a direct contact boiling is greater than 60 W/cm² with the undersized wirebonds and is expected to be much higher with properly sized wirebonds (or maybe with use of ribbon bonding technology).

R134a has a proven compatibility with essentially all materials tested, including an active gate drive circuit with an IGBT that has been submerged in this refrigerant for more than 2 years with periodic successful functional testing.

We have developed a housing for the inverter that is volume and weight efficient, where the choice of direct submersion cooling for the electronics has allowed very tight packaging of the power and control components.

Along with the housing concept, ORNL in FY 2007 developed and successfully tested power feedthroughs that can easily handle 400 amps with a very low temperature rise. These feedthrough prototypes have been shown to be leak-proof to 500 psi. They are a tapered copper-glass-copper feedthrough, based on commercially proven glass-to-metal sealing techniques, but using an ORNL developed copper-to-glass melt assembly technique.

Publications

C. W. Ayers, J. C. Conklin, J. S. Hsu, and K. T. Lowe, "A unique approach to power electronics and motor cooling in a hybrid electric vehicle environment," presented at the IEEE 2007 Vehicle Power and Propulsion Conference, Arlington, Texas, September 2007, IEEE Catalog Number 0-7803-9761-4.

J. B. Campbell, L. M. Tolbert, C. W. Ayers, B. Ozpineci, and K. T. Lowe, "Two-phase cooling method using the R134a refrigerant to cool power electronic devices," *IEEE Trans. Industry Applications* **43**(3), 648–656 (May/June 2007).

C. W. Ayers, J. S. Hsu, and K. T. Lowe, "Fundamentals of a floating loop concept based on R134a refrigerant cooling of high heat flux electronics," presented at the IEEE 22nd Annual Semiconductor Thermal Measurement and Management Symposium, Dallas, Texas, March 14–16 2006, pp. 59–64.

M. R. Starke, C. W. Ayers, J. S. Hsu, and J. C. Conklin, *Potential Refrigerants for Power Electronics Cooling*, UT-Battelle, LLC, Oak Ridge National Laboratory, Oak Ridge, Tennessee, ORNL/TM-2005/219, October 2005.

C. W. Ayers, K. T. Lowe, and J. S. Hsu, *Floating Refrigerant Loop Based on R-134a Refrigerant Cooling of High-Heat Flux Electronics*, UT-Battelle, LLC, Oak Ridge National Laboratory, Oak Ridge, Tennessee, ORNL/TM-2005/223, October 2005.

J. B. Campbell, L. M. Tolbert, C. W. Ayers, and B. Ozpineci, "Two-phase cooling method using R134a refrigerant to cool power electronics devices," 20th Annual IEEE Applied Power Electronics Conference and Exposition (APEC), **1**(1), Austin, Texas, March 6–10, 2005, pp. 141–147.

Patents

J. S. Hsu, D. J. Adams, G. J. Su, L. D. Marlino, C. W. Ayers, and C. L. Coomer, "Method of Making Cascaded Die Mountings with Spring-Loaded Contact-Bond Option," U.S. Patent 7,232,710, June 19, 2007.

J. S. Hsu, C. W. Ayers, C. L. Coomer, and L. D. Marlino, "Floating Loop Method for Cooling Integrated Motors and Inverters Using Hot Liquid Refrigerant," U.S. Patent 7,191,605, March 20, 2007.

J. S. Hsu, C. W. Ayers, C. L. Coomer, and L. D. Marlino, "Floating Loop System for Cooling Integrated Motors and Inverters Using Hot Liquid Refrigerant," U.S. Patent 6,993,924, February 7, 2006.

J. S. Hsu, D. J. Adams, G. J. Su, and L. D. Marlino, "Total Thermal Management System for Hybrid and Full Electric Vehicles," U.S. Patent 6,772,603, August 20, 2004.

J. S. Hsu, D. J. Adams, G. J. Su, L. D. Marlino, C. W. Ayers, and C. L. Coomer, "Cascaded Die Mountings with Special-Loaded Contact-Bond Options," U.S. Patent 6,930,385, August 16, 2005.

Reference

1. *Report on reliability of Wirebonds in Boiling Environment*, Pat McCluskey, University of Maryland, October 2006.

2.2 Thermal Buffer Heat Sink for Time-Averaged Operating Conditions

*Principal Investigator: C. W. Ayers
Oak Ridge National Laboratory
National Transportation Research Center
2360 Cherahala Boulevard
Knoxville, TN 37932*

Voice: 865-946-1342; Fax: 865-946-1400; E-mail: ayerscw@ornl.gov

*DOE Technology Development Manager: Susan A. Rogers
Voice: 202-586-8997; Fax: 202-586-1600; E-mail: Susan.Rogers@ee.doe.gov*

*ORNL Program Manager: Mitch Olszewski
Voice: 865-946-1350; Fax: 865-946-1262; E-mail: olszewskim@ornl.gov*

Objectives

- Determine feasibility of using phase change materials (PCMs) as a thermal buffer in an inverter heat sink to handle transient/peak loads above steady state conditions in a hybrid electric vehicle (HEV) application.
- Design a heat sink that uses PCM to store excess heat from the brief peak operating periods of the inverter and obtain thermal recovery during the steady state periods.
- Research commercially available PCMs suitable over HEV temperature ranges and operating profiles.
- Develop a model of the heat sink design to determine feasibility of using this type of heat sink in HEV applications.

Approach

- Survey commercially available thermal buffer materials.
- Generate heat sink designs.
- Model heat sink designs.
- Evaluate projected size, weight, and cost for device implementation into an inverter.

Major Accomplishments

- Developed several heat sink concepts—some were modifications of the existing baseline heat sink (pin fin heat sink). The following additional solutions were designed to meet the application needs:
 - Hollow pin design
 - PCM surrounded pin design
 - Through-pin design
 - Through-fin design
- Researched PCMs for a 65°C environment—several viable candidates available, mostly paraffin class of materials.
- Researched PCMs for a 105°C environment—some candidates available, but much fewer than with the 65°C candidates. It is believed that applicable paraffins could be easily developed based, though.
- Developed models based on the designs:
 - A temperature boundary based model
 - Improved heat flux based model
- Feasibility has been proven for this concept, showing a 30–50% heat sink volume and weight reduction possible.

Future Direction

This project was terminated at the end of FY 2007. Possible future areas of investigation include

- prototype a through-fin PCM filled heat sink per the ORNL design and test in the laboratory to validate the modeling results;
- investigate concepts based on PCM-impregnated metal and graphite foams;
- evaluate load cycles more in depth: (a) address effects on PCM choices, (b) investigate effects on PCM and coolant channel designs, (c) address effect on cost/benefit; and
- conduct more extensive survey of PCM candidates for 105°C in paraffin blend choices.

Technical Discussion

The bulk of this study was performed under a subcontract with the University of Tennessee, and results are reported in detail in Ref. 1.

Load Cycle Considerations

Initial design concepts and calculations for this project were based on a fundamental load cycle derived for the FreedomCAR Program. This cycle utilized an 18-s peak power transient to simulate vehicle acceleration, such as entering an interstate ramp or passing a vehicle at highway speed. This peak event could occur within a 120-s window, that is, a 102-s steady state period between peak periods. For an electric traction drive that is sized for 55-kW peak power and 30-kW continuous power, and applying the load cycle to it, the time-averaged power is 33.75 kW. Thus, a heat sink under this load cycle constraint can be sized for 34 kW instead of 55 kW (Figure 1).

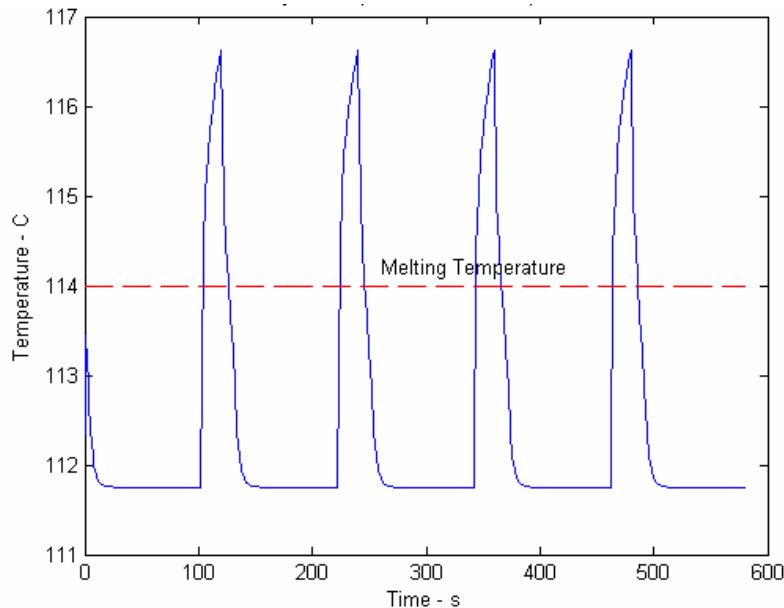


Figure 1. Example of 120-s load cycle with 18-s peaks, where a PCM is buffering the load.

Another load cycle, the US06 cycle, was examined using a Prius type vehicle as the size for the calculations. A portion of the cycle is shown below in Figure 2, where the bottom of the graph is the time-averaged heat load that the subject heat sink design would need to handle. It can be seen that on

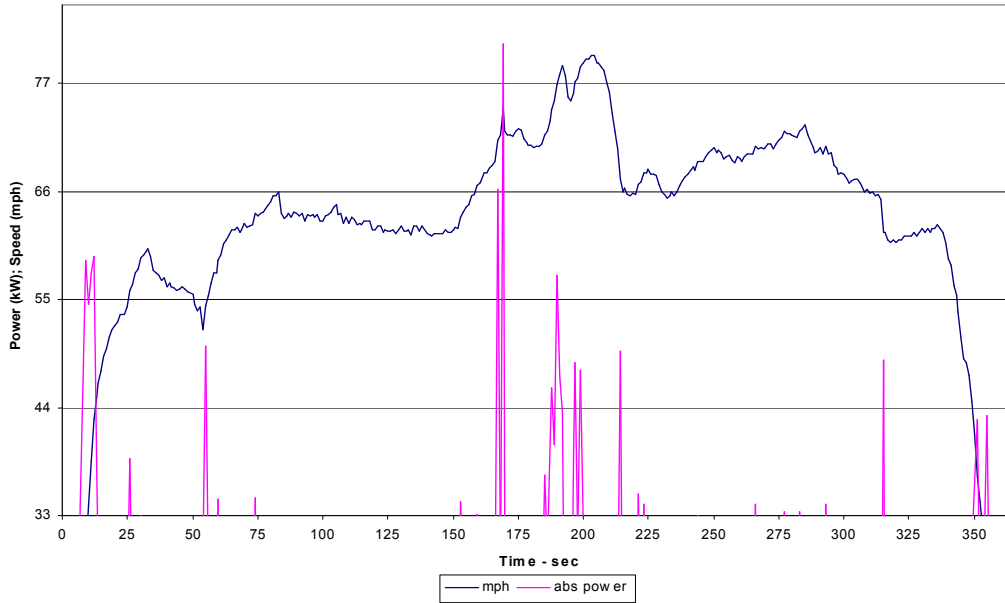


Figure 2. Graph of power and speed over time derived from the US06 load cycle for a Prius-type vehicle.

several occasions that peak absolute power rises above this level, but peak durations are typically well under the 18 s specified in the FreedomCAR cycle. It has been calculated that only about 50 s is required to recover from an 18-s peak event (re-solidify the PCM in the heat sink), where the system is operating at 30 kW continuous duty during this time.

Material Evaluations

For the first part of the study, our PCM evaluation was based on a 65°C coolant scenario. A list of 18 commercially available PCM materials was selected for study.

- | | |
|--------------------|--|
| 1. Rubitherm RT65 | 10. E72 |
| 2. Rubitherm RT80 | 11. E83 |
| 3. Rubitherm RT100 | 12. E89 |
| 4. Paraffin 6403 | 13. Salt Eutectic 1 |
| 5. Paraffin 6499 | 14. Salt Eutectic 2 |
| 6. A61 | 15. Salt Eutectic 3 |
| 7. Stearic acid | 16. DOW TESC-190 |
| 8. Acetamide | 17. Low Melt Alloy 50 Bi 26.7 Pb 13.3 Sn 10 Cd |
| 9. E71 | 18. Low Melt Alloy 52 Bi 30 Pb 19 Sn |

These materials range in cost from \$2–\$10, with some estimation involved to attempt to approach volume quantities as opposed to small research quantities.

During the second part of the study, later in the year, a focus was made on utilizing a 105°C coolant environment. This requires a PCM that melts at a much higher temperature, and a survey was conducted to see what was commercially available for this temperature range. Six candidates were found during this survey:

1. Erythritol
2. MgCl₂
3. Rhombic sulfur
4. Acetanilide

5. Ammonium acetate
6. Ammonium formate

It is believed that paraffins should be added to this list, although none were found at this point to be commercially available. These should be simply a blend of paraffin material to meet the melt temperature specification, so something could be easily developed depending on market need.

Heat Sink Concepts

ORNL/UT developed several heat sink designs to begin comparisons to the Semikron baseline heat sink. The first was simply a PCM bound layer (pin-fin surrounded with PCM) placed in between the Semikron heat load and the existing heat sink (using a computer model), and is depicted below in Figure 3.

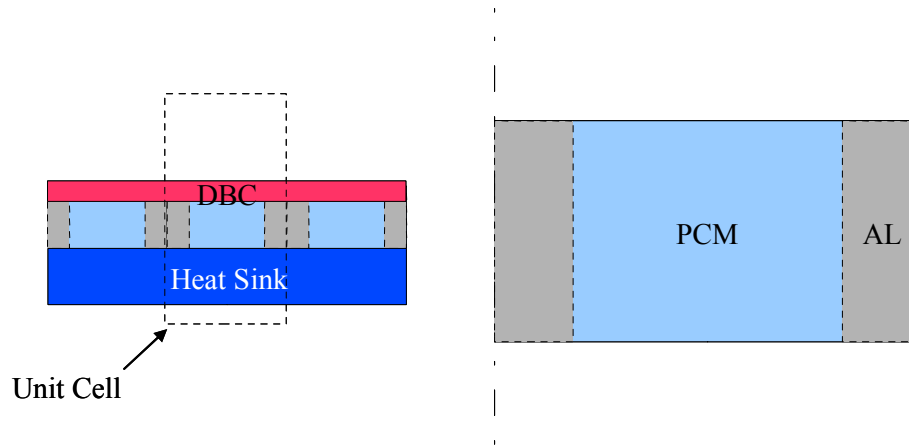


Figure 3. Diagram of the PCM-filled pin-fin insert used as first model in comparison to baseline heat sink.

This first model did not show beneficial improvements in volume, mass, or cost due to some required heat spreading material and pin match-up between layers. This concept was abandoned for concepts that were built from scratch for this application.

Three new designs were investigated: the PCM-surrounded pin design, a hollow-pin design (Figure 4), and a through-pin design (Figure 5).

These designs were all evaluated with a thermal finite element analysis (FEA) model and exhibited volume reductions of 25–50% and mass reductions of 50–75%. These cases were run in a 65°C coolant environment.

The through-pin design was the best of the three designs but, while looking very attractive in the model, exhibits a geometry that would be very hard and expensive to manufacture. This led to a process of thinking that would bring the benefits of this model to a geometry that is much more easily constructed. Thus, the through-fin design was developed, based on an extruded aluminum section that provides the coolant channels and PCM containment volumes.

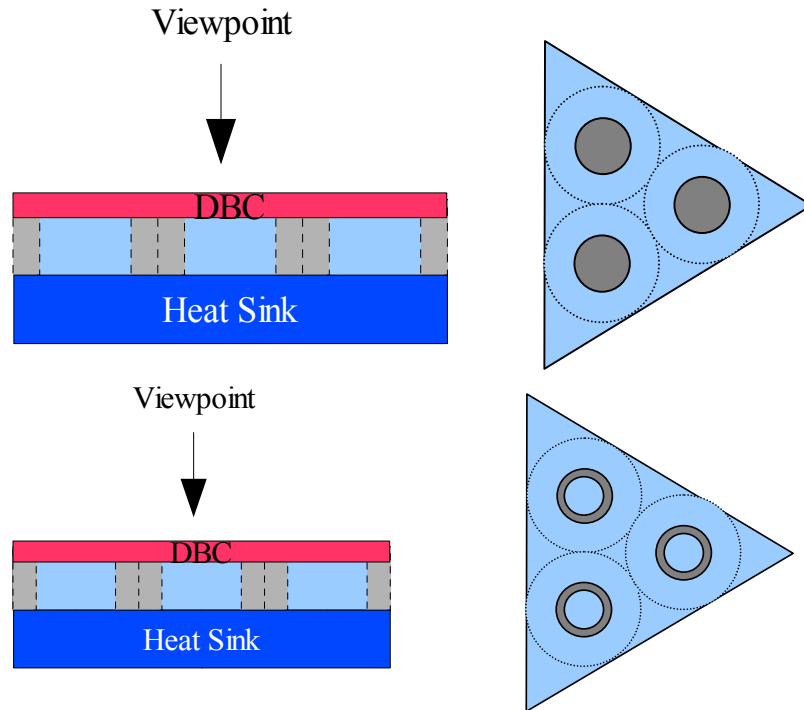


Figure 4. Upper concept depicts a PCM-surrounded pin design, while the lower unit is a hollow-pin with PCM inside and outside.

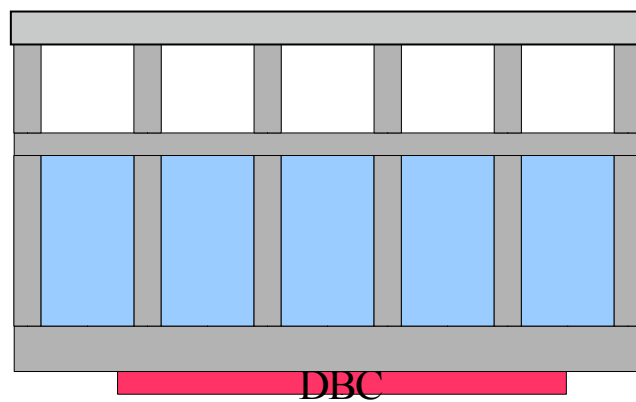


Figure 5. Through-pin design where pin fins extend from the bottom heat load surface past the PCM channels (blue) into and through the coolant flow channels at the top (white).

Two versions of this extruded section idea were studied and are shown in Figure 6 below:

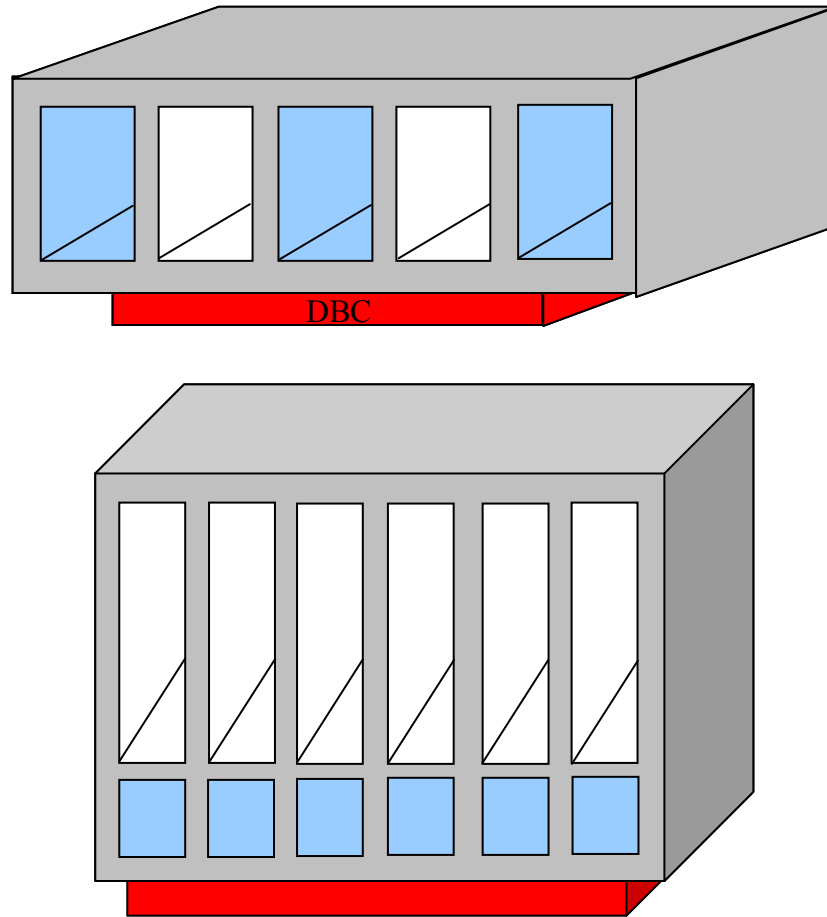


Figure 6. Upper sketch is for a parallel channel PCM/coolant extruded section heat sink, and the lower unit is the through-fin heat sink design.

The upper unit in Figure 6 exhibited fairly good performance, but it presents challenges in sealing the PCM and water from each other and the electronics. The lower unit is the design of choice for ORNL and has extruded fins that protrude from the heated surface all the way through the section into the coolant channels. Sealing on this heat sink is simpler than the parallel channel unit, with reduced zones of interference between coolant, PCM, and electronics.

The first computer model developed was based on temperature boundary conditions. It is of interest to evaluate the heat sink performance based on its ability to maintain an interface temperature between the heat sink and the load (DBC layer) at 125°C , while utilizing a coolant (the ambient condition) at either 65°C as in the earlier PCM cases or 105°C as in the final studies.

The temperature boundary based model provides a simpler closed form solution but has less accuracy for this application. It is of particular interest to maintain the silicon power device junction at or below 125°C during a maximum heat flux condition. It was decided to utilize a model that used heat flux as a boundary condition instead of temperature to get a more accurate result. The modeling requires a more complicated, iterative solution but provides better results. The final model that was used was based on this concept.¹

Results/Size Reductions

The developed computer model was used to compare different PCM characteristics and different heat sink concepts for their effect on volume, mass, and cost.

It can be seen from Figure 7 that all the materials shown exhibit at least small improvements over the baseline, and some exhibit very large improvements in all three desired parameters, volume, mass, and cost.

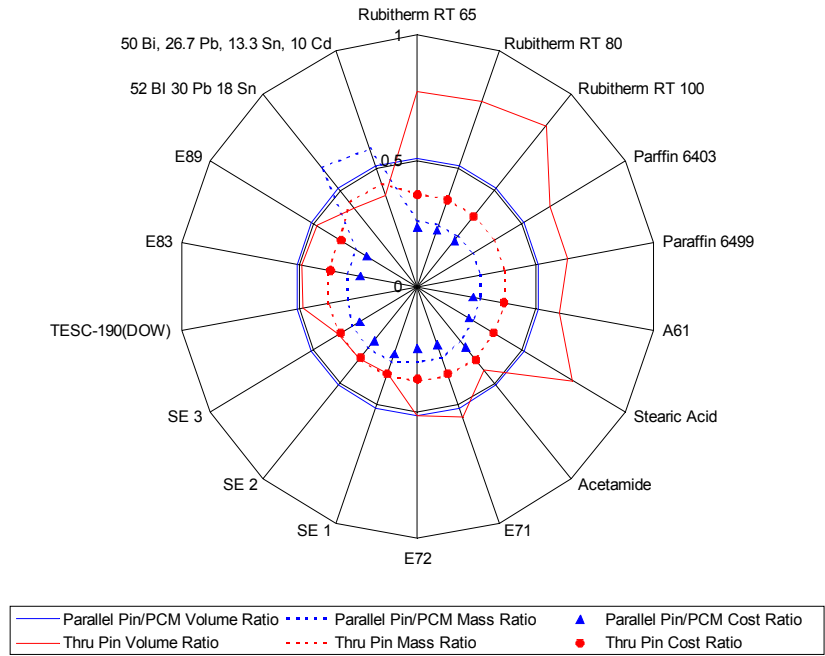


Figure 7. Volume, mass, and cost ratios of various PCM/heat sink combinations in comparison to baseline Semikron inverter heat sink using the early designs.

After the shift of focus to a 105°C environment, the six higher-temperature PCM candidate materials were evaluated using the favored heat sink configuration, the through-fin design. Table 1 shows volume and mass ratios in comparison with the baseline heat sink. The best candidate from this group was the Erythritol, with a 43% reduction in volume and a 48% reduction in mass. Cost numbers for these materials were more difficult to analyze, because large-quantity cost numbers were not readily available.

Table 1. Commercially available 105°C coolant PCM candidates

Material	Design 6—through-fin	
	Volume ratio	Mass ratio
Ammonium formate	0.65	0.60
Rhombic sulfur	0.75	0.75
Acetanilide	0.65	0.59
Erythritol	0.57	0.52
Ammonium acetate	0.68	0.62
MgCl ₂ 6H ₂ O (E117)	0.62	0.57

Conclusions

1. It was found for the FreedomCAR and US06 load cycle cases that a through-fin PCM buffered heat sink concept is feasible for both 65°C and 105°C coolant applications. About 30–50% reductions in volume and/or mass can be achieved with this concept.
2. There are numerous PCM choices for the 65°C case, where the PCM melt temperature is approximately 70–75°C.
3. There are fewer PCM choices for the 105°C case (melt temperature 105–120°C), but demand could easily multiply choices (i.e., paraffin blends not presently commercially available, probably due to lack of applications).
4. The PCM/buffer concept is an enabler to utilize 105°C for 125°C silicon-based systems.
5. There is essentially no real cost change for the PCM/buffer concept.

Reference

1. *Thermal Buffer Heat Sink for Time-Averaged Operating Conditions*, subcontract report, K. T. Lowe, R. V. Arimilli, University of Tennessee, C. W. Ayers, Oak Ridge National Laboratory, September 1, 2007.

2.3 Low-Thermal-Resistance IGBT Structure

Principal Investigator: Thomas P. Abraham

National Renewable Energy Laboratory

1617 Cole Blvd

Golden, CO 80401-3393

Voice: 303-275-3084; Fax: 303-275-4415; E-mail: thomas_abraham@nrel.gov

DOE Technology Development Manager: Susan A. Rogers

Voice: 202-586-8997; Fax: 202-586-1600; E-mail: Susan.Rogers@ee.doe.gov

NREL Program Manager: Kenneth Kelly

Voice: 303-275-4465; Fax: 303-275-4415; E-mail: kenneth_kelly@nrel.gov

Objectives

The objective of this project is to reduce the thermal resistance between the silicon die of the IGBT and the coolant by developing an optimized heat exchanger that eliminates the thermal interface material layer. By reducing the thermal resistance, a target coolant temperature of 105°C can be used to cool the inverter electronics. This project will address one of the important targets of APEEM program which is the use of coolant at 105°C.

Approach

NREL has conducted extensive investigation of the low thermal resistance IGBT structure using CFD, thermal and structural modeling tools [1, 2]. However, the actual hardware testing and evaluation is needed for proof of concept. Working under an existing CRADA with Semikron, NREL will build a small scale and a full scale prototype inverter to be tested on our high heat flux test loop. Experimental results will be used to validate the current modeling results and to improve the existing models. An enhanced design will be developed based on the experimental results and additional modeling to optimize the thermal performance.

This research will significantly improve on existing technology, which currently dissipates 60 W/cm² at a temperature difference of about 50°C.

The major remaining activities for this project are:

- Fully characterize the thermal performance of the prototype low thermal resistance IGBT. This will validate and improve the structural and thermal simulations. The diagnostic tests and characterization shall be compared with current technology to benchmark the progress.
- Work with Semikron to optimize the design of the heat exchanger and implement any newly available thermal control technology being developed in the APEEM program such as boiling jets, oscillating jets, spray cooling, surface enhancements.

Major Accomplishments

- Awarded patent for “Low Thermal Resistance Power Module Assembly” “United States Patent Number 7,190,581.
- Completed flow test on Gen 13 heat exchanger prototype.
 - flow variation between the jets for Gen13 prototype has been quantified and is below 8%.
 - pressure drop for Gen13 is half of the baseline design with elliptical fins.

- A detailed plan has been developed for powering the IGBTs and the diodes for thermal testing.
- Design of the gasket grooves is complete and an appropriate gasket has been identified which would not leak during the life of power electronics (15 years).
- Design improvement to prevent leakages and simplify the next-generation heat exchanger for the low-thermal-resistance IGBT structure is complete.
- Prototype parts are about to be machined and sent to Semikron for the assembly of a complete, functioning unit.

Future Direction

Flow simulation and testing: Flow simulations and tests are planned for the current design with a reduced target distance between the jet exit and the DBC. A more effective impingement is expected for the reduce target distance.

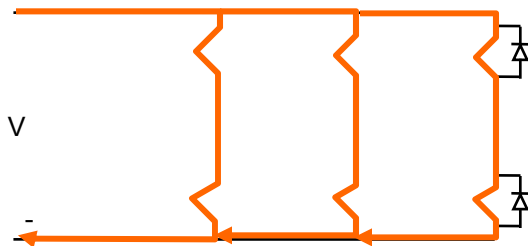
Thermal simulation and testing: Thermal simulations and testing are planned that would predict die temperature and compare to actual test results. This would employ NREL’s ABC100, 125-kW bi-directional power supply (Figure 1). It would also employ recently developed environmental chamber capability for temperature and humidity control.



Figure 1. Environmental Chamber and ABC100—125-kW bi-directional power supply

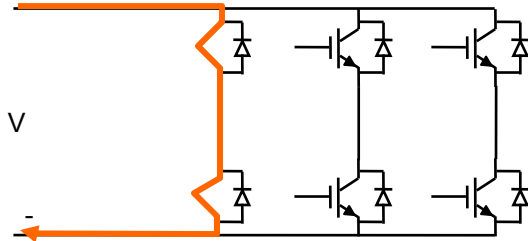
A detailed plan has been developed for thermal testing. It includes several options for powering the IGBTs and the diodes of the Semikron inverter.

A. **Option 1:** All switches are closed



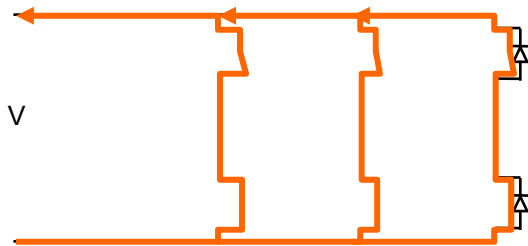
Input voltage will be DC. All the switches will be closed, that is all the phases will have the current flowing. There will be heat dissipation in all the IGBTs. There will not be any power dissipation in the diodes. Heat dissipation in the IGBTs may not be balanced if the resistances of the IGBTs are not equal.

B. Option 2: One top/bottom switch is closed



Input voltage will be DC. Switches of only one phase will be closed, the rest will be open. Heat dissipation will be in the IGBTs of only one phase. The IGBTs in the rest of the two phases will have no heat dissipation. There will not be any heat dissipation in the diodes.

C. Option 3: All switches are open



Input voltage will be DC and the polarity will be switched. There will be heat dissipation in all the diodes. There will not be any heat dissipation in the IGBTs.

Gasket leakage and blow-by tests: Careful attention must be given to the leakage around the bottom gaskets because the coolant must be isolated from the electronics. Blow-by tests will be performed for possible leakage around the nozzle plate.

Optimization studies: Once the simulation results are validated using the test data, optimization studies will be performed with respect to the jet diameters, distance between the jets, number of jets, target distance, inlet/outlet regions, and other parameters.

Reliability studies: Even though the direct back side cooling is very promising from the standpoint of heat transfer, long term reliability is a concern. For the optimized design, reliability studies will be conducted.

Technical Discussion

NREL has recently developed a patented IGBT structure (US Patent # 7190581) that eliminates several layers in the package structure to enable its effective cooling with a 105°C inlet coolant temperature. In the patented design, holes are cut through the base plate all the way to the backside of the DBC (see Figure 2(a)). Nozzles are positioned under the DBC with coolant jets impinging on the backside. The nozzles are positioned such that the jets are directly under the IGBTs and diodes. Because the coolant comes in direct contact with DBC, thermal resistance between the power module and the heat exchanger is eliminated. This design combines the benefits of reducing the overall thermal resistance and applying high convective heat transfer coefficients. A recently published state-of-the-art review of high heat flux cooling technologies refers to direct back side cooling as a very promising technology in the near future [3]. NREL has developed thermal and structural models of the proposed low thermal resistance architecture to assess the design feasibility. Simulations showed very promising results, with overall package thermal resistance reduced by as much as 60%. The weight of the base plate could be reduced as portions of the base plate are eliminated to allow direct coolant access to the DBC. We modeled this structure with various hole sizes, and performed structural and thermal analyses for it (Figure 2(b)).

Figure 3 shows the results of an NREL thermal analysis, showing typical temperature differences across different layers for the conventional IGBT structure and also the low thermal resistance IGBT structure. For the conventional IGBT structure, the temperature increase from the heat exchanger's surface to the chip is about 35°C. The low thermal resistance IGBT structure allows thermal grease to be completely eliminated and the temperature difference is only about 8°C.

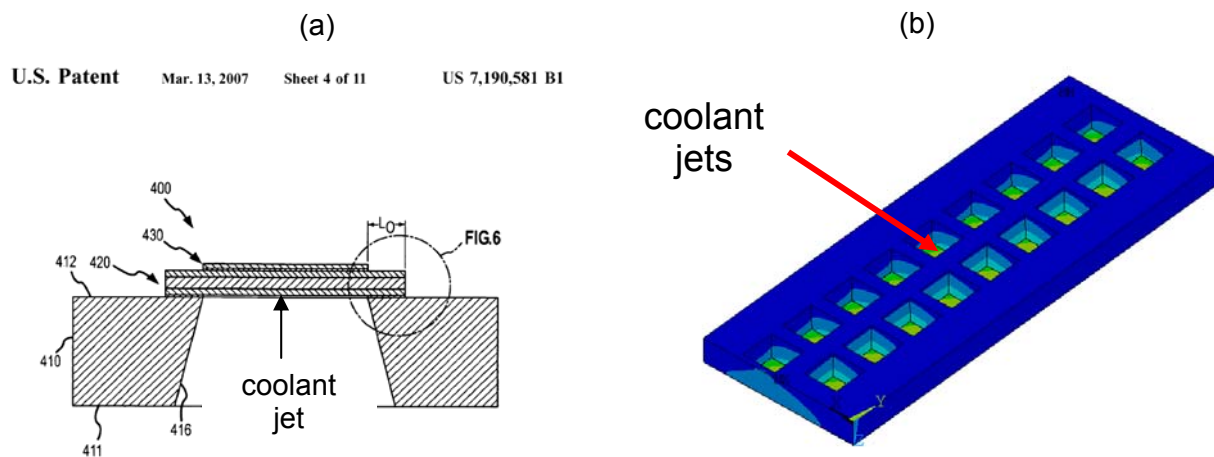


Figure 2. Direct backside cooling of power inverter, (a) cross-section of NREL patented backside cooling, (b) direct backside cooling thermal model

The low thermal resistance IGBT structure with direct backside cooling could have a significant impact on the thermal control of power electronics. If successful, this technology could enable the US automotive industry to eliminate a separate cooling loop and also allow the use of engine coolant at 105°C to cool the power electronics unit directly. This approach also has the potential of reducing the weight of the heat exchanger. In the existing technology, the heat exchanger may represent as much as 30% of the weight of an inverter. The direct backside cooling apparatus shown here could reduce that portion to 20% of the total weight of the inverter. While not fully optimized, our simulations have shown that the current technology using serpentine channel fin heat exchangers can remove approximately 60 W/cm²; the low resistance IGBT structure could remove 100 W/cm² with 105°C coolant, or 2/3 more heat. The direct backside cooling approach appears very promising in terms of cost, weight, and volume reductions. A number of technical challenges, such as the long term reliability of the required seals and the potential for

erosion at the DBC, still remain. Additionally, aspects of the design, such as the nozzle geometry, have yet to be fully optimized. NREL will be conducting experimental investigations of these attributes with a prototype heat exchanger assembled onto an industry supplied inverter. We will also be working with an industry partner to demonstrate the concept integrated with an inverter.

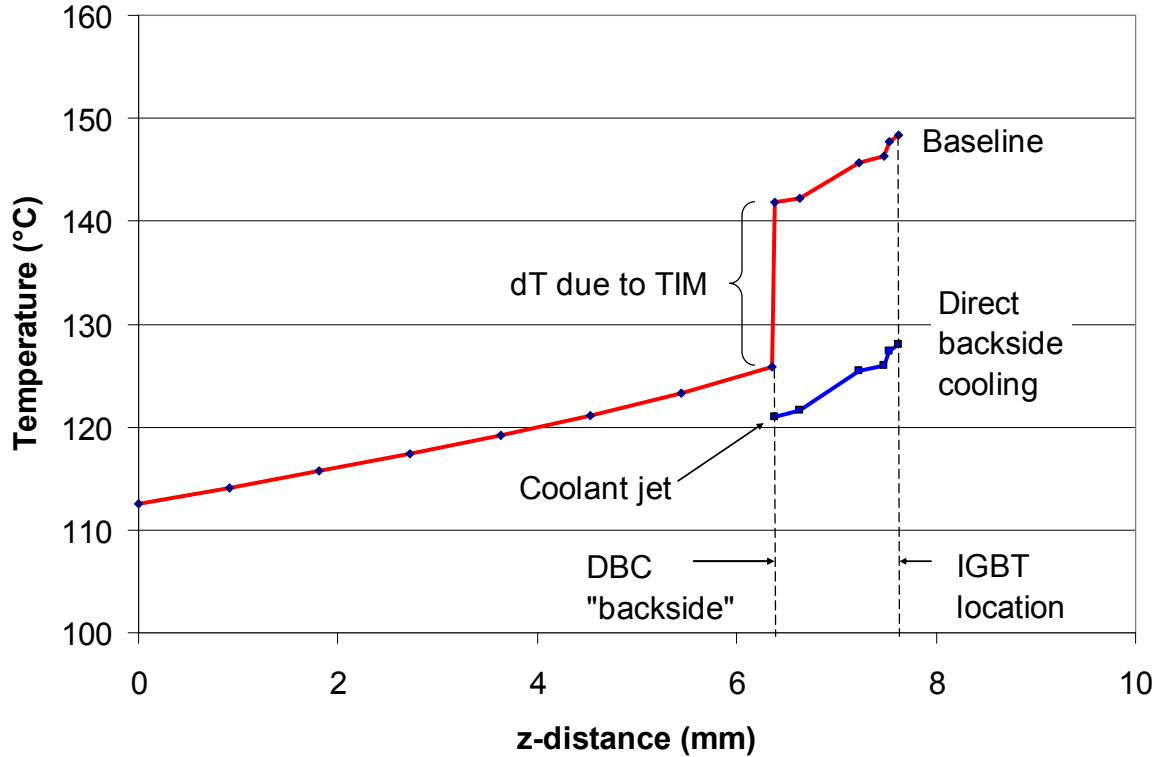


Figure 3. Temperature at different layers for the conventional IGBT structure for baseline configuration vs. a direct backside cooling approach

Simulation and Analysis of Low-Resistance IGBT Structure

The basic concept of Gen13 design is shown in Figure 4. The aluminum base plate, nozzle plate, and flow channel plate have been designed as individual components to reduce the cost of fabrication. Structural simulations found the maximum stresses and deflections to be compatible with Semikron’s assembly process, which applies 3000 psi to the DBC during assembly [1]. The three-dimensional solid model of the coolant domain for the heat exchanger was created using SolidWorks, which is an integrated CAD/CAM/CAE software. The CAD data was exported in IGES format, which is then imported into ICEM-CFD, which is volume-meshing software for creating hexahedral, tetrahedral, and hybrid meshes. The key design parameters such as the flow rates from the individual nozzles, pressure drop, and temperature of each design can be computed from CFD simulations. The CFD/thermal solver used was FLUENT 6.3.26 (2006), which is a general purpose computer program for modeling fluid flow and heat transfer. By repeating the above process, a series of heat-exchanger designs can be evaluated and then the prototype of the optimized design can be built for validation test. For purposes of flow testing, the inlet temperature is fixed at 30° C. The flow rates used for the simulations are 10 lpm and 20 lpm. The coolant used was water.

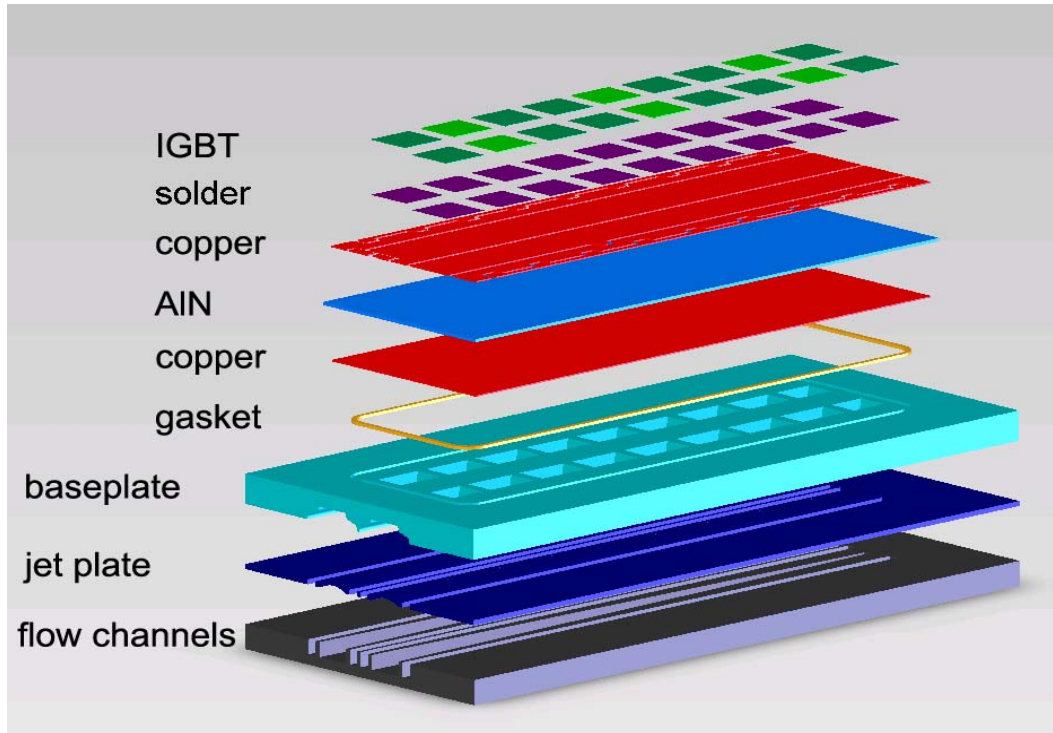


Figure 4. Detailed view of low-thermal-resistance IGBT structure - IGBT is an insulated gate bipolar transistor, the electronic device requiring cooling; AlN is aluminum nitride, a ceramic that insulates electrically, but not strongly thermally and is sandwiched between copper layers to form the direct-bonded-copper or DBC layers. The innovative base plate assembly jets water directly against the DBC rather than having to cool it by conduction via a solid cold plate.

Figure 5 shows results from CFD simulations of the velocity field near the DBC for a flow rate of 10 lpm. Figure 6 shows that flow rates from the individual jets are fairly uniform with variation of less than 8%. It is surmised that once the outlet plenum fills up, fairly constant outlet pressure develops which causes almost equal flow from the individual jets. Each nozzle jet shown in Figure 6 provides jet impingement directly on the backside of an individual IGBT or diode (shown in Figure 7). Uniform flow through these nozzles is required to achieve temperature uniformity across all the dies. This is an improvement over the existing technology that sweeps coolant from one end to another—picking up heat along the way. This causes the last die in the chain to see a higher temperature than the first.

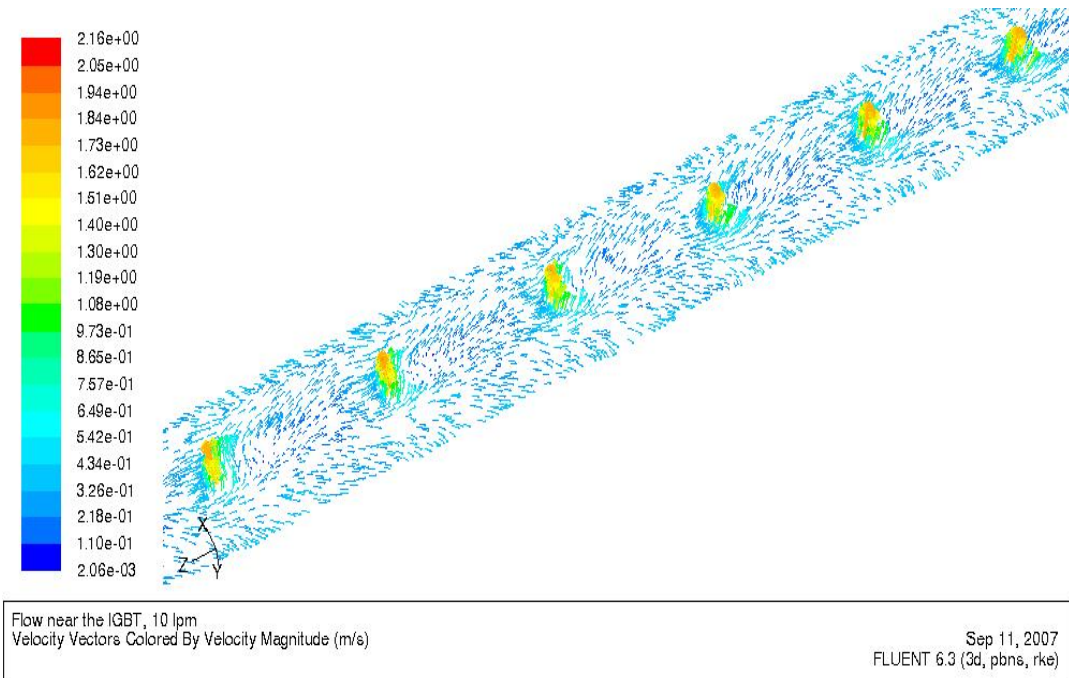


Figure 5. Velocity field near the DBC for a flow rate of 10 lpm

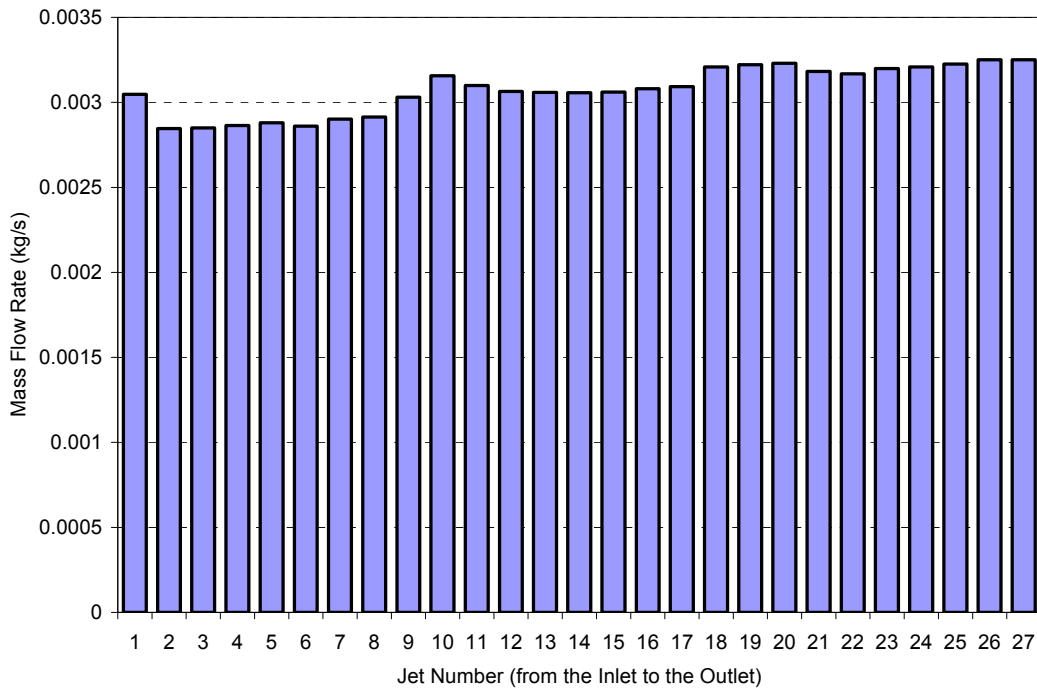


Figure 6. Variation of flow among the jets at 10 lpm

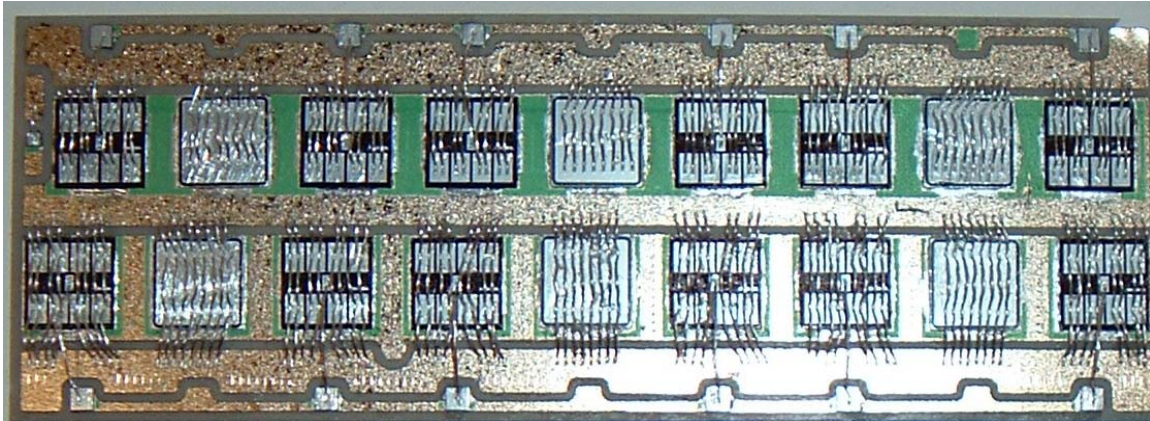


Figure 7. Top view of circuit board containing IGBTs and diodes mounted to a base plate. The DBC surface on the opposite side is cooled by the impinging jets.

Flow Tests

High-heat-flux test-loop facility developed by NREL is as shown in Figure 8. It consists of a reservoir, pump, filter, mass flow meters, turbine flow meters, and valves for regulating flow rates. The loop is fully instrumented with pressure sensors, thermocouples for monitoring temperatures, and a data acquisition system controlled by LabView.

As shown in figure 9, the pressure drop across the heat exchanger for the Gen13 design is about half that for the elliptical design. It is important to note that the baseline design has a single inlet/outlet while the Gen13 design has two inlets/outlets. It appears that significant amount of pressure drop is occurring near the inlet/outlet, which is the possible reason why the Gen13 design has a lower pressure drop.

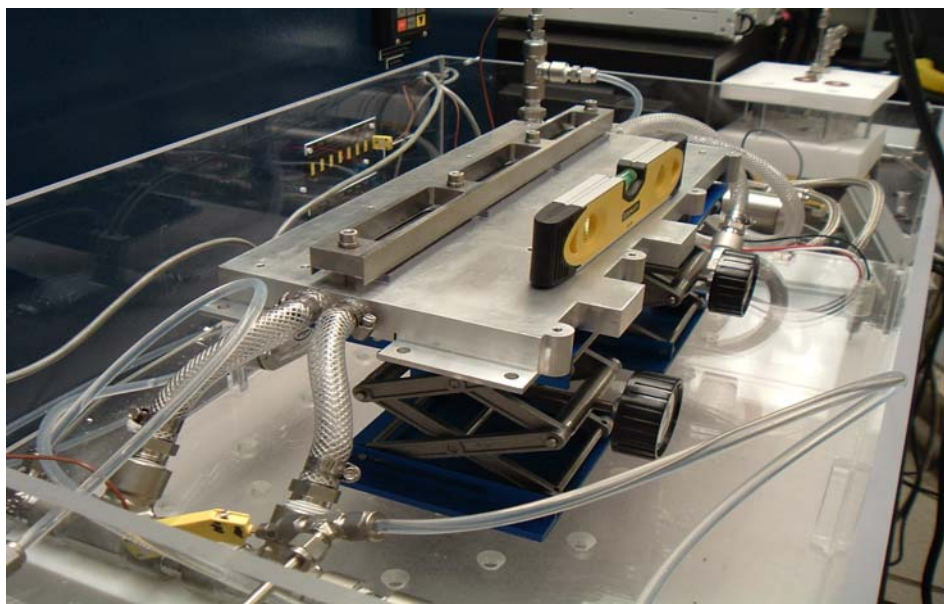


Figure 8. High-heat-flux test facility used for flow tests

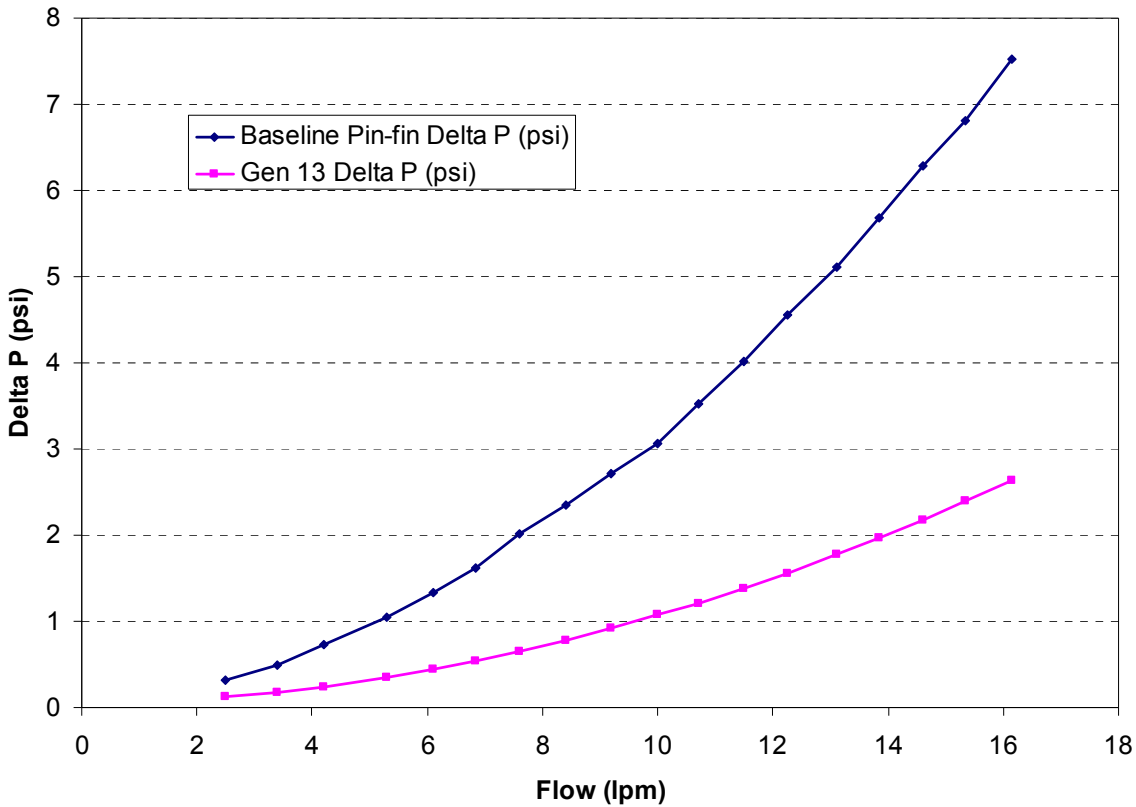


Figure 9. Comparison of pressure drops for the baseline pin-fin design and the Gen13 design

Blow-by Tests

Blow-by tests were performed at a nominal temperature of 24°C to account for the amount of leakage around the nozzle plate and around several structural bosses. Knowing the level of blow-by is important because any significant amount of blow-by would reduce the effectiveness of jet impingement. For these tests, the nozzles were closed and the only leakage paths were the ones around the nozzle plate and around the bosses. Table 1 shows the levels of leakage for different pressures. The operating pressures chosen were in the range relevant to the actual operation. Note that the pressure measured during normal operation was approximately 1 psi for a flow rate of 10 lpm (see Figure 11). The leakage was as high as 7.8% at a pressure drop of 2 psi.

Table 1. Leakages at different pressures

Pressure, psi	Total Flow lpm	Leakage Flow Rate lpm	Percentage of Total, %
1	9.65	0.63	6.5
1.5	12.0	0.87	7.25
2	14.0	1.09	7.8

Because of the significance of this level of leakage, we incorporated an additional gasket groove on the ledge on which the nozzle plate rests. Also, the bosses near the inlet and the outlet were eliminated because they could have been potential leakage paths.

Gasket Leakage Issues

For long term reliability, the bottom and top gaskets should not leak for the life of power electronics (15 years). To effectively address the leakage issues around bottom and the top gaskets, NREL partnered with a gasket vendor. To test the robustness of the design, the system will be subjected to thermal cycling wherein temperature of the engine coolant is cycled between -40°C and 125°C . Design of these grooves was critical because any leakage around the bottom gaskets would cause the coolant to come in contact with the electronics. After the Semikron assembly process, the contact force that the electrical bus bars impose on the DBC is about 20 N/mm. It is assumed that the entire load goes to the gasket. The gaskets chosen are made of material 60 Durometer Buna-N with a depth of 0.031" and a tolerance of 0.003". To confirm that the gaskets will not leak for the life of power electronics, actual testing with thermal cycling is required and is planned for FY 2008.

Updated Design

During FY 2007, we improved on the design for ease of assembly and to prevent leaks by reducing the number of contact surfaces. The structural bosses near the inlet/outlet were eliminated and replaced with solid material. Blow-by tests indicated that there is significant amount of leakage around the nozzle plate. To eliminate this blow-by, a gasket groove was incorporated on the ledge on which the nozzle plate rests. The width of the ledge was increased to 5 mm to accommodate the screws to make sure that nozzle plate compresses firmly onto the base plate. To increase the effectiveness of impingement, the target distance was reduced to 3 mm from 6.35 mm.

Conclusion

The low thermal resistance IGBT structure with direct backside cooling could have a significant impact on the thermal control of power electronics. If successful, this technology could enable the US automotive industry to eliminate a separate cooling loop and also allow the use of engine coolant at 105°C to cool the power electronics unit directly. This approach also has the potential of reducing the weight of the heat exchanger. In the existing technology, the heat exchanger may represent as much as 30% of the weight of an inverter. The direct backside cooling apparatus shown here could reduce that portion to 20% of the total weight of the inverter. While not fully optimized, our simulations have shown that the current technology using serpentine channel fin heat exchangers can remove approximately 60 W/cm^2 ; the low resistance IGBT structure could remove 100 W/cm^2 with 105°C coolant, or 2/3 more heat. The direct backside cooling approach appears very promising in terms of cost, weight, and volume reductions. A number of technical challenges, such as the long term reliability of the required seals and the potential for erosion at the DBC, still remain. Additionally, aspects of the design, such as the nozzle geometry, have yet to be fully optimized. NREL will be conducting experimental investigations of these attributes with a prototype heat exchanger assembled onto an industry supplied inverter. We will also be working with an industry partner to demonstrate the concept integrated with an inverter.

Flow simulations and tests were performed for Gen13 design. CFD simulations showed that the variation of flow rates from the nozzles were below 8%. The pressure drop for Gen13 design is half of the baseline design with elliptical fins. To improve the effectiveness of impingement onto the DBC, the target distance was reduced to 3 mm. To address the leakage issues around the top and bottom gaskets, geometries of the gasket grooves were designed and appropriate gaskets have been identified. To reduce blowby around the nozzle plate, reduce the number of possible leakage paths, and for the ease of manufacturability, the design has been modified and simplified further. A detailed thermal testing plan for powering the IGBTs and the diodes has been developed. A prototype of the simplified heat exchanger is in the process of being machined.

References

- [1] Gawlik, K., 2006, “Low Thermal Resistance IGBT Structure”, NREL Technical/Milestone Report.
- [2] Benhammou, D., 2005, “Jet Impingement Experiment Study”, NREL Technical/Milestone Report.
- [3] Agostini, B., Fabbri, M., Thome, J. and Michel, B., 2007, “State of the Art of High Heat Flux Cooling Technologies”, *Heat Transfer Engineering*, 28(4), 258-281.

Patents

- [1] Hassani, V.; Vlahinos, A.; Bharathan, D. 2007. “Low Thermal Resistance Power Module Assembly.” United States Patent Number 7190581.

2.4 Plug-In Hybrid Electric Vehicle Impacts on Power Electronics and Electric Machines

Principal Investigator: Kevin Bennion

National Renewable Energy Laboratory

1617 Cole Blvd

Golden, CO 80401-3393

Voice: 303-275-4447; Fax: 303-275-4415; E-mail:Kevin_Bennion@nrel.gov

DOE Technology Development Manager: Susan A. Rogers

Voice: 202-586-8997; Fax: 202-586-1600; E-mail: Susan.Rogers@ee.doe.gov

NREL Program Manager: Kenneth Kelly

Voice: 303-275-4465; Fax: 303-275-4415; E-mail: Kenneth_Kelly@nrel.gov

Objectives

With the growth in both the awareness of and interest in plug-in hybrid electric vehicles (PHEVs), the need to understand their potential impacts on the power electronics and electric machines (PEEMs) is apparent. This report summarizes work to quantitatively compare the impacts of PHEVs on the PEEM systems as compared to hybrid electric vehicles (HEVs) to support qualitative expectations. This analysis, funded through the PEEM task, takes advantage of previous work performed by the Vehicle Systems Analysis (VSA) group and applies it to analyzing the impacts of PHEVs on PEEM components. The primary goals of the analysis include the following:

- Provide an overview of energy management strategies with impacts on PEEM systems.
- Illustrate impacts on PEEM components.
- Determine and show cost impacts of PHEVs.

Approach

The analysis consists of both a review of previous work done by the VSA group and an extension of their work directly related to the power electronics and electric machines. The review of the work performed by the VSA group is intended to provide the following:

- Overview of published work involving impacts of different energy management strategies.
- Background of vehicle “real-world” drive cycles used to simulate vehicle operation.
- Understanding of simulated HEV, PHEV20, and PHEV40 configurations.
- Background of cost estimates used within the analysis.

With this understanding of the VSA group’s modeling assumptions, the data were used to illustrate the potential impacts on the electric drive system including the power electronics and electric machines. The analysis focused on the following items:

- PHEV continuous power operation as compared to HEVs.
- PHEV battery bus voltage fluctuation.
- FreedomCAR PEEM cost target impacts on PHEV affordability.

Major Accomplishments

- This analysis was presented to the Advanced Power Electronics and Electric Machines (APEEM) team on August 15th at Oak Ridge National Laboratory.
- This analysis was presented to the Vehicle Systems Analysis group manager on September 26th in Washington, D.C. at the NERL offices.

Future Direction

Since this analysis focused on one type of PHEV configuration and energy management strategy, the primary next step involves additional analysis of other data available from the VSA group. This includes simulated data of different HEV and PHEV configurations, along with real vehicle test data. Owing to the different VSA responsibilities of the national laboratories regarding PHEVs, this would require support from other laboratories to access available data. As PHEV specifications evolve, the cooperation between laboratories would support a better understanding of the thermal impacts of PHEVs on the PEEM components. This would feed into requirements for thermal control research and the overall PEEM task. Additional next steps for this analysis include the following.

- Share the analysis with the VSA Technical Team and the Electrical and Electronics Technical Team.
- Publish report of PHEV impacts in a related conference or journal.

Technical Discussion

Energy Management Strategies

NREL' VSA Group previously completed a comparison of energy management strategies of PHEVs [1]. A summary of their work is included below to highlight the impacts of the energy management strategy on power electronics and electric machines. More details can be found from the referenced report. The strategies discussed in the report are listed below:

- All Electric Range (AER).
- Blended: Engine-Dominate.
- Blended: Electricity-Dominate.

All Electric Range

The all electric range (AER) strategy emphasizes all electric vehicle operation over a desired distance in which the battery discharges to a minimum threshold. This mode of operation is known as the charge depleting (CD) mode, and it is illustrated in Figure 1. Once the battery state-of-charge (SOC) reaches the minimum threshold, the strategy attempts to maintain the SOC of the battery within a desired window similar to conventional HEVs. This second mode is known as the charge sustaining (CS) mode of operation. The critical feature of an AER PHEV is the sole use of the electric machine or "motor" during the CD operating mode. This requires the electric drive components to meet the full power requirements of the vehicle. Once the CS region is reached, the gasoline engine must turn on to maintain the SOC of the battery

The main disadvantage of the AER strategy is the need to size the electric drive system to meet all of the vehicle power and torque demands. This leads to a larger and more expensive system. However, there is no fuel use or emissions during the CD mode of operation. In addition, the AER strategy could receive larger credits towards the California Air Resource Board's (CARB) zero-emission vehicle (ZEV) requirement, which currently provides vehicles with a minimum ten mile continuous all-electric operating range over the Urban Dynamometer Driving Schedule (UDDS) a larger credit weighting [2-4]. This could

change depending on how CARB decides to treat blended PHEVs. Table 1 summarizes the key advantages and disadvantages of the AER strategy.

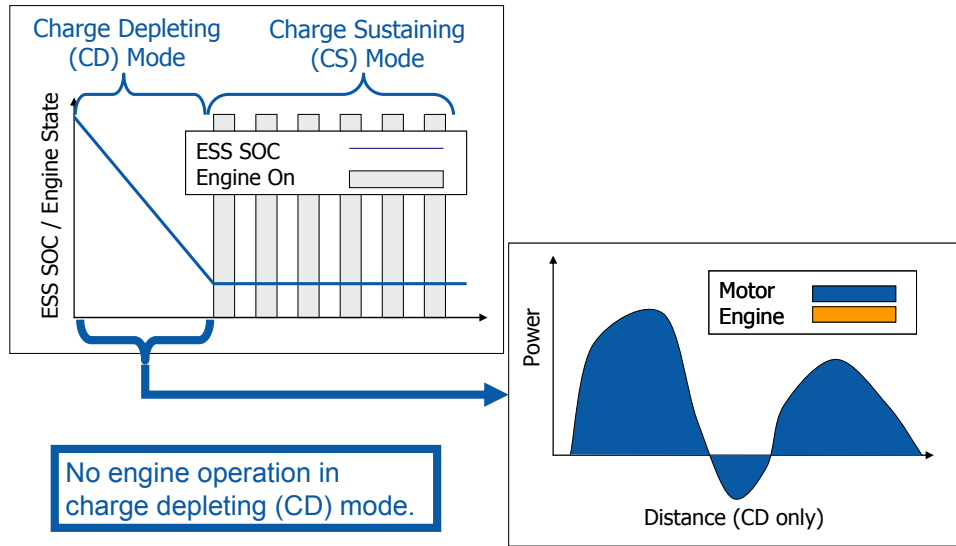


Figure 1. All electric range operation summary.

Table 1. All electric range strategy characteristics.

Disadvantages	Advantages
<ul style="list-style-type: none"> • Larger electric drive • Higher cost • Sensitivity to drive cycle aggressiveness 	<ul style="list-style-type: none"> • No CD Mode Emissions • Full use of battery over shorter driving distances • California Air Resource Board (CARB) Zero-emission vehicle (ZEV) credits

Blended: Engine-Dominate

The engine-dominate blended strategy attempts to maximize the engine or overall system efficiency. This strategy extends the distance the vehicle operates during the CD mode. As shown in Figure 2, the electric machine supplements the engine as needed in the CD mode to meet power demands or maximize system efficiency. When the battery reaches its lower SOC threshold, the CS mode begins and the vehicle operates similar to current HEVs.

The key advantage of the engine-dominate blended strategy is the lower power demand on the electric drive components. This allows for smaller and cheaper components. The benefits of the engine-dominate blended strategy depend on the driving distance between charging events. When driven for short distances, the battery will be underutilized. Table 2 summarizes the key advantages and disadvantages of the engine-dominate blended strategy.

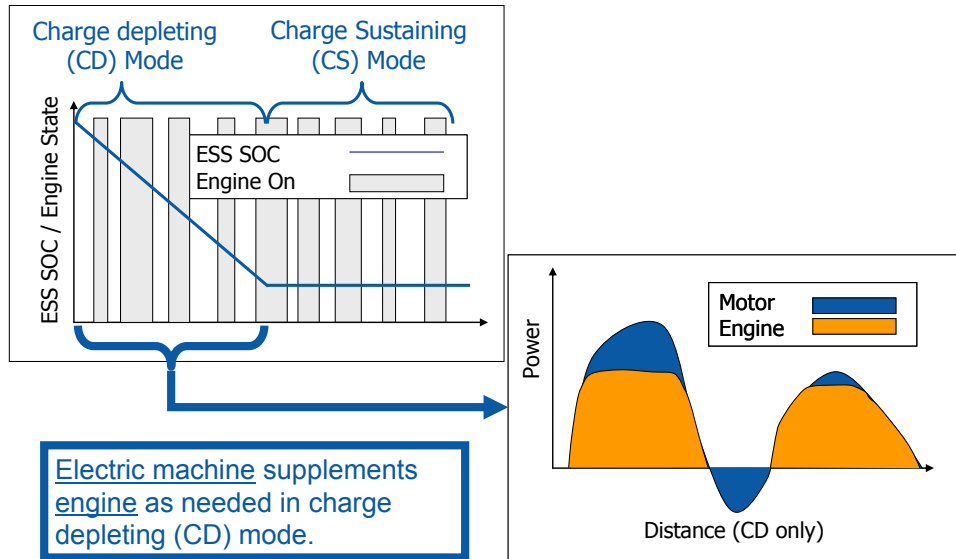


Figure 2. Engine-dominant blended strategy operation summary.

Table 2. Engine-dominant blended strategy characteristics.

Disadvantages	Advantages
<ul style="list-style-type: none"> • Lower petroleum displacement over CD mode • Higher underutilization of battery for short trips • Potentially fewer CARB ZEV credits 	<ul style="list-style-type: none"> • Extends miles driven during CD mode • Smaller components • Lower cost • Highest fuel savings for long driving distances

Blended: Electric-Dominant

The electric-dominant blended strategy attempts to maximize the use of electric power from the energy storage system. The operation is similar to an AER strategy. However, when the power demand of the vehicle exceeds the available electrical power, the gasoline engine must supply the additional power demand. As with the AER and engine-dominant blended strategies, once the lower SOC threshold is reached for the battery the vehicle will run in CS mode. This operation is highlighted in Figure 3.

The key advantage of the electric-dominant blended strategy over the AER strategy is the lower power demand on the electric drive components. The electric drive components can be sized for a lower peak power requirement and rely on the gasoline engine for additional power when needed. This allows for smaller and cheaper components. As with the engine-dominant blended strategy, benefits of the electric-dominant blended strategy depend on the driving distance between charging events. When driven for long distances, the system will consume more fuel than an engine-dominant blended strategy. Table 3 summarizes the key advantages and disadvantages of the electric-dominant blended strategy.

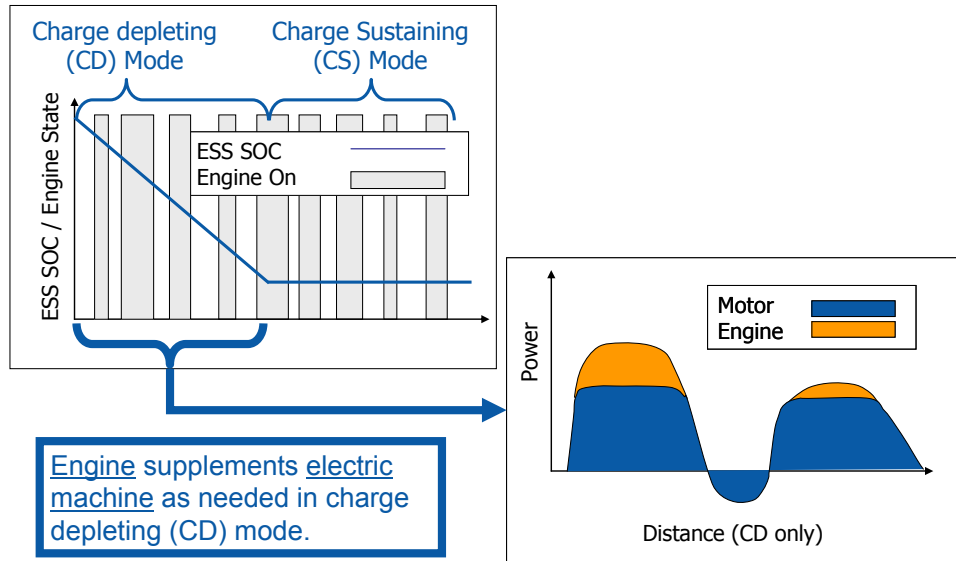


Figure 3. Electric-dominant blended strategy operation summary.

Table 3. Electric-dominant blended strategy characteristics.

Disadvantages	Advantages
<ul style="list-style-type: none"> • Lower fuel savings for long trips • Increased uncertainty regarding emission effects • Potentially fewer CARB ZEV credits 	<ul style="list-style-type: none"> • More effective use of battery over CD range • Smaller components • Lower cost • High CD mode petroleum displacement

Real-World Drive Profiles

To accurately estimate the real-world usage of the power electronics and electric machines, realistic drive profiles were used for the vehicle simulations. Instead of relying on standard test cycles, the drive profiles represented 227 vehicles from the St. Louis area. The second-by-second drive cycles over a 24 hour period were generated from recorded GPS data. The drive cycles were created by the VSA group at NREL and are discussed in the referenced report [5]. The aggressiveness of the real-world drive cycles is comparable to the standard test cycles when the US06 drive cycle is included.

Vehicle Configurations

The VSA group at NREL previously developed and simulated hybrid configurations [5]. We have included a brief summary to provide background for the analysis. The vehicle configurations are based on a midsize sedan with a parallel hybrid drive configuration as shown in Figure 4. In the simulation software, the electric machine, inverter, and converter are not modeled separately. The diagram is only intended to show that they are in series and will experience similar power demands for the parallel hybrid configuration.

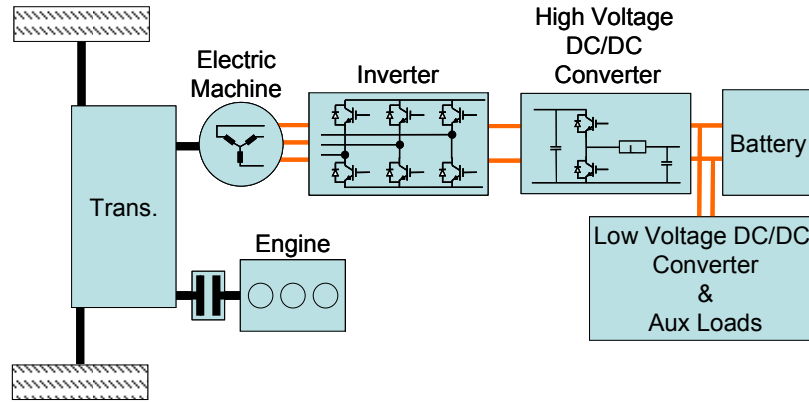


Figure 4. Parallel hybrid vehicle configuration.

The HEV and PHEV vehicle component sizes are listed in Table 4. The model uses a blended electric-dominant energy management strategy. However, the components for the PHEV20 and PHEV40 were sized to provide an approximate AER over the UDDS cycle of 20 and 40 miles respectively. This strategy was chosen because it maximizes the petroleum displacement for an unknown driving distance, and it provides comparable petroleum displacement compared to all-electric configurations for aggressive driving [5].

Table 4. HEV and PHEV component configurations.

	Units	HEV	PHEV20	PHEV40
ESS Power	[kW]	50	47	51.8
ESS Energy	[kWh]	1.9	9.4	18.5
Motor Power	[kW]	39	43.6	48
Curb Mass	[kg]	1399	1488	1567
Fuel Economy (combined MH)	[mpg]	39.2	54	67.4

PEEM Impacts

Using the previously discussed vehicle data generated by the VSA group at NREL, the specific impacts on the PEEM systems were evaluated to confirm and quantify expectations. The critical impacts on the PEEM systems include the increased thermal demands on the PEEM components and the increased battery output voltage fluctuation.

Continuous Power Impacts – Thermal

In current HEVs, the traction drive components are predominately used for providing intermittent power assist, capturing braking energy, and providing power to the low voltage auxiliary loads. Figure 5 compares the critical operating regions of an HEV and PHEV20 from all 227 driving profiles. The figure highlights the critical operating regions based on the time spent at the listed torque and speed points for the traction drive. The darker color represents more time. As seen in Figure 5, HEVs predominately operate at low power and torque. The impact of PHEVs is seen as the operating region shifts into the positive torque or motoring region.

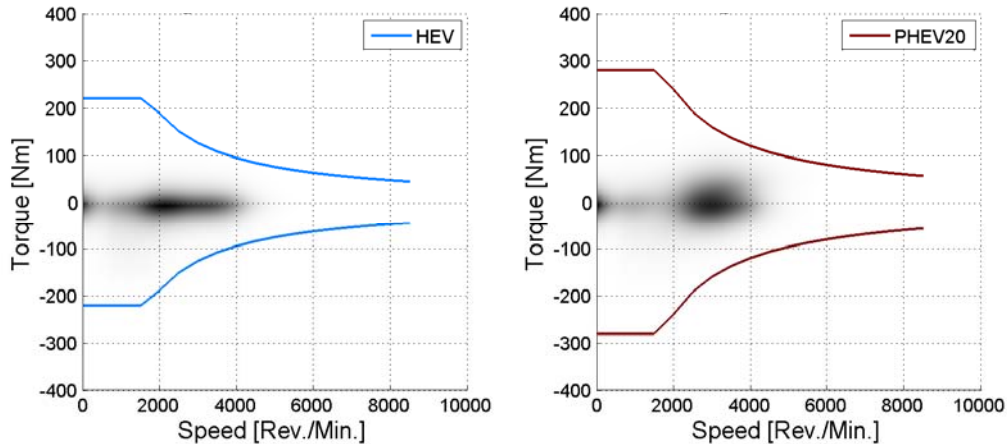


Figure 5. Traction drive operation over 227 drive profiles.

The shift in the operating region for the PHEV20 is comparable to a PHEV40 or an EV¹, as seen in Figure 6. Figure 6 shows the distribution of the cumulative operating time at a specific motoring power level. The increased time spent operating at higher power levels increases the continuous power requirements for the power electronics and electric machine. The increased continuous power requirements lead to increased thermal demands on the electric traction drive components. For a given PHEV energy management strategy the impact on the PEEM systems is primarily due to the transition from HEV to PHEV and not the transition from PHEV20 to PHEV40.

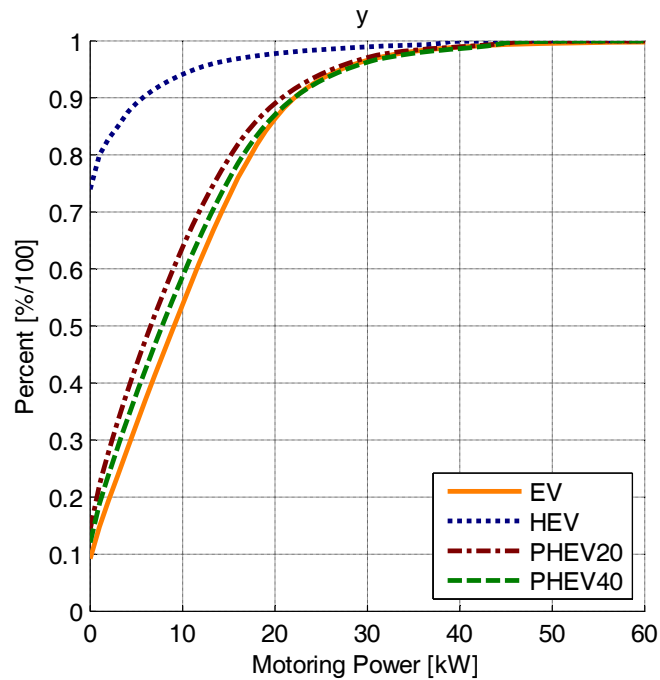


Figure 6. Cumulative motor power distribution for key on data over 227 drive profiles.

¹ The EV comparison is based on the net power flow through the gearbox of the HEV configuration to provide an approximate comparison.

Output Battery Voltage

The operating distribution of the battery output terminal voltage shows a wider range of operation in PHEVs. Two important factors that impact the output terminal voltage of the battery are the SOC of the battery and the power or current provided to or from the battery. Both of these factors change with PHEVs as compared to HEVs. First, an HEV maintains the battery SOC within a narrow region of its total capacity, while the primary benefit of a PHEV is the full use of battery capacity. Second, the PHEV battery operates for longer periods of time at higher power levels. Figure 7 compares the voltage distributions for the HEV and PHEV configurations over all 227 drive profiles. The figure highlights the operating range of the battery over 90% of its use in the drive profiles. The percentage of the voltage change as it relates to the median operating voltage is significantly higher for PHEVs as listed in Table 5.

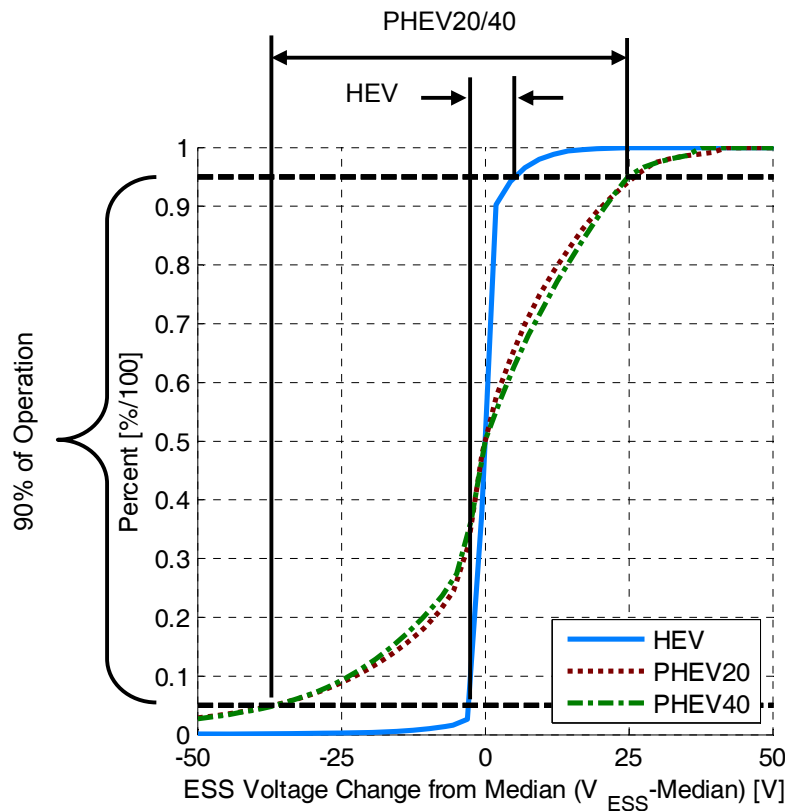


Figure 7. Output battery DC bus voltage variation over 227 drive profiles.

Table 5. Battery voltage fluctuation for 90% of operation.

Vehicle Configuration	Percent Change Relative to Median
HEV	3%
PHEV20	22%
PHEV40	24%

The significance of the voltage variation is important because of the impact on all of the high voltage bus components, both DC and AC. On the DC bus, lower voltages lead to higher operating currents for

the same power levels. This in general leads to higher losses within the components. The AC components such as the inverter and electric machine are also impacted by the voltage variation. The voltage variation can potentially prevent the electric machine from running at a desired location in its torque/speed map, or it can increase the required phase current in the machine to maintain operation at a desired location. The first limits the performance of the machine, while the second increases the operating losses within the machine and inverter.

Cost

We performed a preliminary cost benefit analysis of PHEVs to illustrate the cost impacts of power electronics and electric machines on PHEVs. The analysis used near- and long-term cost estimates from previous work performed by the VSA group at NREL [6]. FreedomCAR targets were also included to determine the impact of the cost targets for power electronics and electric machines on PHEVs [7-8]. The results confirm that the FreedomCAR cost target of the PEEM components has little impact on the affordability of PHEVs, since the cost is dominated by the increasing energy storage requirement of the battery. This is in contrast to current production HEVs, such as the 2004 Toyota Prius, where the costs of the PEEM components are estimated to be over two times the cost of the battery [9].

Table 6. FreedomCAR and VSA cost estimates for figures 8 and 9.

PEEM	\$12/kW [7]
Battery	HEV: \$20/kW [8] PHEV: \$250/kWh [8]
Integrated Charger	\$380[6]
Manufacturer Markup	50%[6]
Dealer Markup	16.3%[6]

Figure 8 provides a comparison of the battery and PEEM component costs using the cost estimates from Table 6. Figure 8 shows how the battery dominates the costs related to PHEVs using FreedomCAR targets. It should be noted however that the costs for the power electronics and electric machine shown in Figure 8 include the cost for one electric machine and one inverter, which reflects the analyzed parallel vehicle configurations.

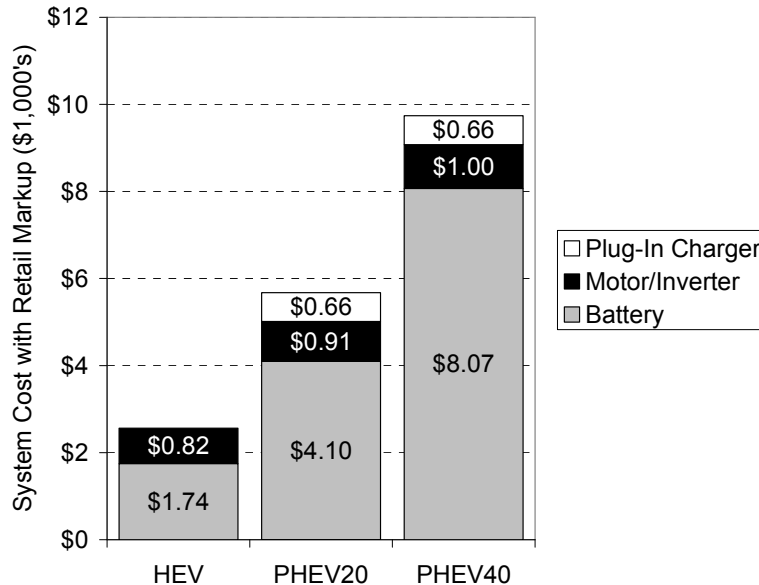


Figure 8. Electric drive system cost with FreedomCAR targets, VSA cost estimates, and markups.

The dominance of the battery costs in PHEVs is also reflected in the payback period from fuel savings. Figure 9 shows the discount in initial purchase price that is required for PHEVs to have a three year payback relative to a conventional vehicle based on fuel savings alone, assuming an annual vehicle miles traveled (VMT) of 15,000 miles. For example, at a fuel price of \$4/gallon the PHEV20 configuration would require a decrease of over \$1,500 in the initial vehicle purchase price. However, when compared to an HEV the required discount is approximately \$2,200. This exceeds the total target cost of the power electronics and electric machine for the analyzed PHEV20 vehicle configuration as shown in Figure 8.

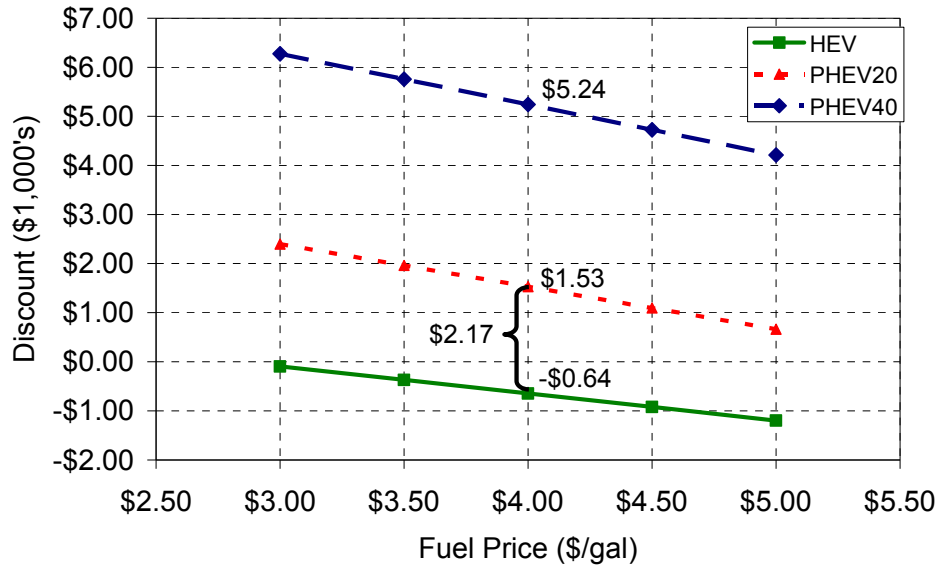


Figure 9. Discount for 3-year payback with FreedomCAR targets, VSA cost estimates, and markups.

Conclusion

The analysis confirms and quantifies the impacts of PHEVs on power electronics and electric machines. First, the electric traction drive’s continuous power requirement increases for PHEVs relative to HEVs. This leads to increased thermal demands on the electric traction drive components. The increased thermal load requires significant thermal control improvements to electric machines and incremental improvements to power electronics relative to current production HEV components that use dedicated liquid cooling. Removing the dedicated liquid cooling system would add additional complications to both the power electronics and electric machines. Second, the increased fluctuation of the battery voltage within a PHEV shows a greater need for a high voltage DC/DC converter. The voltage fluctuation of the battery causes additional losses within the traction drive, leading to increased thermal demands. Also the voltage drop causes the potential inability to effectively control the electric machine at the desired operating location. Finally, fuel cost savings alone do not make PHEVs economical when compared to HEVs. A cost target decrease in the electric machine and inverter is not sufficient to make PHEVs cost competitive with HEVs. Other potential benefits related to PHEVs need to be considered, such as diversification of transportation fuel sources, emissions, vehicle noise, and vehicle to grid applications.

References

1. J. Gonder and T. Markel, "Energy Management Strategies for Plug-In Hybrid Electric Vehicles," presented at the 2007 Society of Automotive Engineers (SAE) World Congress, Detroit, Michigan, April 16-19, 2007.
2. California Air Resource Board, "California Exhaust Emission Standards and Test Procedures for 2005 and Subsequent Model Zero-Emission Vehicles, and 2001 and Subsequent Model Hybrid-Electric Vehicles, in the Passenger Car, Light-Duty Truck and Medium-Duty Vehicle Classes," as of March 26, 2004 (last amended December 19, 2003), [Online]. Available: <http://www.arb.ca.gov/msprog/zevprog/zevregs/zevregs.htm>.
3. California Air Resource Board, "ZEV Regulation Amendments," 2007 ZEV Technology Review, [Online]. Available: <http://www.arb.ca.gov/msprog/zevprog/zevreview/zevreview.htm>.
4. California Air Resource Board, "Status Report on the ARB's Zero Emission Vehicle Program," 2007 ZEV Technology Review, [Online]. Available: <http://www.arb.ca.gov/msprog/zevprog/zevreview/zevreview.htm>.
5. J. Gonder, T. Markel, A. Simpson, and M. Thornton, "Using GPS Travel Data to Assess the Real World Driving Energy Use of Plug-In Hybrid Electric Vehicles (PHEVs)," presented at the Transportation Research Board (TRB) 86th Annual Meeting, Washington, D.C., Jan. 21-25, 2007.
6. A. Simpson, "Cost-Benefit Analysis of Plug-In Hybrid Electric Vehicle Technology," presented at the 22nd International Battery, Hybrid and Fuel Cell Electric Vehicle Symposium and Exhibition (EVS-22), Yokohama, Japan, Oct. 23-28, 2006.
7. FreedomCAR Power Electronics and Electrical Machines, "Electrical and Electronics Technical Team Roadmap," Washington, D.C., Nov. 2006.
8. FreedomCAR Energy Storage, "Electrical Energy Storage: Plug-In Hybrid Electric Vehicle Battery Research and Development Activities," U.S. Department of Energy PHEV Stakeholder Workshop, Washington, D.C., Jun. 13, 2007, [Online]. Available: <http://avt.inel.gov/phev.shtml>.
9. Energy and Environmental Analysis, Inc., "Technology and cost of the 2004 Toyota Prius," July 28, 2006.

2.5 Air Cooling Technology for Power Electronics Thermal Control

Principal Investigator: Desikan Bharathan

National Renewable Energy Laboratory

Center for Transportation Technologies and Systems

1617 Cole Boulevard MS 1633

Golden, CO 80401

Voice: 303-887-4215; Fax: 303-275-4415; E-mail: Desikan_Bharathan@nrel.gov

DOE Technology Development Manager: Susan A. Rogers

Voice: 202-586-8997; Fax: 202-586-1600; E-mail: Susan.Rogers@ee.doe.gov

NREL Program Manager: Kenneth Kelly

Voice: 303-275-4465; Fax: 303-275-4415; E-mail: Kenneth_Kelly@nrel.gov

Objectives

The overall objective of the thermal control activities is to develop advanced technologies and effective integrated thermal control systems aimed to meet DOE FreedomCAR program goals. They address key requirements for power electronics such as target values for volumes, cost, and weight of various subcomponents. The objective of the present task is to assess the potential for reducing the cost and complexity of cooling systems for power electronics using air. This study and assessment aim to quantify the relative merits of the use of air for cooling power electronic devices to achieve high-heat flux removal rates under steady-state and transient conditions.

Approach

- Assess hardware options that may be available in the industry for varied air-cooling devices.
- Conduct system level analyses to identify areas of critical needs.
- Conduct computational analyses of fluid flow and heat transfer for promising devices and geometries. Arrive at recommendations for future activities in this area.

Major Accomplishments

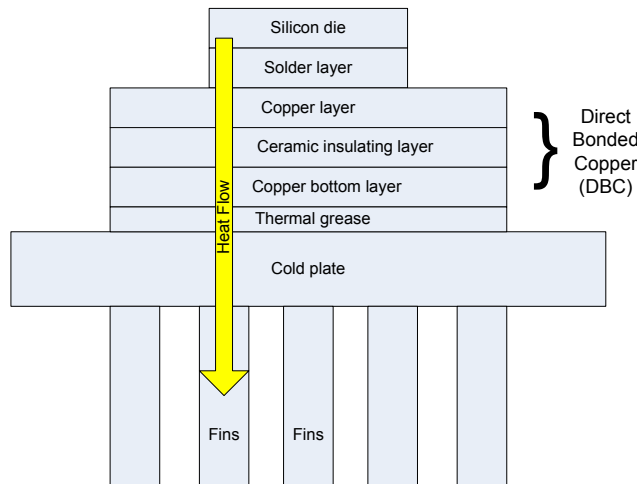
- Characterized the potential for cooling with micro-channel geometries various fluids
- Developed simplified user-friendly software for quick assessment for various parameters
- Verified performance with computational fluid dynamic (CFD) analyses
- Identified air cooling heat exchanger geometries viable for use with automobiles

Future Direction

- Fabricate and test micro-channel heat exchangers
- Validate experimental performance against models
- Fabricate and test inverter with air cooling option

Technical Discussion

Figure 1 shows a cross-sectional view of a die mounted on a cold plate with the heat being removed by a coolant supplied to the bottom of the die. Various layers that impede the heat flow from the die to the cooling fluid are indicated. A major contributor to the overall thermal resistance turns out to be the thermal grease. However, the use of thermal grease is necessary to eliminate interlayer thermal stresses that result from differential thermal expansion between the layers.

Figure 1. Heat flux path and the various intervening layers

The next higher resistance usually comes from the heat exchanger rejecting heat to the cooling fluid. Ambient air is assumed to be available at a nominal 30°C for all the vehicle cooling strategies. Use of such air increases the overall temperature-driving potential available to reject heat from the chips. Air, as the cooling medium, is benign, nontoxic, and free when compared to many other fluids. Airflow is also amenable to be modulated in a transient manner to suit the needs the system, as the system load varies during operation.

The use of air on both sides of the silicon switches remains an attractive option. Use of air for cooling has many advantages. Air remains the ultimate heat sink for all heat rejection from an automobile. All the heat to be rejected, either directly or through the use of an intermediate coolant loop must end up in air. Direct use of air can eliminate many components of the cooling loop and the necessity for carrying a secondary coolant.

Air cooling has many drawbacks as well. Air is a poor heat transfer medium, with low thermal conductivity and low density. A fan or a compressor must move the air stream to the required hot spots requiring additional parasitic power loads. The coefficient of performance for such a system tends to be low.

Cooling with air may or may not meet requirements for current generation silicon-based devices that the temperatures at the chip be limited to 125°C maximum. Future technology changes, however, are expected to allow higher temperatures at the chip, with the trench IGBTs operating at 175°C, and Si-C devices operating at even higher temperatures. With these higher temperatures, air cooling becomes even more practical.

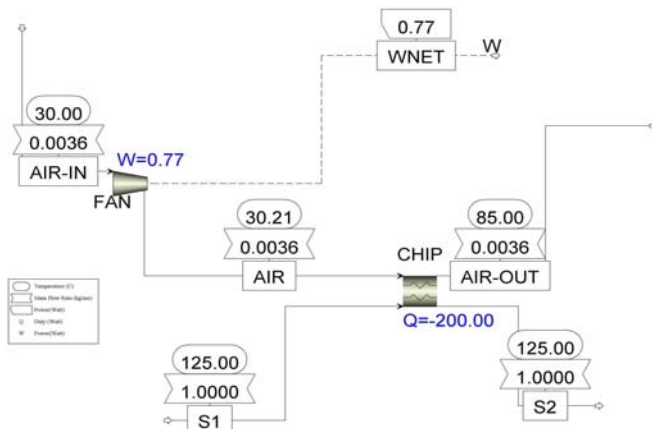
To address many thermal control issues, NREL has undertaken many distinct areas of research and development. Multiple avenues of research are expected to result in significant advancement in thermal control of power electronics with a high degree of flexibility in design to meet the targeted goals and objectives of the FreedomCAR initiative. Progress made toward evaluating air cooling as a viable option for power electronic components in FY2007 under the FreedomCAR Program follow.

Initial assessment for air cooling focuses on a simple heat transfer that occurs on a single chip. We assume a chip frontal area of nominal 1 cm² with the chip generating a heat load of 200 W. Air at ambient pressure and a temperature of 30°C is used to remove the heat.

Use of Ambient Air with Conventional Devices

Figure 2 shows a flow sheet for cooling with air developed using the commercially available software ASPEN. The chip is maintained at a temperature of 125°C.

Figure 2. Flow sheet for air cooling with a target chip held at 125°C, generating 200W heat load



Only key parameters are shown in this figure. The air approach temperature is fixed at 40°C below that of the target hot surface (a value typical for airflow applications). The fan operates with an efficiency of 56 %, once again typical for airflow.

Based on this simulation, we find that the airflow requirement per chip is about 3.6 g/s. The required UA product (the product of the heat-transfer coefficient and the available area for heat transfer) is 3.15 W/K (Watts-thermal). Typical industrial airflow applications nominally achieve a heat transfer coefficient of about 40 W/m²K. If we use this value, the

required area is about 800 square centimeters. That is, the heat generated in the chip area of nominal 1 cm² must be spread out over an area, larger by a factor of 800. This can be accomplished through the use of fins or other means. We find, however, that nominal heat transfer coefficients fall well below the needs to accomplish the task at hand. To enhance the heat transfer coefficient and provide large area enhancements, we looked into micro-channel geometries.

Micro-Channels and Micro-Jet Arrays

We attempted to find hardware suitable for use with air cooling. We found two types of devices that are currently being offered as cooling devices for personal computer central processor units (CPUs). These are microchannel devices and microjet arrays. Figure 3 (a) shows the internal elements of a CPU cooler with micro-channels and 3 (b) shows a micro-jet array. (Courtesy Preytek, Co, Inc, and International Mezzo Technologies, Inc., respectively).

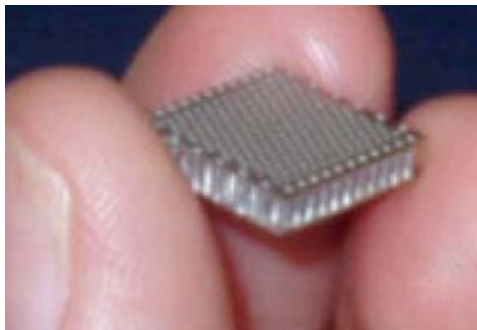


Figure 3. Photographs of micro-channel and micro-jet devices

Table 2. Nusselt number and product fRe variation with aspect ratio H/W, from Cengel[1997]

Aspect ratio (H/W)	Nusselt number	Product fRe
1	2.98	56.92
2	3.08	62.2
3	3.39	68.36
4	3.96	72.92
6	4.44	78.8
8	5.6	82.32
infinity	7.54	96

Further details of the calculations may be found in Muller and Frechette [2002].

As part of this project, we developed a “Micro-Channel Performance Estimator” program that was developed provides a quick means to estimate micro-channel heat transfer with a variety of configurations and fluids. An “executable” file for this program is attached to this report. Specifically the aspect ratio of the channel, H/W can be varied from 50 to 1000 in increments of 50. The channel width, W, can be varied from 80 μm to 200 μm in steps of 10 μm. Choices of three fluids, namely, air, water, and ethylene glycol/water 50/50 mixture are available. Choices for fin and plate materials in the form of copper and aluminum are available. Base-plate thickness can be varied from 0.5 mm to 5 mm in steps of 0.5 mm.

Figure 6 shows the output page for the estimator program. The calculated results are listed on the top right with various parameters called out. The bottom half of the page provides the summary of the results in a graphical form. A required base-plate temperature is first selected, in the range of 125°C to 200°C (with steps of 25°C). The heat flux q (W/cm²) and the parasitic power (W) are calculated and plotted along the left axis as functions of the fluid velocity (m/s) within the channel passage. The program goal of 200 W/m² heat flux at a base temperature of 125°C for silicon-based chips is indicated in the figure. A coefficient of performance (COP) for the device is evaluated as the ratio of heat flux to the parasitic power. COP is also plotted on the right-side axis as a function of the base plate temperature. COP values over 150 are not indicated in the figure, but are listed in the output window along with other variables. This program allows one to quickly evaluate the performance of a micro-fin geometry for removing heat from hot spots in a printed circuit board.

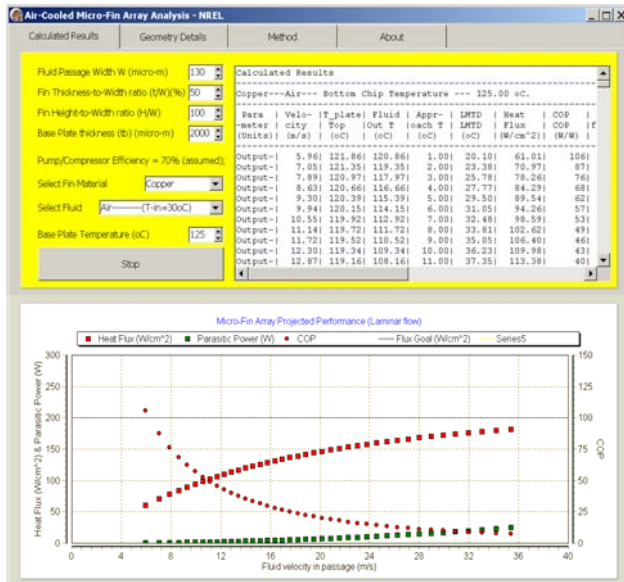


Figure 6. Output page from the “Micro-Channel Performance Estimator” program

For air flow through the micro-fin channels, with copper as the fin material and base plate held at 125°C, we are able to achieve heat fluxes in the range of 60 W/m² to 180 W/m² over the selected range to parameters. With aluminum as the fin material, the range narrows down to 50 W/m² to 150 W/m². The COP ranges from about 12 to well over 150, with most values falling in the range of 50 to 100.

For a 50/50 ethylene glycol/water mix flow through the micro-fin channels, with copper as the fin material, and with the base plate held at 125°C, we achieve heat fluxes in the range of 60 W/m² to

Table 3. Assumptions related to comparison of air and liquid cooling options

Quantity	Air Cooling	Liquid Cooling
Inlet Temperature (°C)	30	105
Approach Temperature (°C)	40	5
Mass flow rate (g/s)	54	50
Volume flow rate	94 (SCFM)	0.8 (GPM)
Configuration	Open loop	Closed loop

Detailed breakdown of the components for each system allowed us to calculate the component masses, volumes, required parasitic power, and cost. Table 4 summarizes the results of this analysis.

Table 4. A quantitative and qualitative comparison of air-cooling versus liquid-cooling options

Quantity	Air Cooling	Liquid Cooling
System mass (kg)	1.4	3.8
Volume (cc)	7000	3800
Parasitic Power (W)	80	28
MPG penalty for excess power	- Negligible -	- Negligible
MPG penalty for excess mass	- Negligible	- Negligible
Relative component and system fabricated costs (\$)	48	78
Number of components	+++	
Reliability	+++	
Maintenance Ease	+++	
Feedback to customer for attention	+++	+++
Simplicity in installation	+++	
Overall comparison	+++	

We find that the air-cooling system compares very favorably with the liquid cooling system. Air cooling system mass turned out to be one-half of that for the liquid cooling system. However, the air system is bulkier, occupying more volume. The parasitic power for the air cooling system is close to three times that for the liquid system, reflecting its lower COP. However, the impact on the vehicle’s gasoline usage, in terms of miles per gallon (MPG), for both systems is negligible. The air cooling system scores higher in less tangible areas, such as decreased number of components, increased reliability, ease of maintenance, and simplicity in design and installation.

Based on this set of comparisons, we find that air-cooling provides a viable option for heat removal from power electronic systems. Potential for cooling both sides of the heat-generating chips remains an even more attractive option.

Experimental efforts

Efforts are underway at NREL to fabricate and test micro-fin air-cooled heat exchangers. Figure 8 shows how an air-cooled heat exchanger may be incorporated with the inverter design (as used by Semikron). The figure shows an exploded view. The heat exchanger fins fall directly below the high-heat generating switch mounted on a printed circuit board (PCB).

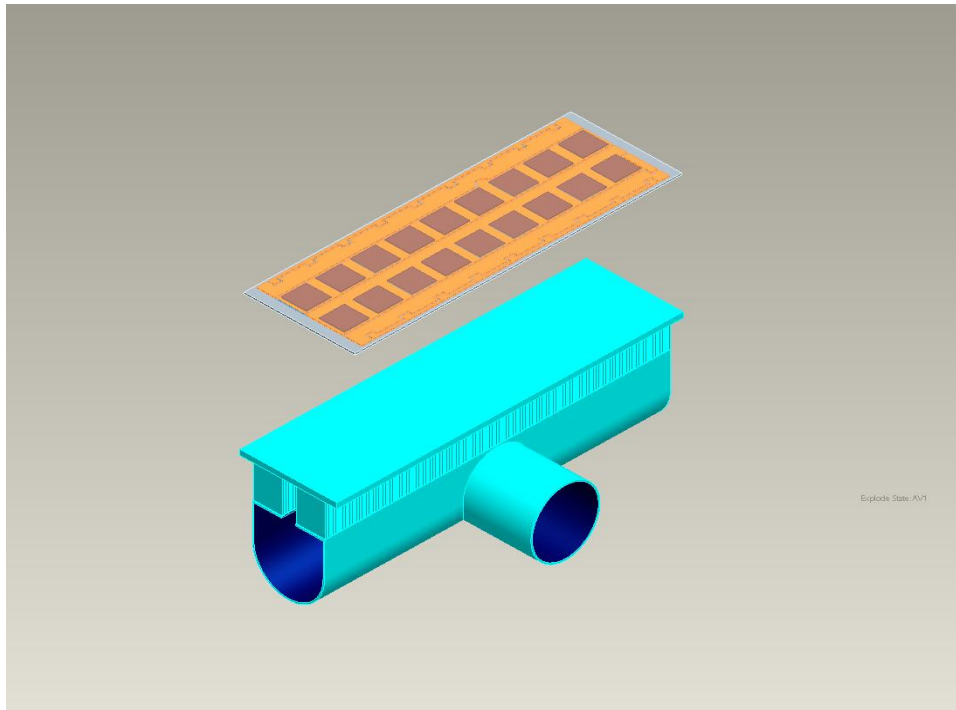


Figure 8. Air-cooling system with micro-channels shown directly below the heat generating chips on a printed circuit board.

Air is supplied from a side port of nominal 40-mm diameter. Air flows through the distribution manifold and enters the array of fins on both sides of the device. The bottom of the PCB is in intimate contact with the bottom plate of the heat exchanger. These two parts may be soldered together to achieve a low-resistance heat transfer path.

Computational fluid dynamics modeling results

We conducted a variety of computational fluid dynamics (CFD) simulations for the air-cooled heat exchanger using Fluent. A single passage surrounded by one-half fin on each side was modeled. Figure 9 shows a side view of the geometry. The central portion is the region of interest occupied by a copper bottom plate and copper fins extending from it up above.

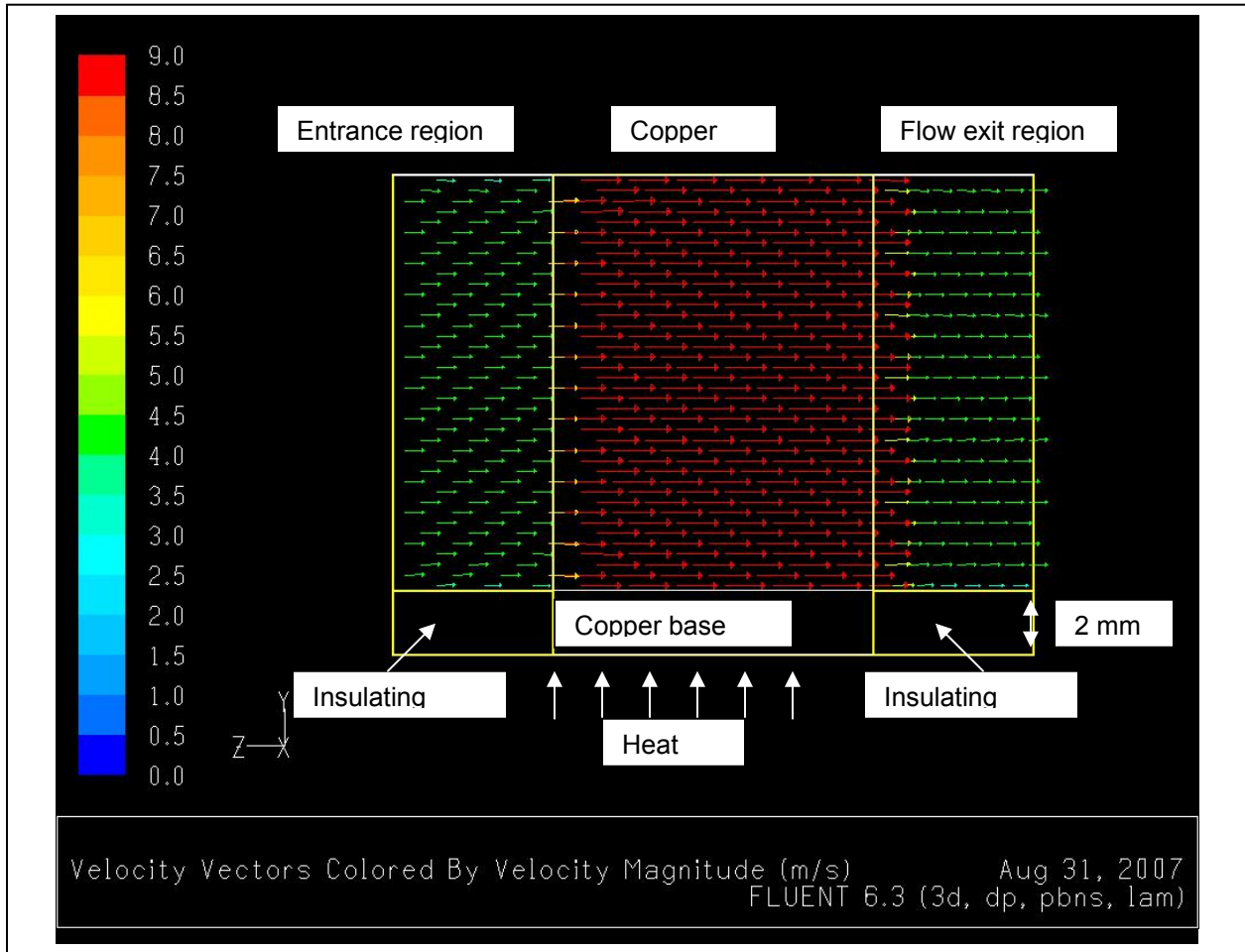


Figure 9. Micro fin geometry as modeled in Fluent

The central portion is extended both downstream and upstream to establish the fluid flow. Results are shown indicating velocity vectors for air flow at a nominal mean passage velocity of 6 m/s. The vectors are illustrated at the central plane of the passage; thus they indicate higher velocity values on account of the laminar flow. Air enters on the left and exits to the right as indicated by the arrows. Nominal values for the dimensions of the geometry are also indicated.

The results shown use incompressible flow for air as an approximation. The air velocity increases as the air enters the space between the fins. Heat enters the copper block from below. We imposed a constant temperature boundary condition at the bottom of the conducting block. All simulations were done at a bottom plate temperature of 125°C.

Figure 10 shows the mid-plane temperature distribution for the above simulated condition. We find that air enters at the inlet temperature of 30°C and begins heating up as it contacts the fins. There are large temperature gradients both in the stream-wise direction and perpendicular to it. Such variation is far from the assumptions used in the simplified model described earlier.

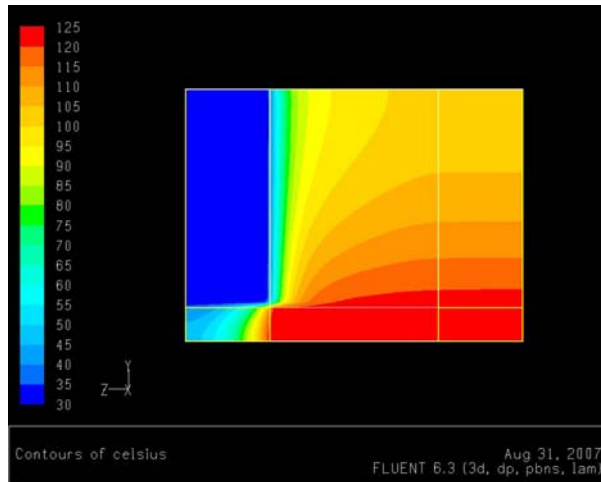


Figure 10. Temperature distribution at the mid plane of the passage for air flow at 6 m/s.

Because of these gradients, we find that our performance estimator program over-predicts the heat flux by about 20%. At higher air velocities, the stream-wise gradients lessen, and the perpendicular gradients increase, generated using a much higher air mean passage velocity of 27 m/s.

On account of the cross flow, such gradients will prevail and simplified methods such as our estimator are likely to yield large errors. We summarize the errors in Table 5.

Table 5. Comparison of results from the "Micro-Channel Performance Estimator" and more detailed Fluent CFD simulations

Mean Passage Velocity (m/s)	Parameter	Units	Simplified Performance Estimator	Fluent Model	Error (%)
6	Bottom heat flux	(W/m ²)	61	51	20
	Pressure loss	(Pa)	780	782	0
	Parasitic Power	(W)	0.58	0.58	0
	COP	(---)	106	88	20
12	Bottom heat flux	(W/m ²)	106	87	22
	Pressure loss	(Pa)	1601	1591	1
	Parasitic Power	(W)	2.33	2.35	-1
	COP	(---)	46	37	24
21	Bottom heat flux	(W/m ²)	149	123	21
	Pressure loss	(Pa)	3032	2854	6
	Parasitic Power	(W)	7.83	7.38	6
	COP	(---)	19	17	12
27	Bottom heat flux	(W/m ²)	166	140	19
	Pressure loss	(Pa)	4105	3728	10
	Parasitic Power	(W)	13.79	12.42	11
	COP	(---)	12	11	9

Considering that the passage length is the key variable dictating pressure loss and parasitic power, we attempted to reduce this passage length by one half as shown in Figure 12. Note that in this case, the fluid enters the passage centrally from up above, splits into two streams in the middle, and flows horizontally through the fin passages and exits. Key dimensions are indicated in this figure. The fins are slanted to accommodate the entrance region. At the same mass flow of air, the fins now see only one half of the flow, at one half of the value for non-split fins. The passage length is also reduced by one half.

Since the air must change direction, there are low pressure regions that occur at the corners, and a stagnation region occurs at the center of the passage. A certain amount of recirculation can be seen in the path lines indicated in this figure.

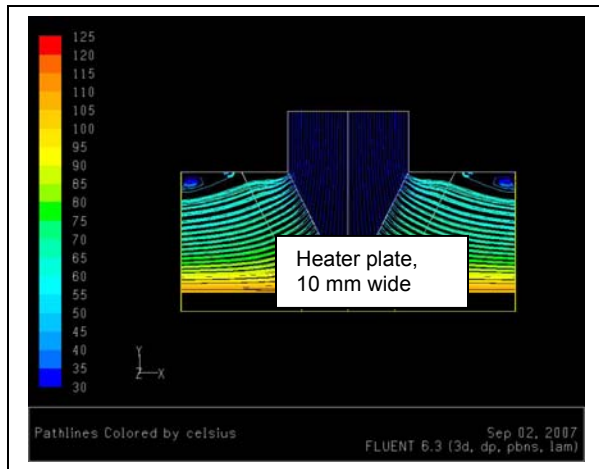


Figure 12. Split channel geometry indicating flow path lines at a mean passage velocity of 10.5 m/s

The corresponding pressure and temperature contours are illustrated in the accompanying figures 13(a) and 13(b).

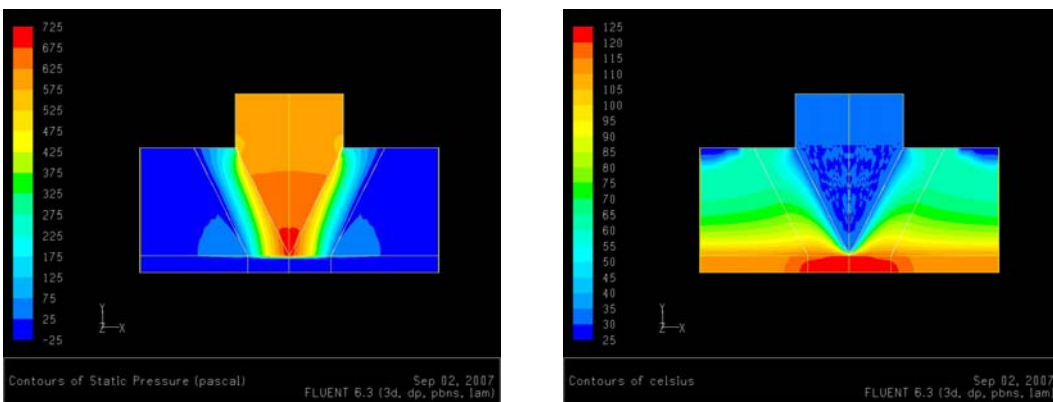


Figure 13. Pressure (a) and temperature contours (b), respectively

A comparison of the key parameters for the straight passage and the split passage are summarized in Table 6, below.

Table 6. A comparison of the straight channel with the split channel at varied flow conditions.

Parameter	Units	Fluent Model			
		Straight Channel	Split Channel		
Passage length	(mm)	10	5	5	5
Mean passage velocity	(m/s)	21	10.5	21	31.5
Air mass flow	(g/s)	2.22	2.22	4.43	6.65
Bottom heat flux	(W/m ²)	123	110	150	171
Pressure loss	(Pa)	2854	594	1334	2433
Parasitic power*	(W)	7.38	1.54	6.90	18.88
COP	(---)	17	72	22	9
*assumes a fan efficiency of 70%					

We find that parasitic power can be reduced significantly without losing heat flux removal capacity at the same air mass flow. Doubling the mass flow still yields a higher COP and a higher heat flux. Simple modifications can boost the performance of the micro-channel considerably. This example was shown as an illustration. Depending on the specific applications, key modifications to the geometry to maintain highly aerodynamic passages will result in further improvements in the overall performance of the micro-channel geometry.

Conclusion

Air cooling is likely to meet the program goal for heat-flux removal at a rate of 200 W/cm² with relatively low cost and complexity. While air cooling may not be appropriate for the current generation of silicon-based devices, it remains an attractive option for devices that can operate at higher temperatures. Use of air helps avoid the need for a secondary cooling fluid in vehicles. Improving chip manufacturing technologies continue to push the envelope for the highest temperature environment that these chips may see during operation. Air cooling remains a viable option for power electronics. Continued research in this area will result substantive progress in this cooling technology. We recommend fabricating and testing working inverters that use advanced air cooling for heat removal.

References

- Cengel, Y.A., *Introduction to thermodynamics and heat transfer*, McGraw-Hill, New York, 1997.
- Hans, J.C.; Dutta, S.; Ekkad, S., *Gas Turbine Heat Transfer and Cooling Technology*, Taylor and Francis, 2001.
- Incropera, F.P., *Introduction to heat transfer*, Wiley, New York, 1996.
- Marques, C. and Kelly, K.W., "Fabrication and Performance of a Pin Fin Micro Heat Exchanger," *J. Heat Transfer*, v126, pp 434-444, June 2004.
- Muller, N and Frechette, L.G., "Optimization and design guidelines for high flux micro-channel heat sinks for liquid and gaseous single-phase flow," *Inter Society Conference on Thermal Phenomena*, IEEE paper 0-7803-7152-6/02.
- Shen, J.R.; Wang, Z.; Ireland, P.T.; Jones, T.V.; Byerley, A.R. "Heat Transfer Enhancement Within a Turbine Blade Cooling Passage Using Ribs and Combinations of Ribs With Film Cooling Holes," *ASME J. of Turbomachinery*, v118, pp 428-434, 1996.

2.6 Jet and Spray Impingement Cooling for Power Electronics

Principal Investigator: Sreekant Narumanchi

National Renewable Energy Laboratory

MS 1633

1617 Cole Blvd

Golden, CO 80401-3393

Voice: 303-275-4062; Fax: 303-275-4415; E-mail: sreekant_narumanchi@nrel.gov

DOE Technology Development Manager: Susan A. Rogers

Voice: 202-586-8997; Fax: 202-586-1600; E-mail: Susan.Rogers@ee.doe.gov

NREL Program Manager: Kenneth Kelly

Voice: 303-275-4465; Fax: 303-275-4415; E-mail: kenneth_kelly@nrel.gov

Objectives

In hybrid electric vehicles, inverters are used for bidirectional DC-AC conversion. These inverters involve a number of insulated gate bipolar transistors (IGBTs) that function as on/off switches. The heat dissipated in these transistors can result in significant heat fluxes, which makes the thermal management problem quite important. The broad objective of this task is thermal control of automotive power electronics components. The FreedomCAR goal is to dissipate high heat fluxes from the device and keep it under the maximum stipulated temperature for that technology. For conventional silicon devices, the maximum temperature rating is 125°C, for trench IGBT devices 150°C, and for silicon carbide-based devices 200°C. The automotive industry would like to eliminate any additional cooling loops. Hence, using a glycol-water mixture drawn from the engine cooling outlet at 105°C as the coolant is preferable for the power electronics components. The capability to remove high heat fluxes enables us to reduce the size and number of the power electronics devices, which helps reduce weight, volume, and cost.

The specific objectives of this task are to explore liquid jets and sprays in the single- and two-phase regimes to cool the IGBT package. This helps meet program goals of cost, weight, and volume of power electronics components. We performed detailed experiments with self-oscillating jets, investigated jets and sprays in the boiling regime, and achieved boiling curves up to critical heat flux (CHF). All the results are cast in the context of cooling IGBT package in an inverter of a hybrid electric vehicle.

Approach

NREL is exploring the performance of single- and two-phase jets and sprays. The rationale is to characterize the heat transfer performance of these technologies in the context of cooling automotive power electronics and establish a consistent, non-biased scientific database of the thermal performance of spray and jet cooling technologies. This information is fed into overall system-level modeling (a separate task) to ascertain the cooling technologies most suited for automotive applications.

To meet the objectives outlined earlier, the following approach was adopted in FY 2007. This is a continuation of the approach for FY 2006.

Experiments with Steady and Self-Oscillating Single-Phase Jets

One FreedomCAR goal is to use glycol water at 105°C to cool the automotive power electronics components. It is desired to maintain the conventional silicon-based device at 125°C, which means there is only a 20°C difference between the die and the coolant temperature. This implies that high heat transfer

coefficients would be required in conjunction with concepts like enhanced surfaces. Some studies in the literature demonstrate that oscillating jets could enhance heat transfer over steady jets by as much as 50% to 70% [1-4]. In some of these studies [1-3], the oscillation is induced by mechanical means; in others [4] the jets are self-oscillating. Self-oscillating jets involve no moving parts and the oscillations are induced strictly by pressure differences in the fluid. The pressure differences are in turn caused by the geometry of the nozzle. The fact that there are no moving parts makes self-oscillating jets attractive. However, there is very limited literature on the heat transfer performance of self-oscillating jets.

Hence, in FY 2006, we decided to explore the heat transfer potential of self-oscillating jets. Bowles Fluidics Corporation (BFC) has a long history of fabricating fluidic nozzles for a variety of applications. NREL established a CRADA with BFC to explore the heat transfer performance of various types of fluidic nozzles. We fabricated an apparatus that allows us to characterize the heat transfer performance of various types of fluidic nozzles. We obtained fluidic nozzles from BFC and performed some initial heat transfer experiments to characterize their performance.

In FY 2007, detailed experiments that use concepts from design of experiments were performed for the free surface and submerged configurations. Jet flow rate, oscillation frequency, and nozzle-to-target distance were also investigated. Response curves were generated for parameters of interest such as heat transfer coefficient. These heat transfer results are interpreted in terms of cooling the IGBT package in an inverter of a hybrid electric vehicle.

Experiments with Jets and Sprays in the Single Phase and Nucleate Boiling Regime

In FY 2006, a subcontract was established with Mudawar Thermal Systems to construct an apparatus that would enable spray and jet experiments in the nucleate boiling regime.

The test apparatus was constructed and experiments performed with the fluid HFE7100. The intent was to characterize the heat transfer performance of HFE7100 spray and jet on a test surface in a simple configuration and, if promising heat transfer performance is observed, test these cooling schemes on an actual IGBT package. HFE7100 was chosen as coolant because it is particularly suitable for automotive power electronics applications. HFE7100 can be operated at close to atmospheric pressure, which eliminates the need for a high-pressure loop. In addition, this coolant is environmentally friendly. A detailed study about the suitability of coolants for power electronics applications is presented in references [5-7].

Experiments were performed with sprays and jets of HFE7100 in the single-phase and nucleate boiling regime up to CHF. Heat fluxes from 150 to 250 W/cm² were dissipated and the target surface temperature kept below 125°C. Numerical (CFD) modeling is also being performed, and the goal is to corroborate the numerical results against experimental data for jets.

Major Accomplishments

The main accomplishments of FY 2007 are listed below.

- Fluidic nozzles provided by BFC were used to perform detailed experiments that use concepts from design of experiments to characterize the heat transfer performance of self-oscillating water jets. Results indicated that at a short nozzle-to-target distance of 1.1 mm, the heat transfer from some of these self-oscillating free surface jets is almost 30% higher than steady free surface jets, given the same nozzle exit area and jet velocity. For the same parasitic power consumption (defined as the power required to drive the pump which circulates the coolant), some of the fluidic nozzles (free surface jet configuration) yield up to 18% higher heat transfer than the corresponding steady free surface jets. In the submerged configuration the self-oscillating fluidic

nozzles that have been explored did not show heat transfer enhancement over the corresponding steady jets.

- Numerical simulations were performed to explore the performance of HFE7100 in cooling an IGBT package. Results were published in the International Journal for Heat and Mass Transfer, “Numerical Simulations of Nucleate Boiling in Impinging Jets: Applications in Power Electronics Cooling, August 15, 2007.
- Mudawar Thermal Systems, under subcontract with NREL, finished fabricating a test vessel that enables experiments with jets and sprays in the nucleate boiling regime. Experiments were also performed with jets and sprays of HFE7100 and boiling curves up to the CHF limit were generated. Heat fluxes of 150 to 250 W/cm² were dissipated and the target surface temperature was kept lower than 125°C.

Future Direction

Significant experimental data were generated in FY 2007 with single-phase jets and jets and sprays in the nucleate boiling regime. Aspects related to reliability, system implications, and cost still need to be studied.

Surface enhancements may also be beneficial in increasing the surface area for heat transfer and also the heat transfer coefficient via flow and boundary layer disruptions.

There is a need to conduct experiments in an actual inverter to conclusively prove these concepts. This includes single-phase self-oscillating jets, surface enhancements, and jets and sprays in the nucleate boiling regime.

Results from the oscillating jet experiments and the two-phase spray and jet experiments will be published in the technical literature in FY2008.

Technical Discussion

The section outlines in some detail the progress made in FY 2007. It elaborates on the major accomplishments outlined in the previous section. This section is divided into three parts: 1) discussion of the impact of heat transfer coefficient and fluid temperature, 2) single-phase self-oscillating jet experiments, and 3) experiments with sprays/jets in the nucleate boiling regime.

Impact of Fluid Heat Transfer Coefficient and Fluid Temperature

In this section, we provide a general examination of the impact of fluid heat transfer coefficient as well as fluid temperature via an ANSYS 3D thermal model with appropriate boundary conditions. The domain is depicted in Figure 1. Figure 1(a) shows the full domain, which is basically an IGBT half bridge; Figure 1(b) shows a view of the backside of the structure. Part of the aluminum plate is cut out and heat transfer coefficients (h) are imposed directly on the exposed copper layer. For each cutout on the surrounding aluminum faces, half the heat transfer coefficient is imposed ($h/2$). The choice of $h/2$ on the aluminum walls is appropriate as shown by detailed CFD modeling [8]. Curves for maximum die temperature versus the imposed heat flux on the silicon die were obtained with different heat transfer coefficient values (Figure 2).

Figure 2(a) shows that very high heat transfer coefficient values will be required to achieve 125°C die temperature with 250 W/cm² heat dissipation in the die and 105°C inlet coolant temperature. Even a heat transfer coefficient of 140,000 W/m²K brings the die temperature to only 140°C. For the trench IGBT configuration, a heat transfer coefficient of 60,000 W/m²K would result in 210 W/cm² heat flux dissipation (Figure 2(a)) if the maximum temperature is kept at 150°C. For silicon carbide-based technology, up to 225 W/cm² can be dissipated with a heat transfer coefficient of only 20,000 W/m²K if the die temperature

is kept at 200°C. When the coolant inlet temperature is reduced to 70°C (Figure 2(b)), a heat flux of 250 W/cm² can be dissipated with a heat transfer coefficient of 60,000 W/m²K if the maximum temperature is kept at 125°C. Broadly, Figure 2 gives a sense of the effect of heat transfer coefficients of 60,000 to 65,000 W/m²K (a number we obtained experimentally with single-phase jets) for IGBT package cooling.

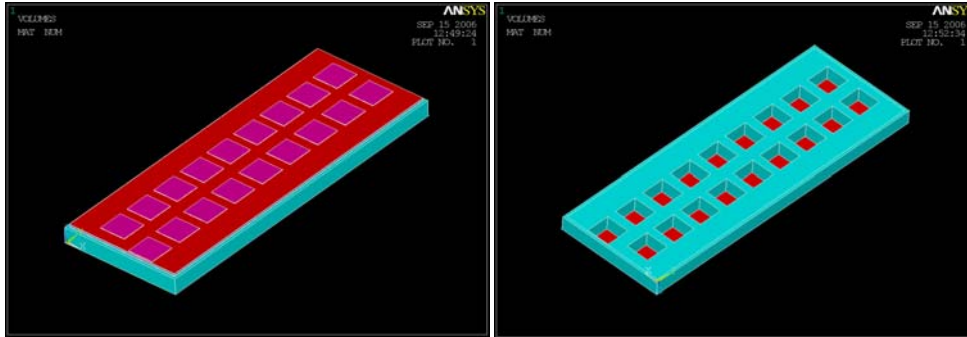


Figure 1. (a) IGBT half-bridge, (b) bottom view of the IGBT half-bridge showing the cut through the aluminum plate

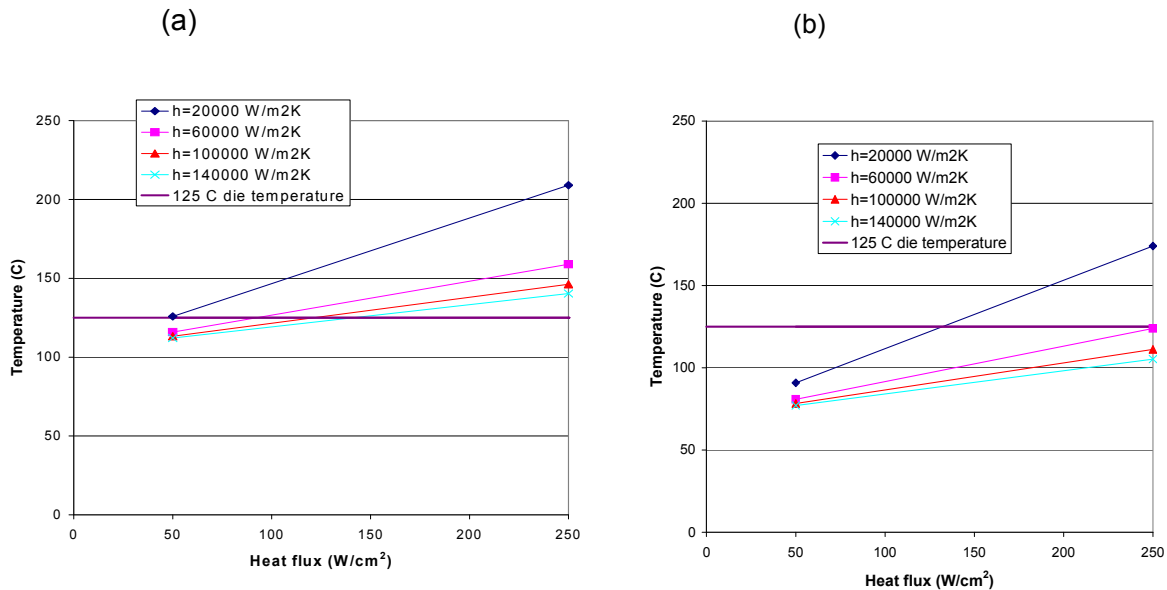


Figure 2. Die temperature versus heat flux for (a) $T_{inlet} = 105\text{ C}$; (b) $T_{inlet} = 70\text{ C}$

Single-Phase Jets

As mentioned previously, one FreedomCAR goal is to use a glycol-water mixture as a coolant at 105°C in the single-phase regime. Hence, in FY 2006 NREL established a test loop that enables experiments with single-phase jets. This loop was described in detail in the FY 2006 milestone report [8]. For completeness, this loop is shown in Figure 3(a). In FY 2006, we also fabricated an apparatus (Figure 3b) to enable the heat transfer performance to be characterized via single-phase jets. The apparatus is also described in detail in [8]. Figure 3(c) shows the sample nozzles obtained from BFC. Six types of fluidic nozzles are shown.

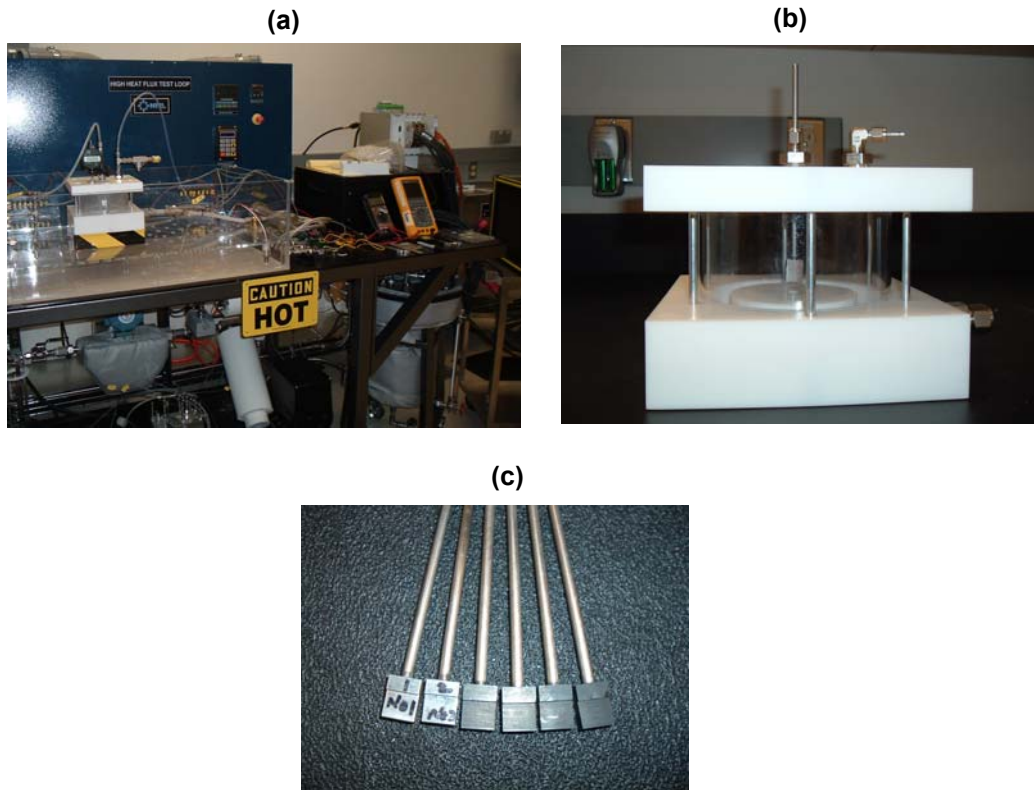


Figure 3. (a) Test loop; (b) experimental apparatus; (c) nozzles

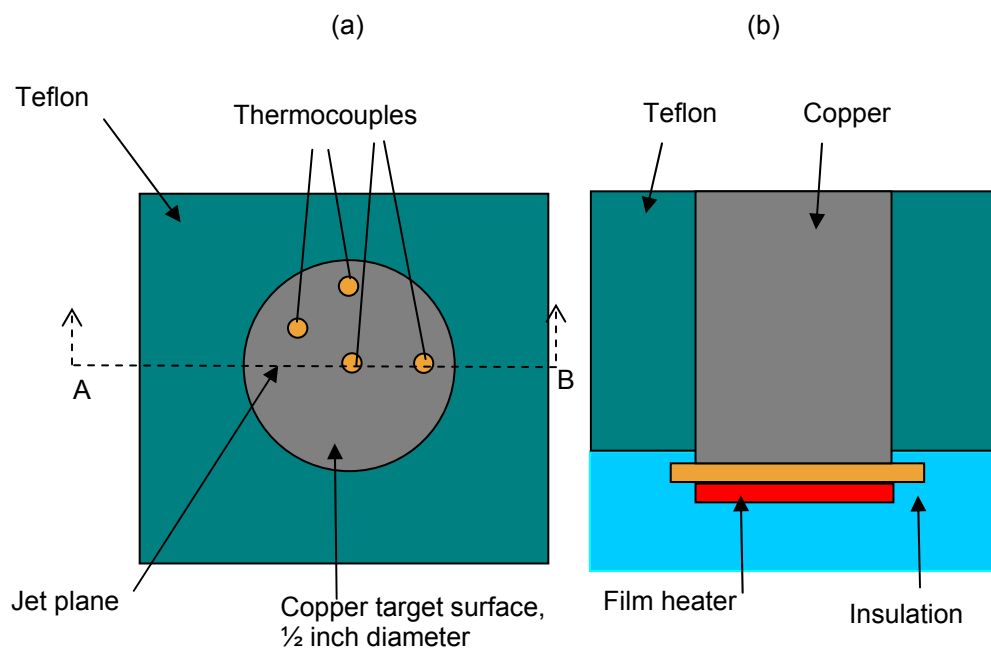


Figure 4. Surface of the copper plug that serves as the target surface (a) top view, (b) cross-sectional view along AB

Details of the heat transfer test apparatus are shown in Figure 4. Key measurements include the jet inlet and outlet temperatures, temperatures at four points on the copper target surface, the jet flow rate, the pressure drop across the jet, and the power input to the heater. The apparatus and the concept behind self-oscillating jets are described in detail in the FY 2006 report [8], and details will be excluded here. Three jet velocities (2, 7, and 12 m/s) and three target distances (1.1, 4.4, and 7.7 mm) have been explored in the free surface and the submerged configurations. Overall, a three-level (for velocity and target distance) full factorial design of experiments was used to perform about 130 experiments.

Figure 5 shows the pressure drop versus flow rate curves for the nozzles in the free surface and submerged configurations at a target distance of 1.1 mm. Target distance does not have a significant impact on the pressure. Results with other target distances (4.4 and 7.7 mm) look similar to those presented in Figure 5. Free surface or submerged configuration also does not affect the pressure drop. At any given flow rate, fluidic 1 has the highest pressure drop. At most flow rates or velocities (Figure 5), the frequency and fan angle of fluidic 1 are also the highest of the nozzles tested. Figure 5 also shows that the steady jet has the lowest pressure drop at all flow rates for all nozzles.

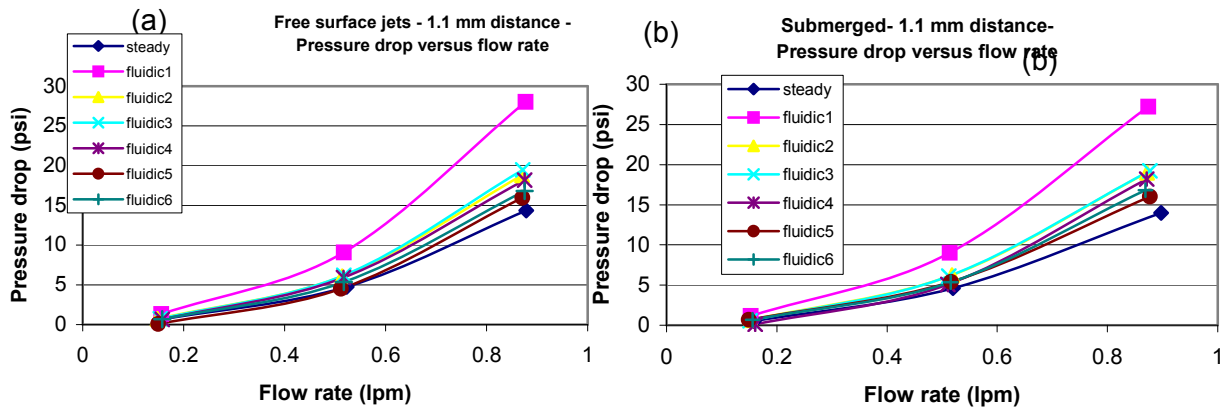


Figure 5. Pressure drop as a function of flow rate for nozzles in the (a) free surface configuration, (b) submerged configuration

Figure 6 reveals the impact of target distance on heat transfer for a single fluidic nozzle in both the free surface and submerged configurations. Overall, in the free surface configuration, the impact of target distance on heat transfer for the nozzles is noticeable, but not very strong. However, in the submerged configuration, target distance has a big impact on the heat transfer from the different fluidic nozzles. As shown in Figure 6(b), as target distance increases, at any given flow rate, the heat transfer attenuates.

At elevated flow rates, the impact of target distance becomes even more pronounced. At the lowest flow rate (Figure 6(b)), the difference in heat transfer results for the different target distances is about 10%; for the highest flow rate in Figure 6(b), the difference is almost 35% to 40%. Though results are not shown here, similar trends are observed for other fluidic nozzles as well. This aspect is more pronounced for the fluidic nozzles compared to the steady jets, since the oscillations and the sweeping motion are damped out with increasing target distance. Figure 6 reveals that at a short target distance (1.1 mm), heat transfer coefficients in the free surface and submerged configuration are almost identical. However, at a greater target distance (7.7 mm), the free surface configuration yields much higher heat transfer performance than the submerged configuration. The reason for this is most likely the damping effect mentioned previously.

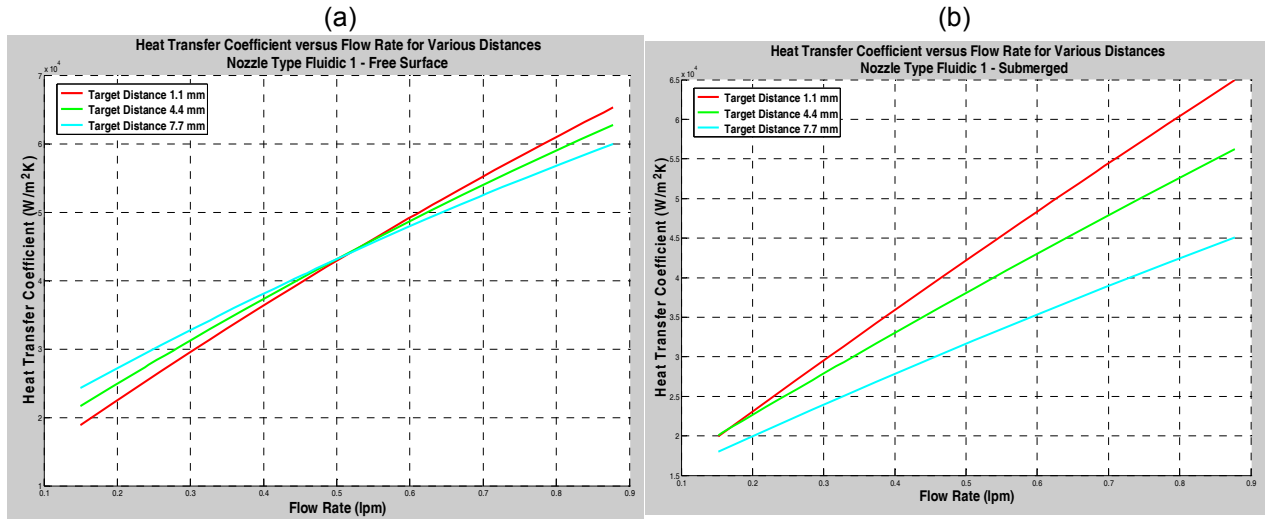


Figure 6. Impact of target distance on heat transfer with fluidic 1 in the (a) free surface, (b) submerged configuration

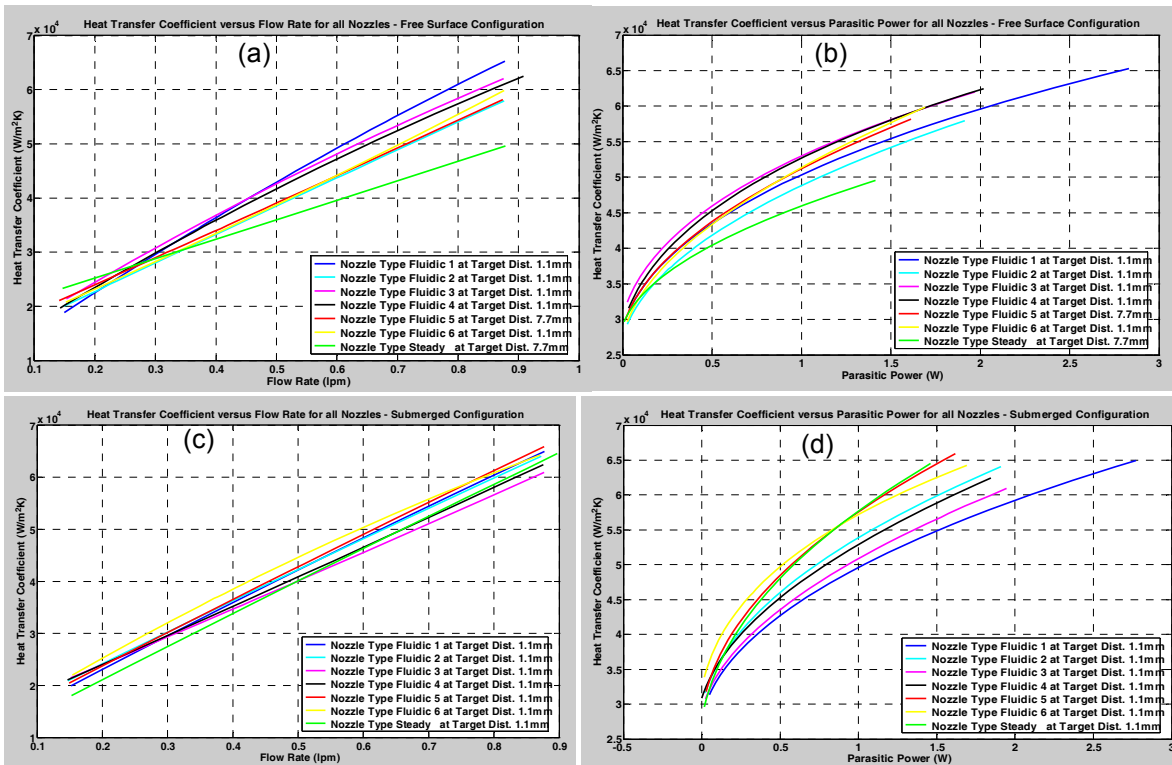


Figure 7. Heat transfer performance of nozzles at optimum target distance, (a) h versus flow rate in the free surface configuration, (b) h versus parasitic power in the free surface configuration, (c) h versus flow rate in the submerged configuration, (d) h versus parasitic power in the submerged configuration.

Figure 7 shows the heat transfer performance of all the test nozzles at their optimum target distance for the free surface and submerged configurations. Figures 7(a) and 7(b) show the heat transfer coefficients as a function of flow rate and parasitic power, respectively, for the free surface configuration. Figures 7(c) and 7(d) show the same for the submerged configuration. For any given flow rate, different nozzles have different pressure drops, which means the parasitic power consumed (product of flow rate and pressure drop) is different. The performance of the different nozzles must be compared for the same parasitic power consumed. This is the rationale for plotting heat transfer as a function of parasitic power.

Additionally, at close target distances, the sweeping motion of the oscillating jet causes significant disruptions in the boundary layer growth, which reduces the fluid-to-solid heat transfer resistance. Figure 7 illustrates that in the free surface configuration, the fluidic nozzles can yield up to 30% enhancement over a steady jet at comparable flow rates. For the same parasitic power, the enhancement over a steady jet is about 18%. For a sense of the numbers, at a flow rate of 0.87 lpm (velocity of 12 m/s), a heat transfer coefficient of about 65,000 W/m²K has been achieved with fluidic 1.

Figure 7(d) shows that fluidic 3 and the steady jet are the best performing nozzles in the submerged configuration. In the submerged configuration, virtually no enhancement is achieved from the self-oscillating jets over a steady jet; i.e., the best performing fluidic nozzles are nearly identical to the steady jet. Another important point is that the best heat transfer at a given parasitic power in the submerged configuration is higher than that in the free surface configuration.

There may be two reasons for the results achieved in Figure 7: (a) in the submerged configuration, the steady jet heat transfer performance picks up because there is no splashing, which is a problem, as mentioned earlier for the free surface steady jet configuration; (b) in the submerged configuration, the strength of the oscillations is somewhat dampened and attenuated. This is particularly true at greater target distances. The reason mentioned in (a) is certainly more important than (b).

Further analysis will be conducted and the complete set of results published in the technical literature during the FY2008 fiscal year.

Two-Phase Sprays and Jets—Experiments

In addition to our efforts with direct backside cooling with liquid jets, we are also exploring impinging jets with phase change to cool the IGBT package. Our initial efforts have focused on identifying appropriate coolants for the two-phase application [5-7] and in developing computational fluid dynamics models of the two-phase jet impingement process [8,9]. R134a (currently used in automotive air conditioning systems) and HFE7100/7200 have been identified as fluids which are particularly suitable for use as coolants for automotive applications [5-7]. HFE7100 and HFE7200 have good thermal and dielectric properties, can be used at atmospheric pressure, have low global warming potential, and zero ozone depletion potential.

During this past year, NREL worked with Mudawar Thermal Systems to fabricate a test vessel/experimental apparatus that would enable experiments with jets and sprays in the two-phase regime. The test apparatus and a cross section of the test vessel are shown in Figure 8. The test surface area 10x10 mm, which is a typical semiconductor switch size. The test surface is the top surface of an oxygen-free copper block, which is surrounded by fiberglass insulation. Cartridge heaters supply heat on the bottom side of the copper block. One thermocouple is embedded into the copper block and the temperature of the center of the copper block close to the target surface is measured. The surface temperature is backed out from a thermal conduction analysis. The liquid inlet temperature, the liquid flow rate, the temperature in the chamber, the pressure in the chamber, and the inlet pressure are all measured. Further details of the apparatus have been provided in an NREL report to DOE on spray cooling [9].

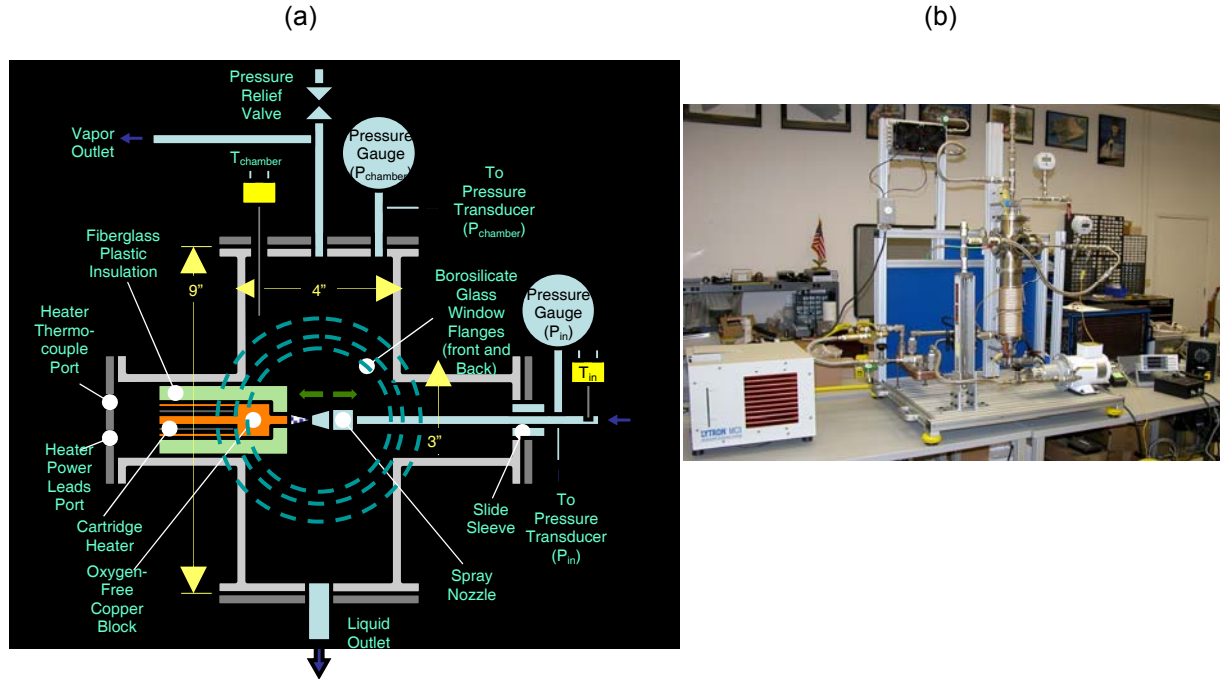


Figure 8. (a) Cross-section of the test vessel, (b) snapshot of the entire two-phase loop

A number of experiments have been completed with HFE7100, spanning a range of flow rates for both jets and sprays. Spray nozzles were acquired from an industry vendor, while rectangular slot jets (0.25 mm width) were used for the jet impingement experiments. Figure 9 shows sample boiling curves for spray and jet experiments. Figure 9(a) shows a sample spray experiment in which the fluid inlet temperature is 32.3°C and the rest of the parameters are indicated on the graph. The effective heat transfer coefficient at critical heat flux ($CHF=245 \text{ W/cm}^2$) is about $31,370 \text{ W/m}^2\text{K}$.

For the sample jet experiment (Figure 9(b)), the fluid inlet temperature is 34.8°C and the effective heat transfer coefficient at CHF (222 W/cm^2) is $26,942 \text{ W/m}^2\text{K}$. Broadly, this set of experiments demonstrates the conditions under which 200 to 240 W/cm^2 can be dissipated from a heated surface using HFE7100 as the fluid.

To understand these results in the context of IGBT package cooling, we performed numerical modeling in FLUENT. Figure 10 shows the domain that was used for this analysis. In this model, the silicon die temperature was maintained at 125°C and appropriate heat transfer coefficients mentioned have been imposed on the copper as well as the aluminum layers as shown in Figure 10. Figure 10(a) indicates the performance of a spray while Figure 10(b) shows the performance of a jet. The results show that jets and sprays of HFE7100 could be used to extract upwards of 200 W/cm^2 while keeping the die temperature at 125°C.

While the heat transfer performance of two-phase jets and sprays appear to meet the program requirements, the greatest challenge will be to develop a system that has an acceptable overall system cost. Outstanding thermal performance may allow the individual electronic switches to be operated at higher power levels, which could reduce the system cost and the number of devices.

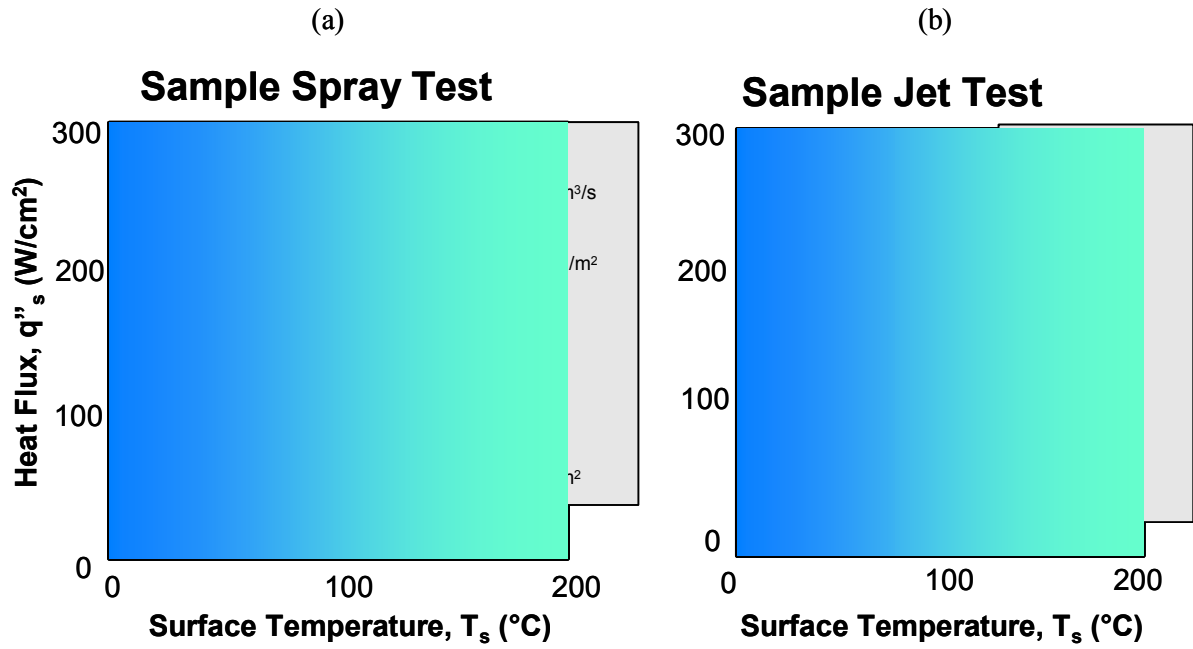


Figure 9. (a) Boiling curve for a sample spray experiment, (b) boiling curve with a sample slot jet experiment

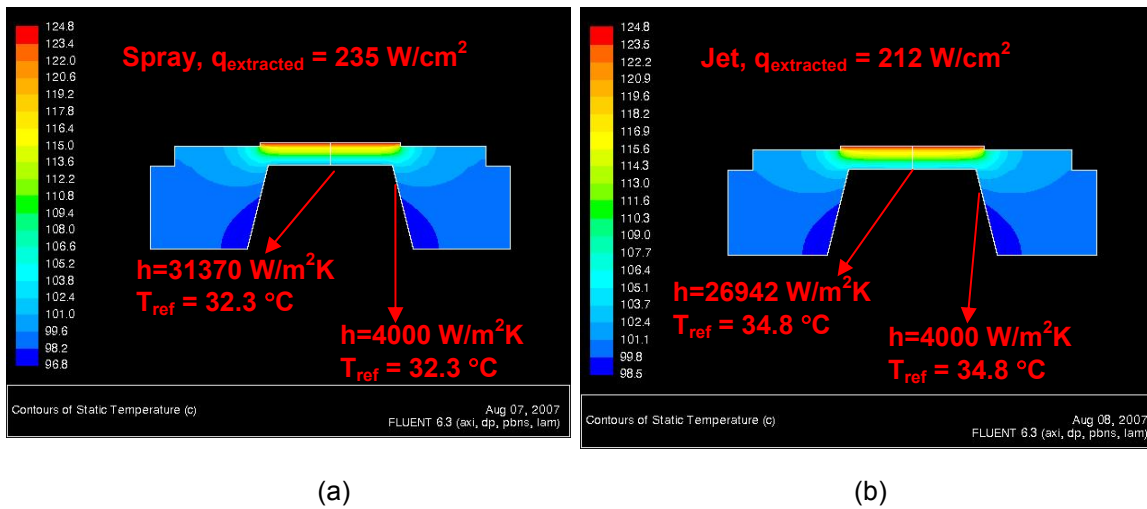


Figure 10. (a) Performance of an HFE 7100 spray (b) performance of an HFE 7100 jet

Conclusion

Based on the results and discussion presented in the previous sections, single- and two-phase jets/sprays could be used to dissipate 250 W/cm^2 heat flux while a maximum die temperature of 125°C is maintained. Meeting this goal with glycol-water at 105°C is very challenging. For trench IGBT configurations that allow for a maximum die temperature of 150°C , the problem is more tractable. A heat transfer coefficient of $60,000 \text{ W/m}^2\text{K}$ can dissipate over 210 W/cm^2 while the die temperature is maintained at 150°C and the coolant at 105°C .

In the free surface configuration, self-oscillating jets can offer enhancements over comparable steady jets by almost 20%. Hence, there is a need to continue exploring concepts like self-oscillating jets as well as enhanced surfaces to improve the heat transfer rates and increase the surface area available for heat transfer. Results presented in this report suggest that when 70°C glycol-water coolant is used, 250 W/cm^2 can be dissipated while the maximum die temperature is maintained at 125°C with heat transfer coefficients of about $60,000 \text{ W/m}^2\text{K}$. Conditions have been experimentally demonstrated in the report for achieving these heat transfer coefficients, although these results were obtained with deionized water.

The performance of jets and sprays of HFE7100 in the nucleate boiling regime have been characterized on a simulated electronic chip surface. Conditions have been demonstrated for dissipating upwards of 200 W/cm^2 while the maximum temperature is maintained at 125°C or lower. For the jet and spray results with HFE7100 in the nucleate boiling regime, the coolant inlet temperatures are very low (30° to 35°C) and the effective heat transfer coefficients are $26,000$ to $32,000 \text{ W/m}^2\text{K}$. Implementing this cooling scheme in an automobile would certainly add to the system complexity. A separate cooling loop would be required. In addition, a condenser would be required to condense the vapor and a cooling unit would also be required to bring the coolant to 30° to 35°C .

At this point, we must focus on the system-level implications and the packaging challenges that will arise as these cooling technologies are implemented in an automotive system. The results from this study have been fed to thermal systems modeling [9]. System-level modeling must be done to explore the feasibility of these cooling schemes from an overall systems perspective and to understand practical aspects such as system complexity and cost.

Publications

Narumanchi, S.V.J.; Troshko, A.; Hassani, V.; and Bharathan, D., 2007, "Numerical Simulations of Nucleate Boiling in Impinging Jets: Applications in Power Electronics Cooling," *International Journal of Heat and Mass Transfer*, in press, online August 15, 2007 at <http://dx.doi.org/10.1016/j.ijheatmasstransfer.2007.05.026>.

References

- [1] Zumbrunnen, D.A. and Aziz, M., 1993, "Convective Heat Transfer Enhancement Due To Intermittency in an Impinging Jet," *ASME Journal of Heat Transfer*, **115**, pp. 91–98.
- [2] Mladin, E.C. and Zumbrunnen, D.A., 1994, "Nonlinear Dynamics of Laminar Boundary Layers in Pulsatile Stagnation Flows," *Journal of Thermophysics and Heat Transfer*, **8**(3), pp. 514–523.
- [3] Mladin, E.C. and Zumbrunnen, D.A., 1997, "Local Convective Heat Transfer to Submerged Pulsating Jets," *International Journal of Heat and Mass Transfer*, **40**(14), pp. 3305–3321.
- [4] Camci, C. and Herr, F., 2002, "Forced Convection Heat Transfer Enhancement Using a Self-Oscillating Impinging Planar Jet," *ASME Journal of Heat Transfer*, **124**, pp. 770–782.
- [5] Mudawar, I., 2006, *Spray Cooling of Power Electronics and Technical Support for Advanced Power Electronics*, Technical report 1 submitted to NREL by Mudawar Thermal Systems under subcontract No. YEV-6-55511-01.

- [6] Mudawar, I., 2006, *Spray Cooling of Power Electronics and Technical Support for Advanced Power Electronics*, Technical reports 2 and 3 submitted to NREL by Mudawar Thermal Systems under subcontract No. YEV-6-55511-01.
- [7] Starke, M.R., Ayers, C.W., Hsu, J.S., and Conklin, J.C., 2005, *Potential Refrigerants for Power Electronics Cooling*, Oak Ridge National Laboratory Technical Report, ORNL/TM-2005/219.
- [8] Narumanchi, S.V.J., 2006, *Modeling Two-Phase Spray and Jet Impingement Cooling*, NREL Technical/Milestone Report, NREL Report No. TP-540-40618.
- [9] O'Keefe, M., and Bennion, K., 2007, "A Comparison of Hybrid Electric Vehicle Power Electronics Cooling Options," IEEE Vehicle Power and Propulsion Conference, VPPC 2007 Paper #7024.

2.7 Thermal Systems for Advanced Power Electronics and Electric Machines

Principal Investigator: Michael P. O'Keefe

National Renewable Energy Laboratory

Center for Transportation Technologies and Systems

1617 Cole Boulevard MS 1633

Golden, CO 80401

Voice: 303-275-4268; Fax: 303-275-4415; E-mail: michael_okeefe@nrel.gov

DOE Technology Development Manager: Susan A. Rogers

Voice: 202-586-8997; Fax: 202-586-1600; E-mail: Susan.Rogers@ee.doe.gov

NREL Program Manager: Kenneth Kelly

Voice: 303-275-4465; Fax: 303-275-4415; E-mail: Kenneth_Kelly@nrel.gov

Objectives

- The objective of the thermal systems effort is to facilitate the integration of APEEM thermal control technologies into commercially viable advanced automotive systems including hybrid electric, plug-in hybrid electric, and fuel cell vehicles by evaluating technologies in a systems context.

Approach

- Analyze thermal duty cycles of real HEV and PHEVs
- Perform a trade study of how various inverter packaging and design characteristics affect cooling performance
- Develop a fast transient 1D model for quick prediction of the inverter junction temperatures

Major Accomplishments

- Characterized the thermal duty cycle of the Toyota Prius hybrid traction inverter. Findings have been submitted as a DOE milestone report.
- Explored how various design factors for an inverter's thermal design affect cooling performance. Findings will be published at the 2007 IEEE Vehicle Power and Propulsion Systems Conference (VPPC) and have also been submitted as a DOE milestone report

Future Direction

- Further explore system implications of thermal designs by increasing analysis scope to include weight, cost, volume, and/or reliability
- Additionally, increase depth of analysis to include transient effects
- Explore promising technologies and package designs such as double-sided cooling more in-depth to confirm their merit. Include laboratory-level confirmation testing
- Expand the scope of our efforts to include investigation of motor thermal issues
- Expand the scope to investigate the cooling system as a whole. This is especially important for technology such as the PHEV where the PEEM system and internal combustion engine may need to run at significant load simultaneously while on the same cooling loop

Technical Discussion

In this section, we will elaborate on the three main projects for thermal systems this year: a thermal duty-cycle analysis, an inverter package design trade-off study, and fast transient thermal network model development.

Thermal Duty-Cycle Analysis

This study predicted heat rejection for the traction motor inverter (MG2 inverter) of a tested model year 2006 Toyota Prius. For additional detail, please refer to the full report (O’Keefe, Albright, and Bennion 2007). The Prius power module consists of the following components: two inverters—one to drive the motor (MG2) and another to drive the generator (MG1), a voltage-buck/boost converter, an air-conditioning compressor inverter, and a 12-V DC-to-DC converter. We considered the two inverters and the voltage-buck/boost converter with the majority of focus on the MG2 inverter. We used the results from an efficiency characterization effort on the MG2 inverter by ORNL to predict heat generation (Staunton et al 2006). The vehicle was examined in both an HEV and PHEV configuration. The same vehicle was used in both instances. Both on-road and dynamometer testing was conducted on the vehicle. The PHEV conversion was done by EnergyCS, which converts Priuses to PHEVs. However, the reader is cautioned that the PHEV configuration is a conversion and not a purpose-built PHEV; there are limitations in the Prius platform that prevent it from achieving optimal PHEV operation. For example, the Prius cannot run all-electrically above approximately 35 mph. Thus, a full display of PHEV benefits is not anticipated.

ANL’s PSAT vehicle simulation software was used to supplement the in-vehicle experimental data. The PSAT model was used to predict HEV operation over any drive cycle. The operational data are combined with the efficiency data from ORNL to predict heat generation (as depicted in Figure 1). Good agreement was achieved between modeling and test data for the HEV. We expect to be able to draw conclusions about thermal duty cycles for the HEV versus PHEV at the end of the testing.

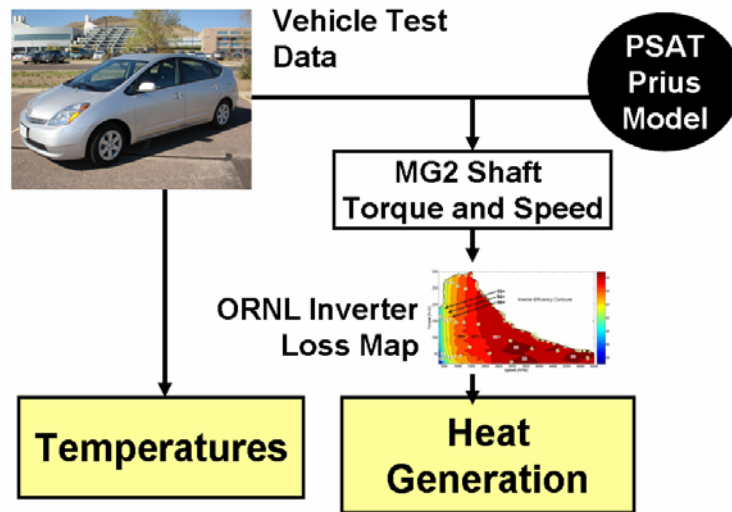


Figure 1. Prius thermal duty cycle data analysis flowchart

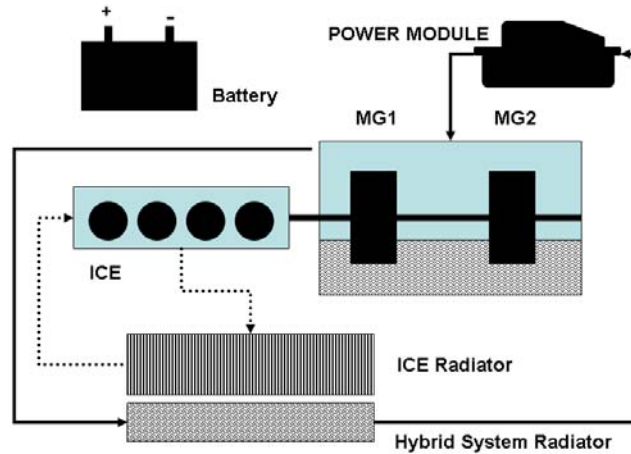


Figure 2. Prius cooling system for ICE and PEEM Components

Figure 3 depicts the heat generation predicted using the PSAT model and ORNL data over four test cycles: the highway fuel economy test (HWFET), the LA92 aggressive urban driving cycle, the Federal Test Procedure (FTP) cycle, and the US06 aggressive highway cycle (see O’Keefe, Albright, and Bennion 2007 for more information on these cycles). Table 1 summarizes the average heat generation rates predicted using ORNL efficiency data and vehicle test data. Four driving profiles were considered: the FTP cycle and US06 aggressive highway cycle were tested for the HEV configuration on a chassis dynamometer. For the PHEV, two on-road cycles were considered: a drive down an urban street in Denver (Colfax) and a drive along a Colorado highway (CO HW). Note that two of the cycles differ between simulation and testing results as the on-road cycle data (Colfax and CO HW) were not available at the time the simulations were conducted.

Table 1. Prius MG2 Inverter Heating by Cycle (from Test Data)

Vehicle and Cycle	Total Heat Energy (kJ)	Heat Energy per Distance (kJ/km)	Average Motor Power over the Total Cycle(kW)	Average Heat Generation over Total Cycle (W)	Average Heat Generation While Driving (W)
HEV/FTP Test Cycle	355.6	20.1	4.5	143.6	231.1
HEV/US06 Test Cycle	151.4	11.7	12.7	252.3	269.9
PHEV/Colfax Urban Driving	592.1	20.9	6.1	204.8	260.4
PHEV/CO HW Driving	400.0	5.2	10.0	137.5	150.6

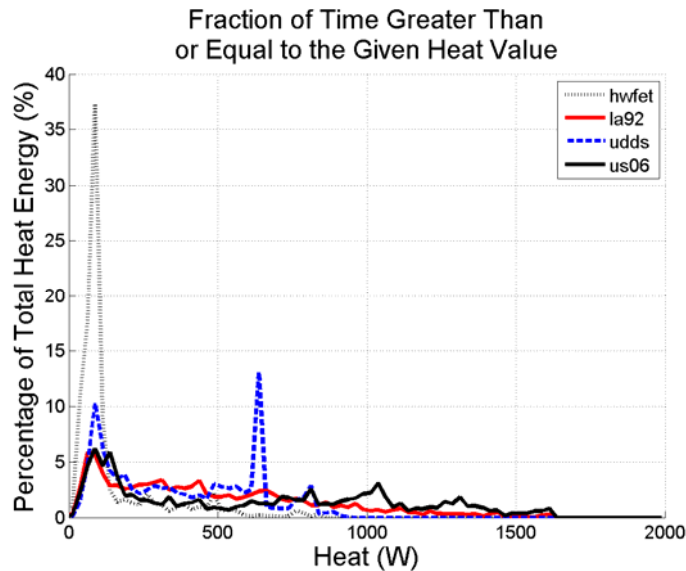


Figure 3. Prius HEV MG2 Inverter Predicted Heat Generation by Cycle (from simulation)

The maximum heat generation from the MG2 inverter is estimated based on vehicle operation and the ORNL efficiency data to be less than 1700 W for all cycles and simulations considered, and most of the heat energy dissipated is less than 1000 W. Heat generation events that approach 1700 W are brief in duration. Average heat generation is between 100 and 300 W for the cycles we observed. This heat is generated by the 12 IGBTs and 12 diodes of the MG2 inverter.

We observed from simulation, dynamometer, and on-road testing that the Prius MG2 does not provide either the 55 kW peak power or 30 kW continuous power requirements specified by the FreedomCAR and Fuels Partnership. The highest observed peak power was ~44 kW with average motoring power closer to 10 kW. The thermal duty cycles discussed here would be more intense for a FreedomCAR target electric machine.

The data from our study shows measured temperatures from the Prius CAN (controller area network) bus to be lower than the maximum rated silicon junction temperature of 125°C assumed for the Prius inverter. This data is summarized in Table 2. The Toyota Prius uses a dedicated cooling loop to cool the power module using coolant temperatures at 70°C or lower. The FreedomCAR and Fuels Partnership 2020 cost target for the electrical traction system is \$8/kW—a total system cost of \$440 for a 55-kW system (EETT 2006). A significant wholesale vehicle cost saving of between \$150.00 and \$200.00 has been estimated if the engine cooling loop could be coupled with the electric traction system cooling loop (Hsu et al. 2006). The integration of these cooling loops is a research goal for the FreedomCAR and Fuels Partnership. An integrated cooling loop requires use of an inlet coolant temperature of up to 105°C (EETT 2006). Additionally, the FreedomCAR target for the inverter volume is approximately 25% of the current Prius inverter volume for the same power rating implying that more heat must be transferred over a smaller footprint. The data we observed in examining the heat rates for the Prius show that the Prius HEV components have a relatively low utility in the sense of average power to peak power. Average traction motor (MG2) powers ranged from 9% to 25% of peak while the maximum CAN temperature reading for the inverter was 76 °C. To achieve the APEEM program goals, we would expect to see inverter temperatures over 105 °C with higher motor utilizations for platforms such as PHEVs. This represents a substantial change from Prius operation. Having a better understanding of the thermal duty cycle for a modern HEV such as the Prius gives us insight into the requirements for advanced thermal control that will be required to meet FreedomCAR goals.

Table 2. Prius Power Electronics Component Temperatures by Drive Cycle (°C)

	Colfax (PHEV Test)	CO HW (PHEV Test)	FTP (HEV Test)	US06 (HEV Test)
Ambient Temperature	15.6	16.1	23.9	23.9
Converter Average	32.2	47.8	NA	NA
Standard Deviation	5.3	6.3	NA	NA
Maximum	58	75	NA	NA
MG1 Inverter Average	22.2	42.2	32.6	51.9
Standard Deviation	6.2	3.5	5.1	4.2
Maximum	39	53	48	67
MG2 Inverter Average	25.8	36.5	33.6	49.4
Standard Deviation	6.2	3.4	4.8	6.6
Maximum	48	57	49	76

Inverter Package Design Trade-off Study

In this study, we quantified the heat dissipation potential of three inverter package configurations over a range of control factors. By the term package, we mean one IGBT, one diode, and the associated materials to thermally manage the IGBT and diode. For further information on this project, please refer to the full paper (O’Keefe and Bennion 2007).

The factors we examined include coolant temperature, number of sides available for cooling, effective heat transfer coefficient, maximum semiconductor junction temperature, and interface material thermal resistance. Heat dissipation potentials were examined in contrast to the FreedomCAR research goal to use 105 °C coolant and dissipate a target heat flux of 200 W/cm² across the insulated gate bipolar transistor (IGBT) and diode silicon areas.

The three package configurations we examined are as follows. An isometric view from CAD of the baseline package is given in Figure 4. Details of the baseline and the two other packages that were examined are presented in Table 3 and Figures 5 and 6. Double-sided concepts of each configuration were considered. The baseline package is representative of a modern HEV inverter cooling design. Because of the space considerations associated with packaging an inverter in a vehicle, it is unlikely that the two-dimensional projected area or footprint available to each package would be increased. In fact, the trend is to further decrease the inverter’s footprint. Thus, increased package footprints were not considered.

The two other package configurations considered here include a direct backside cooling (DBSC) concept (Figure 5—left) and an integrated heat-sink (IHS) concept (Figure 5—right). The DBSC is currently under evaluation in prototype form here at NREL. In the DBSC concept, the backside of the Direct Bond Copper (DBC) layer is opened up to direct contact with the coolant for convective heat transfer. Convective heat transfer via jet impingement is currently being examined for use with DBSC. For the IHS concept, the baseplate functions as a heat sink. Both concepts eliminate the need for TIMs. However, the reliability of these concepts is still under investigation (for example, with regard to differential thermal expansion problems). Another concept not considered here is the ability to use air jets directly on the chip (i.e., even less packaging than the DBSC concept). Double-sided air cooling may be an option as well.

Table 3. Package Configuration Key

Name	Configuration
BASELINE (BL)	<i>Power semiconductor:</i> Silicon <i>Substrate:</i> Aluminum Nitride DBC <i>Baseplate:</i> Copper <i>TIM:</i> 5 to 100 mm ² -K/W <i>Heat Sink:</i> Aluminum
DIRECT BACKSIDE COOLING (DBSC)	<i>Power semiconductor:</i> Silicon <i>Substrate:</i> Aluminum Nitride DBC <i>Baseplate:</i> None <i>TIM:</i> None <i>Heat Sink:</i> None
INTEGRATED HEAT SINK (IHS)	<i>Power semiconductor:</i> Silicon <i>Substrate:</i> Aluminum Nitride DBC <i>Baseplate:</i> Copper (baseplate is heat sink) <i>TIM:</i> None <i>Heat Sink:</i> None

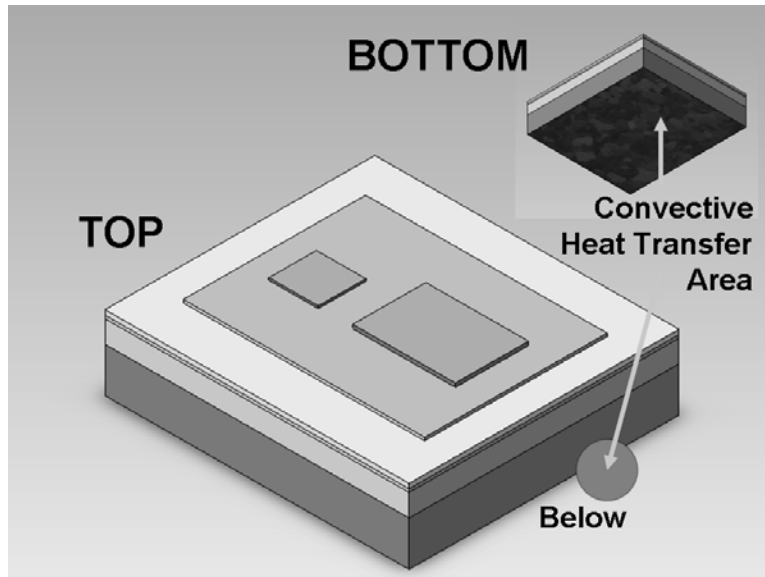
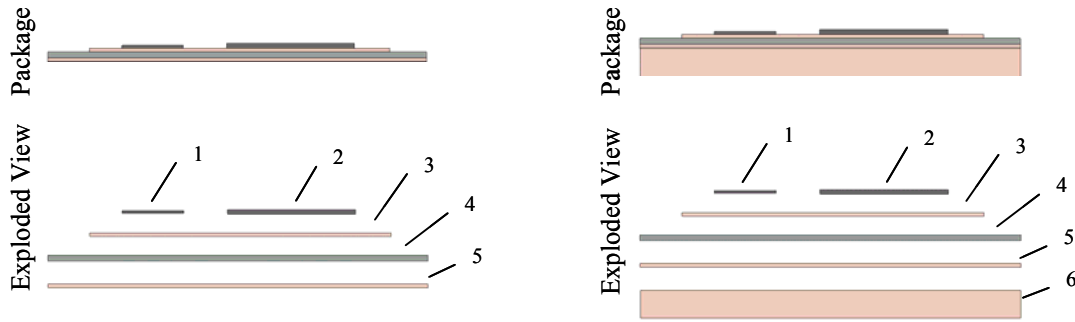


Figure 4. Isometric view of the baseline package



key: 1. diode, Si; 2. IGBT, Si; 3. DBC top layer: Cu; 4. DBC substrate layer: AlN; 5. DBC bottom layer: Cu; 6. baseplate: Cu; 7. heat sink: Al

Figure 5. DBSC package (left) and IHS package (right) configurations

For comparison purposes, the area open to convective heat transfer for each package configuration was fixed. Double-sided cooling concepts are assumed to have twice that area available for heat dissipation to the coolant. An *effective* heat transfer coefficient was applied to the convective heat transfer areas of each package from 5,000 to 80,000 W/m²-K representing a range of cooling options from advanced air cooling to liquid jet impingement.

Figures 6 and 7 show how effective heat transfer coefficient affects the total heat flux dissipated for coolant at 105 °C. Total heat flux is measured as total heat dissipated divided by the area of semiconductor devices (IGBT plus diode area for a total of 1.76 cm² in this instance). Horizontal dashed lines in the figures indicate our heat flux dissipation goal of 200 W/cm². The width of the region for the baseline results is due to changes in TIM thermal resistance which was evaluated at 5 mm²-K/W and 100 mm²-K/W. The TIM resistance has a significant impact on the baseline results especially at higher convective heat transfer values. Figure 6 assumes both IGBT and diodes are at 125 °C while Figure 7 assumes both IGBT and diodes are at 200 °C. Figure 6 shows the challenge of cooling conventional silicon-based devices with 105 °C coolant when maximum junction temperature is limited to 125 °C. However, the simulation does seem to indicate that there are possible 2-sided cooling solutions that meet the flux goal with advanced packaging concepts at 30,000 W/m²-K and greater heat transfer coefficients. Further investigation is needed.

In contrast, the results of Figure 7 with a 200 °C maximum junction temperature tolerance are more favorable. All designs can dissipate the target heat flux over the range of heat transfer coefficients considered. However, even under these favorable conditions, the package configurations require effective heat transfer coefficients of 5,000 W/m²-K to 15,000 W/m²-K to meet the heat flux dissipation goal of 200 W/cm². Cooling strategies such as conventional forced air cooling with fins and free convection to air may be challenged to provide sufficient convective cooling under these conditions. However, investigations with advanced forced air cooling show promise as discussed elsewhere in this summary report. If SiC with high-temperature package designs can enable junction temperatures larger than 200 °C, opportunities for minimal cooling designs or for extremely small extremely high heat flux designs may present themselves.

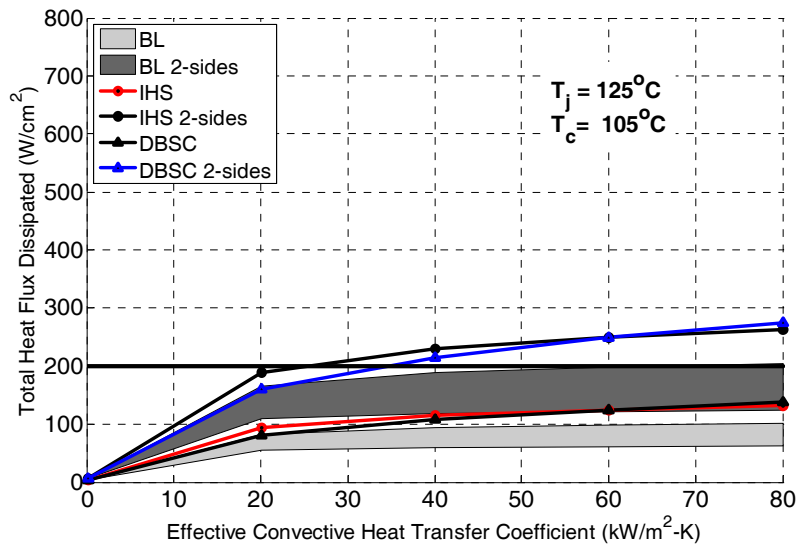


Figure 6. BL package with 105 °C coolant and a max junction temperature of 125 °C

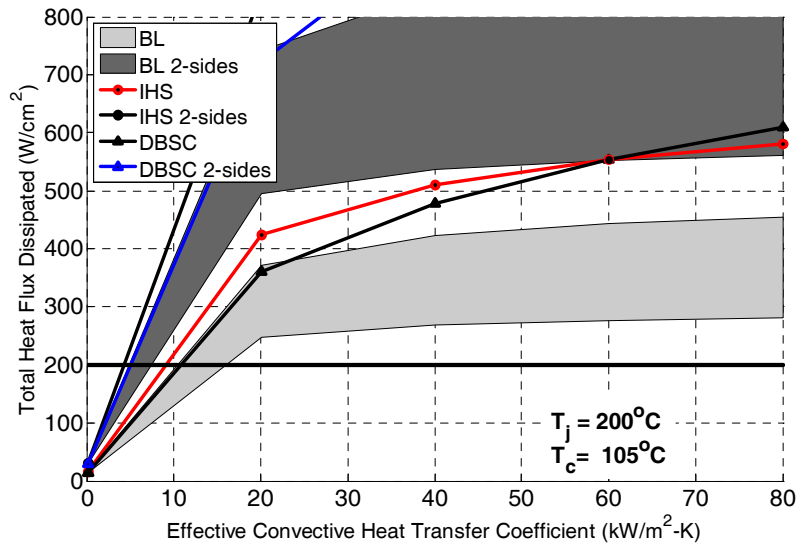


Figure 7. BL package with 105 °C coolant and a max junction temperature of 200 °C

In terms of packaging concepts, the results from the IHS and DBSC concepts are quite similar. The DBSC has higher dissipation rates than the IHS concept when higher convection coefficients are used. In contrast, the IHS design has slightly better heat dissipation potential at lower convection coefficients because of more effective heat spreading and area utilization. The double-sided packaging concept shows significant potential to increase heat dissipation. Although double-sided cooling receives only an initial treatment in this study, the potential indicates this concept should be further investigated. The IHS and DBSC concepts show the greatest potential.

Fast Transient Thermal Network Model Development

The focus of the fast transient thermal network model (FTTNM) is to allow for quick prediction of temperatures over long periods of time. We are focusing initially on the inverter. We are collaborating with ORNL on this project as there are many synergies with ORNL's electro-thermal modeling.

We have demonstrated the ability to take a temperature step response from either FEA or actual data and build a network model. Predicted temperatures from the network model show good agreement with temperature results predicted by the FEA model used to create the network model. However, the network model runs at a fraction of the FEA's simulation time.

Our vision for the FTTNM is depicted in Figure 8. Starting from the left, the user will be able to input material properties and geometries for all the layers in an inverter package stack-up. A "detailed model" created with the FEA method or possibly an analytical solution is then automated to generate a temperature response to a step-input of heat. An optimization algorithm is then used to fit thermal resistance and capacitance coefficients of a network model to reproduce the original temperature response. Unless the original geometry and/or material properties change, this network model can act as a surrogate for the "detailed model", but run at much greater speeds. We hope to make this process entirely automated.

Once the network model is created, it only requires information on the initial temperature and heat generation versus time to quickly predict the dynamic temperature change. An optional step would be to include a temperature-sensitive electrical device model that takes in temperature and predicts heat generation. The coupling between the electrical and thermal aspects of the inverter makes this step worthwhile.

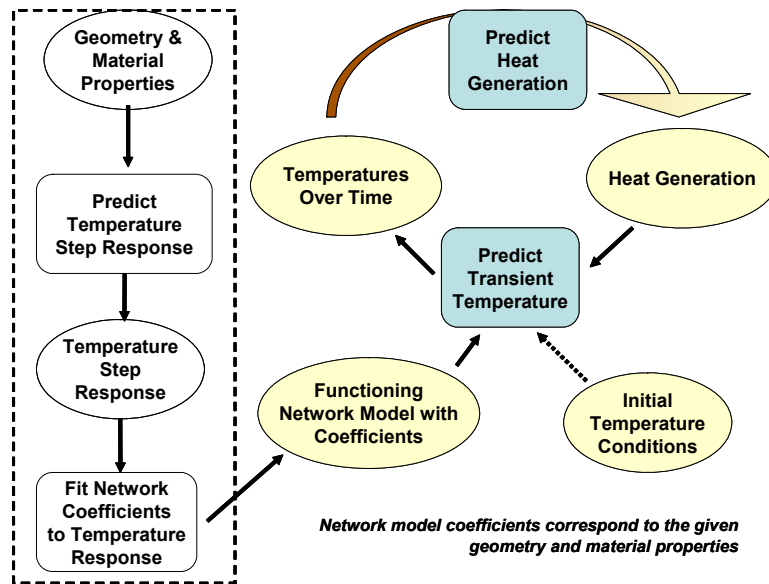


Figure 8. Workflow for the Fast Transient Thermal Network Model (FTTNM)

ORNL's current focus is on the electrical modeling and NREL's focus is on the thermal modeling. There is an obvious synergy here since both the electrical and thermal problems are coupled. We hope to be able to demonstrate this concept by the end of FY07.

Future functionality would include introducing thermal coupling between components and coupling to a cooling circuit model that would include the radiator, motor, inverters, and engine. The dynamic heat rejection and interplay between all of these components will be critical to understand moving forward. This model will be useful to NREL for future thermal systems work, to ORNL for coupled electro-thermal circuit analysis, and for future reliability studies to generate time-at-temperature profiles.

Conclusion

In conclusion, NREL has begun several efforts in the thermal systems area this fiscal year. The intent of these projects is to predict how the thermal management technologies we are working on and considering both internal and external to the DOE program will perform and what implications they will have on vehicle PEEM in a systems context. Important attributes we plan to eventually be able to address

for the thermal management subsystem include cost, performance, weight, volume, and reliability (both of the cooling system itself and the components it cools). To execute this project, we need to know about three things:

1. The system cooling requirements (i.e., the thermal duty cycles)
2. The characteristics of the cooling technologies themselves and
3. The system implications of the cooling technologies when used in systems of interest.

The NREL thermal systems effort is growing towards addressing points (1) and (3) above with the remainder of NREL's thermal efforts focus on point (2).

This fiscal year, we have developed an understanding of the transient heat generation at the main traction inverter of the Toyota Prius HEV system and also have performed a system trade-off study examining how major package design factors affect inverter thermal performance. Additionally, we are developing the capability to do fast transient temperature analysis of inverter designs.

Some noteworthy observations from each of these activities are as follows:

- The average heat rejection of the Toyota Prius main traction inverter (MG2) is typically within 100 to 300 W with excursions up to 1700 W; reported temperatures from the inverter CAN bus never rose above 80 C; these conditions are less stringent than the FreedomCAR targets both in maximum temperatures (due to the desire to couple engine and electric powertrain cooling loops) and also in terms of average heat rejection (especially for a PHEV system)
- Several design factors were examined that relate to inverter cooling including coolant temperature, number of sides available for cooling, effective heat transfer coefficient, maximum semiconductor junction temperature, and interface material thermal resistance. We observed that:
 - It may be possible to cool silicon-based junction temperatures to 125 °C using double-sided cooling with advanced package designs while running a heat flux rate of 200 W/cm² with 105 °C coolant.
 - Even at a 200 C junction temperature tolerance, active cooling will likely be required to support a heat dissipation of 200 W/cm².
 - Double-sided cooling shows much promise and should be further examined.
- NREL is collaborating with ORNL to create a fast thermal transient network model (FTTNM) to support work on electro-thermal modeling, NREL thermal systems studies, and future reliability studies

Publications

O'Keefe, M.; Albright, G.; Bennion, K. (June 2007). *Thermal Duty Cycles of Hybrid Electric Vehicle Power Electronic Components*. National Renewable Energy Laboratory Report No. TP-540-41829.

O'Keefe, M. and Bennion, K. (August 2007). *A Comparison of Hybrid Electric Vehicle Power Electronics Cooling Options*. National Renewable Energy Laboratory Technical Report No. CP-540-41886.

References

1. EETT. (2006). Electrical and Electronics Technical Team Roadmap. FreedomCAR and Fuel Partnership. http://www1.eere.energy.gov/vehiclesandfuels/pdfs/program/eett_roadmap.pdf
2. Hsu, J.; Staunton, R.; and Starke, M. (2006). *Barriers to the Application of High-Temperature Coolants in Hybrid Electric Vehicles*. Oak Ridge National Laboratory Technical Report ORNL/TM-2006/514.
3. O'Keefe, M.; Albright, G.; Bennion, K. (June 2007). *Thermal Duty Cycles of Hybrid Electric Vehicle Power Electronic Components*. National Renewable Energy Laboratory Report No. TP-540-41829.

4. O'Keefe, M. and Bennion, K. (August 2007). *A Comparison of Hybrid Electric Vehicle Power Electronics Cooling Options*. National Renewable Energy Laboratory Technical Report No. CP-540-41886.
5. Staunton, R.; Ayers, C.; Marlino, L.; Chiasson, J.; Burrell, T.; and Olszewski, M. (2006). *Evaluation of 2004 Toyota Prius Hybrid Electric Drive System*. Oak Ridge National Laboratory Technical Report ORNL/TM-2006/423

Patents

None

2.8 Thermal Interface Materials for Power Electronics

Principal Investigator: Sreekant Narumanchi

National Renewable Energy Laboratory

MS 1633

1617 Cole Blvd

Golden, CO 80401-3393

Voice: 303-275-4062; Fax: 303-275-4415; E-mail: sreekant_narumanchi@nrel.gov

DOE Technology Development Manager: Susan A. Rogers

Voice: 202-586-8997; Fax: 202-586-1600; E-mail: Susan.Rogers@ee.doe.gov

NREL Program Manager: Kenneth Kelly

Voice: 303-275-4465; Fax: 303-275-4415; E-mail: kenneth_kelly@nrel.gov

Objectives

The overall objectives of this research project are:

1. Fabricate an advanced TIM which significantly reduces the overall package thermal resistance to facilitate use of 105°C engine coolant and/or air cooling.
2. Achieve thermal resistance below 10 mm²K/W (3 to 5 mm²K/W)
3. Meet automotive system requirements for performance, reliability, cost, quality, etc.

The project was initiated in FY 2006 to thoroughly characterize the state-of-art conventional interface materials as well as novel materials and recommend a suitable candidate material for automotive power electronics applications. The specific objectives for FY 2007 were:

- Identify and assist in the development of low thermal resistance, low-cost, thermal interface materials. We are currently trying to understand the thermal performance and behavior of conventional interface materials such as greases.
- Characterize the thermal performance of some of these interface materials over extended temperature and pressure ranges characteristic of automotive applications.

Beyond FY 2007, the objectives include:

- Characterize the performance of materials such as phase change materials, metallic TIMs, phase change metallic alloys, graphite sheets, and carbon nanotubes.
- Characterize the impact of thermal cycling on the thermal performance of the interface materials.
- Characterize the in-situ performance of these materials. Often, the package in-situ performance is not exactly the same as the material performance under more idealized conditions.

Approach

- NREL acquired and modified in-house a test stand to perform thermal resistance measurements over the automotive temperature (-40° to 150°C) and pressure ranges (20 to 150 psi). This test stand is based on the standard ASTM-D5470 steady-state test method for thermal resistance measurements. The goal is to perform consistent and unbiased characterization of interface materials.
- We initiated interactions with industry partners such as Semikron, UQM, and Delphi to make our work relevant to the automotive industry. In conjunction with industry partners, we want to compare NREL results with those obtained by alternative methods such as the transient laser flash method.
- We acquired samples of several conventional thermal interface materials, including greases, filler pads, phase change materials, metallic TIMs, and graphite sheets from manufacturers. Some of the

greases we acquired are currently being used by suppliers to the automotive industry such as Semikron and UQM.

- We have performed experiments to characterize the performance of several conventional thermal greases. Since greases are predominantly used in the automotive industry, this is a benchmarking exercise and establishes the baseline data against which the performance of any other thermal interface material will be measured.
- We have performed thermal finite element modeling to understand the performance of the apparatus as well as to design modifications to the apparatus to improve it. This modeling has been performed within the framework of the finite element software ANSYS.
- The results obtained with thermal greases are cast in the context of a realistic inverter power electronics cooling. The impact of thermal resistance on the maximum junction temperature in an IGBT package is clearly outlined.

Major Accomplishments

The following are the main accomplishments of this project in FY 2007:

- Acquired and modified the test apparatus for making thermal resistance measurements, based on the ASTM D5470 steady-state methodology to make consistent, reliable, and repeatable measurements of thermal resistance of interface materials.
- Initiated development of a non-biased material thermal performance database. The thermal performance of a variety of thermal greases has been characterized over a range of temperatures and material thicknesses characteristic of automotive applications. Results indicate that the best greases may not be in widespread use in the automotive industry. The results presented here could bring this aspect to the attention of the automotive industry.
- Performed numerical finite element modeling to understand the behavior of the apparatus, improve it, and characterize the impact of TIM thermal resistance on the maximum die temperature.
- Initiated significant industry collaboration and interaction (UQM, Delphi, and Semikron). The scope of collaboration currently includes testing samples provided by industry partners, exchange of experimental results obtained via different test methods, and seeking information about the practical industry perspective on TIMs.

Future Direction

The following activities are planned for FY 2008 and beyond:

Complete the experiments with greases.

Explore other materials such as metallic TIMs, graphite-based materials, phase-change materials, filler pads and carbon nanotube-based materials. Characterize these materials via the test apparatus at NREL.

In collaboration with industry, characterize the performance of the best performing materials in a realistic package configuration. The thermal resistance of the package/composite structure will be characterized on the NREL test stand. This test apparatus and approach that has been described is a steady-state methodology. A transient test methodology will also be explored.

Purchase a benchtop environmental chamber to conduct studies related to thermal cycling of the package with the TIM in place. The impact of thermal cycling on the thermal performance of the TIM will be characterized. This cycling will be performed over a temperature range of -40° to 150°C and after cycling, the thermal resistance of the package will be characterized on the NREL test stand. Aspects such as the impact of aging (long-term exposure of the package at an elevated temperature) on the thermal performance of these interface materials will also be explored. These studies will also be conducted in the environmental chamber.

For each interface material that is explored (grease, filler pad, phase change material, metallic sheet, graphite sheet, carbon-nanotube based TIM), consider all the manufacturing aspects and costs in addition to the thermal performance.

Technical Discussion

Importance of Thermal Interface Materials

This section demonstrates why thermal interface materials are important. Figure 1 shows the different layers constituting a typical IGBT package in an inverter. The silicon die is soldered to the DBC layer, which is composed of an aluminum nitride layer sandwiched between two copper layers. This DBC layer is attached to an aluminum base plate/heat sink via thermal grease. This thermal grease is 25 to 50 microns thick (bond line thickness) and has a thermal conductivity of 0.4 to 0.7 W/mK.

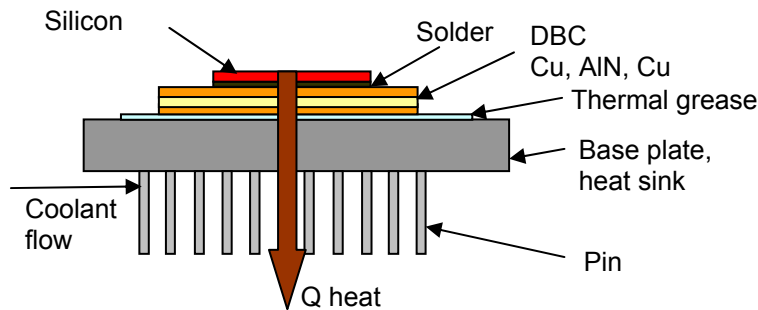


Figure 1. Layers constituting the IGBT package in an inverter

In an actual IGBT package, manufacturing constraints can cause the DBC layer to have a camber of 100 microns. This implies that even though the intent is to keep the bond line thickness to a minimum, the TIMs sometimes fill gaps of 100 microns or greater. Typically, the inverter has a heat sink in which the coolant flows through pin fins in a channel flow configuration. To assess the impact of thermal resistance, we performed a 3-D ANSYS finite element modeling. The domain used for the simulation is shown in Figure 2. Figure 2(a) shows the IGBT half-bridge and Figure 2(b) shows a close-up revealing the different layers constituting the IGBT package. Further details about this have been provided in the FY 2006 report on thermal interface materials [1].

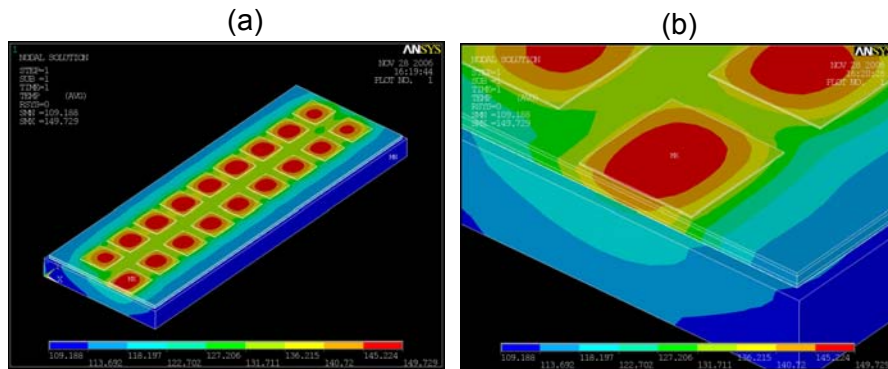


Figure 2. Domain for ANSYS 3D conduction model for illustrating the impact of TIM on the temperature fields; (a) IGBT half-bridge; (b) close-up showing part of the structure and the different layers

For the simulations, the coolant temperature was fixed at 105°C, representing a glycol-water mixture at 105°C. Except for the resistance of the interface material, all other material properties in the model are based on a typical IGBT package. The heat flux was fixed at 100 W/cm² and the convective heat transfer coefficient used on the back of the aluminum baseplate was set at 50,000 W/m²K. This represents an aggressive liquid cooling scheme. Figure 3 shows the impact of the TIM thermal conductivity on the maximum die temperature. The baseline case shown corresponds to the best of the grease samples measured at NREL with a thermal conductivity of 3.7 W/m-K. For the analysis the grease thickness was set at 75 microns for a thermal resistance of 26.5 mm²K/W. The 5x TIM case corresponds to a TIM thermal resistance of 5.3 mm²K/W (5-times lower than the baseline), while the 10x TIM case corresponds to 2.65 mm²K/W. It should be noted that the thermal resistance values include the material bulk thermal resistance as well as the contact resistance.

Figure 3 shows that for the baseline case, there is a significant temperature jump across the TIM (approximately 17°C). For the 5x TIM case, the temperature rise across the TIM is small (about 4°C), while for the 10x TIM case, the temperature rise is even smaller (about 2°C). Interestingly, increasing the thermal conductivity beyond 5x does not significantly change the maximum die temperature. This implies that once the thermal resistance of the interface material is not the dominating resistance, it does not matter if its resistance is reduced further. Other layers in the package start dictating the thermal map of the package. It is also worth noting that the baseline case corresponds to a TIM thermal resistance of 26.5 mm²K/W. If a higher thermal resistance were chosen as the baseline (which could be the case in an actual inverter), the impact of TIM resistance on the temperature results would be even more dramatic.

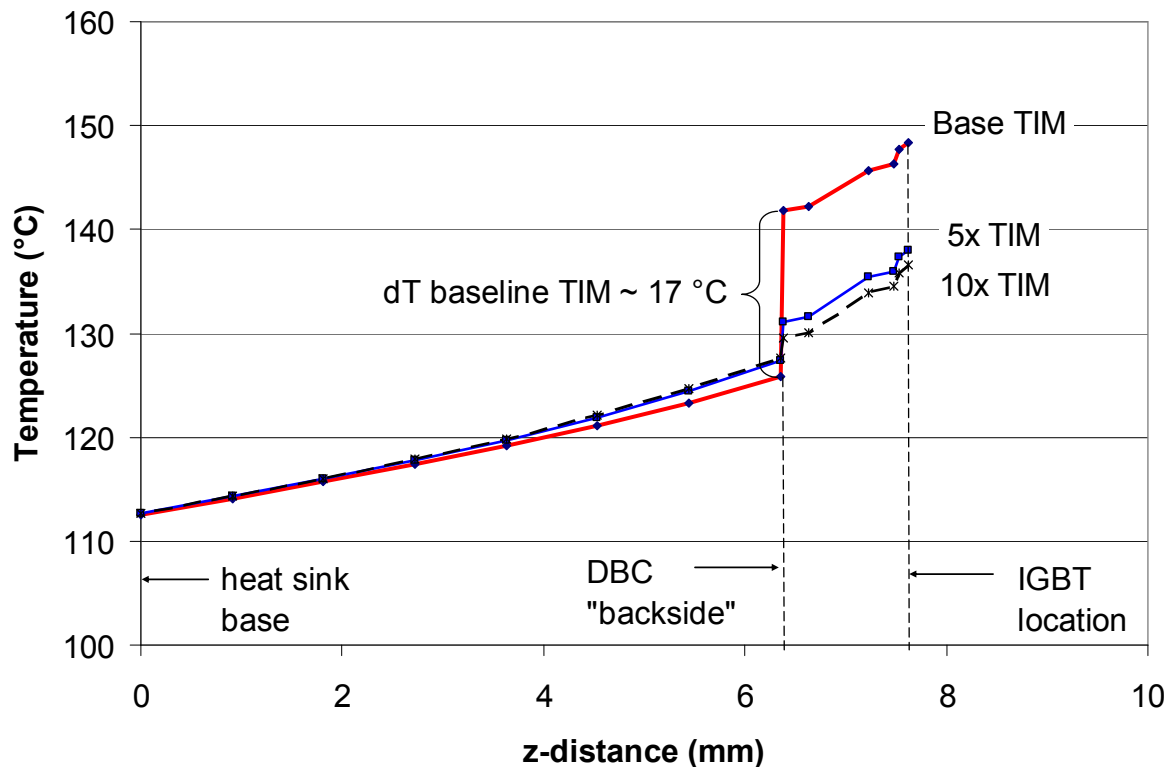


Figure 3. Temperature impacts of TIM thermal resistance for base TIM, 5-times lower resistance, and 10-times lower resistance

State-of-the-Art of Thermal Interface Materials

In this section, we briefly review the state-of-the-art of thermal interface materials. The total thermal resistance of an interface material is composed of the bulk resistance (= thickness/thermal conductivity) and the contact resistances. A high thermal conductivity can reduce the bulk thermal resistance of the interface material; however, the contact resistance must also be minimized. Contact resistance is an area where significant attention has been focused in the literature (e.g. [2-4]).

The focus here is on the automotive power electronics cooling, but thermal interface materials also play a key role in connecting various components of the thermal solution in other microelectronics and high power applications as well [4]. The continual increase in cooling demand for microprocessors has led to increased focus on improving the thermal interface materials. Figure 4 shows the state-of-the-art of thermal interface materials. Significant advances have been made in the development of thermal greases/gels, phase change materials, solder, phase change metal alloys, advanced polymers, and carbon nanotubes as interface materials. In the automotive industry, greases are still predominantly used as interface materials.

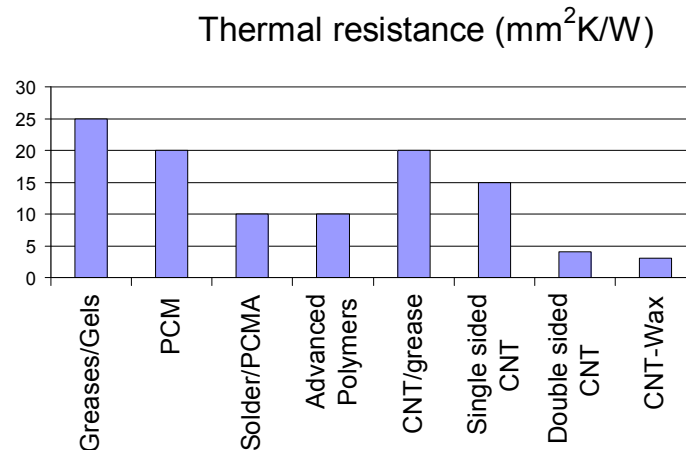


Figure 4. State-of-the-art of thermal interface materials

Some problems with greases are pump-out during repeated thermal cycling, dry-out over time (aging effects), and nonuniform application. One reason for the widespread use is that greases fill up the microscopic voids and cavities between mating surfaces very well. This results in a fairly low contact resistance at even moderate pressures (lower than 50 psi). This aspect will be elaborated upon in a subsequent section.

Test Apparatus for Thermal Resistance Measurements

NREL acquired, tested, redesigned and improved a test stand, based on the ASTM D 5470 test method [5] for measuring thermal resistance. The intent of acquiring the test stand is to characterize the thermal performance of novel as well as state-of-the-art thermal interface materials that are suitable for automotive applications and develop an unbiased, consistent database.

Figure 5 shows the test apparatus in the Electrical Systems Laboratory at NREL as well as details of the components of the test stand. The basic principle of ASTM D5470 has been outlined in the FY 2006 report [1]. Figure 5(b) shows various components of the apparatus, which are the hot plate with the cartridge heaters embedded in it, the cold plate with silicone oil circulating through it, the spreader blocks, the metering blocks, the resistance temperature detectors (RTDs) for accurate temperature measurement, and the pneumatic press for applying load on the sample under test.

The load for the pneumatic press is controlled via Labview, the required load is set by the user, and a proportional control with a deadband and adaptive gain has been implemented in Labview. The RTD

temperatures are also acquired via Labview. The thermal resistance of the sample under test is determined as: $R = \Delta T A/Q$, where, ΔT = temperature difference across the sample, Q = average power going through the sample, A = area of the sample.

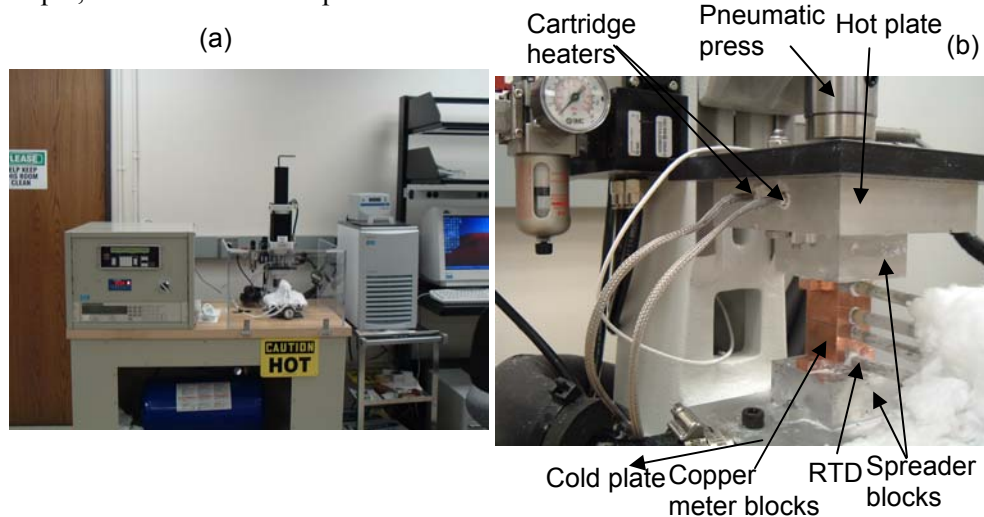


Figure 5. Test apparatus for thermal resistance measurements, (a) facility setup at NREL, (b) apparatus

Modeling of the Apparatus and Design Improvements

Several modifications have been made to the original test apparatus that was acquired from DS&A LLC. To understand the behavior of the apparatus, we performed 3-D finite element modeling in ANSYS. The original geometry of the metering blocks was square. We studied the impact of cylindrical metering blocks, material of the blocks (copper versus aluminum), the thickness and material of the spreader blocks, and the impact of insulation. Figure 6(a) shows the simulation domain for the square meter block geometry and Figure 6(b) shows the domain with the round meter blocks. In the simulations, three main aspects were studied: (a) the uniformity of temperature in a given plane in the metering blocks; (b) the standard deviation of temperature in any given plane; and (c) the linearity of temperature in the blocks as a function of vertical distance. The goal was to increase uniformity, reduce the standard deviation and maintain as close to a linear profile as possible under various TIM thermal resistances. The final design that was implemented is shown in Figure 7. Round copper metering blocks screw into a square copper spreader block. There are holes in the metering blocks for the four RTDs (two in the “hot” block and two in the “cold” block). These holes are 1-1/8 inches deep. The RTDs have been found to have different sensitivity to the depth of insertion. When inserted together in a silicone oil bath, more than 1 inch deep, they give readings that are within 0.05°C of one another. However, when the insertion depth is less than 1 inch, the reading of one of the RTDs starts diverging from those of the other three RTDs.

Test Results with Conventional Thermal Greases

In this section, we discuss some experimental results that were obtained with the square metering blocks. As mentioned earlier, since greases are still predominantly used in the automotive industry, this is a benchmarking exercise. The intent is to compare the performance of any alternative TIM that is explored against the performance database that is collected for greases. Figure 8 shows the experimental and corresponding modeling results with a conventional grease Wacker Silicone P12 used in an inverter as a thermal interface material between the IGBT package and the heat sink. The average temperature in the metering blocks is plotted as function of the vertical distance, i.e., moving from the cold plate (0) to the hot plate (2 inches). The two graphs provided as insets show the temperature contours that were obtained in the apparatus via modeling.

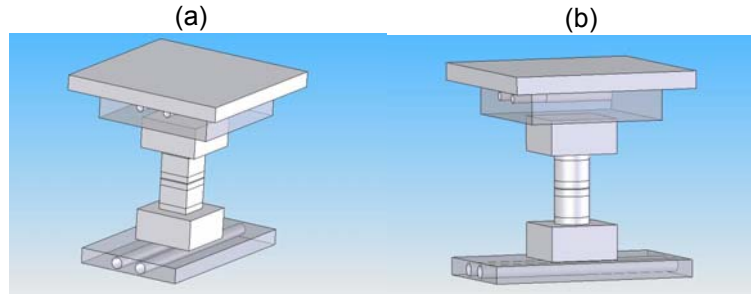


Figure 6. Simulation domain, (a) square geometry, (b) round geometry

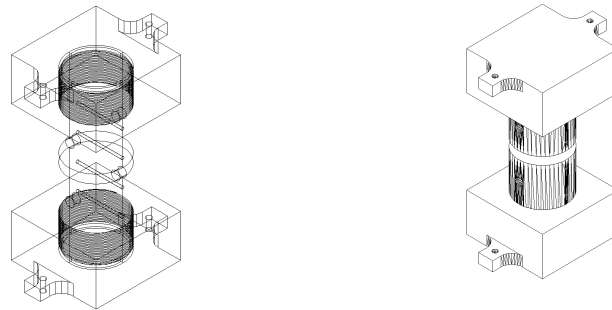


Figure 7. New apparatus design

Results with two different grease thicknesses of 25 and 150 microns are shown. The step change in temperature is across the TIM. The modeling results indicate that the model is capturing the trend. Of course, in the modeling, there are a number of uncertainties such as the heat loss coefficients on the boundaries and the contact resistance between the various layers in the apparatus. However, between the modeling results for the 25- and 150-micron grease layer cases, the only difference is the resistance of the interface material. This shows that the model is capturing the changes in the interface material quite well.

Since grease is still the most predominantly used interface material in the automotive power electronics industry, we performed experiments with some brands of commercially available thermal greases. Some of these greases (Aavid Thermalloy Thermalcote 251G, Wacker Silicone P12) are currently in use in actual inverters. These experiments were performed over a sample temperature range of 55° to 80°C, thickness range of 25 to 150 microns, and an applied pressure of 50 psi. Figure 9 shows the thermal resistance as a function of grease thickness at an average sample temperature of 80°C for the various greases. Though not shown here, such curves have also been generated at other temperatures (e.g. 55° and 80°C). To maintain the thickness of the grease layer, we used glass spheres acquired from Mo Sci Corporation. Figure 9 shows that as the grease thickness increases, the thermal resistance also increases linearly, as expected. For any given grease thickness, the thermal resistance may also change as a function of temperature. We found this change to be as much as 8% in some cases over a temperature range from 55° to 80°C. However, not all greases exhibited this behavior. For any given brand of grease in Figure 9, the inverse of the slope gives a sense of the thermal conductivity of the material and the y-intercept gives approximately the contact resistance. From a thermal perspective, the Shinetsu X23-7762-S grease is a very high-performance material. For a 25-micron thick layer, the thermal resistance is 13 mm²K/W. Even for a 150-micron thick layer, the thermal resistance is only about 45 mm²K/W. In our study, we are exploring a TIM thickness range of 25 to 150 microns, because in actual packages manufacturing constraints may cause unavoidable gaps of 100 to 150 microns.

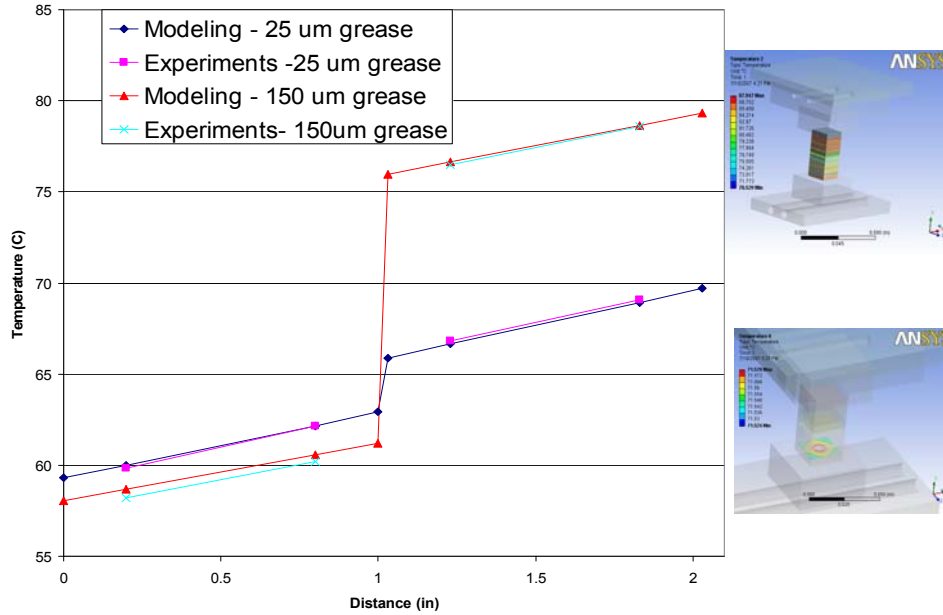


Figure 8. Comparison of experimental and modeling results

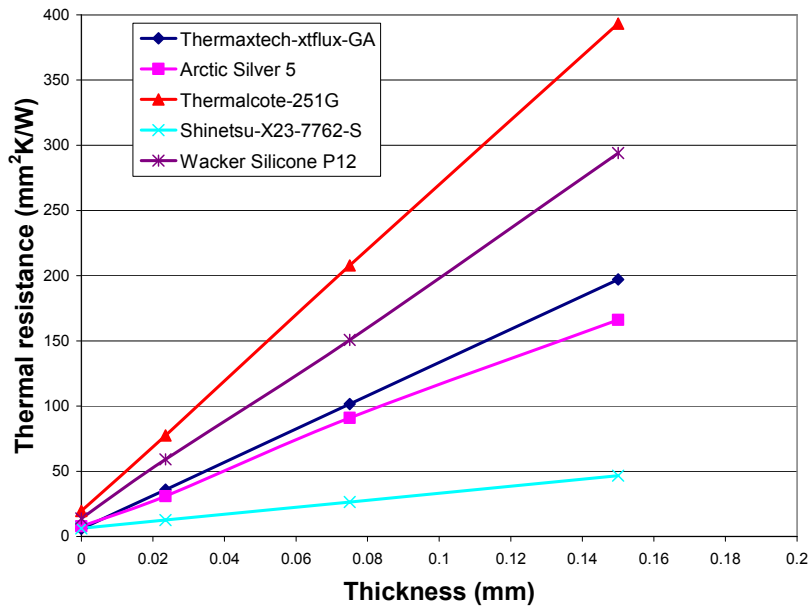


Figure 9. Thermal resistance versus thickness for different greases at 80°C average sample temperature

Figure 9 also gives a sense of the contact resistances for the various greases. The Arctic Silver 5 grease has a contact resistance in the range (over a temperature range of 55° to 80°C) of 7.8 to 8.5 mm²K/W, the Shinetsu-X23-7762-S grease in the range of 6.3 to 7.7 mm²K/W, the Thermalcote 251G grease in the range of 15.8 to 19.6 mm²K/W, the Thermatech-Xtflux-GA grease in the range of 6.0 to 6.5 mm²K/W,

and the Wacker Silicone P12 in the range of 13.6 to 13.8 mm²K/W. The individual differences in the greases maybe a result of how well they wet the surfaces and fill up the microscopic surface irregularities. The Shinetsu-X23-7762-S and Thermatech-Xtflux-GA greases have the lowest contact resistances. However, for all the greases, the contact resistances are in the range of 6 to 20 mm²K/W, which arguably is a fairly narrow range. As mentioned in an earlier section, this implies that the contact resistance of greases is quite low which maybe one reason for their widespread use despite significant drawbacks.

We plan to characterize aspects related to reliability in FY 2008. Figure 9 provides a sense of the thermal resistance numbers associated with the various greases. The question that remains to be answered is the impact of these numbers on the maximum die temperature in a realistic power electronics package. Toward this end, Figure 11 shows 3-D finite element (ANSYS) simulations of the Toyota Prius inverter. Figure 11(a) shows the actual Prius inverter [6], Figure 11(b) shows the representation of the inverter in ANSYS, Figure 11(c) shows the simulation domain, which consists of 1 IGBT-diode pair, and Figure 11(d) gives some representative temperature contours in the simulation domain.

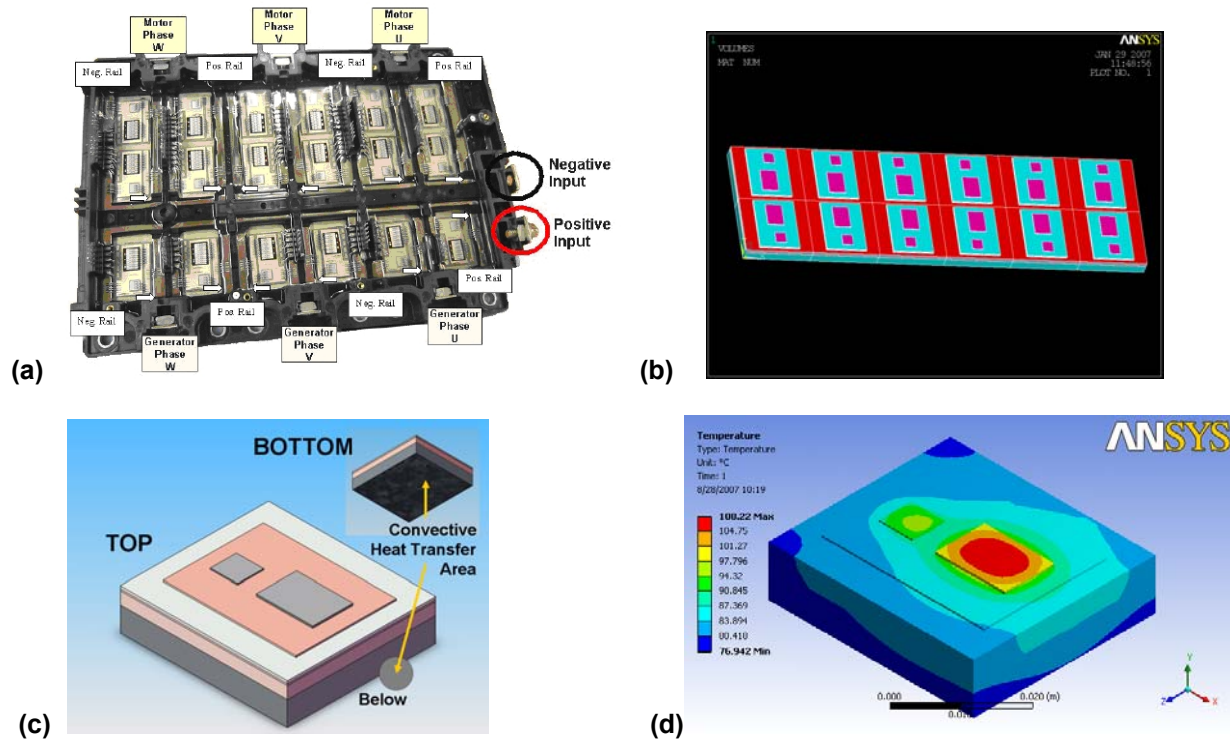


Figure 11. (a) Prius inverter [6], (b) Representation of the Prius inverter in ANSYS, (c) Simulation domain, (d) Sample temperature contours in the simulation domain

Making use of symmetry boundary conditions helps reduce the size of the simulation domain. For the results presented here, 40 W are dissipated in the diode and 160 W are dissipated in the IGBT. A convective heat transfer coefficient of 15000 W/m²K was imposed at the base of the baseplate, as shown in Figure 11(c). The coolant temperature is 105°C. This represents glycol-water coolant at 105°C, since using glycol-water at 105°C is an important FreedomCAR goal. Figure 12(a) shows the maximum IGBT junction temperature as a function of total TIM thermal resistance. The lowest grease thermal resistance from Table 1 is 12.6 mm²K/W; the highest is about 393 mm²K/W. Figure 12(a) shows that the difference in the maximum IGBT temperature for the lowest and highest thermal resistance cases is almost 58°C, which is a significant difference.

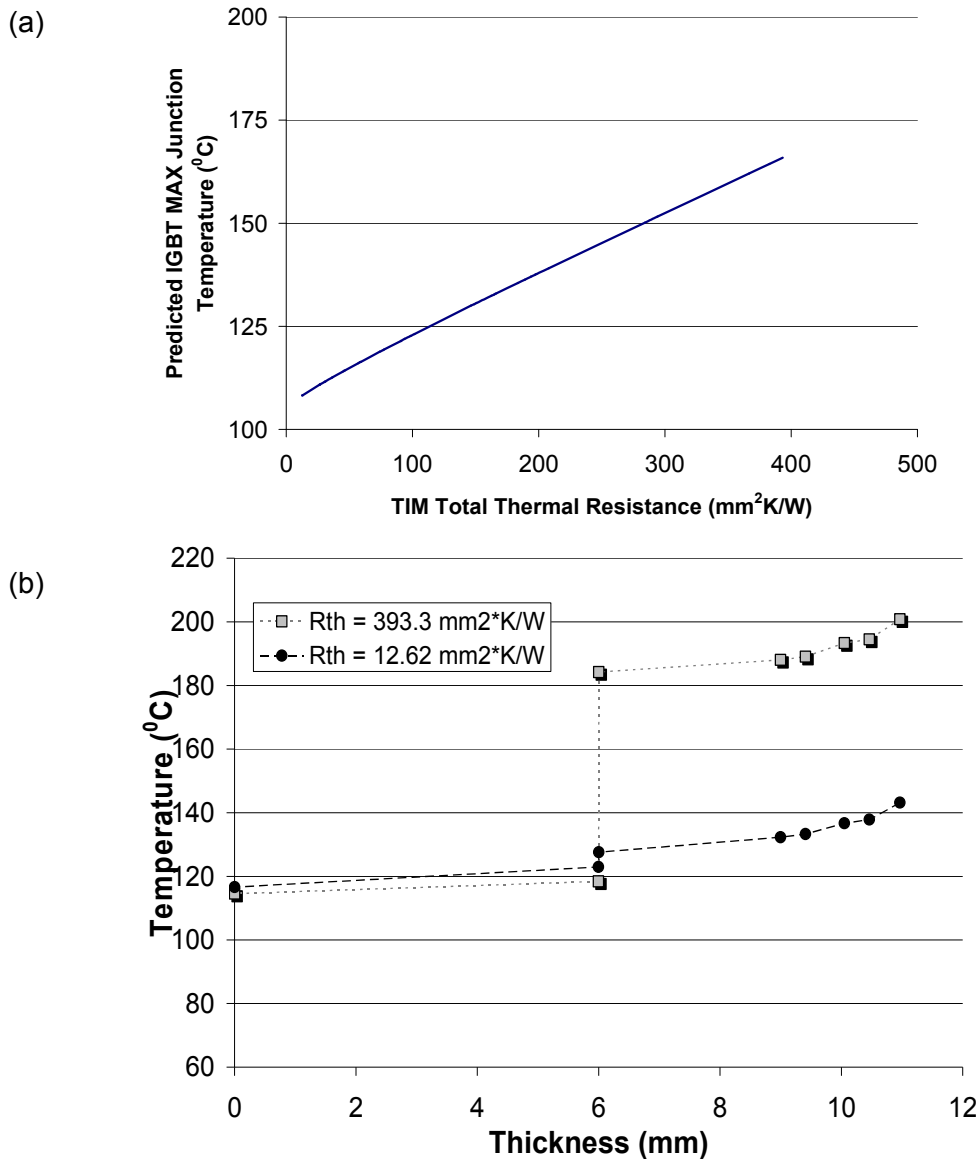


Figure 12. (a) Predicted maximum IGBT junction temperature as a function of the total TIM thermal resistances for the various greases; (b) Temperature across cross section of the IGBT package(Figure 11 (c)) for two extremes of the TIM thermal resistance

Figure 12(b) shows the temperatures across a cross-section through the IGBT package for the Prius inverter for the two extremes in TIM thermal resistance (12.6 and 393 mm²K/W). For a TIM resistance of 12.6 mm²K/W, the temperature jump across the TIM is only 4.7°C. However, when the TIM resistance is 393 mm²K/W, the temperature jump across the TIM is about 66°C, which is a big number. This suggests that even within greases, one has to be careful of the type and thickness of grease that is applied, since this can have a significant impact on the die temperatures, as demonstrated in the results presented here.

Conclusion

As demonstrated in this report, TIMs pose a significant bottleneck to heat removal from the IGBT package. The in-situ behavior of TIMs is also not well understood, and often there are discrepancies in the results obtained from fundamental tests characterizing material behavior and from in-situ characterization. From a FreedomCAR and automotive industry perspective, a reliable, cost-effective, and high thermal performance TIM can help meet some program goals such as cooling with 105°C glycol-water or even air cooling, and extracting maximum heat flux from the device, whether it be conventional silicon-based, trench IGBT or silicon-carbide based, and keeping the maximum temperature within acceptable limits.

NREL acquired, tested, redesigned, and improved a test stand to make thermal resistance measurements of conventional and novel thermal interface materials. We initiated significant industry collaborations during FY 2007 to better understand the industry perspective on TIMs. Experiments have been performed with several conventional thermal greases and their performance has been characterized over a range of temperatures and bond line thicknesses. The Shinetsu grease is superior in thermal performance over other greases. The results here suggest that even among greases, care has to be taken in choosing the type of grease and the thickness of the grease that is applied, since the impact on die temperatures is significant. Also, greases tested indicate that none are able to go below a resistance of about 33 mm²K/W at bond line thicknesses of 100 microns or greater. Practical inverter configurations are likely to require a TIM thickness of about 100 microns. Hence, a conservative goal would be identify/fabricate a TIM which would have a thermal resistance of about 5 mm²K/W at bond line thicknesses approaching 100 microns.

Publications

Narumanchi, S.V.J., 2007. "Thermal Interface Materials for Power Electronics Applications," abstract submitted to the 2008 ITherm conference, May 28-31, 2008, Orlando, Florida.

References

- [1] Narumanchi, S.V.J. 2006. *Advanced Thermal Interface Materials to Reduce Thermal Resistance*, NREL Technical/Milestone Report, NREL Report No. TP-540-40617.
- [2] Madhusudana, C.V. 1996. *Thermal Contact Conductance*, New York: Springer-Verlag.
- [3] Yovanovich, M.M. and Marotta, E.E. 2003. "Thermal Spreading and Contact Resistances," in *Heat Transfer Handbook*, A. Bejan and A.D. Kraus, Editors, Hoboken, NJ: John Wiley & Sons, pp. 261–395.
- [4] Prasher, R. 2006. "Thermal Interface Materials: Historical Perspective, Status and Future Directions." In *Proceedings of the IEEE*, Vol. 94, No. 8, pp. 1571–1586.
- [5] ASTM. ASTM D5470-01 Standard. 2005.
- [6] Staunton, R.H., Marlino, L.D., Chiasson, J.N. and Burress, T.A. 2006, *Evaluation of 2004 Toyota Prius Hybrid Electric Drive System*, Oak Ridge National Laboratory Technical Report, ORNL/TM-2006/423.

3. Electric Machinery Research and Technology Development

3.1 Uncluttered Rotor PM Machine for CVT Design

Principal Investigator: Donald Adams

Technical Team: John Hsu, Randy Wiles

Oak Ridge National Laboratory

National Transportation Research Center

2360 Cherahala Boulevard

Knoxville, TN 37932

Voice: 865-946-1321; Fax: 865-946-1262; E-mail: adamsdj@ornl.gov

DOE Technology Development Manager: Susan A. Rogers

Voice: 202-586-8997; Fax: 202-586-1600; E-mail: Susan.Rogers@ee.doe.gov

ORNL Program Manager: Mitch Olszewski

Voice: 865-946-1350; Fax: 865-946-1262; E-mail: olszewskim@ornl.gov

Objectives

The objective of this project is to develop a new machine that combines the motor and generator/motor into one unit that has the potential to be used as a continuously variable transmission (CVT) as well as other applications that require two electric machines. The expected advantages of this new machine are

- additional torque coupling between the two rotors for producing more wheel torque;
- the combination of a motor and generator into one machine with only a single permanent magnet (PM) rotor with the potential for a simpler and less costly CVT; and
- increased reliability due to elimination of brushes in the design.

Approach

Because the use of a secondary rotor working in conjunction with a PM rotor is a totally new technology, there is no previous experience that can be used for reference. The development process is an iterative process in determining the positive and negative aspects of various structural arrangements through simulations. This report presents the challenges associated with this technology and the process required to model, simulate, and derive results based on the complications it represented. A scalable design method including three-dimensional (3-D) finite element and lump parameter circuit approaches will eventually be established when this process is completed.

Major Accomplishments

In FY 2006 a proof-of-concept secondary rotor that had no rotating windings and a wound core stator for exciting the secondary rotor were fabricated. The secondary rotor teeth were machined from solid steel instead of laminations in order to lower costs for the proof-of-concept prototype. The brushless secondary rotor concept was validated through tests conducted on the prototype motor. The physics of the CVT machine were explained in the FY 2006 report. For any conventional motor, the stator encounters a counter-torque to the shaft torque. The magnitude of the stator counter-torque is the same as that of the shaft torque. The stator counter-torque can be added to the shaft torque at a given rotor speed by allowing the stator to rotate on additional bearings and transferring the stator torque to the shaft through gears, such as a set of planetary gears.

In FY 2007 simulations were initially conducted for axial-gap and radial-gap approaches. The radial-gap machine was selected for detailed simulations. The simulation results further confirmed that the principle of this new type of machine is workable; the torque of the PM rotor can be transferred directly to that of the secondary rotor, the stationary excitation core of the secondary rotor sees no rotational torque, and the axial force can be practically eliminated by an axially symmetrical arrangement.

Future Direction

Detailed design of the uncluttered CVT is extremely complex and computationally intensive. A comprehensive technical report of the design evolution and progress to date has been written and will be released when cleared by the U.S. Patent Office. Further research will be conducted to find a more effective magnetic flux transfer method that turns the axially moving flux into a rotational flux. This can be achieved by optimizing the number of phases, the geometry of the transfer coupling, and the overall placement of the components, which include the stator, PM rotor, secondary rotor, and the stationary excitation core for the secondary rotor.

Technical Discussion

The Toyota Prius motor has been well characterized and is the baseline design for this program. The stator core and winding dimensional envelopes of the baseline (Prius) motor were used as an initial design criterion for the CVT to facilitate a direct comparison. To accommodate the secondary rotor that faces the PM rotor, various new PM rotors, secondary rotors, and their stationary excitation cores were studied through simulations. Figure 1 shows the general layout of the CVT machine and its interface with the vehicle system.

Secondary (Uncluttered) Rotor

The ORNL technology for eliminating the brushes and slip rings is derived from the uncluttered rotor concept [1–3]. When three-phase currents are fed into the windings of a conventional slip-ring wound-rotor core, a rotating magnetic flux is produced, which goes through the air gap and reaches the stator for returning the rotating flux. The rotating speed of this flux observed from the rotor, regardless of whether the stator is stationary or rotating, is determined by the frequency and number of poles of the wound-rotor winding. The function of the secondary rotor is to produce a rotating flux; the speed of this flux observed from the secondary rotor is determined only by the excitation frequency and by the number of poles of the secondary rotor. There are no brushes and slip rings for the excitation of the secondary rotor. The excitation wound core for the

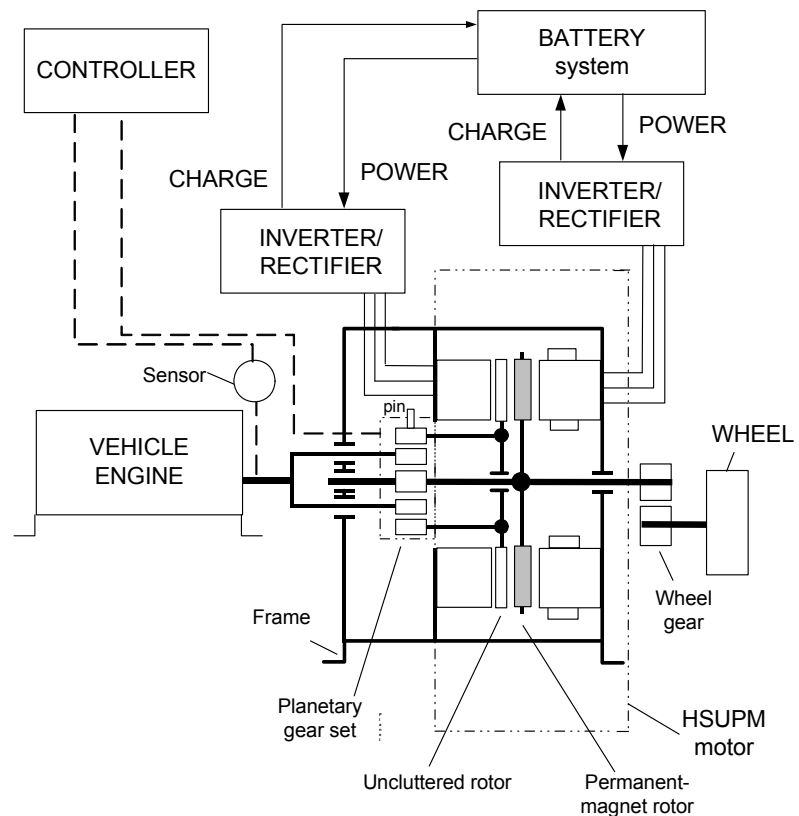


Figure 1. General layout of the CVT machine and its interface with the vehicle system.

secondary rotor is stationary. The secondary rotor has no conductors; hence, no brushes and slip rings are required.

A traditional radial gap reluctance interior permanent magnet (RIPM) machine has both a stator and a rotor. The electromagnetic interaction in the air gap between the outer peripheral surface of the rotor and the bore of the stator produces the required torque. The CVT machine is designed with an additional secondary rotor. The secondary rotor interacts with the inner surface of the PM rotor and produces an additional torque. With only one set of PMs in the machine for two rotors, the power density goes up, and the cost per unit power decreases.

Flux Transfer from Excitation Core to Secondary Rotor

The simulated machine used the same wound stator core dimensions and windings as those of the baseline motor. Table 1 shows the simulated torques and axial forces of the wound stator, PM rotor, secondary rotor, and exciter of the simulated machine. The axial force acting on the four parts listed in the table is negligibly low; the wound stator torque (222 Nm) is not noticeably affected by the added secondary rotor; the PM rotor torque (-251 Nm) is in opposite direction to the wound stator torque and with a value equal to the sum of the wound stator torque and the secondary rotor torque; the stationary exciter (-0.5 Nm) torque value is negligible.

Table 1. Simulated torque and axial force of sample machine

Parts	Axial force (Newton)	Torque (Nm)
Wound stator	-2.4	222
PM rotor	0.3	-251
Secondary rotor	-0.5	29
Stationary exciter	9	-0.5
Three-phase stator currents	200A 45°, 200A 165°, 200A 285°	
Three-phase exciter currents	200A -60°, 200A 60°, 200A 180°	

Basic Lump Parameter

The basic lump parameters for the PM machine with an additional secondary rotor are currently under development. This will provide a scalable design tool for future motor designs of this nature. Because of the saliency of the PM rotor, the self and mutual inductances of the stator windings are influenced by the PM rotor position, $\vartheta_{A,d}$. For every 360° (electric angle) the value of the permeance caused by the change of the PM rotor location varies twice as shown in Figure 2. The inductance consists of a $\sin(2\vartheta_{A,d})$ term.

The sinusoidal flux distribution components in the outer and inner air gaps of the PM rotor are the components to be considered. The winding self, mutual, and stator-secondary rotor excitation winding inductance are stator, PM rotor, and secondary rotor dependent. The stator windings and the secondary rotor excitation windings are coupled through their mutual inductance; the turn ratio and the angular positions of these windings must be considered in the calculation of their mutual inductance values. The mutual inductance value is the same using either stator current for rotor flux linkage, or using rotor current for stator flux linkage. Either approach considers the turn ratio effect. Because of the nature of magnetic coupling between the secondary rotor and its excitation core, there is no torque produced between them. The torque-production air gaps are those between the stator and the PM rotor and between the secondary rotor and the PM rotor. Therefore, the PM rotor mechanical torque is the combination of the opposite stator torque and the opposite secondary rotor torque.

$$T_{PM} = -T_s - T_u \quad (1)$$

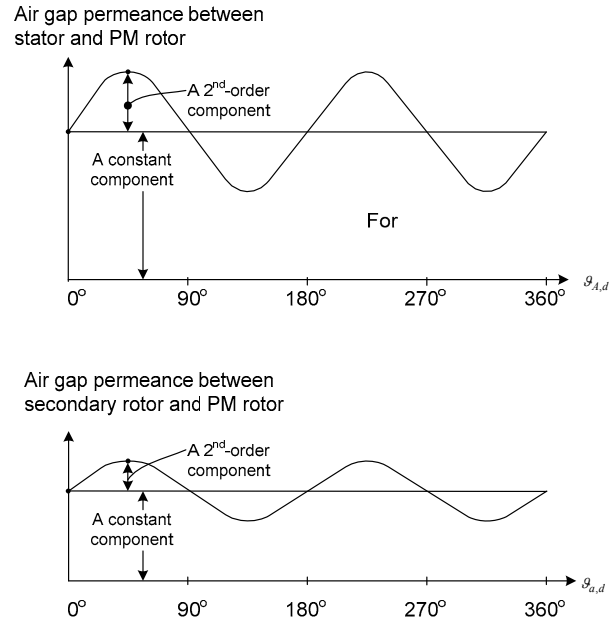


Figure 2. Constant and second-order permeance caused by location of PM rotor.

The phase arrangement for the secondary rotor excitation core is symmetrical with respect to the center of the rotor axial length. Consequently, the axial force of the secondary rotor can be cancelled.

Conclusion

The physics of the CVT concept were explained in the FY 2006 FreedomCAR Annual report. For any conventional motor, the stator sees a counter-torque to the shaft torque. The magnitude of the stator counter-torque is the same as that of the shaft torque. The stator counter-torque can be used to double the shaft torque at a given rotor speed by allowing the stator to rotate on additional bearings, and transferring the stator torque to the shaft through gears, such as a set of planetary gears.

In FY 2007 the radial-gap machine was selected for detailed simulations. The axial force can be eliminated by the axially symmetrical arrangement.

The simulated torques and axial forces of the wound stator, PM rotor, secondary rotor, and exciter of the simulated machine confirm that the axial forces acting on the parts are negligibly low. The wound stator torque (222 Nm) is not noticeably affected by the added secondary rotor. The PM rotor torque (-251 Nm) is in opposite direction to the wound stator torque and with a value equal to the sum of the wound stator torque and the secondary rotor torque (29 Nm). The torque of the PM rotor is increased by the same amount of torque as the secondary rotor torque, and the stationary exciter torque value is negligible.

Future design iterations such as optimizing the number of phases; the geometry of the transfer coupling; and the overall arrangement of the components that include the stator, PM rotor, secondary rotor, and stationary excitation for the secondary rotor will be investigated to overcome the challenge of obtaining more torque from the uncluttered rotor as determined from the simulation discussed.

The scalable design tools that include 3-D finite element and lump circuit approaches are currently under development.

Publications

To be issued.

Patents

John Hsu, "Hybrid-Secondary Uncluttered Permanent Magnet Machine and Method," U.S. Patent No. 6,977,454, December 20, 2005.

John Hsu, "Simplified Hybrid-Secondary Uncluttered Machine and Method," U.S. Patent No. 6,891,301, May 10, 2005.

John Hsu, "Hybrid Secondary Uncluttered Induction Machine," U.S. Patent No. 6,310,417, October 30, 2001.

Patent Application 05473, "Radial Gap Hybrid Secondary Uncluttered Permanent Magnet Electric Machine."

References

1. J. Hsu, "Hybrid-secondary uncluttered induction (HSUI) machine," *IEEE Transactions on Energy Conversion* **16**(2), ITCNE4 (ISSN 0885-8969), 192–197 (June 2001).
2. J. Perahia, "Discussion of hybrid-secondary-uncluttered induction (HSUI) machine," *IEEE Transactions on Energy Conversion* **17**(1), ITCNE4 (ISSN 0885-8969), 150 (March 2002).
3. J. Hsu, "Closure on hybrid-secondary-uncluttered induction (HSUI) machine," *IEEE Transactions on Energy Conversion* **17**(1), ITCNE4 (ISSN 0885-8969), 150 (March 2002).

3.2 16,000-rpm Interior Permanent Magnet Reluctance Machine with Brushless Field Excitation

Principal Investigator: Donald Adams

Technical Team: J. Hsu, T. Burrell, S. Lee, R. Wiles, C. Coomer, J. McKeever

Oak Ridge National Laboratory

National Transportation Research Center

2360 Cherahala Boulevard

Knoxville, TN 37932

Voice: 865-946-1321; Fax: 865-946-1262; E-mail: adamsdj@ornl.gov

DOE Technology Development Manager: Susan A. Rogers

Voice: 202-586-8997; Fax: 202-586-1600; E-mail: Susan.Rogers@ee.doe.gov

ORNL Program Manager: Mitch Olszewski

Voice: 865-946-1350; Fax: 865-946-1262; E-mail: olszewskim@ornl.gov

Objectives

- Avoid the primary drawbacks of the conventional reluctance interior permanent magnet (RIPM) machines that have a set of fixed permanent magnets (PMs). For a conventional RIPM machine with fixed strong PMs, the drawbacks are the requirement for field weakening and high core losses at high speed. For conventional RIPM machines built with fixed weak PMs, the drawback is a larger wound stator to compensate for the weaker starting torque.
- Design a high-speed RIPM machine that requires thick bridges to hold the PMs.
- Improve three-dimensional (3-D) design methods, including the 3-D finite element simulations and saturated lump parameter computations for motors.

Approach

Brushless field excitation was incorporated into the third dimension of a high-speed RIPM motor. The motor was designed, built, and tested. The detailed mechanical stress and deformation of the high-speed motor's rotor laminations were studied. The 3-D finite element simulation and the saturated lump parameter computation method for electromagnetic performance predictions were improved during the design and test process.

Major Accomplishments

- This research effort proves that brushless field excitation from the third dimension (i.e., the axial direction) for an RIPM machine is practical and effective. The back-emf is easily controlled with an external field excitation current in the 0- to 5-A range. The excitation dc voltage does not exceed 80 V. This field excitation range is capable of changing the air-gap flux density up to 2.5 times at any speed. This enables the motor to have the high power density advantage of conventional strong PM reluctance motors as well as the low back-emf and lower core loss advantage of weak PM reluctance motors. The circuitry required to supply the excitation current to the coils is projected to cost under \$10 in production quantities of 100,00 or more.
- While the rotor is rotating at high speed with no field current, the core loss is significantly lower than that of fixed PM motors.
- The prototype motor design requires the rotor punching bridges to be thicker to satisfy the mechanical stress requirements of high speed. Due to this rotor design, flux produced by the PMs can leak through, causing the air-gap flux density produced by the PMs to be reduced more than in

conventional IPM machines. The weaker air-gap flux density improves high-speed operation and can be compensated with BFE (brushless field excitation) current for increased torque production at lower speeds.

- The machine was evaluated up to the full design speed of 16,000 rpm.
- If an interior short-circuit fault occurs in the windings, the excitation current can be turned off to prevent damaging the motor.
- The RIPM-BFE motor benefits from using an optimal field current combined with the capability of reducing the air gap flux when not needed. This results in increased efficiencies at low torques for both partial loads and high speeds.
- Test data showed significant advantages, particularly in terms of motor efficiency, over conventional RIPM motors of a similar power level. The benefits of variable field excitation were clearly observed.
- An aluminum frame was successfully used in the prototype design so as to not increase the total machine weight due to the addition of field excitation components.
- Tests confirmed that the asymmetrical rotor can increase the forward performance at the expense of reducing the backward performance. Further study on this topic is needed.
- The RIPM-BFE motor should not present any manufacturing issues in mass production. Design improvements on the excitation coils to motor housing interface will result in a reduction of both mass and volume, thereby reducing manufacturing costs.
- As a result of this research effort, a significant improvement in the development of accurate 3-D finite element simulations and a magnetically saturated lump parameter computational method for 3-D electric machine designs was achieved.
- A detailed technical report of this project has been issued (ORNL/TM-2007/167).

Future Direction

This project has been completed.

Technical Discussion

Prototype Machine

A CAD assembly cross section of the Oak Ridge National Laboratory (ORNL) 16,000-rpm RIPM-BFE motor design is shown in Figure 1.

Table 1 compares the dimensions of the ORNL 16,000-rpm motor with those of the Toyota/Prius motor [1,2] that was selected as a baseline motor for this project. The masses and sizes derived from Table 1 provide a basis for a cost comparison with the baseline motor. The extra excitation coils and cores of the ORNL motor are made of copper wires and mild steel. Cost savings can **be realized by having a shorter stator core (1.88 in. vs 3.3 in.) as** well as shorter stator windings. The cost of the low-current control of the field excitation is minimal because of the low-current component requirements. This design approach enables better motor performance as well as system cost savings. Additionally, if used in a vehicle architecture having a boost converter, the output of this motor design can be further increased.

The design calls for the thickness of the rotor punching bridges (Figure 2) to be increased to satisfy the high-speed mechanical stress requirements. More flux produced by the PMs can leak through these thicker bridges, causing an air gap flux density reduction for no excitation coil current when compared with similar IPM machines such as the baseline motor, which does not have the benefit of BFE.

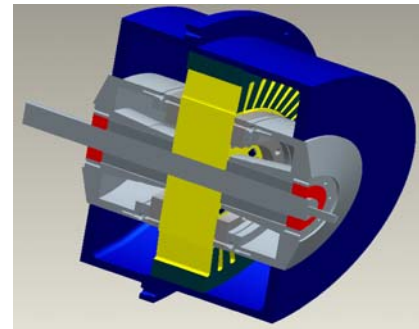
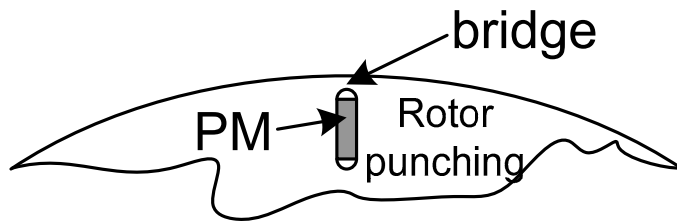


Figure 1. Assembly of ORNL 16,000-rpm RIPM-BFE motor design.

Table 1. Comparison of dimensions of the ORNL 16,000-rpm RIPM-BFE motor and the baseline motor

	Baseline	ORNL
Speed	6000 rpm	16,000 rpm
Stator lam. OD	10.6 in.	Same
Rotor OD	6.375 in.	Same
Core length	3.3 in.	1.88 in.
Bearing to bearing outer face	7.75 in.	7.45 in.
Magnet weight, lb	2.75	2.57
Estimated field adj. ratio	None	2.5
Rating	33/50 kW	Same
Boost converter	Yes	No
High-speed core loss	High	Low

**Figure 2. Location of bridge in a rotor punching.**

The detailed parts descriptions of the prototype machine can be obtained from the FY 2006 Annual Report. To have a stronger forward torque at the expense of a weaker backward torque, the rotor surface is made asymmetrical with respect to the pole center, creating the saw-tooth appearance as shown in the FY 2006 report.

The mass and volume of the prototype motor can be further reduced by redesigning the interface between the excitation coils and the motor housing. This improvement will reduce the cost to manufacture the motor by using less material and by eliminating some machining steps. This prototype high-speed motor was used to prove the brushless excitation concept; it has not yet been optimized.

Air gap flux, inductance, performance parameter computations, and comparisons of simulation with test results

Figure 3 shows the calculated air-gap flux density distributions at various excitation levels. The field excitation, I_{exc} , is the product of current flowing through the 865 turns in the field excitation coil. The excitation current, I_{exc} , can be calculated by dividing the ampere-turns by the number of turns in the field coil. The air-gap flux density is adjusted by varying the field excitation current. When high torque is required, the air gap flux density is enhanced by increasing I_{exc} . When low torque and low core loss are required, I_{exc} is reduced to zero.

Figure 4 shows the expected motor torque vs load angle at $I_{max} = 200$ A for different field excitations. Greater excitation produces stronger motor torque.

Figure 5 shows the motor's expected back-emf voltage. The calculated root mean square (rms) voltages from the fundamental values are plotted vs speed for different field currents. In addition to the 3-D finite element simulations, the parameters for the equivalent lumped parameter circuit are computed. Magnetic saturation in high-power-density motors is high; consequently, linear extrapolations for the direct axis and quadrature axis inductance can no longer be applied. Finite element flux plotting is used to obtain the magnetic flux linkages for the inductance calculations when there is nonlinear magnetic saturation. Figure 6 shows the motor's saturated inductance values vs the current angle at $I_{ph} = 100$ A_{rms}.

The need for power factor adjustment and low core losses across a wide range of speeds was also addressed by designing into the motor a field adjustment ratio of 2.5. With this ratio, the 16,000-rpm motor with BFE provides flexibility for a drive system design to meet field strength requirements that vary at different loads and speeds.

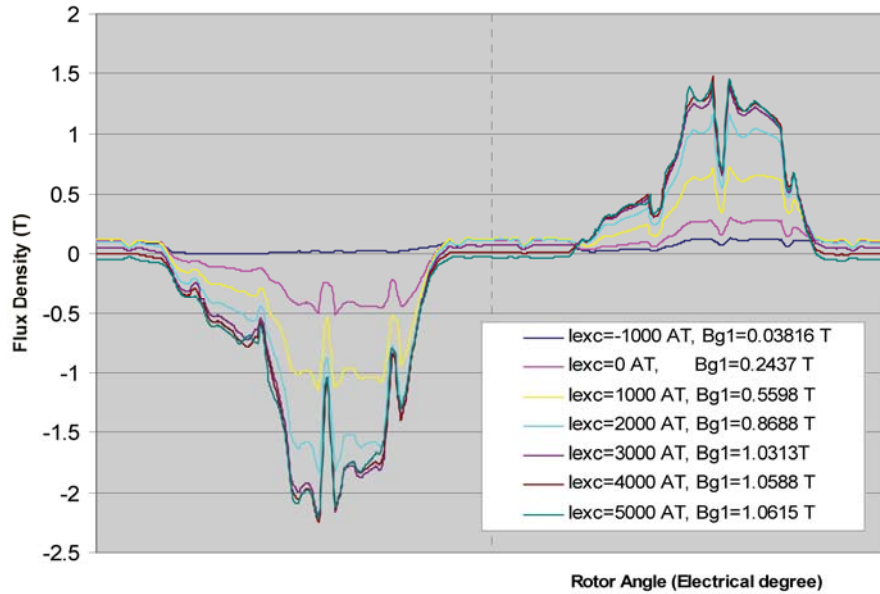


Figure 3. Air gap flux density distributions for various field excitations.

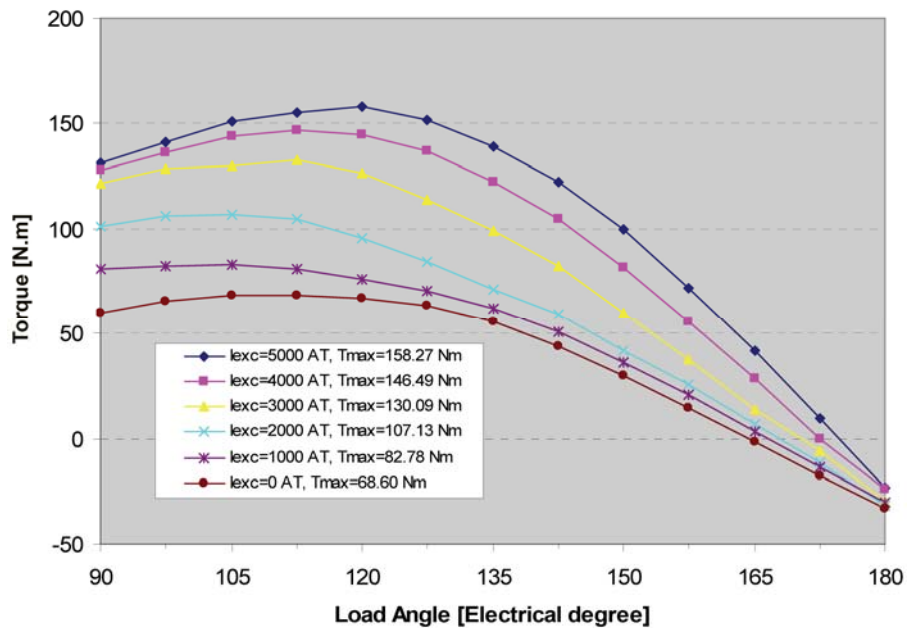


Figure 4. Expected motor torque vs load angle at $I_{max} = 200$ A for different field excitations.

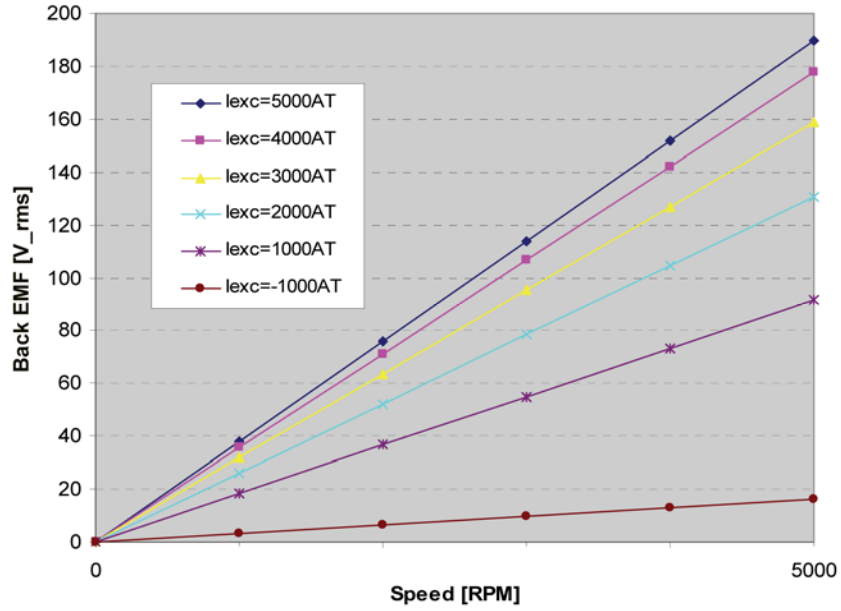


Figure 5. Calculated back-emf voltages.

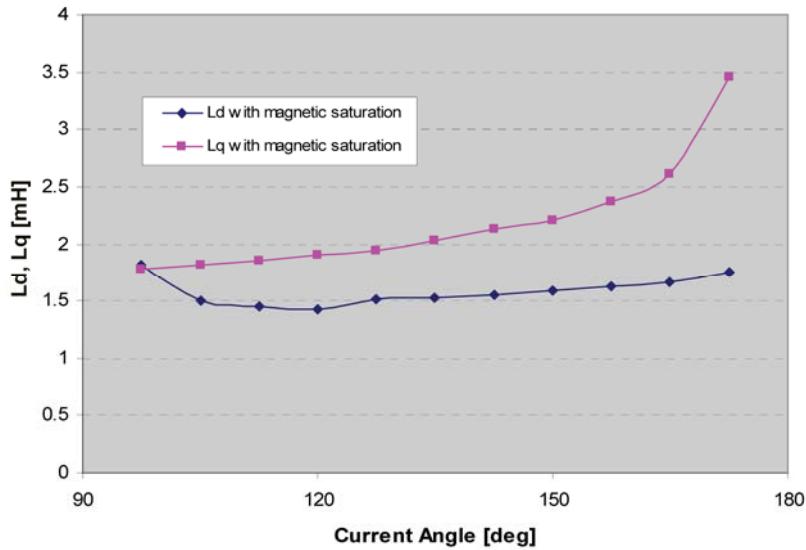


Figure 6. Saturated inductance values vs current angle at 3300-rpm, 5 A at $I_{ph} = 100 A_{rms}$.

The performance of the RIPM-BFE motor with 5 A in the BFE coil was calculated with saturated inductances at the input current of 102.39 A. Figure 7 shows the corresponding phasor diagram. The comparison between the simulated and test results appears in Table 2. Use of the saturated inductances appears to have good agreement between the simulation and test results.

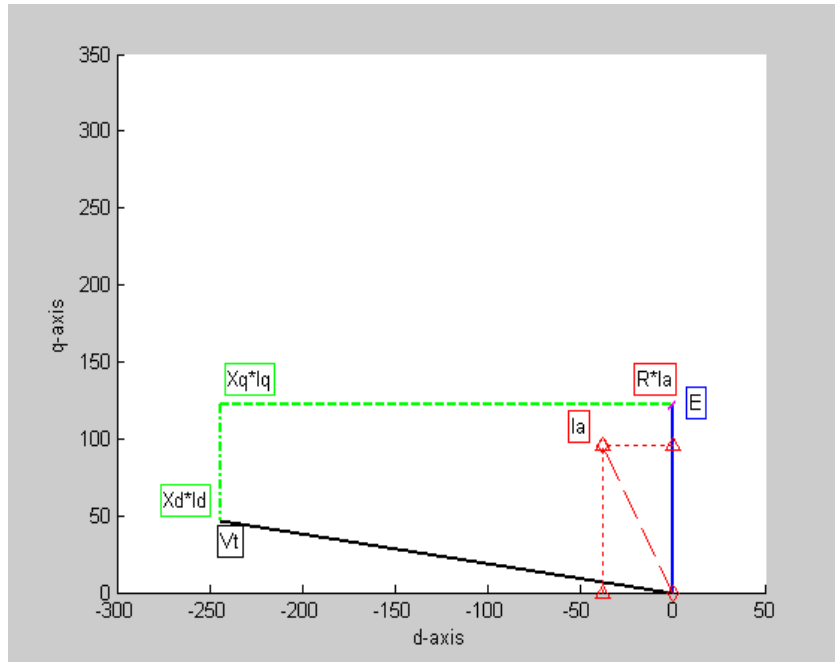


Figure 7. Simulated phasor diagram excitation, and 100 A_{rms}.

Table 2. Comparison between simulated results and test results at given speed and input current

	Unit	Simulation results	Test results	Simulation/test
Torque	Nm	102.24	105.02	0.97
Speed	rpm	3300	3300	1.00
P _{motor}	kW	35.33	36.29	0.97
Back-emf ^a (rms)	V	121.32	129.39	0.94
Input voltage (rms)	V	248.22	270.01	0.92
Input current (rms)	A	102.39	102.39	1.00
Power factor	–	0.53	0.47	1.13
P _{input}	kW	40.41	38.89	1.04
Efficiency	%	87.43	93.33	0.94

^aBack-emf voltage is from no-load simulation and test.

Mechanical stress computations and operation tests

The simulations of the mechanical stress and deformation of the rotor were presented in the FY 2006 report. The tests conducted in FY 2007 confirm that the rotor runs satisfactorily within the entire speed range from 0 to 16,000 rpm.

Back-emf tests

The RIPM-BFE machine was spun up to 5,000 rpm to measure the open circuit voltages generated in the stator windings by the PMs with BFE using the Yokogawa PZ4000. Figure 8 shows the phase back-emf vs speed at various field currents. The slope of the -5- to 0-A back-emf curves is relatively constant. The slope increases dramatically as the excitation field is increased from 0 to 3 A, yet saturation appears

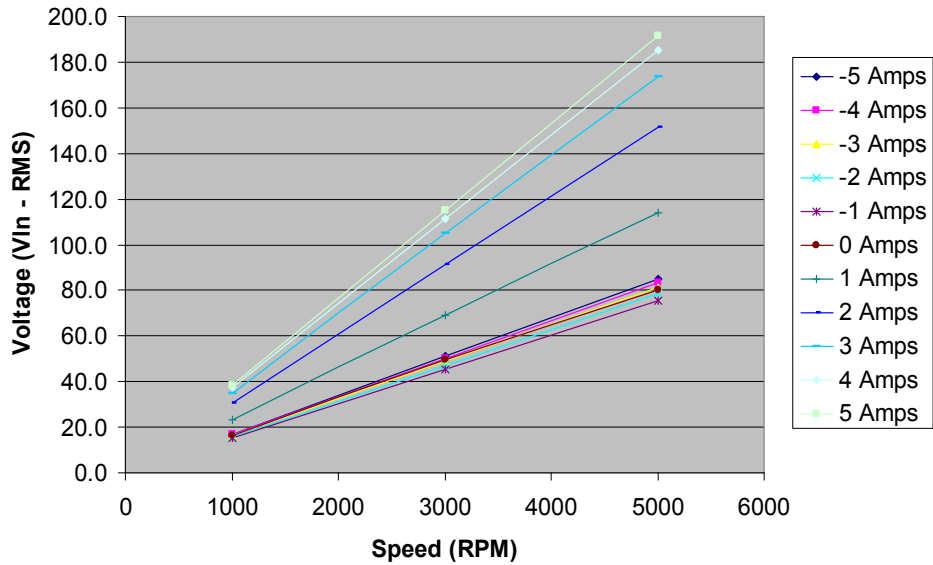


Figure 8. Influence of field current on unloaded back-emf curves.

to begin at 3 A. The top two lines indicate a large amount of saturation between 4 A and 5 A of field excitation current as evidenced by a very small change in slope. The lines also indicate that a back-emf adjustment ratio of 250% between 0- and 5-A field current can be obtained.

Core/friction loss tests

These tests were conducted by spinning the RIPM-BFE motor while measuring the load created at the RIPM-BFE shaft due to friction and core effects, with the motor leads disconnected and floating. The spinning losses vs field current at various speeds are plotted in Figure 9. This test confirms the advantage of the field control capability of the RIPM-BFE motor; the loss is significantly reduced when spinning at high speed with zero field current.

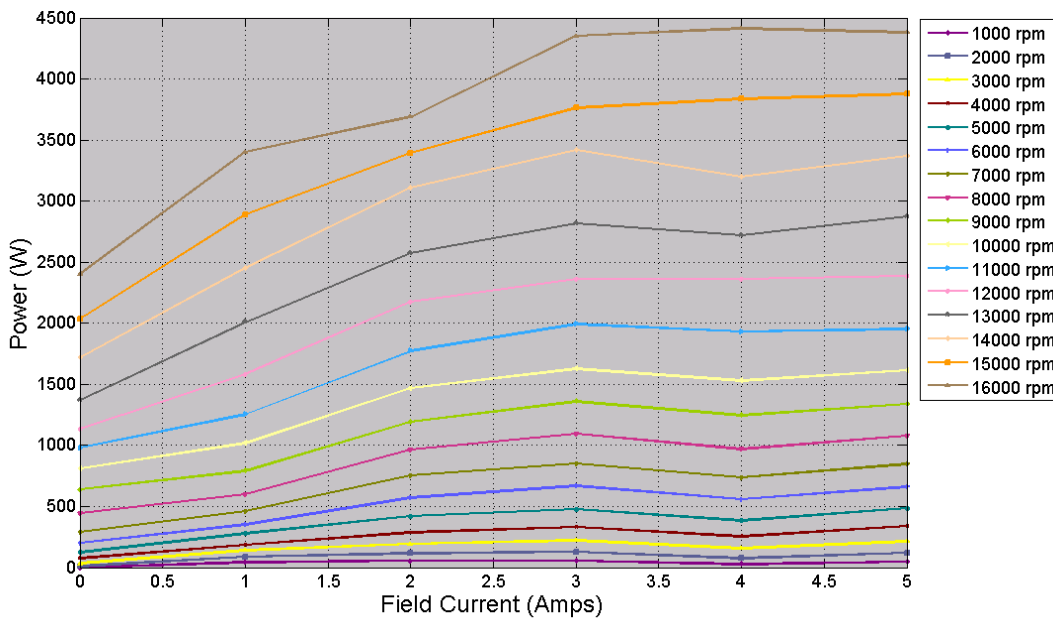


Figure 9. Spinning losses vs field current for various rotor speeds.

Locked rotor tests

During the locked rotor tests, the rotor was fixed at selected angular positions as positive direct current (dc) was fed to phase “a” and returned through phases “b” and “c” connected in parallel. The results for a stator current of 50 A and various field currents are shown in Figure 10. Contrary to the waveform shape of typical PM synchronous machines, these torque waveforms are not symmetrical about the horizontal axis. For example, for no field excitation current, the magnitude of the peak positive torque, 16 Nm, does not equal the magnitude of the peak negative torque, -24 Nm. This feature was purposely designed into the RIPM-BFE motor to produce more torque while spinning in one direction than in the opposite direction; consequently, it was necessary to spin the motor in the appropriate direction during testing.

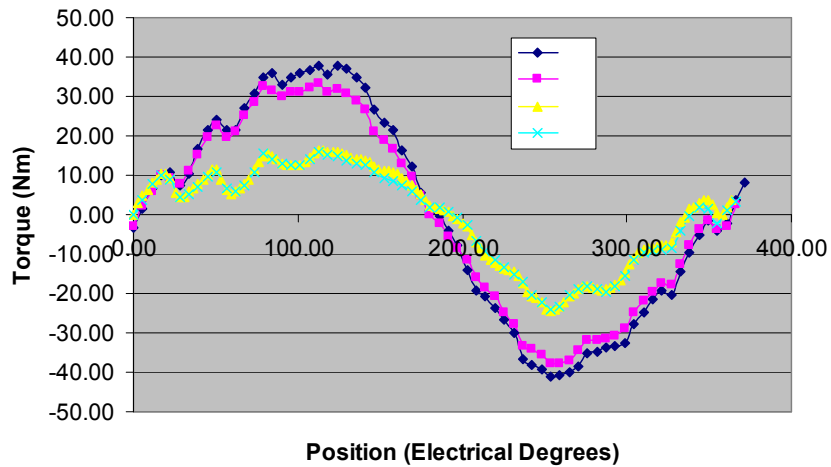


Figure 10. Locked rotor torque.

As expected, the peak torque is obtained while using the highest field excitation current of 5 A. The torque measurements for all stator currents with 5-A field current are shown in Figure 11. The graph shows that the peak torque capability of the motor is about -155 Nm.

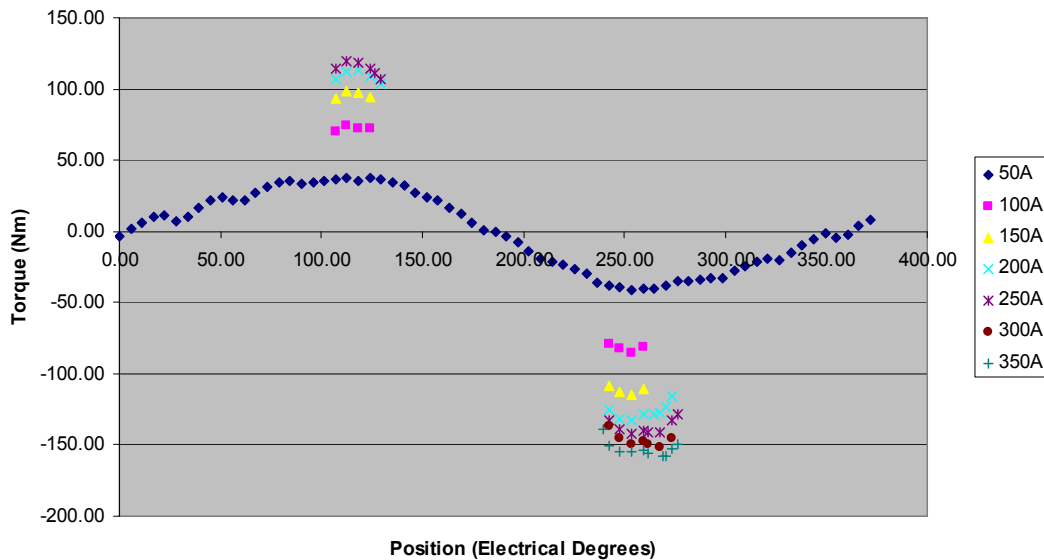


Figure 11. Locked rotor torque with 5-A field current.

Performance/efficiency tests

The motor was driven at various speed-torque operation points in order to collect a vast amount of data, which includes temperatures, powers, currents, voltages, and efficiencies. The temperatures remained well within the stator winding limitation, which is 220°C (class R). For most of the data points, all temperatures remained below 100°C, yet for high-current conditions, temperatures reached about 135°C.

To provide a good comparison with the baseline, a high-speed gear could be included in the mapping to convert from a maximum speed of 16,000 rpm to 6,000 rpm. A gear ratio of about 2.6 would suffice, which also changes the maximum torque from 155 Nm to about 400 Nm. The resulting efficiency map is shown in Figure 12 for comparison with the baseline (Prius) efficiency map in Figure 13. Although a large portion of the RIPM-BFE map is missing, a comparison of the low-speed efficiencies is informative. The efficiency of the RIPM-BFE in the low-speed region is significantly better. It is also apparent that the 93% and 94% contours would be much larger.

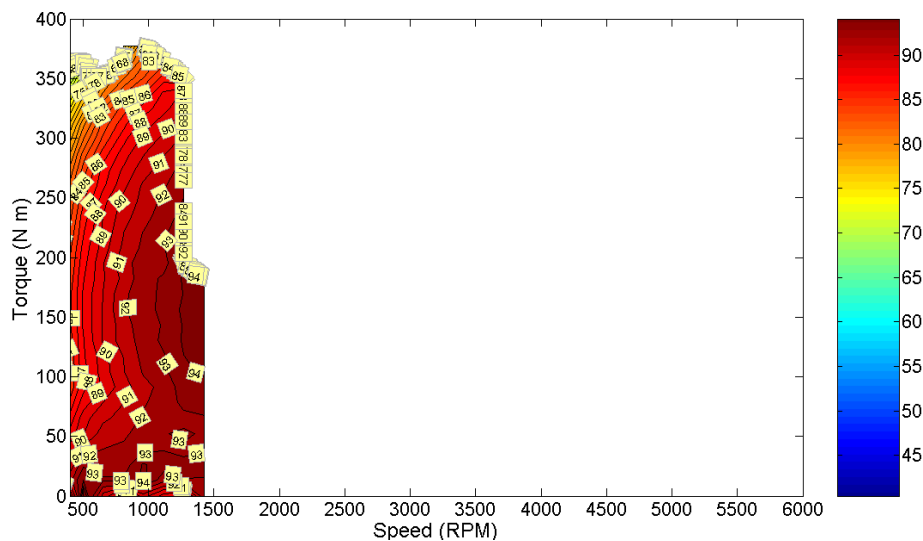


Figure 12. RIPM-BFE efficiency map with high-speed gear ratio of 2.6.

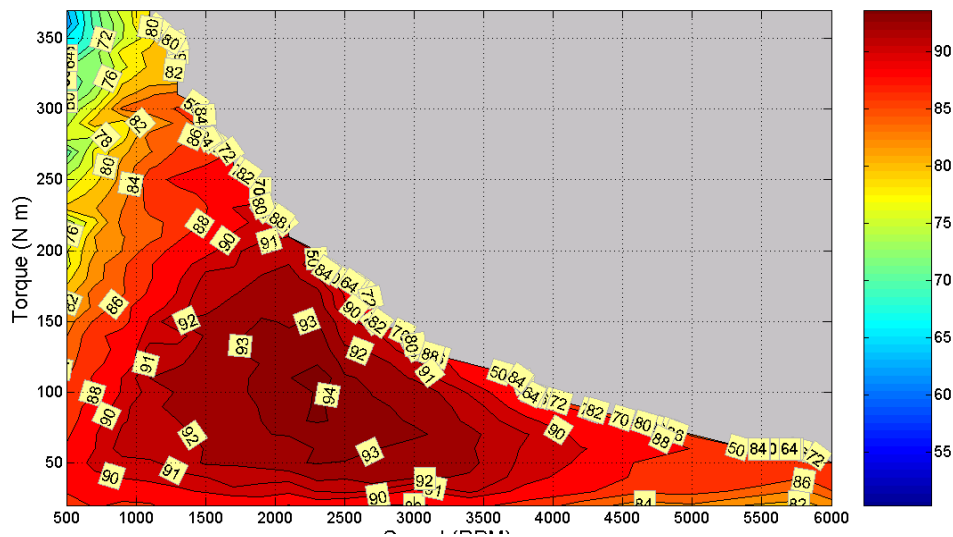


Figure 13. Baseline (Prius motor) efficiency map.

Comparison of the efficiency maps between the ORNL motor (Figure 12) and the baseline (Prius) motor (Figure 13) shows that the 94% efficiency contour of the ORNL motor starts at 1,400 rpm. The baseline motor starts at 2,200 rpm and covers a very small region. The available performance test data up to 3,700 rpm (or $3,700/2.6 = 1,423$ equivalent rpm after gears) confirm that the ORNL motor has higher efficiency than the baseline motor.

Rewound motor tests

During the first series of tests on the 16,000-rpm RIPM-BFE, a failure occurred in the stator windings in which a short was created to ground. The failure was possibly due to localized lamination vibration that eventually wore down the slot insulation between the stator windings and stator laminations in the corner of a slot opening. The stator was sent to the original manufacturer to be rewound, wherein the inner diameter of the stator laminations was increased slightly to enable removal and cleaning of the defective windings. Therefore, the air gap between the rotor and stator was increased and the flux generated by the permanent magnets, stator windings, and field windings was further inhibited. A second series of tests was conducted with the rewound stator installed in the same housing used in the first series of tests. A spline was added to the original rotor to provide an interface with the high-speed side of a newly installed dynamometer speed reduction gearbox. A comparison of efficiencies obtained from the first and second series of tests yields significant discrepancies. The back-emf test shows that the second (rewound) stator is about 4% lower than that of the first stator, which indicates that the flux through the stator windings is about 4% lower, as the back-emf voltage is directly proportional to flux and speed. Because the 0-A back-emf results indicate a similar decrease of voltage, the field windings are not suspected to be defective. The reduced performance was most likely caused by the machine parameters changing as a result of the stator laminations size increase during removal for repair.

Efficiency mapping

Efficiency tests were conducted using the same approach that was taken in the first series of tests. Optimal motor control was ensured by observing efficiency feedback as control conditions were varied throughout the entire operation range. Data points for each efficiency map were taken from 1,000 rpm to 16,000 in 1,000-rpm increments and from 0 Nm increasing in 10-Nm increments to a final high torque value at each speed. Six efficiency maps were generated for corresponding dc field currents of 0 A, 1 A, 2 A, 3 A, 4 A, and 5 A. For instance, the efficiency contours with a 5-A field along with field losses are shown in Figure 14.

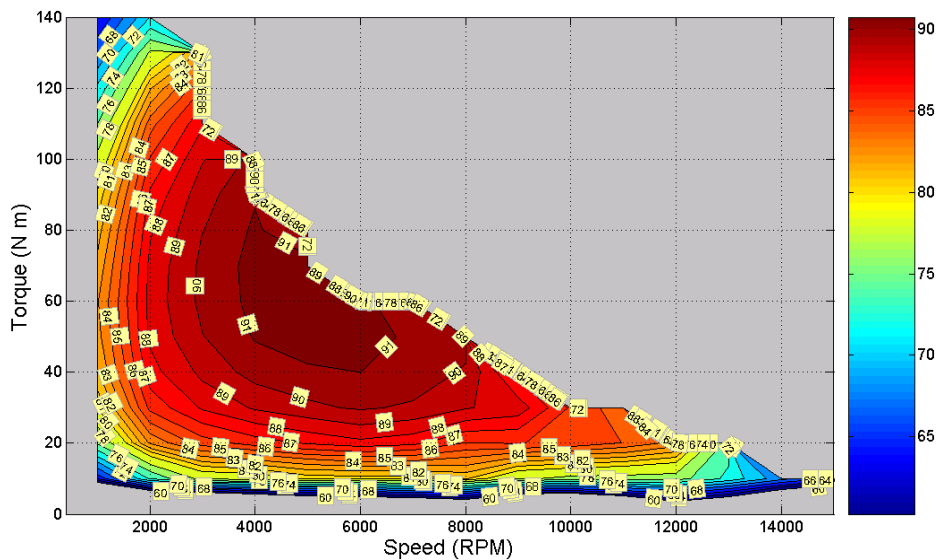


Figure 14. Efficiency contours with 5-A field—including field losses.

The optimal field currents, when including field losses, can be obtained by comparing efficiency contours of 0-A to 5-A excitation fields. Consequently, the optimal efficiency contour is obtained by selecting the optimal field current for a load. The regions of the optimal field currents are shown in Figure 15.

Figure 16 shows a higher efficiency map by using the optimal field current.

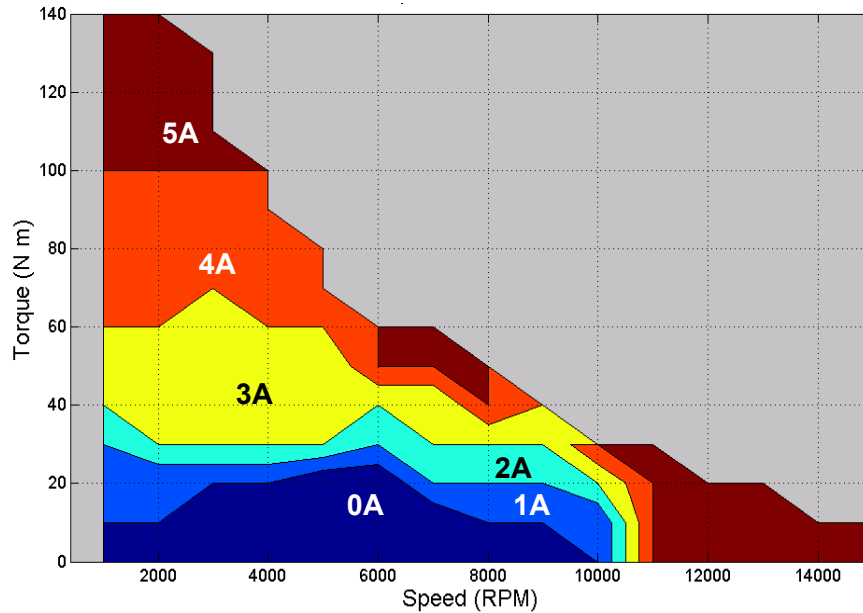


Figure 15. Optimal field currents when including field losses.

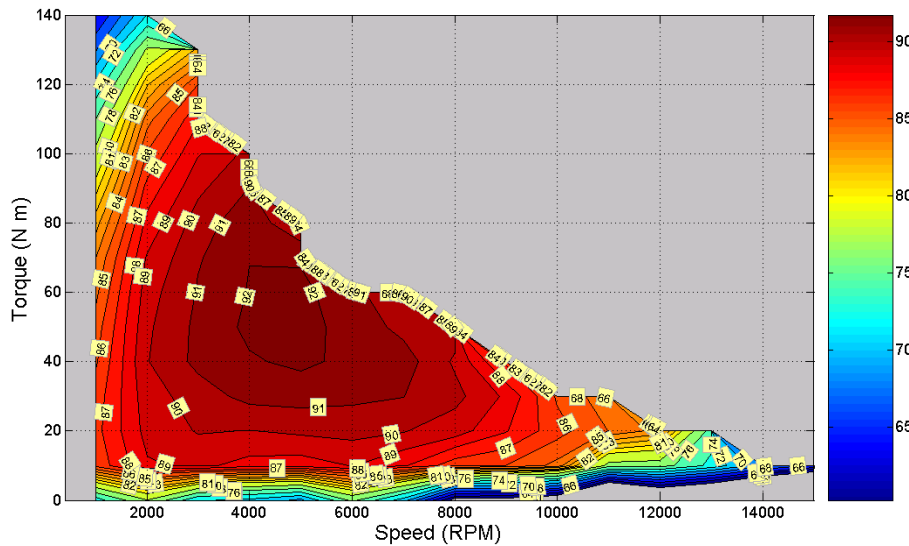


Figure 16. Efficiency contours using optimal field current—including field losses.

Projected efficiency contours using optimal field current with field losses included. The efficiency map shown in Figure 16 is obtained from the rewind machine. It is informative to project what the efficiencies should be if the tests were conducted on the original motor before rewinding. The detail of the projection rationale is presented in the project’s detailed technical report

(ORNL/TM-2007/167). To compare with the baseline motor, the speed and torque are scaled according to the 2.6 gear ratio. The projected efficiency map of the ORNL motor is shown in Figure 17.

A comparison of Figure 17 with Figure 13 shows that the projected efficiency map of the ORNL RIPM- BFE machine is substantially superior to the baseline (Prius) efficiency map. Note that the efficiencies below 5,000 (or $\sim 1,923$ in this figure) have been experimentally verified, as indicated in Figure 12.

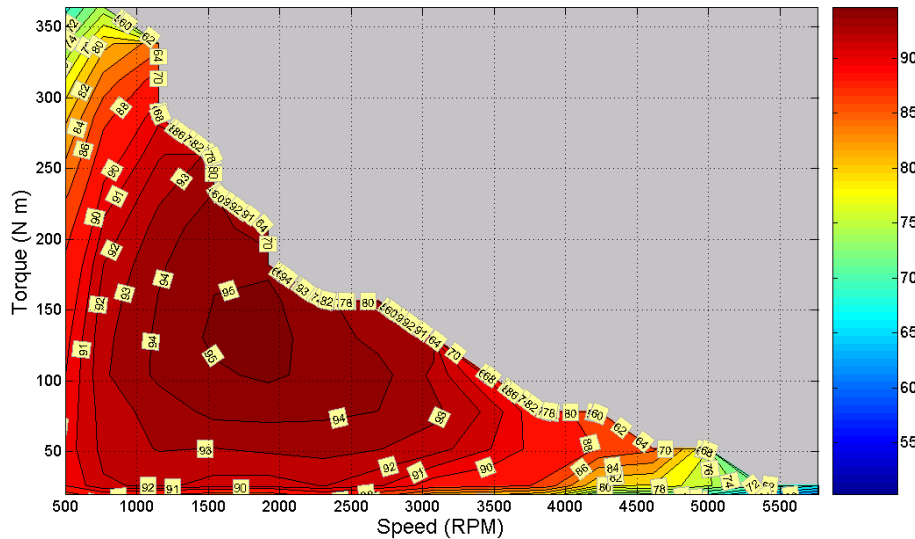


Figure 17. Projected efficiency contours using optimal field current with field losses included.

Conclusions

- This research effort proves that BFE from the third dimension (i.e., the axial direction) for an RIPM machine is practical and effective. The back-emf is easily controlled with an external field excitation current in the 0- to 5-A range. The excitation dc voltage does not exceed 80 V. This field excitation range is capable of changing the air-gap flux density up to 2.5 times at any speed. This enables the motor to have the high-power-density advantage of conventional strong PM reluctance motors as well as the low back-emf and lower core loss benefits of weak PM reluctance motors. The circuitry required to supply the excitation current to the coils is projected to cost under \$10 in production quantities of 100,000 or more.
- While the rotor is rotating at high speed with no field current, the core loss is significantly lower than that of fixed PM motors. The core and friction loss test results show the benefits of lower air-gap flux density. For example, at 5,000 rpm, the core and friction loss is 200 W at zero field excitation, compared with 600 W at high field excitation for a high air-gap flux density. This should positively impact the highway fuel efficiency of the vehicle.
- The prototype motor design permits the rotor punching bridges to be thicker to satisfy the mechanical stress requirements of high speed. Due to this rotor design, flux produced by the PMs can leak through, causing the air-gap flux density produced by the PMs to be reduced more than in similar IPM machines (such as the lower-speed baseline motor). The weaker air-gap flux density improves high-speed operation and can be compensated with BFE current for increased torque production at lower speeds.
- The machine was evaluated up to the full design speed of 16,000 rpm.
- The PM in the rotor acts as a flux barrier; thus, the air gap flux depends mainly on the adjustable field excitation. The ideal PM property for the field excitation should be a high coercivity, H_c , and a

relatively low remanence, Br. These would enhance the field adjustment ratio and lower the high speed core losses.

- If an interior short-circuit fault occurs in the windings, the excitation current can be turned off to prevent damaging the motor.
- The RIPM-BFE motor benefits from using an optimal field current combined with the capability of reducing the air gap flux when not needed. This results in increased efficiencies at low torques for both partial loads and high speeds. This can be confirmed by comparing Figures 12 and 13 for the low speed region of the tests. The projected RIPM-BFE motor performance from the rewound motor show greater efficiency advantages than those of the baseline motor. The benefits of variable field excitation were clearly observed.
- Rewound motor tests indicated a variable 2–5% drop in efficiency from the initial motor tests. It was determined that the stator bore was enlarged by the winding fabricator during cleaning before rewinding. This was confirmed by lower back-emf results in subsequent testing. The original stator showed significant advantages, particularly in terms of motor efficiency, over motors of similar power level. Although the rewound motor had a lower efficiency, the benefits of variable field excitation are still clearly observed. The efficiency map for the high-speed region was projected from the test results of the rewound motor to indicate what the efficiency would be if the tests were conducted on the initial motor.
- An aluminum frame was successfully used in the prototype design so as to not increase the total machine weight due to the addition of field excitation components.
- Tests confirmed that the asymmetrical rotor can increase the forward performance at the expense of reducing the backward performance.
- The RIPM-BFE motor should not present any manufacturing issues in mass production. Design improvements on the excitation coils to motor housing interface will result in a reduction of both mass and volume of the prototype motor, thereby reducing manufacturing costs.
- As a result of this research effort, a significant improvement in the development of accurate 3-D finite element simulations and a magnetically saturated lump parameter computational method for 3-D electric machine designs was achieved.
- The prototype motor is not the optimal possible design of a high-speed motor that uses the 3-D field excitation technology. It was initially designed to compare with the lower speed baseline motor. Various improvement options learned from this project can be used to meet different design constraints.
- A detailed technical report (ORNL/TM-2007/167) of this project has been issued.

Publications

FY 2006 FreedomCAR Annual Report.

ORNL technical report (ORNL/TM-2007/167) has been issued.

Patents

J. S. Hsu et al., “Method and Radial Gap Machine for High Strength Undiffused Brushless Operation,” U.S. Patent No. 7129611, October 31, 2006.

J. S. Hsu et al., “Auxiliary Power Generation in a Motor Transformer,” U.S. Patent No. 7,092,267, August 15, 2006.

G. J. Su et al., “Integrated Inverter for Driving Multiple Electrical Machines,” U.S. Patent No. 7,023,171, April 4, 2006.

J. S. Hsu et al., “Rotor Apparatus for High Strength Undiffused Brushless Electric Machine,” U.S. Patent 6,989,619, January 24, 2006.

J. S. Hsu et al., “Hybrid-Secondary Uncluttered Permanent Magnet Machine and Method,” U.S. Patent 6,977,454, December 20, 2005.

J. S. Hsu et al., "Permanent Magnet Machine and Method with Reluctance Poles for High Strength Undiffused Brushless Operation," U.S. Patent 6,972,504, December 6, 2005.

J. S. Hsu et al., "Simplified Hybrid-Secondary Uncluttered Machine and Method," U.S. Patent 6,891,301, May 10, 2005.

J. S. Hsu et al., "High Strength Undiffused Brushless (HSUB) Machine," U.S. Patent 6,573,634, June 3, 2003.

J. S. Hsu et al., "Hybrid Secondary Uncluttered Induction Machine," U.S. Patent 6,310,417, October 30, 2001.

J. S. Hsu et al., "Permanent Magnet Energy Conversion Machine," U.S. Patent 5,952,756, September 14, 1999.

References

1. M. Kamiya, *Development of Traction Drive Motors for the Toyota Hybrid System*, Toyota Motor Corporation, 1, Toyota-cho, Toyota, Aichi, 471-8571, Japan.
2. M. Okamura, E. Sato, and S. Sasaki, *Development of Hybrid Electric Drive System Using a Boost Converter*, Toyota Motor Corporation, 1, Toyota-cho, Toyota, Aichi, 471-8572, Japan.

3.3 IPM Drive Motor with Selectable Windings for HEVs

Principal Investigator: Donald Adams

Technical Team: Pedro J. Otaduy, John Hsu

Oak Ridge National Laboratory

National Transportation Research Center

2360 Cherahala Boulevard

Knoxville, TN 37932

Voice: 865-946-1321; Fax: 865-946-1262; E-mail: adamsdj@ornl.gov

DOE Technology Development Manager: Susan A. Rogers

Voice: 202-586-8997; Fax: 202-586-1600; E-mail: Susan.Rogers@ee.doe.gov

ORNL Program Manager: Mitch Olszewski

Voice: 865-946-1350; Fax: 865-946-1262; E-mail: olszewskim@ornl.gov

Objectives

- Investigate the system-level benefits of changing the effective number of turns in the stator windings of a vehicle's electric motor.
- Develop practical mechanisms to perform reconfiguration of the stator's winding on a running motor.

Approach

- Develop mathematical models for interior permanent magnet (IPM) motors and vehicle drive cycle dynamics.
- Implement the models with a flexible user-friendly interface.
- Perform comparative simulation studies of two identical vehicles, one fitted with a typical IPM traction motor with nine stator turns and the other fitted with the reconfigurable 9-18-turn version of the same IPM motor.
- Perform electric vehicle (EV) and hybrid electric vehicle (HEV) drive cycle simulations
 - In the EV computations, the motors were the only prime movers while traveling along a set of eight characteristic industry-standard driving cycles.
 - In the HEV versions, the motors provided propulsion only from vehicle start until it reached a set speed. The set speed chosen was 20 mph and the starting profiles were those of the eight driving cycles.
- Investigate switching approaches.
- Perform simulations to determine the magnitude of the voltage and current transients occurring during the time of the winding switching.

Major Accomplishments

We have demonstrated that a motor with reconfigurable stator windings has significant benefits compared with motors of traditional designs with a fixed number of stator turns.

In a vehicle with the 9- 18-turns motor, for EV and HEV configurations, over eight driving cycles analyzed, our work showed the following results:

- Available voltage is better utilized.
- Stator currents are lower.
- Motor efficiency is higher.
- Efficiency of power electronics, battery, and cabling is higher.
- Overall vehicle system efficiency is higher.

- Battery size and cost are reduced.
- Power demand is met under all conditions during the drive cycles without voltage boosting.

For the EV configuration, the vehicle with the reconfigurable turn motor consumes between 3.6% and 27% less energy and requires between 5.1% and 19.6% less peak power than the vehicle with the conventional 9-turn motor.

For the HEV configuration, the vehicle with the reconfigurable turn motor consumes between 13% and 23.4% less energy and requires between 16% and 39% less power than the vehicle with a conventional 9-turn motor.

A novel electronically commutated connection-change switch was developed that offers the possibility of

- Low cost
- Benign failure mode
- High efficiency, over 99%
- Small size
- Long life expectancy
- Easy cooling

Future Direction

This project has been completed. If further research were to be conducted, the following would be pursued:

- Regenerative braking by the reconfigurable turn motor would be added to the performance simulation model and the magnitude of the additional savings would be assessed.
- Validation of the modeling would be performed by testing a motor before and after modification of its winding. This would confirm the performance gains and contact switching performance predicted by the models.
- The switching mechanisms would be instrumented and their performance evaluated while running the motor tests.

Technical Discussion

Introduction

Torque is produced in an electric motor by the interaction of two magnetic fields, one in the rotor and the other in the stator. The magnitude of the torque is proportional to the product of the magnitudes of the two magnetic fields. The stator's magnetic field is produced by electric currents circulating through coils wound around the stator teeth. In permanent magnet (PM) machines, the rotor's magnetic field is produced by PMs placed in the rotor and is essentially of constant magnitude.

As the rotor's magnetic field crosses the stator coils, a voltage (also referred to as the back-electromotive force [back-emf]) is induced at the stator terminals. The amount of electric current circulating in the stator coils, and thus the strength of the magnetic field they produce, depends on the coils' impedance and the vectorial difference between the applied terminal voltage and the induced back-emf.

Below the base speed, the combination of low induced back-emf and low stator inductance forces the reduction of the effective terminal voltage in order to keep the stator current below pre-determined safe limits. Since the torque is proportional to the number of turns and the magnitude of the current, the maximum torque that can be produced in this operating region is traditionally constant.

As speed increases, both the stator coils' impedance and the back-emf increases. Consequently, the magnitude of the current in the coils decreases with increasing rotor speed, and so does the strength of the stator's magnetic flux and of the torque output. When the magnitude of the back-emf equals that of the

terminal voltage, then the stator's magnetic field is shut down, since no current circulates in the coils. Consequently, no torque is produced and higher speeds cannot be achieved.

Traditional approaches to extending the speed range of the operation of PM motors include weakening the rotor's magnetic flux as the speed increases, thus decreasing the magnitude of the back-emf and allowing for higher electric currents to circulate in the stator windings. The drawback inherent in this approach is that the linked rotor field is suppressed and additional current and complexity in the drive system and/or stator are needed. In addition to the current invested to suppress the rotor's field, extra current is needed to compensate for the reduction in the magnitude of the rotor's field.

A promising alternative way to produce more torque in the low-speed operating region and to extend the operating speed range is to change the effective number of turns involved in the electrical-to-mechanical energy transformation. Increasing the number of turns increases the torque produced with the same amount of current, which is of particular interest in the low-speed region. Reducing the effective number of turns in the stator windings reduces the back-emf without expending stator current to weaken the magnitude of the linked rotor's field. As a result, higher currents can be reached at a given speed with the same terminal voltage limit. This extends the operating speed region by allowing torque generation at higher speeds without having to boost the terminal voltage.

A motor with the capability to change the number of turns continuously in one-turn steps for optimal performance can be simulated readily; but considerations of added cost, complexity, and energy losses associated with the switches may not justify the performance gains. Instead, considering that the stator coils are often made with several wires bundled together and welded at the ends, instead of with a single thicker wire, the simplest implementation of reconfiguring the number of turns appears to be by factors of two or more. A factor of two is the most feasible since it can be accomplished by splitting the wires in each phase into two groups and connecting their ends in parallel or in series to have N or $2N$ turns per phase, depending on the motor's speed and load demand. At low speeds, having twice the number of turns doubles the torque for the same current limit and decreases the need for voltage regulation. At high speeds, switching back to the reduced number of active turns reduces the back-emf for the same speed, thus increasing the speed range of operation. As shown in this study, adjusting the number of stator turns up and down appropriately results in better performance with better copper and battery voltage utilization over the whole range of operation.

In this report we present the main results obtained with our simulator for two vehicles: EV1 is fitted with a typical IPM motor with nine stator turns. EV2 is fitted with a modified version of the same IPM capable of switching between 9 and 18 stator turns as it travels, following eight different standard speed-vs-time driving profiles. Note that a more detailed description of this work can be found in Ref. 1.

Simulation Approach

The simulation includes a vehicle model that computes the power needed at the vehicle's tires in order for it to follow a specified speed-vs-time profile, subject to wind speed and road slope perturbations. Power transmission losses between the prime-mover's output axle and the tires are added to determine the power demand to be met by the vehicle's prime mover. In our case, the prime mover is an IPM electric motor.

To model the performance of the IPM motor, we followed the standard d-q transformation approach described in Ref. 1. The IPM simulation has been implemented in a form that allows changing the number of effective stator turns at will. At every time step, the optimal voltage, electrical current, and control angles needed to meet the power demand with the best efficiency are computed for each of the set of stator turns desired. The number of turns yielding the best efficiency is selected, and the corresponding power level, voltage, current, and control angle characteristics constitute the demand for the inverter. A model of the inverter and cabling losses computes the power demand for the battery. The total power demand on the battery at each time step also includes the losses of energy at the battery.

A set of eight standard driving cycles were implemented to study the impact of using a motor with reconfigurable stator windings on total vehicle performance.

Evaluation of factor-of-two turn-switching for a base motor with nine stator turns

The mechanical and electrical characteristics of the base reference IPM motor are shown in Figure 1. The number of turns of this reference IPM is nine, maximum current is 212 A, and voltage is 250 V.

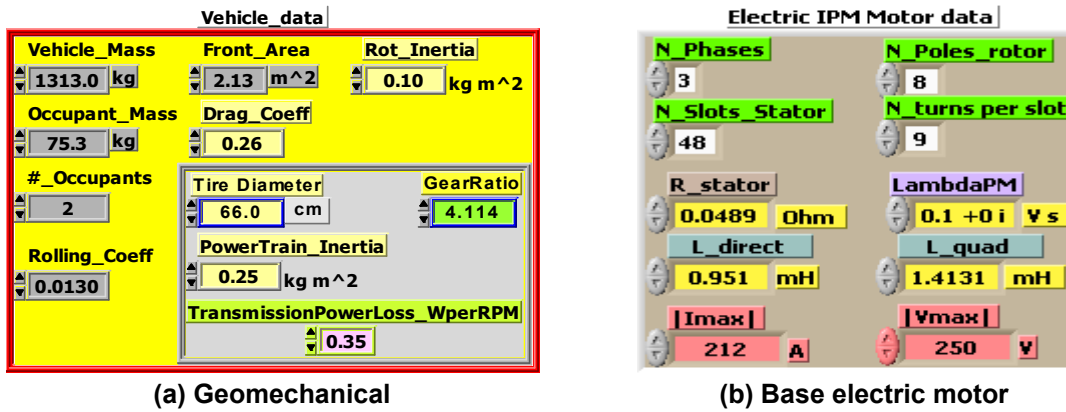


Figure 1. Characteristic parameters of the reference vehicle.

Switching the turns of our reference motor by a factor of two implies switching between 9 and 18 turns. Operation with 18 turns can be attained by grouping the wires in each phase in two bundles and connecting their ends in series. To operate with the original nine turns, the two bundles are connected in parallel. While it is operating with 18 turns, the motor’s ohmic resistance and inductances are four times larger and the rotor-linked flux is two times larger than the base 9-turn values shown in Figure 1(b).

A. Electric vehicle following standard driving cycles

A summary of data of interest for the reference vehicle over all the cycles is included in Table 1. Data shown are time lengths of failed, motor-OFF, and motor-active periods, and the energy deficit for each

Table 1. Time in seconds the prime-movers in EV1 and EV2 failed to meet the power demand, EV1’s energy deficit in percent of cycle total, total time the prime-mover was OFF, and time the prime-mover succeeded in supplying the vehicle’s demand for each driving cycle

Cycle ID #	Driving Cycle Name	Failed Time s		% Energy Deficit EV1	OFF Time s	Success Time s	
		EV1	EV2			EV1	EV2
# 1	FUDS	0	0	0	568	805	805
# 2	FHDS	0	0	0	74	691	691
# 3	HDV_FUDS	2	0	0.03	519	520	522
# 4	NewEurope	0	0	0	447	714	714
# 5	NYCity	7	0	1.97	323	236	243
# 6	NYCityTruck	4	0	0.14	689	320	324
# 7	US06	43	0	3.69	182	377	420
# 8	US06_hwy	8	0	1.65	61	301	309

driving cycle for each type of motor. Table 1 shows that the reference vehicle equipped with the base 9-turn motor failed to follow the speed profile between 2 and 43 one-second time steps during cycle numbers 3, 5, 6, 7, and 8. The energy deficit ranged from a negligible 0.03% to a significant 3.69% of the total cycle’s energy demand. The 9–18-turn motor, though, did not fail to provide the power demanded a single time. A full discussion for all driving cycles can be found in Ref. 1. For brevity, only the US06 cycle 7, which failed the most with the regular motor, is discussed in detail below.

Performance comparison of EV with 9-turn and 9–18-turn switching motors on the US06 cycle.

Figures 2(a) and 2(b) show the performance of the vehicle on the US06 driving cycle speed versus time curve. The red areas indicate zones where the vehicle could not follow the demand curve; the black areas indicate motor-OFF periods, and brown and green indicate the number of turns active during propulsion. Comparing Figures 2(a) and 2(b), it is clear that EV2, by switching between 9 and 18 turns, not only provided the fully needed torque in regions where EV1 could not, but also—operating with 18 turns—provided better overall efficiency.

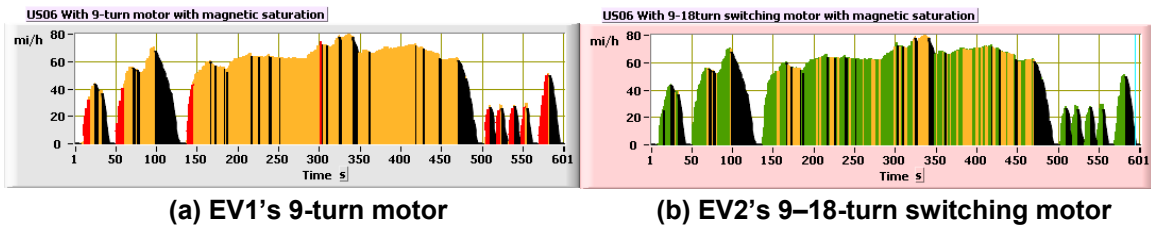


Figure 2. Speed vs time for the US06 cycle; red = fail, black = OFF, orange = 9 turns, green = 18 turns.

Figures 3(a) and 3(b) show the terminal voltages for EV1 and EV2, respectively, as a function of time for the US06 driving cycle. It is clear that the reconfigurable turn motor in EV2 makes better use of the available 250 V. The motor requires less voltage regulation, places fewer switching demands on the electronic power drive, and therefore has better efficiency.

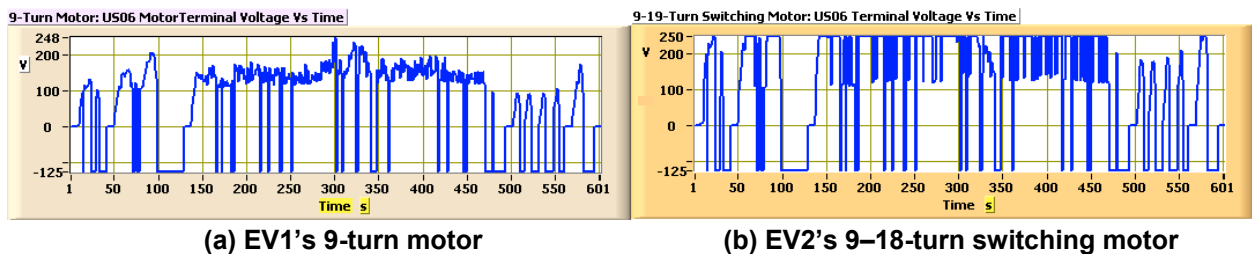


Figure 3. Terminal voltage along the US06 cycle.

Similarly, Figures 4(a) and 4(b) show the stator current for EV1 and EV2, respectively, as a function of time for the US06 driving cycle. These figures show consistently lower current levels for EV2 with the reconfigurable turn motor, which reduces ohmic losses and enables it to meet all power demands without ever reaching the 212 A maximum limit.

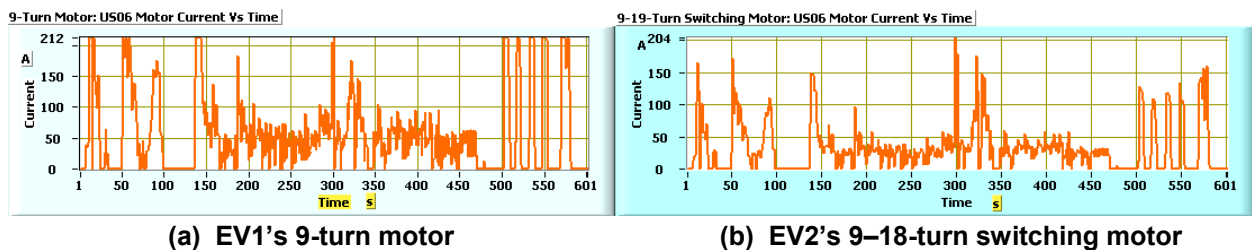
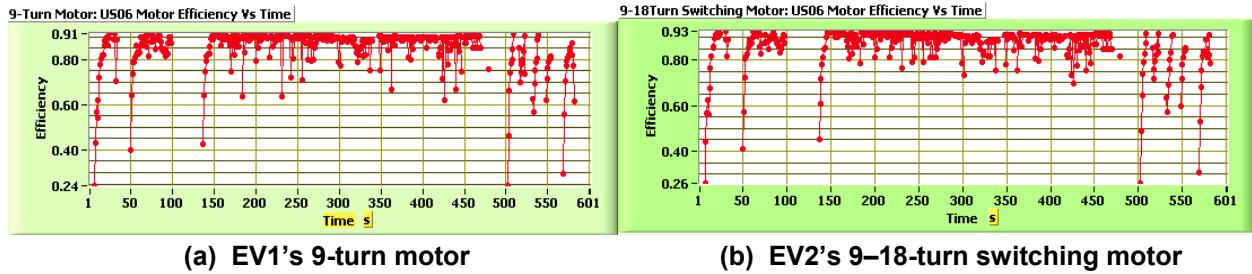


Figure 4. Stator current along the US06 cycle.

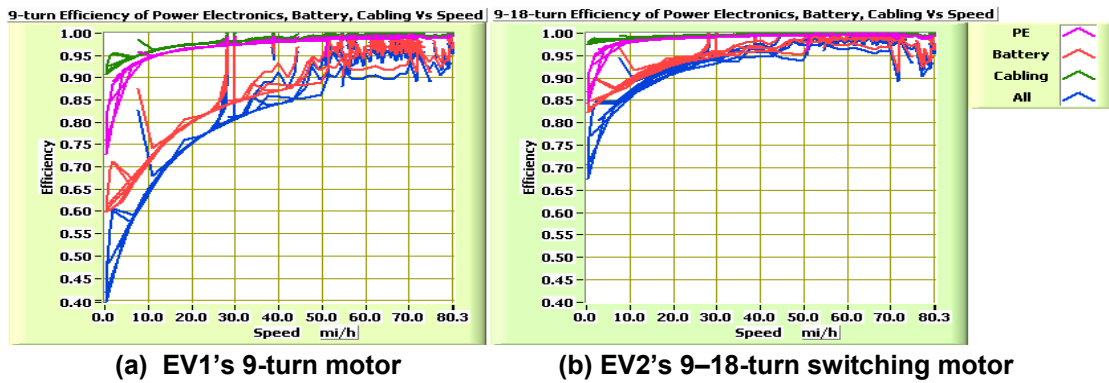
Figures 5(a) and 5(b) show the efficiency of the motor in each vehicle as a function of time for the US06 driving cycle. There is a clear efficiency advantage of over 2% for the motor with reconfigurable turns capability, over most time periods.



(a) EV1's 9-turn motor (b) EV2's 9-18-turn switching motor

Figure 5. Efficiency of electrical-to-mechanical conversion along the US06 cycle.

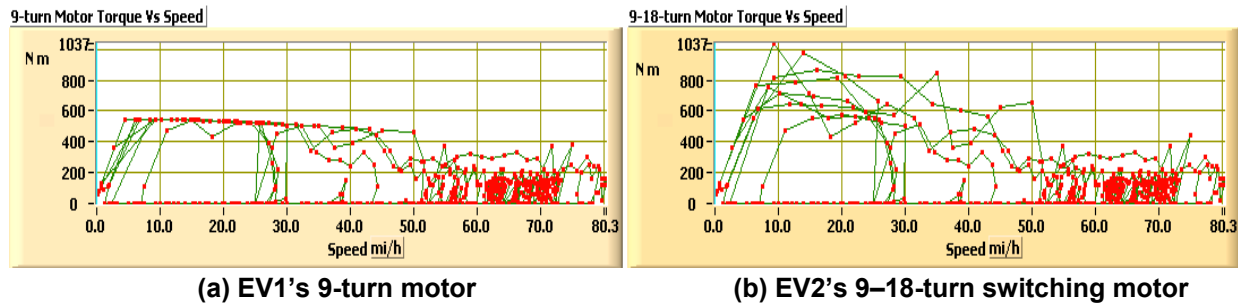
Figures 6(a) and 6(b) show the efficiency of the remainder of the electrical components in each vehicle as a function of vehicle speed. There is a clear gain of efficiency in the electrical system of vehicle EV2, with the highest gains at low speeds. At 20 mph, for instance, the overall electrical system efficiencies are about 75% for EV1 and 91% for EV2, for a net gain of 16%. The summary in Table 2 and Ref. 1 show that the overall increase in full vehicle efficiency, for the US06 cycle, is 6% when the reconfigurable turn motor is used, i.e., the efficiency of vehicle EV2 is 6% higher than that of EV1 on the US06 cycle.



(a) EV1's 9-turn motor (b) EV2's 9-18-turn switching motor

Figure 6. Efficiency of power electronics, battery and cabling vs US06 cycle speed.

The motor's output torque as a function of vehicle speed for the US06 cycle is shown in Figures 7(a) and 7(b). The points above the 600 Nm torque level shown in Figure 7(b) that are missing in Figure 7(a) correspond to instances in which the standard motor failed to fully deliver the power demanded by the vehicle.



(a) EV1's 9-turn motor (b) EV2's 9-18-turn switching motor

Figure 7. Output torque vs US06 cycle speed.

Failure analysis of the EV with the 9-turn motor on the US06 cycle. Figures 8(a) through 8(d) show speed, motor power demand, power output, terminal voltage, and stator current of EV1 on the US06 cycle at three different resolutions: full, first minute, and midpoint seconds. The stator current curves in Figure 8(d) clearly show that the times of failure coincide with instances when the motor attempted to draw more current than the allowed maximum limit.

Figure 8(c) shows that the voltage remained below the limit of 250 V for the duration of the cycle. Only once, around the 300-second point, does the voltage get within 2 V of the limit, at a time when, as seen in Figure 8(d), the current reached the 212 A limit.

Consequently, in order to correct EV1's performance problem, the current limit must be increased or more torque must be produced with the same amount of current by switching to a higher number of turns. It is clear, though, that voltage boosting will have no impact in this case since, as shown in Figure 8(c), the available voltage is not being fully utilized at the critical times.

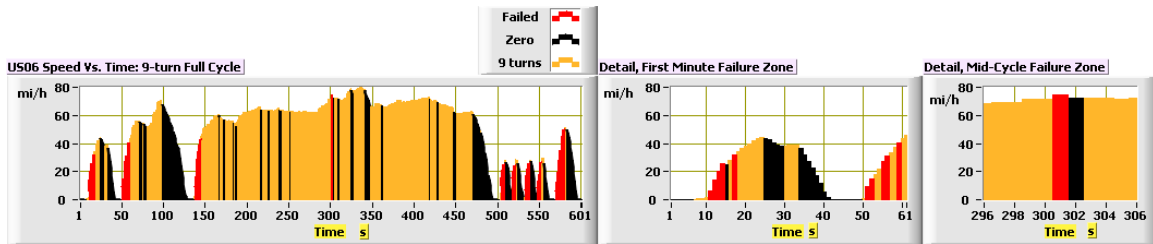


Figure 8(a). US06 cycle failed zones of EV with 9-turn motor.



Figure 8(b). US06 cycle power demand and supply for EV with 9-turn motor.

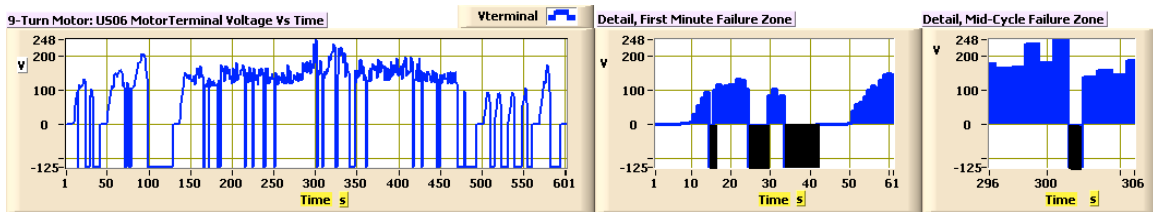


Figure 8(c). US06 cycle voltage at terminals for EV with 9-turn motor.

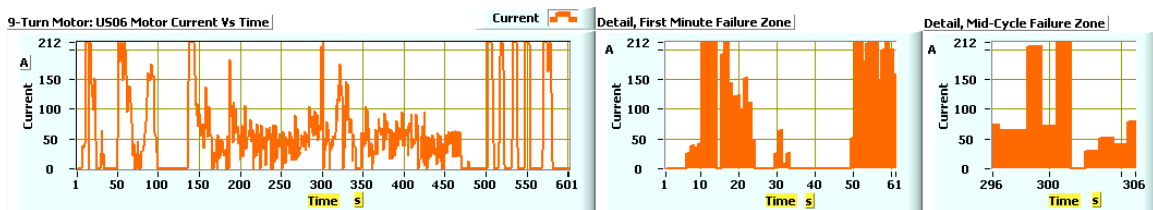


Figure 8(d). US06 cycle stator current for EV with 9-turn motor.

Note: The black zones in the voltage graph, Figure 8(c), correspond to the back-emf generated by the rotor’s PM as it turns. This voltage depends on the rotor speed and number of turns in the stator and can be measured at the motor terminals when the terminals are electrically open. Also note that the negative power areas, colored black in Figure 8(b), equal the amount of active braking energy required by the vehicle, which in turn indicates the amount of energy available for regeneration.

B. HEV for standard driving cycle starts

Some hybrid vehicles use the electric motor to accelerate from zero to a set speed, at which time the internal combustion engine starts and fulfills all or part of the power demand. In order to assess the impact of the reconfigurable turn motor on these hybrids, we have analyzed the reference vehicle at the initial, 0 to 20 mph, start of the eight driving cycles discussed earlier.

As seen in Figure 8(a), the HEV with the regular motor fails to follow the power demanded in the start from 0 to 20 mph in both US06 cycles. Consequently, its performance can only be compared with that of the HEV with the reconfigurable turn motor on the other six cycles.

A summary of the gains for this type of HEV is shown in Table 2. (The corresponding gains in battery size and cost for the battery technology chosen are shown later in Figure 11.)

C. Summary of gains for the EV and HEV using a reconfigurable turn motor

Table 2 shows the EV and HEV gains for each driving cycle when the reconfigurable turn IPM motor is used for propulsion instead of the traditional fixed turns motor.

Table 2. Summary of savings achieved by stator turn-switching
(Maximum and minimum values for each column are shown in bold.)

Figure No. →	Electric vehicle				0-to-20 mph HEV			
	Vehicle energy and power savings				Vehicle energy and power savings			
Cycle name	19(b)	21(a)	21(b)	16	29	31(a)	30	31(b)
	kJ/mile	% Energy	% Energy relative	% Peak power relative	kJ	% Energy relative	kW	% Power relative
FUDS	119	6.4	12.6	16.3	32	22.4	4.3	18.3
FHDS	28	2.8	3.6	13.5	34	23.4	6	22
HDV FUDS	74	5	8.5	17.3	24	13.5	2.5	16.1
New Europe	62	4.3	7	5.1	56	15.1	2.9	14.2
NY City	265	8.4	26.9	19.6	32	21.3	5	18.7
NY City truck	175	6.3	16.7	17.3	38	17.1	9.1	38.9
US06	63	6	10.4	INC ^a	INC	INC	INC	INC
US06 highway	43	3.7	5.1	INC	INC	INC	INC	INC

^aINC stands for “incomparable,” because the base motor failed to fully satisfy the demand.

For the EV configuration, the vehicle with the reconfigurable stator IPM motor consumes between 3.6% and 26.9% less energy and requires between 5.1% and 19.6% less peak power than the vehicle with the conventional 9-turn IPM motor.

For HEVs, the vehicle with the reconfigurable stator IPM motor consumes between 13.5% and 23.4% less energy and requires between 16.1% and 38.9% less power than the vehicle with the conventional 9-turn IPM motor.

Note that the maximum EV savings of 265 kJ/mile shown for the New York City cycle amounts to a savings of about 1 gallon per 151 miles of driving, when a value of 40 MJ/gallon is used for the equivalence between battery energy and gasoline in the tank.

D. Effect on battery size and cost of using a turn-switching motor

Battery size is determined by the total energy and peak power demands by the vehicle system and by the capabilities and price of the battery technology selected. Power delivery capability sets the minimum battery size, whereas the energy storage capability, which depends on the travel range without recharging, may determine the actual size. As shown in Ref. 1, the battery size needed to satisfy the vehicle’s power demand in each cycle stores more energy than that required to travel the full cycle; consequently, it can be stated that for runs of a single cycle length, the battery is power-bound for all eight cycles considered.

In relative percentage terms, the reductions in battery weight and cost using a reconfigurable turn motor are shown in Table 2 independent of the type of battery used. The magnitude of the benefits depends on whether the battery is power-bound or energy-bound.

- For the energy-bound case, the gains are shown in the “% Energy relative” column of Table 2; i.e., for the EV, between 3.6% for the Federal Highway cycle 2 and 27% for the New York City cycle 5; and for the HEV, between 13% for the Heavy Vehicle Federal Urban cycle 3 and 23.4% for the Federal Highway cycle 2.
- For the power-bound case, the gains are shown in the column “% Power relative” in Table 2; i.e., for the EV, between 5.1% for the NewEurope cycle 4 and 19.6% for the New York City cycle 5; and for the HEV, between 16% for the NewEurope cycle 4 and 39% for the New York City Truck cycle 6.

To provide an insight into the range of weights and costs considered for this study, the reference vehicles were simulated with batteries that meet the U.S. Advanced Battery Consortium’s minimum goals for EV batteries of 50 W h/kg, 300 W/kg, and 150 \$/kWh, which imply costs of 22.5 \$/kg and 75 \$/kW.² Note that batteries cannot be discharged fully without reducing their life spans. Presently, 20% is the low-charge limit for “deep-discharge” batteries so that, at most, 80% of the stored energy can be discharged routinely. The sizing values shown below are based on ideal 100% discharge of the batteries; consequently, actual values will be larger. For instance, for an 80% discharge limit, the weights and costs would be 25% larger than shown.

EV battery size gains with stator turn-switching. When the battery sizing is power-bound, Figure 9 shows that the highest absolute gains in peak battery power correspond to both the Heavy Duty Vehicle Federal Urban cycle 3 (HDV_FUDS) and the New York City Truck cycle 6, with peak gains of 9.6 kW, 32 kg and \$720. Note that, as shown in Figure 24 of Ref. 1, power-bound for EV1 in these two cycles means that the driving distances are shorter than 100 and 73 miles, respectively.

When the battery sizing is energy-bound, Figure 10 shows that a reconfigurable turn motor benefits the most when the vehicle runs the New York City cycle 5, with per-mile savings of 265 kJ, 0.5 kg, and \$11. For a 100 mile range, the savings in battery cost will amount to \$1,125 and the weight savings to over 50 kg.

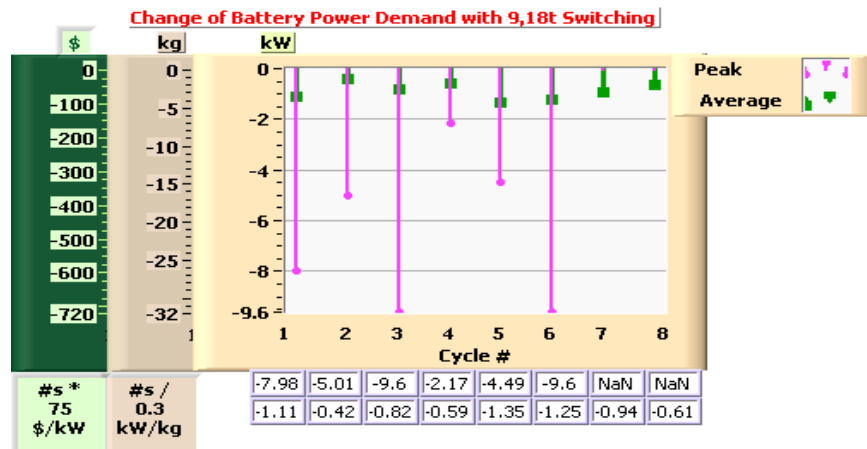


Figure 9. Change in EV battery power, weight, and cost using the 9–18-turn motor.

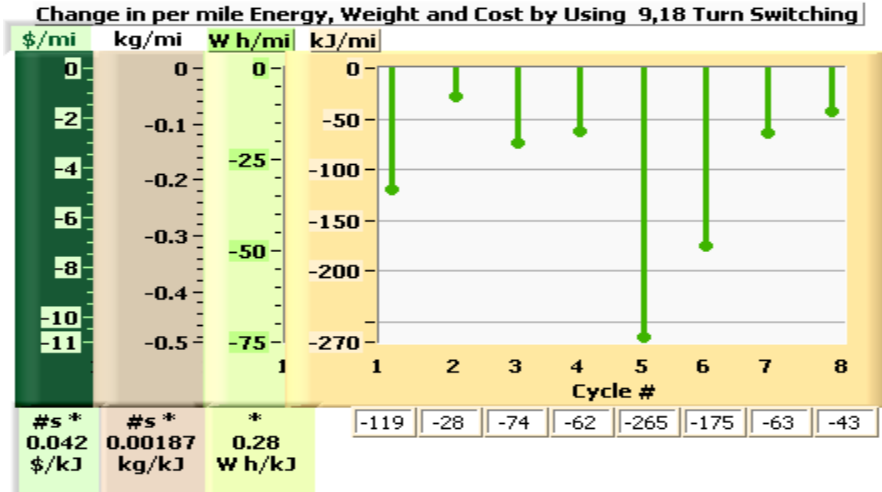


Figure 10. Change in EV battery energy, weight and cost per mile with the 9–18-turn switching motor.

To illustrate driving-range effects, we compared the two vehicles exercising the Federal Urban (FUDS) cycle 1 over 50- and 100-mile ranges. For the 50-mile range, the battery is power-bound, as shown in Figure 9, and the battery savings for the vehicle with the reconfigurable turn motor amounts to about 27 kg and \$600. For the 100 mile range, the battery is energy-bound and the savings depend on the distance; according to Figure 10, they will amount to 22 kg and \$500.

HEV battery size gains with stator turn-switching. In the HEV case, the battery is always power-bound; thus Figure 11 shows the change in battery size and cost for the reference HEV when the reconfigurable turn motor is used instead of the fixed 9-turn base motor. The biggest savings occurred over the New York City cycle 6, with 30.3 kg and \$682 reductions. The minimum savings are for the HDV_FUDS cycle 3, with reductions of 8.3 kg and \$188.

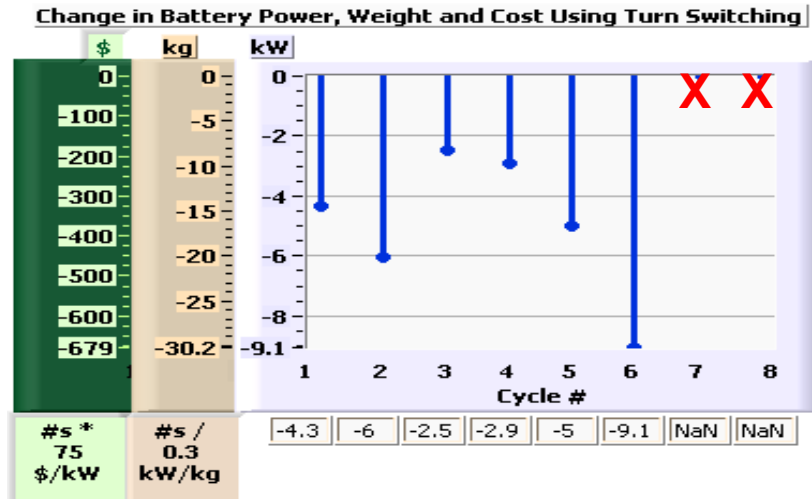


Figure 11. Change in HEV battery size and cost based on power required from zero to 20 mph. (Note that for US06 cycles 7 and 8, data are not included because the regular motor could not meet the power demand.)

E. Mechanisms for implementation of stator turn switching

Figure 12 shows a schematic of a typical inverter driving a motor with the capability to connect its winding conductors (a) in series or (b) in parallel by means of eight on/off bidirectional switches. The winding terminals are labeled with A1, B1, C1, X1, Y1, Z1, A2, B2, C2, X2, Y2, and Z2.

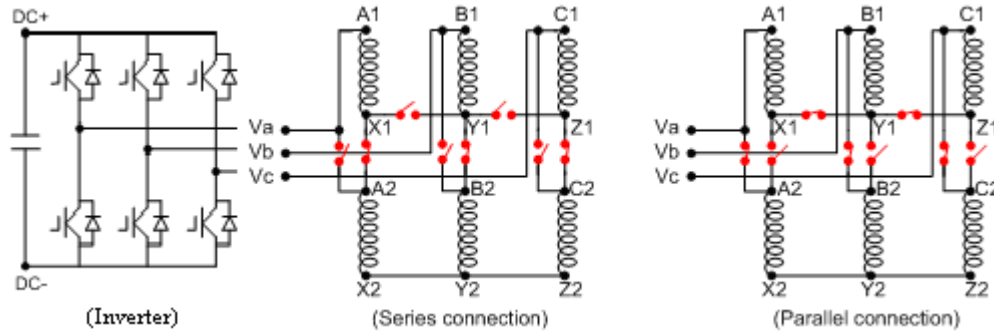


Figure 12. Schematic of inverter and motor windings with switches for series-to-parallel reconfiguration.

Changing between series and parallel configurations blindly while current circulates through the windings would result in arc flashes that would rapidly destroy the contacts. Figure 13 shows that if, while in a series configuration, contacts are opened at the instant the current in phase-a is at its peak 400 A value (top waveform), a spike of 62,000 V develops across the opening contacts (middle waveform).

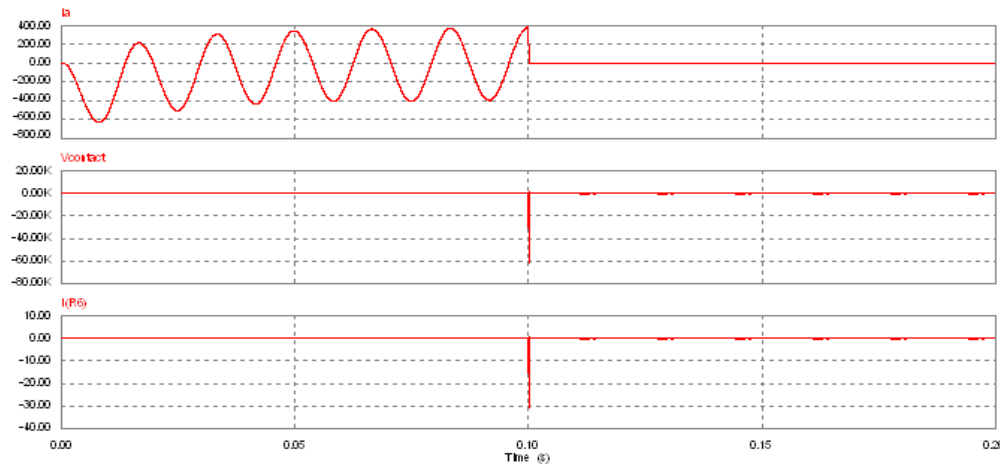


Figure 13. Current and voltage waveforms at serial winding opening transition (top: winding current; middle: voltage at the contacts; and bottom: current at the shunt-resistor).

A better approach to changing between series and parallel configurations while current circulates through the windings is to switch each phase at the moment the alternating current crosses the zero value. This can be accomplished using a combination of high-current electronics switches such as insulated gate bipolar transistors (IGBTs) and silicon controlled rectifiers (SCRs). The SCR automatically stops the conduction when it sees the zero current. A minimum number of 16 high-current SCRs would be required for the three-phase series/parallel diagram shown in Figure 12. With this approach, the SCRs stay in the current path continuously and thus contribute additional losses and cooling requirements. In addition, at the present time, the cost for high-current electronics switches is high.

A novel approach in which the SCRs are taken out of the winding's electrical current path has been developed during this research that has the potential for being low in cost, small, easy to cool, and long lived and for having a benign failure mode. We refer to it as the "electronically-commutated configuration switcher." It is basically a hybrid mechanical and electronic switch arrangement. One movable disc per phase, consisting of alternating insulator and conductor regions and signal triggering nodes, moves in contact with a set of four stationary brushes welded to the ends of each coil. The triggering nodes send pulses to a set of SCRs prior to circuit opening. Figure 14 shows the computed current and voltages for this novel approach when opening the series connection and closing to parallel configuration. For a more detailed description, see Ref. 1.

Reducing the winding current will reduce the magnitude of the voltage spikes, which is proportional to the square of the current fraction. Damage to the contacts will be fully prevented by switching at a zero current level. This subject is discussed in more detail in Ref. 1.

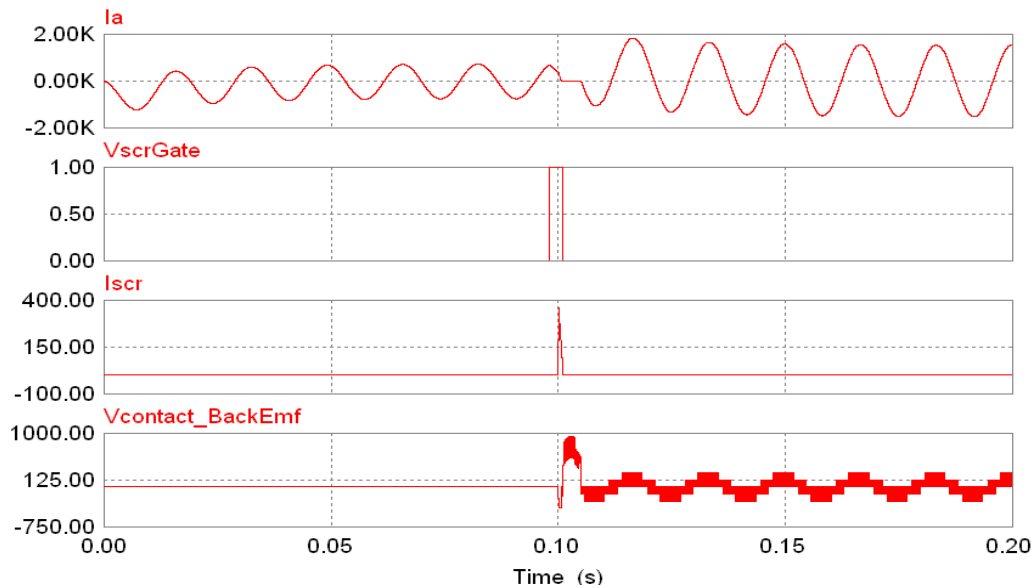


Figure 14. Simulation results for winding opening from series and reconnection to parallel configuration with the electronically-commutated configuration switcher.

Conclusion

The benefits and the feasibility of stator reconfigurable turn motors to be used in electric vehicles and hybrids have been demonstrated.

Substantial gains in efficiency and reductions in battery size and cost have been quantified for eight different standard drive cycles.

A novel concept for a cost-effective mechanical-electric switch for reconfiguration of the turns while the motor is loaded has been developed.

Publications

P. J. Otaduy, J. S. Hsu, and D. Adams, *Study of the Advantages of Internal Permanent Magnet Drive Motor with Selectable Windings for Hybrid Electric Vehicles*, ORNL/TM-2007/142, Oak Ridge National Laboratory, 2007.

References

1. P. J. Otaduy, J. S. Hsu, and D. Adams, *Study of the Advantages of Internal Permanent Magnet Drive Motor with Selectable Windings for Hybrid Electric Vehicles*, ORNL/TM- 2007/142, Oak Ridge National Laboratory, 2007.
2. Goals for Advanced EV Batteries, http://www.uscar.org/guest/article_view.php?articles_id=85

3.4 Control of Surface-Mounted Permanent Magnet Motors with Special Application to Motors with Fractional-Slot Concentrated Windings

Principal Investigator: John W. McKeever

Oak Ridge National Laboratory

National Transportation Research Center

2360 Cherahala Boulevard

Knoxville, TN 37932

Voice: 865-946-1316; Fax: 865-946-1262; E-mail: mckeeverjw@ornl.gov

DOE Technology Development Manager: Susan A. Rogers

Voice: 202-586-8997; Fax: 202-586-1600; E-mail: Susan.Rogers@ee.doe.gov

ORNL Program Manager: Mitch Olszewski

Voice: 865-946-1350; Fax: 865-946-1262; E-mail: olszewskim@ornl.gov

Objectives

- Test and evaluate Oak Ridge National Laboratory's (ORNL's) parameter-based low-cost (sensor-less) controller, which produces maximum torque per amp below base speed and maximum power per amp above base speed for the complete drive system.
- Collaborate with the University of Wisconsin at Madison (UWM) on a second control algorithm that employs an iron-loss model and modifies a conventional vector control algorithm to improve the efficiency of surface-mounted permanent magnet (SPM) motors with fractional-slot concentrated windings (FSCW) by using negative d-axis current to field weaken core flux at partial-loads so that core losses may be reduced.

Approach

- Interface ORNL's low-cost algorithm with the prototype motor designed by the UWM utilizing the OPAL RT rapid prototype system to achieve maximum torque per amp below base speed and maximum power per amp above base speed.

Major Accomplishments

- Completed the interface of the prototype 6-kW FSCW SPM motor with the OPAL RT rapid prototyping system and the new Danfoss inverter to evaluate the drive system.
- Completed dynamometer characterization measurements on the 6-kW FSCW SPM motor driven by ORNL's low-cost motor parameter-based control algorithm. The control scheme was programmed in MatLab, compiled for use with OPAL RT, and then used to drive the motor.
- Completed a report [1] evaluating ORNL's low-cost parameter based control algorithm, which achieves maximum torque per amp below base speed and maximum power per amp above base speed.
- Completed the analysis of UWM's modified vector control algorithm to improve the partial-load efficiency of FSCW SPM motors. UWM's final report is referenced in [2].

Future Direction

- All testing of the 6-kW FSCW SPM motor at ORNL has been completed, and the motor has been returned to UWM. UWM plans to test its modified vector control algorithm in house. Once UWM has

data, they may be compared with ORNL's low-cost algorithm test results, which are published in ORNL/TM-2007/007.

Technical Discussion

The overall objective has been to develop techniques to analyze, design, and control FSCW SPM synchronous machines, to investigate their possible use in a hybrid electric vehicle (HEV) traction drive system and, if appropriate, to bring them into competition with internal permanent magnet (IPM) motors. FSCW motors have potential for fault tolerant and wide constant power speed range (CPSR) operation because of their high inductance. They also have features that can reduce copper costs through improved slot utilization and elimination of copper end turns and reduce fabrication costs through simplified assembly methods.

Emphasis of this specific task has been on control of SPM motors with special application to stators that use concentrated windings. This control is accomplished with an algorithm that provides logic to control the gate drives of an inverter so that it meets the load demands of a FSCW SPM motor.

ORNL and UWM have developed two very different control algorithms. ORNL's algorithm is based on a motor's parameters, which are manipulated by a simple motor model to estimate the current necessary to meet the load demands. Detailed simulation of the algorithm predicts that it can effectively control motor speed while minimizing the motor current magnitude during operation above and below base speed. Laboratory testing has applied this control scheme to complete characterization testing of a 6-kW FSCW SPM motor. UWM's algorithm is a vector control algorithm modified to use negative d-axis current to depress (weaken) magnetic flux levels in the core to reduce core losses, which increases efficiency. This algorithm requires a model that accurately estimates core losses, which is more detailed than the model used in the ORNL algorithm.

ORNL's Motor Parameter-Based Low-Cost Algorithm

ORNL has used simplified per-phase models with considerable success [1] to study the performance of permanent magnet (PM) machine drives with either trapezoidal or sinusoidal back-electromotive force (emf) wave shapes. The per-phase model represents only the fundamental frequency component response of the machine; consequently, some factors such as torque ripple cannot be studied while using this simplification. In general the fundamental frequency component dominates the motor current response and accurately preserves power. The main advantage of the simplified fundamental frequency model is that it eliminates the need for simulating the phase width modulation (PWM) switching actions. Although the effects of switching are not explicit in this model, it was recently extended to predict all of the inverter loss mechanisms [1]. The model is shown in Figure 1. This model was used extensively in the development of the closed-loop control schemes.

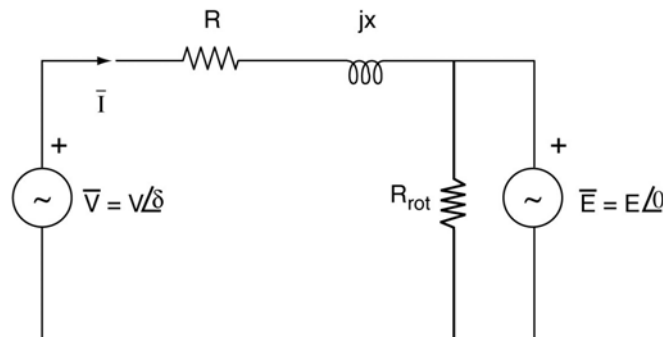


Figure 1. Fundamental frequency model of a PM motor driven by a PWM controlled voltage source inverter.

The control objective is to develop the required motor torque/power while minimizing the losses using a simple sine triangle PWM technique. In this type of PWM control there are two variables, the amplitude modulation index, m_a , and the inverter lead angle, δ . The value of m_a is defined as the ratio of the applied fundamental frequency control voltage to the peak value of a carrier switching voltage. The fundamental control voltage establishes the magnitude and frequency of the desired phase voltage. In this section, expressions, which include winding resistance and rotational losses, are given for m_a and δ for a permanent magnet synchronous motor (PMSM) traction drive. The availability of these expressions is useful for analyzing the performance of the new dynamic PWM controller.

During low-speed operation at constant torque, both the amplitude modulation index, which controls voltage magnitude, and the inverter lead angle can be adjusted. This allows the motor current to be placed in phase with the motor back-emf. Because all of the motor current produces torque, the rotor copper losses are minimized because the control delivers maximum torque per amp. The required torque is

$$I_r = \frac{T}{3K_t} = \frac{T_{out} + T_{rot}(n)}{3K_t}, \quad (1)$$

where T_{out} is the useful output torque and T_{rot} is the torque required to supply rotational losses. Using the equivalent circuit of Figure 1 with $X = nX_b$, the applied fundamental frequency of the rms voltage required to drive this current into the motor is

$$\begin{aligned} V \angle \delta &= nE_b + I_r (R + jnX_b) \\ &= \sqrt{(nE_b + RI_r)^2 + (nX_b I_r)^2} \angle \tan^{-1} \left(\frac{nX_b I_r}{nE_b + RI_r} \right). \end{aligned} \quad (2)$$

The necessary amplitude modulation index to provide this voltage is

$$m_a = \frac{V}{\frac{V_{dc}}{2\sqrt{2}}} = \frac{2\sqrt{2}\sqrt{(nE_b + RI_r)^2 + (nX_b I_r)^2}}{V_{dc}}, \quad (3)$$

while the lead angle is given by

$$\delta = \tan^{-1} \left(\frac{nX_b I_r}{nE_b + RI_r} \right). \quad (4)$$

It is revealing that the amplitude modulation index and the lead angle depend on speed and not on the load.

Assuming full over-modulation, the constant torque control region ends at the “true base speed,” n_{bt} , which causes the amplitude modulation index to be equal to $\frac{4}{\pi}$; consequently, the true base speed is implicitly defined using Eq. (3) as

$$\frac{4}{\pi} = \frac{2\sqrt{2}\sqrt{(n_{bt}E_b + RI_r)^2 + (n_{bt}X_b I_r)^2}}{V_{dc}}, \quad (5)$$

which leads to a quadratic equation whose solution is

$$n_{bt} = \frac{\sqrt{\frac{2V_{dc}^2}{\pi^2} (E_b^2 + X_b^2 I_r^2) - R^2 X_b^2 I_r^4 - E_b R I_r}}{(E_b^2 + X_b^2 I_r^2)} \quad (6)$$

Constant power mode is above the true base speed. The torque producing component of current, which is in phase with the back-emf, required to sustain speed and load is given by

$$I_r = \frac{P}{3nE_b} = \frac{P_{out} + P_{rot}(n)}{3nE_b} \quad (7)$$

where P is the total required power, P_{out} is the useful shaft output power, P_{rot} and is the power that must be supplied to compensate for rotational losses. Because the applied voltage is maximum in this mode,

$$m_a = \frac{4}{\pi} \quad (8)$$

while the appropriate inverter lead angle required to achieve power, P , is

$$\delta = \theta_z - \cos^{-1} \left(\frac{\frac{ZP}{3} + (nE_b)^2 \cos \theta_z}{nE_b V_{max}} \right) \quad (9)$$

where

$$\begin{aligned} V_{max} &= \frac{\sqrt{2}V_{dc}}{\pi} \\ Z &= \sqrt{R^2 + (nX_b)^2} \quad (10) \\ \theta_z &= \tan^{-1} \left(\frac{nX_b}{R} \right) \end{aligned}$$

Although the lead angle of Eq. (9) assures that the required power is developed, it does not guarantee that the rms motor current is within rating unless the inductance is L_∞ or greater. Only having motor phase inductance greater than L_∞ will guarantee current lower than rated motor current [2].

Equation (9) is derived from

$$I = \frac{V \angle \delta - E \angle 0}{R + jnX_b} = \frac{V \angle \delta - E \angle 0}{Z \angle \theta_z} = \frac{V \angle (\delta - \theta_z) - nE_b \angle (-\theta_z)}{Z} \quad (11)$$

and the equation for total per-phase power that the motor must provide,

$$\frac{P}{3} = \text{Re}(\tilde{E}\tilde{I}^*) = \text{Re}\left(\frac{nE_b V \angle(\theta_z - \delta)}{Z} - \frac{(nE_b)^2 \angle\theta_z}{Z}\right) = \frac{nE_b V \cos(\theta_z - \delta)}{Z} - \frac{(nE_b)^2 \cos\theta_z}{Z}, \quad (12)$$

which, with $V = V_{max}$, leads directly to Eq. (9).

Figure 2 is a schematic of the algorithm for simulating a vehicle's performance when it is controlled by ORNL's model-based control scheme. It assumes that the motor parameters, which include inductance, resistance, and back-emf are constant; it also assumes that the expression for losses, which is proportional to the square of the rotational frequency, is known. When this control is used for laboratory testing the PWM/inverter block is replaced by gate drives and inverter switches, the Motor Model block is replaced by the motor itself, and the Vehicle Dynamics block is replaced by the dynamometer with its torque absorption capability and position and speed sensors. The only remaining change when this control is used in an HEV on the road is that the Vehicle Dynamics block is replaced by the vehicle itself.

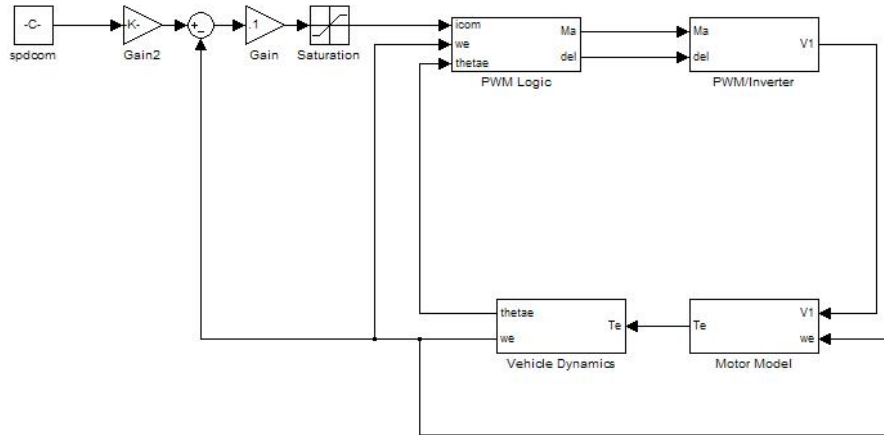


Figure 2. Simulation of vehicle performance using ORNL's sensorless control.

Control of the vehicle's performance in the simulator is straightforward. The operator supplies a request for a change in speed with the speed command, $spdcom$, to which a gain is applied so that the mechanical speed matches the electrical speed, ω_e . The electrical speed is compared with the actual speed of the vehicle to determine the speed correction. A gain of 0.1 is applied to the speed correction to provide a linear command current, i_{com} , which is not allowed to exceed the rated current.

Below true base speed, whose expression is presented in Eq. (6), the modulation coefficient, m_a , is given by Eq. (3) and the angle, δ , by which the PWM voltage leads the back-emf, is given by Eq. (4) in terms of speed and current, or by Eq. (9) with V_{max} replaced by V in terms of speed and power. Equation (2) is the expression for the PWM voltage, $V1$.

Above true base speed the modulation index is $4/\pi$ from Eq. (8); and the inverter lead angle, δ , required to achieve power, P , is given by Eq. (9). The PWM voltage, $V1$, has its maximum value, $V_{max} = \sqrt{2}V_{dc}/\pi$, from full over-modulation.

The PWM voltage and the rotational frequency determine the torque, Te , in Figure 2. In the Motor Model block, the user may alternately specify the power, which is related to the torque by the equation, $P = T \omega_e$. In the simulation, the Vehicle Dynamics block applies the torque determined by Eq. (1) to calculate the new value of ω_e and keeps up with the reference back-emf angle to which the PWM voltage lead is applied.

Test Application of ORNL's Low-Cost Algorithm

The test setup and measured results have been reported in ORNL/TM-2007/007, *Control of Surface Mounted Permanent Magnet Motors with Special Application to Motors with Fractional-slot Concentrated Windings*, issued in June 2007. Some of the results follow.

Parameters of the 6-kW FSCW SPM motor are included in Table 1. The line-neutral back-emf voltage constant, K_v , is the slope of the no-load rms back-emf averaged over the three phases and plotted against motor speed.

Table 1. Parameters of the 6-kW FSCW SPM motor

Parameter	Rated or measured values
Number of poles	30
Base speed	900 rpm
Top speed	4000 during testing (6000 rpm)
CPSR requirement	6.667:1
Back-emf magnitude at base speed, E_b (rms volts per phase)	49.45 @ 900 rpm
Voltage constant, K_v (rms volts per elec. rad/s)	0.03497
Rated power	6 kW
Rated torque	63.66 Nm
Rated rms current	40.44 A
Resistance per phase	76 m Ω
Inductance per phase	1.3 mH

Base speed is the highest speed at which rated torque is required. True base speed is the highest speed at which rated torque can be developed. The true base speed will be the same as base speed when the dc supply voltage is selected as the minimum value that permits rated torque to be developed at the base speed and is given by

$$V_{dc-\min} = \frac{\pi}{\sqrt{2}} \sqrt{E_b^2 + (X_b I_R)^2} . \quad (13)$$

This expression assumes that the PWM control will be in full over-modulation when developing rated torque at base speed. Equation (13) ensures that sufficient dc supply voltage is provided so that at base speed the driving voltage is sufficient to overcome the back-emf voltage, E_b , and the voltage drop across the internal impedance of the motor, $X_b I_R$, as it supplies rated current to the windings.

Figure 3 shows measured losses for different load conditions. Because both dc supply voltages, 250 and 300 V_{dc} , used during testing exceed the full over-modulated value from Eq. (13), which was $V_{dc-\min} = 202.15 V_{dc}$, true base speed, which exceeds the actual base speed of 900 rpm, is given by

$$n_{bt} = \frac{V_{dc}}{V_{dc-\min}} \cdot n_b . \quad (14)$$

True base speed is 1113 rpm for a supply voltage of 250 V_{dc} and 1335 rpm for 300 V_{dc} . Above base speed the motor operates in field weakening mode [3]. Figure 3 shows that losses below base speed exceed no-load losses and increase as the load increases. This reflects Joule heat losses in the copper, which increase as the square of the current.

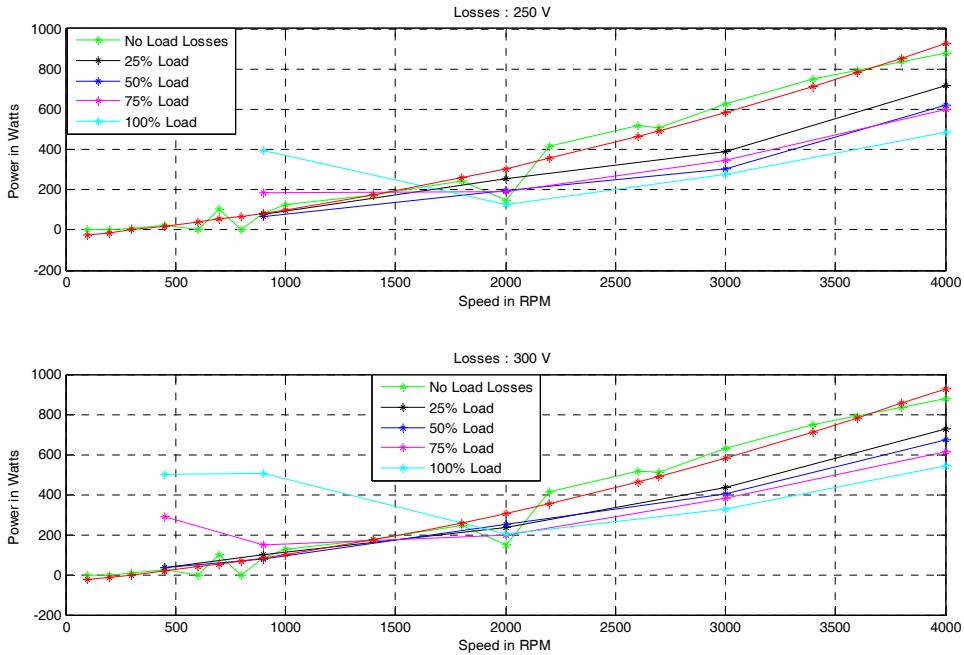


Figure 3. Measured motor losses.

Of greatest interest is the overall drive efficiency, which is compared in Figure 4 for 250 and 300 V_{dc} . The solid color surface and the white surface correspond to the 250- V_{dc} and the 300- V_{dc} supply voltage, respectively. The overall drive efficiency is slightly better at the 250- V_{dc} supply voltage.

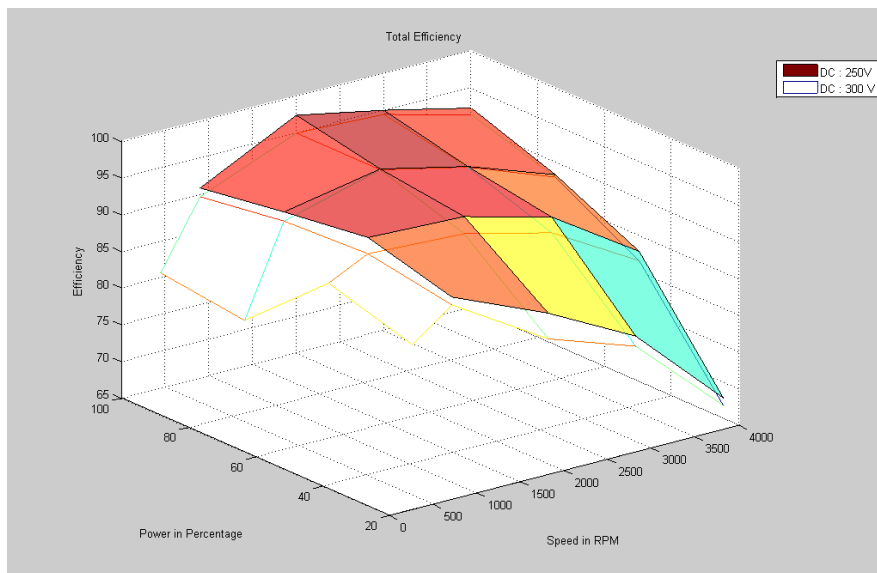


Figure 4. Efficiency comparison at supply voltages of 250 and 300 V_{dc} .

UWM's Maximum Motor Efficiency Algorithm

SPM synchronous motors using fractional-slot concentrated windings are being studied as candidates for high-performance traction drives for automotive propulsion systems. Analysis and testing have shown that they can achieve wide CPSR ratios [4,5]. Additional studies have shown that this type of machine can achieve very low cogging torque amplitude as well as a significant increase in power density [6–8] when compared to SPM machines with a distributed winding pattern. Increased efficiency has already been achieved for SPM motors with the concentrated winding pattern by suppressing eddy-current losses in the magnets [9–11]; additional increases may be achieved by minimizing iron losses in the rotor and stator cores.

Considerable attention has traditionally been devoted to maximizing the full-load efficiency of traction motors at their rated operating points and along their maximum-power vs speed envelopes for higher speeds [12,13]. For example, operating control approaches have sought to maximize the full-load efficiency of PMSMs, including the use of negative d-axis stator current to reduce the core losses [14,15].

However, another important performance specification for electric traction applications is the machine's efficiency at partial loads. Partial-load efficiency is particularly important if the target traction application exercises long periods of cruising operation at light loads that are significantly lower than the maximum drive capabilities. While the design of the machine itself is important, investigation has shown that this is a case where the choice of the control algorithm plays a critical role in determining the maximum partial-load efficiency that the machine actually achieves in the traction drive system.

Extended partial load operation takes on even greater significance for FSCW SPM machine designs because maximizing the torque/power density of this class of SPM motor leads to machine designs with a high number of poles. The subharmonics and harmonics and the high number of poles introduced by the concentrated windings can easily result in high stator core losses. These losses can be directly reduced by reducing the magnetic flux in the core, which is the goal of this algorithm.

Report ORNL/TM-2007/048, which is the ORNL issue of the *Final Report on Control Algorithm to Improve the Partial-Load Efficiency of Surface PM Machines with Fractional-slot Concentrated Windings* by T. B. Reddy and T. M. Jahns, discusses the modified vector control algorithm for an FSCW SPM machine that has been developed to maximize the motor's partial-load efficiency over a wide range of operating conditions. Two algorithms are discussed, one for maximum torque per amp and one for maximum torque per volt.

The first part of the report presents a 55-kW (peak) machine design, SPM1, to demonstrate the proposed control technique using closed form [16] as well as finite element analysis. Their calculations show that the maximum torque per amp algorithm is significantly better for minimizing the total machine losses at low speeds where the iron losses tend to be the lowest, but the maximum torque per volt algorithm demonstrates its region of excellence at higher speeds above 2000 rpm where iron losses are much higher. Unfortunately, their calculations also show that neither extreme algorithm is capable of achieving the 93% efficiency target. In between these two extremes, however, are an infinite number of alternative formulations. This research was launched to determine whether there might be another combination of I_q , which determines the resulting torque, and I_d , which adjusts the flux level in the core, that would lead to higher machine efficiency values.

Results were positive. At 2000 rpm (10,000 is maximum speed) and 20% of rated torque, the predicted efficiency for $I_d = 0$ was 86.5% and for $I_d = -140$ was 88.5%. Between the two extremes the partial-load motor efficiency peaked at a value very close to 93%, showing that choosing the optimum combination of I_d and I_q can significantly increase the partial-load efficiency.

In the second part of their report, they calculate the performance of the 6-kW FSCW SPM motor, SPM2, using the new algorithm. At 6000 rpm (6000 is maximum speed), the achievable efficiency increase is 5.5%, but at 1800 rpm it is only 2.2%. While the increase is not as large as the predicted efficiency increases for the SPM1 machine, it does indicate that the partial-load efficiency algorithm can have beneficial impact even on the SPM2 machine.

Conclusions

ORNL's test evaluation of the low-cost algorithm:

- The ORNL control system does not require any type of current feedback, although it needs accurate information about dc voltage, motor speed, and rotor position, which can be obtained from the same speed feedback sensor.
- Even though testing with the ORNL algorithm was carried out at 9-kHz PWM switching frequency, when the modulation index approached 1, the PWM output became a little bit unstable. Since IO cards are FPGA based, sine triangle PWM can be implemented in the card itself. This will free a lot of CPU time, and also PWM outputs will be more stable and reliable.
- For the ORNL control, the speed at which minimum current, n_{min} , occurs depends linearly on developed power and inversely on the maximum fundamental inverter voltage. The unique speed, n_{min} , varies with the voltage leaving room for optimization. If a motor spends a substantial amount of time at a certain speed, such as 60 mph, it could be desirable to choose a dc supply voltage that causes the minimum current at half speed. This would involve using a dc supply larger than the minimum and using control to restrain the torque envelope.
- Characteristic motor current, which permits operation at high CPSR, depends solely on machine parameters E_b , Ω_b , and L and is independent of motor load and dc supply voltage. This lowers its efficiency at partial load conditions at higher speeds. Providing voltage higher than necessary to support rated torque at base speed cannot reduce the current at high speed.
- It is advantageous to have the inductance higher than "optimal" because it enables the motor to develop the required power with lower current and attendant efficiency increase.
- Control of the voltage lead angle at high speeds allows a PMSM to operate at constant power, but it does not assure operation within rated current. Inductance is the critical factor that assures operation within rated current.

UWM's analysis of the partial-load efficiency algorithm.

- The partial-load efficiency algorithm is designed to improve the operating efficiency of SPM motors under partial-load operating conditions by using negative d-axis current to reduce the magnetic flux amplitude in the machine stator and rotor iron, thereby reducing the motor's iron losses.
- Based on analytical results, the partial-load efficiency algorithm is capable of improving the baseline machine efficiency using maximum torque per amp control by 5% or more in some SPM machines operating in the vicinity of the corner point speed.
- All SPM machines will not be good candidates to use this partial-load algorithm. The best candidates are expected to be SPM machines that have been designed to achieve high power densities, resulting in high magnetic flux densities in the motor stator and rotor iron, which significantly increase the iron losses during maximum torque per amp control.

Publications

N. Patil, J. S. Lawler, and J. W. McKeever, *Control of Surface Mounted Permanent Magnet Motors with Special Application to Motors with Fractional-Slot Concentrated Windings*, ORNL/TM-2007/007, Oak Ridge National Laboratory, June 2007.

P. B. Reddy and T. M. Jahns, *Final Report on Control Algorithm to Improve the Partial-Load Efficiency of Surface PM Machines with Fractional-Slot Concentrated Windings*, ORNL/TM-2007/048, Oak Ridge National Laboratory, April 2007.

Patents

None.

References

1. J. S. Lawler, *Control of Surface Mounted Permanent Magnet Motors with Special Application to Fractional-slot Motors with Concentrated Windings*, ORNL/TM-2005-184, Oak Ridge National Laboratory, September 2005.
2. J. S. Lawler, J. M. Bailey, J. W. McKeever, and J. Pinto, "Extending the constant power speed range of the brushless dc motor through dual mode inverter control," pp. 783–793 in *IEEE Trans. Power Electron.* **19**(3) (May 2004).
3. J. S. Lawler, J. M. Bailey, J. W. McKeever, and J. Pinto, "Limitations of the CPA method for constant power operation of the brushless dc motor," pp. 174–180 in *Proc. IEEE Southeast Conference, April 2002*.
4. M. EL-Refaie and T. M. Jahns, "Optimal flux weakening in surface PM machines using concentrated windings," *IEEE Trans. Ind. Appl.* **41**, 790–800 (May–June 2005).
5. M. EL-Refaie, T. M. Jahns, P. J. McCleer, and J. W. McKeever, "Experimental verification of optimal flux weakening in surface PM machines using concentrated windings," *IEEE Trans. Ind. Appl.* **42**, 443–453 (March–April 2006).
6. J. Cros and P. Viarouge, "Syntheses of high performance PM motors with concentrated windings," *IEEE Trans. Energy Conver.* **17**, 248–253 (June 2002).
7. F. Magnussen and C. Sadarangani, "Winding factors and joule losses of permanent magnet machines with concentrated windings," *Proc. of 2003 IEEE Intl. Elec. Mach. and Drives Conference (IEMDC'03), Madison, WI*, **1**, 333–339 (June 2003).
8. Z. Q. Zhu and D. Howe, "Influence of design parameters on cogging torque in permanent magnet machines," *IEEE Trans. Energy Conversion* **15**, 407–412 (December 2000).
9. K. Atallah, D. Howe, P. H. Mellor, and D. A. Stone, "Rotor loss in permanent-magnet brushless ac machines," *IEEE Trans. Ind. Appl.* **36**, 1612–1618 (November–December 2000).
10. D. Ishak, Z. Q. Zhu, and D. Howe, "Analytical prediction of rotor eddy current losses in permanent magnet brushless machines with all teeth and alternate teeth windings, Part I: Polar co-ordinate model," *Proc. 7th Int. Conf. on Electr. Machines and Systems (ICEMS'04)*, CD-ROM, 2004.
11. D. Ishak, Z. Q. Zhu, and D. Howe, "Analytical prediction of rotor eddy current losses in permanent magnet brushless machines with all teeth and alternate teeth windings, Part II: Rectangular co-ordinate model," *Proc. 7th Int. Conf. on Electr. Machines and Systems (IDEMS'04)*, CD-ROM, 2004.
12. W. Soong and T. J. E. Miller, "Field weakening performance of brushless synchronous ac motor drives," *IEE Prod. Electr. Power Appl.* **141**, 331–340 (November 1994).
13. Z. Q. Zhu, Y. S. Chen, and D. Howe, "Iron loss in permanent-magnet brushless ac machines under maximum torque per ampere and flux weakening control," *IEEE Trans. Magnetism* **38**, 3285–3287 (September 2002).
14. S. Morimoto, Y. Tong, Y. Takeda, and T. Hirasa, "Loss minimization control of permanent magnet synchronous motor drives," *IEEE Trans. Ind. Electr.* **41**, 511–517 (October 1994).
15. Cavallaro, A. O. Di Tommaso, A. Racit, G. R. Galluzzo, and M. Trapanese, "Efficiency enhancement of permanent-magnet synchronous motor drives by online loss minimization approaches," *IEEE Trans. Ind. Electr.* **52**, 1153–1160 (August 2005).
16. A. M. EL-Refaie, T. M. Jahns, and D. W. Novotny, "Analysis of surface permanent magnet machines equipped with concentrated windings," *IEEE Trans. Energy Conversion* **21**, 34–43 (March 2005).

3.5 Development of Improved Powder for Bonded Permanent Magnets

Principal Investigator: Iver E. Anderson
Materials and Engineering Physics Program
Ames Laboratory, Iowa State University
Ames, IA 50011

Voice: 515- 294-9791; Fax: (515) 294-8727; E-mail: andersoni@ameslab.gov

DOE Technology Development Manager: Susan A. Rogers

Voice: 202-586-8997; Fax: 202-586-1600; E-mail: Susan.Rogers@ee.doe.gov

ORNL Program Manager: Mitch Olszewski

Voice: 865-946-1350; Fax: 865-946-1262; E-mail: olszewskim@ornl.gov

Objectives

- Increase the maximum operating temperature (from about 125 to 200C) and environmental stability of permanent magnet (PM) materials to enable advanced electric drive motors with improved operating characteristics and lifetime.
- Reduce the overall manufacturing cost of traction motors and enable a new generation of machine designs by developing magnets that can be molded efficiently into net-shapes or in-place as motor component assemblies.

Approach

- Develop surface passivation methods for enhanced oxidation resistance of MRE-Fe-B isotropic magnet alloy particulate by completing fabrication and testing of up-scaled fluidized-bed batch processing and continuing development of in situ passivation during the gas atomization process.
- Continue nano-crystalline isotropic magnet alloy improvements by evaluating potential for magnetic property gains in MRE-Fe-B nano-composite magnets in melt spun ribbon and by designing additions to promote direct crystallization of hard magnetic (2-14-1) phase during gas atomization.
- Examine isotropic bonded magnet fabrication capabilities by determining the practical upper range of active loading for flake and spherical particulate in polymer without significant modification of the size distributions and complete characterization (with partners) of bonded magnets made from coated and uncoated flake particulate vs. benchmark commercial material, using environmental and magnetic tests.
- Seek industrial partnerships to compare of experimental isotropic bonded isotropic magnets against equivalent commercial magnets in motor trials at elevated temperatures and identify and communicate the choice of an expert to provide technological and commercial validation of the current directions of the experimental magnet material development.

Major Accomplishments

- Demonstrated a 70% decrease in the oxidation rate at 300C of coated flake particulate (MQP-11HTP) compared to uncoated particulate of the same magnet alloy (WT-096) with thermal-gravimetric analysis (TGA), showing greatly enhanced stability at the PPS polymer compounding temperature planned for bonded magnet processing.

- Verified by X-ray photoelectron spectroscopy (XPS) an improved (ambient air) oxidation resistance trend for in situ fluorination coating of fine spherical magnet alloy powder over a series of gas atomization experiments that spanned the transition from He to Ar gas atomization processing.
- Achieved significant improvement of the room temperature maximum magnetic energy product (9.1 to 10.1 MGOe) in fine spherical powder of the MRE-(Fe,Co)-B-ZrC magnet alloy with in situ coating and a "cross-over" temperature of 75C, i.e., has magnetic strength superior to commercial spherical powder from 75-200C.
- Determined experimentally that the enhanced magnetic exchange-coupled concept does not promote an increased magnetic energy product in a series of simplified MRE-(Fe,Co)-B magnet alloys over a selected range of compositions and processing parameters, discouraging this alloy design direction from further consideration.
- Compression molded a partial set of bonded magnet samples from coated magnet flake particulate (MQP-11HTP) from an enhanced Ames magnet alloy design (WT-096) for the second stage of industrial environmental testing.
- Brought a polymer compounding mixer into operation after sitting idle for about 7 years, where equipment operation software was verified and various sensor and control problems were fixed, along with polymer flushing of the "frozen" and contaminated twin-screw extrusion barrel. Note: unavoidable delays from a lack of parts and information on this early unit (circa 1988) setback the planned examination of the upper limit of loading in polymer for flake and fine spherical particulate.
- Identified and participated in assembling a proposal entitled "Advanced Electric Traction System" to form an industrial partnership (in a CRADA with GM and AMT) that successfully competed in a recent RFP issued by the PEEM office, which will provide an industrial test of the isotropic (nanocrystalline) bonded magnet technology (with level 1&2 benefits) that was developed in this project for such IPM motors.
- Selected an industry expert to conduct an independent analysis of the total manufacturing cost for an advanced electric drive motor with either sintered or bonded permanent magnets in appropriately designed interior PM rotor electric machines.

Future Directions

- To maximize the potential capabilities of high temperature isotropic bonded magnets for fabrication by injection molding, the development of fine spherical magnetic particles will continue to be pursued. This objective requires further MRE-Fe-B alloy development for the control of both nucleation and growth of nano-crystalline grains during rapid solidification of the gas atomized powders.
- To make very large gains in saturation and remnant magnetizations, as well as the energy product of bonded magnets without sacrificing high temperature performance, development of an anisotropic (aligned cellular or single crystal) magnetic microstructure will be attempted in particulate of MRE-Fe-B magnet alloys.
- To improve their durability and processing characteristics, further improvement of the fluoride protective coating process will be pursued in both batch mode for melt spun flake and with in situ and batch mode for gas atomized spherical powders of the MRE-Fe-B magnet alloys.
- To explore the prospects for sintered (near-full density) aligned permanent magnets from the MRE-Fe-B alloys, an effort will be initiated to develop an extrinsic alloy additive to enable liquid phase sintering of an aligned magnetic particle assembly without undesirable metallurgical reactions.

- To provide technological and commercial validation of the current directions of the experimental magnet material development, the selected expert will be contracted to conduct a detailed analysis of the total manufacturing cost for a high torque, high speed drive motor system with either sintered or bonded permanent magnets in appropriately designed interior PM rotor electric machines.

Technical Discussion

Executive Summary

To meet performance and cost goals for advanced electric drive motors, it is essential to improve the alloy design and processing of permanent magnet (PM) powders. This project is expected to develop the materials and processes needed to fabricate high performance, bonded permanent magnets (PM) that can be used for traction motors with an internal PM rotor design. It should be noted that the starting alloy cost will be about the same as current alloys, but the total magnet material used per motor could be less, if motor design is optimized for the intricate shapes and magnetization patterns possible with bonded magnets. The fully developed PM material must be suitable for elevated temperature (180-200°C) operation to minimize motor cooling needs, where the increased high temperature magnetic performance is more critical than room temperature magnetic properties. Such a magnetic alloy design for high temperature operation may be implemented at a first level of advantage with nano-crystalline isotropic flake particulate using conventional isotropic bonded magnet processing methods and a high temperature polymer. A second level of advantage may be realized if this high temperature magnet alloy flake particulate is protected with an oxidation resistant surface coating by a batch process that is being developed in this project. A third level of advantage may be realized for isotropic bonded magnets, if the high temperature magnet alloy can be translated successfully to a fine spherical isotropic powder production process based on inert gas atomization with capability for in situ protective powder coating. This third level of manufacturing advantage is derived from reduced molding pressures and enhanced performance and reliability for isotropic bonded magnets, through increased magnetic powder loading and reduced irreversible magnetic losses from oxidation and corrosion. A fourth (much higher) level of advantage may be achieved if nano-crystalline anisotropic fine particulate can be produced so that a bonded magnet (insert) molding process can be accompanied by the application of an external magnetization field sufficient for full alignment (and locking) of the particulate in the desired field pattern within the complex cavities of an advanced rotor. This fourth level of advantage comes from the possible 4X multiplication of the magnetic torque available from such anisotropic bonded magnets with a shaped field direction, compared to isotropic bonded magnets of the same loading. If the project is continued at least until the third level of advantage is achieved, the outcome is likely to be a significant reduction in the total manufacturing cost of PM traction motors, since injection or compression molding technology can be practiced with heavily loaded polymer compound in a net shape/assembly forming approach for mass production of internal PM rotors containing bonded magnets. In a novel blend of two magnet types, if a sintered aligned permanent magnets can be made from micron-sized single crystal particles of the high temperature magnet alloy and an extrinsic alloy phase for liquid phase sintering, an alternative fourth level of advantage may be achieved from a rotor insert alignment/compaction/sintering method that has been conceptualized. These advantages should all accelerate the widespread introduction of fuel-saving hybrids and could be claimed by the AEEP program as a clear beneficial outcome.

Introduction

Permanent magnets based on RE₂Fe₁₄B intermetallic compounds, with Nd₂Fe₁₄B as a prototype, have had a large technological impact because of their unsurpassed (theoretical) magnetic energy density. Over the past 20 years, extensive research has been performed to develop and improve the technological properties of these magnetic compounds. Commercially, two classes, aligned-sintered (microcrystalline) and isotropic nano-crystalline, Nd₂Fe₁₄B magnets have been successfully developed. It should be noted that aligned-sintered Nd₂Fe₁₄B magnets are used in current hybrid vehicle systems with interior PM motor designs that require high magnetic torque, but this magnet class and magnetic torque-dominated motor

design have been judged (by at least one of the OEM partners) to be impractical for very large scale mass production at reduced cost. Alternatively, the opportunity exists to use a new motor designs that utilize increased reluctance torque, and, as such, are well suited to the reduced magnetic flux available from bonded magnets. Because there is some uncertainty about the total manufacturing cost advantage for the new type of drive motor system from this revolutionary shift in magnet type and motor design, there is a need to perform an “industry expert” cost analysis of this situation. As an example, cost/magnetic flux unit of each type of magnet is only one of the many aspects of the actual motor manufacturing cost and, hence, this militates the performance of this task by an expert in both magnet processing and motor design.

To fully exploit this opportunity to switch to bonded magnets with great potential advantage for mass production, one primary focus of this project is to develop an improvement of the existing magnet alloy that will enhance the performance of advanced motors that need high temperature tolerance. Current $\text{Nd}_2\text{Fe}_{14}\text{B}$ magnet alloys exhibit excellent room temperature magnetic properties and they are well suited for applications with operating temperature at or below about 125C, due in part to their low Curie temperature of about 310C. The poor temperature stability of these magnets above 125C limits their current performance in existing motors and their potential application for advanced drive motor designs. The intrinsic properties of the Nd-dominated “2-14-1” phase dictate large negative values of the temperature coefficients for coercivity and remanence, although many approaches have been tried to improve high temperature properties of $\text{Nd}_2\text{Fe}_{14}\text{B}$ magnets. Consequently, it was necessary to find other compositions to improve the thermal stability of $\text{RE}_2\text{Fe}_{14}\text{B}$ magnets. We conducted a systematic study by melt spinning on magnetic properties of a series of isotropic nano-crystalline magnet alloys where a Y+Dy mixture replaces Nd or Pr as the primary RE constituent in $\text{MRE}_2\text{Fe}_{14}\text{B}$ ($\text{MRE}=\text{Y}+\text{Dy}+\text{Nd}$). Our results have shown that the Y+Dy based $\text{MRE}_2\text{Fe}_{14}\text{B}$ alloy can develop into isotropic magnets with superior magnetic properties above 115°C by a judicious combination of Y, Dy, and Nd, along with a minor Co substitution for Fe.

It should be noted that current $\text{Nd}_2\text{Fe}_{14}\text{B}$ (2-14-1) bonded magnets are produced from fragmented melt spun ribbon particulate with a flake morphology, and that the improved $\text{MRE}_2\text{Fe}_{14}\text{B}$ alloy could be used as a “first level” outcome to generate bonded magnets for experimental motor trials. In fact, this has been done recently within this project to help generate useful motor performance data to assess the benefits of the new alloy design. As stated above a second level of advantage could be exploited if the batch coating process is also practiced with flake particulate of the new alloy. However, the unmodified flake particulate morphology has been judged unsuitable for optimum injection molding characteristics (critical for mass production of motor components) due to its excessive viscosity when heavily loaded into a polymer matrix. This results in molding pressures that are too high for practical use, requiring the magnet particulate loading to be reduced, which places a reduced upper limit on magnetic strength of the finished magnet. To overcome this limitation, the second primary focus of this project is to translate the enhanced alloy design that is being optimized for melt spinning to work with an alternative rapid solidification process, high pressure gas atomization (HPGA). The beneficial result (third level of advantage) of HPGA is a fine spherical powder that is known to have ideal (lowest viscosity) behavior in an injection molding process and, therefore, low injection molding pressure for bonded magnets with increased magnetic strength. The challenge of translating the alloy design from melt spinning to HPGA lies in the differences in the heat transfer during solidification and the resulting microstructure patterns between the two processes, although their average quenching rates are similar. Our latest results show the promise of using an alloy addition to promote direct nucleation of the most desirable phase in the HPGA powder along with an in situ protective powder coating, as will be discussed.

Based on knowledge of the magnetic behavior of the 2-14-1 compound, it is likely that the ability to produce a fine particulate, where each particle is an anisotropic (highly aligned, cellular) nano-crystalline structure or an anisotropic (single crystal) micro-crystallite, can result in a very large gain (4X) in magnetic properties (fourth level of advantage). This advantage level can be realized if the ensemble of

particulate can be aligned in a polymer during net-shape forming (either outside or inside the rotor) to produce an anisotropic bonded magnet or can be aligned in a metallic (extrinsic) bonding matrix (outside or inside the rotor) to form a "fully dense" anisotropic, sintered magnet. These concepts can be pursued within the scope of the present project by focusing on the particulate production processes in an initial effort. There is a choice of using a solidification process or a solid-state annealing/comminution route for these concepts. Both will be explored in future efforts.

Approach

Surface passivation methods for enhanced oxidation resistance of MRE-Fe-B isotropic magnet alloy particulate continued in development by further improvement of the in situ method during the gas atomization process and by completing fabrication and testing of up-scaled fluidized-bed batch processing for both spherical powder and flake particulate. A fluorination (gas reaction) process was developed for in situ treatment during the high-pressure gas atomization process to reduce the hazard and oxidation losses that are typical for powders with high surface area of this type of RE alloy. This process built on the results of our post-atomization fluidized bed coating experiments and used the atomization spray chamber as a reaction vessel with the dispersed, high temperature particulate spray as a natural fluidized (turbulent) state. The reaction was stimulated by the downstream addition of an NF_3 -Ar gas mixture during He (and later Ar) atomization, where the downstream location was determined by process chamber temperature analysis and by consideration of the spray chamber flow patterns and dynamic thermal conditions. The powder surface film effects were investigated by bulk oxygen measurements on the powder, by air oxidation tests in a thermo-gravimetric analyzer (TGA), and by explosivity testing at an independent laboratory. Since the current hazard reduction measurement (to a "moderate" explosivity level) was confirmed, both the larger scale and research scale atomization systems can be employed to produce prototype spherical powder batches for experimental injection molding trials. Resulting surface film structure and composition also was characterized by x-ray photoelectron spectroscopy (XPS), by Auger electron spectroscopy, and by microstructural analysis for both spherical powder and flake particulate.

Efficient screening of magnet alloy design modifications was accomplished by melt spinning methods, primarily using parameters that simulate the quenching rates accessible during gas atomization, the desired spherical powder processing method. The alloy approach for MRE-Fe-B magnetic alloys (MRE = mixed rare earth, e.g., Y, Dy, Nd) was refined to increase the remanence and energy product at ambient temperatures for isotropic PM material while maintaining superior temperature coefficient values to 200°C. The magnetic properties of commercial spherical atomized powder and isotropic flake particulate were benchmarks. For gas atomized spherical powders the design target favored direct solidification to a nanocrystalline 2-14-1 phase, without annealing. An alloy additive of ZrC+Zr was developed to enhance the crystallization potency for 2-14-1 phase and was gas atomized successfully during this year. For melt spun ribbon, one type of nano-composite microstructure design direction was tried extensively, using BCC-Fe as the minority soft magnetic phase with the hard magnetic 2-14-1 phase in an attempt to boost the energy product over the full temperature range, while using a lower MRE content. Comprehensive characterization of closely related gas-atomized and melt-spun samples of a variety of promising MRE-Fe-B compositions continued as a strong emphasis in both as-solidified and annealed states. The initial magnetic characterization at both ambient and elevated temperatures was accompanied by x-ray diffraction and calorimetric characterization on all new samples. In addition, microstructural analysis with SEM and TEM added critical understanding about the product phase morphologies and spatial distributions that give rise to differences in as-solidified properties and in annealing response. Our overall goal remained exploration of the generality of MRE-Fe-B alloy rapid solidification behavior during gas atomization that minimizes glass formation and allows annealing to be avoided, because of the potential processing simplification advantage that could lead to reduced costs for bonded magnet production.

Extensive injection molding process trials also were intended for this project with recently re-installed compounding and injection molding equipment, in collaboration with an industrial partner, AMT. This

was the motivation for the efforts that were performed this year to bring the polymer compounding (Haake) mixer into operation after sitting idle for about 7 years. As part of these efforts, equipment operation software was verified and various sensor and control problems were fixed. Also, the "frozen" and contaminated twin-screw extrusion barrel was rectified by a polymer flushing procedure. If progress on the extruder mixer had not been delayed unavoidably by a lack of parts and information on this early unit (purchased in 1987 on a previous contract), the practical upper range of active loading for flake and spherical particulate in polymer would have been examined without significant modification of the size distributions. Scale-up of the gas atomization process also was intended for this project to enable injection molding trials with fine spherical powder, in comparison to flake particulate from the commercially prepared batch of our WT-096 alloy, termed MQI-1 IHTP. As will be discussed in the results, an alloy with a similar promise for fine spherical magnet powder was gas atomized this year and may work well for injection molding trials, if produced in sufficient quantity in the larger (5X capacity) Ames gas atomizer or, eventually, in an appropriate commercial system. It should be noted that the plans for injection molding trials have been removed from future work in this project, but will be a part of a companion project with an application focus that will start in FY2008.

Industrial partnerships were sought to compare experimental isotropic bonded isotropic magnets against equivalent commercial magnets in motor trials at elevated temperatures. This search was aided by the issuance of an request for proposals that included this type of work by EERE. Our existing resources and network of contacts also was utilized to select a qualified outside expert with significant experience and expertise both in electric motor design and testing and in permanent magnet (PM) manufacturing to be involved in a detailed cost analysis of the choice between bonded and sintered magnets for interior permanent magnet motors. The critical criteria for these recommendations will be a comparison to robust industrial manufacturing processes using both existing commercial magnets and the expected performance of experimental magnet material in conventional and experimental motor designs to characterize expected performance and temperature tolerance, measuring progress against accepted APEEM goals.

Results

Surface Passivation Methods

Significant advances in both the scale and the control, as well as the understanding of the fluidized bed coating process have been achieved. A major variable resulting in large batch-to-batch variations in the coating process was determined to be the oxidation of the ribbon in the initial heat up stage prior to the actual coating process. The oxidation was a result of absorbed gas on both the ribbon and chamber surfaces as well as minute quantities of oxygen in the Ar process gas. A Zr gettering furnace placed in the Ar supply line reduced the oxygen content of the Ar below detectable limits. The process was modified so that the absorbed gas was removed prior to heating by repeatedly pumping out the chamber and backfilling with the oxygen free Ar. Using these procedures, analysis of the process gases now shows systematic behavior as a function of reaction temperature and time. Runs at 170°C, 180°C, and 185°C have provided information on the reaction rate and time to completion as a function of the reaction temperature. It appears that the gas analysis may also provide a clear correlation to the coating thickness as a function of these parameters.

Verification of the quality and thickness of the coatings obtained in this new reaction chamber was performed by thermo-gravimetric analysis (TGA) on fluorinated flake and revealed that the formation of RE-type fluorides on the particle surfaces was capable of reducing the rate of oxidation up to 300°C by a factor of 3 (see Fig. 1). Based on the TGA results on fluorinated flake particulate, the most promising result (seen at 185°C) was chosen as the fluorination temperature to "mass-produce" fluorinated flake for bonded magnet fabrication in the up-scaled fluidized bed system. This fluorination parameter is believed to provide a sufficient and near-optimal fluoride surface coating on the magnet particulate in order to

prevent ambient and processing atmosphere oxidation from degrading magnetic properties. The initial “production” batch of (5) fluorinated compression molded bonded magnet samples was sent to Arnold Engineering for short term and long term irreversible flux loss testing. Each bonded magnet sample was prepared from a 30g batch of MQP-11-HTP flake (produced on contract by Magnequench International from Ames Lab alloy composition WT-096) that was mixed with polyphenylene sulfide (PPS) in a 60/40 vol.% loading ratio, respectively. The results from these samples, when completed by AMT, will be compared directly to the results from the set of bonded magnets that were previously prepared in the non-fluorinated condition and already tested accordingly by AMT.

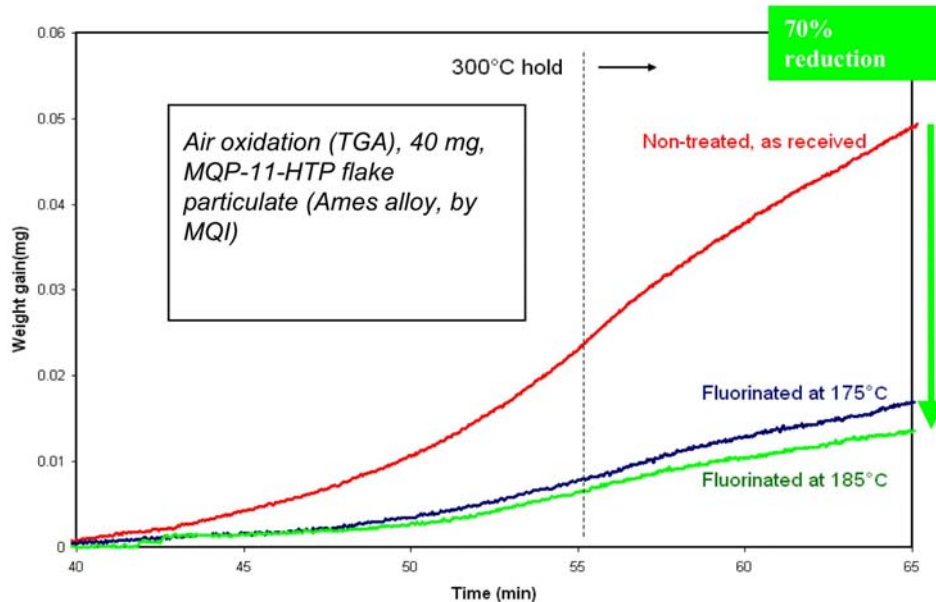


Figure 1. Summary of thermo-gravimetric results that compares uncoated and coated flake particulate of the WT-096 magnet alloy.

Work has continued on development of the in situ version of the protective fluoride coating that is stimulated by a reactive gas injection during the gas atomization process. This process has now been demonstrated for both He gas and Ar gas atomization processes for production of fine spherical powders of the MRE-Fe-B magnet alloys. Initial XPS measurements on the in situ fluorinated powders, GA-1-100 show a measurable level of fluorine on the powder surfaces in comparison to the oxygen concentration, while XPS and AES measurements on the most recent in situ fluorinated powders, GA-1-106 and GA-1-114, show a dominant fluorine peak and a significantly reduced bulk oxygen content. These results support the capability of the novel in situ surface passivation approach to retain useful magnetic material during further processing. A comparison with the results from last year also shows clear progress in measurement and control of the coating process.

Magnet Alloy Improvements

Nanocomposites: The current class of “nanocomposite” permanent magnets with enhanced exchange coupling are typically composed of $\text{Nd}_2\text{Fe}_{14}\text{B}$ and a small amount of either $\alpha\text{-Fe}$ or Fe_3B and exhibit not only better resistance to corrosion and lower cost due to lower rare earth content, but also a very high ratio of remanence to saturation magnetization, which predicts a high maximum energy product. The nanocomposite approach was investigated as a possible means of enhancing the performance of our high temperature alloys, where the alloy development was carried out using melt spinning. Based on the model of Nd-based nanocomposite alloys, a pair of YDy-based nanocomposite alloys was developed.

Studies of MRE-Fe-B alloys, including $[\text{Nd}_{0.45}(\text{Y}_2\text{Dy}_1)_{1/3*0.55}]_9\text{Fe}_{86}\text{B}_5$ (MRE₂Fe₁₄B/ α -Fe) and $[\text{Nd}_{0.45}(\text{Y}_2\text{Dy}_1)_{1/3*0.55}]_9\text{Fe}_{79}\text{B}_{12}$ (MRE₂Fe₁₄B/ Fe₃B), WT153 and WT155, respectively, indicated that the Fe-enriched (α -Fe) nanocomposites were preferable. These MRE₂Fe₁₄B/ α -Fe nanocomposite materials exhibited high saturation and remanence, but low coercivity. In order to control the microstructure, TiC additions were studied in these modified YDy-based nanocomposite compositions, including WT165 $\{[\text{Nd}_{0.45}(\text{Y}_2\text{Dy}_1)_{1/3*0.55}]_{10.5}\text{Fe}_{84}\text{B}_{5.6}\}_{1-2x}+\text{Ti}_x\text{C}_x$ and WT166 $\{[\text{Nd}_{0.45}(\text{Y}_2\text{Dy}_1)_{1/3*0.55}]_{11}\text{Fe}_{83.4}\text{B}_{5.6}\}_{1-2x}+\text{Ti}_x\text{C}_x$, $x=0.02$). The WT165 and WT166 ribbons were melt-spun at 25 m/s to generate a conventional overquenched (amorphous) product phase and annealed at 700 and 750°C for 15 min., respectively (see Fig.2), which are conventional annealing treatments for devitrification of a nanocomposite magnet microstructure.

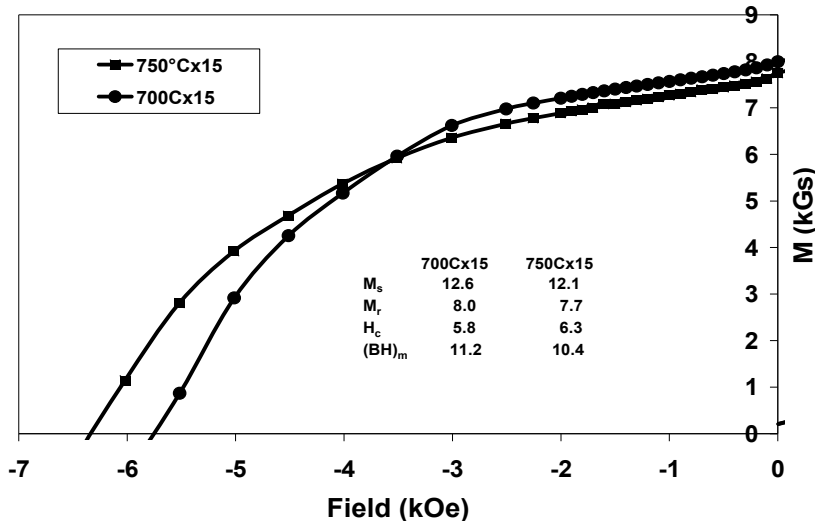


Figure 2: Second quadrant demagnetization loops for a nanocomposite magnet composition, showing the effect of annealing temperature on the permanent magnet properties.

It was determined that the YDy based alloys were more sensitive to annealing temperature than the typical Nd-based ones, i.e., a higher annealing temperature resulted in a slightly higher coercivity. In addition, as predicted, an increased MRE content raised the coercivity at the expense of reduced saturation magnetization. The highest $(BH)_{\max}$ of 11.2 MGOe was obtained in the sample annealed at 700°C for 15 minutes. However, the $(BH)_{\max}$ was still lower than the optimum value (12.5 MGOe) of our previous alloys with a single phase (2:14:1) structure.

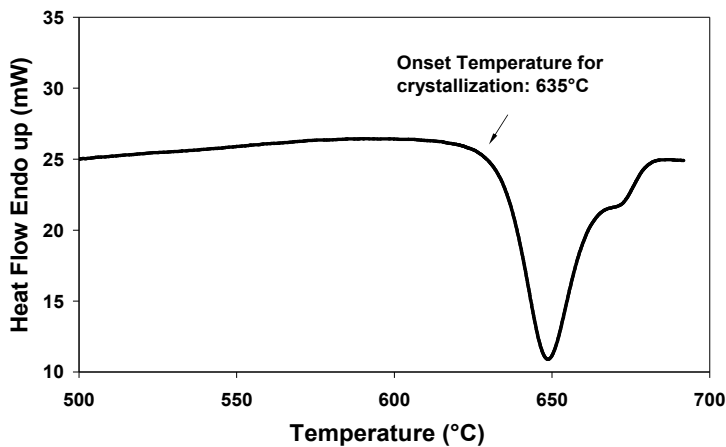
In a further effort to improve the coercivity of WT165 and WT166, studies of Pr substitution for Nd (WT165) and Gd substitution for Y (WT166) were also conducted. The Pr substitution for Nd did not yield the anticipated increase in coercivity. Gd substitution for Y did enhance coercivity, however the associated decrease in saturation magnetization resulted in insignificant changes in $(BH)_{\max}$. Attempts to increase the coercivity by changing the ratio of Y:Dy from 2:1 to 1:1, which increases the anisotropy, did not produce the expected increase in coercivity, but did decrease the remanence. Thus, while the nanocomposite alloys WT165 and WT166 exhibited higher saturation magnetization and, therefore, have the potential to exhibit higher $(BH)_{\max}$ magnets, a means to increase the coercivity of these materials was still elusive in order to realize that potential.

Since composition changes in the nanocomposite alloys were unsuccessful in obtaining high coercivities, a study the microstructure of these alloys was performed to discover the extrinsic factors controlling coercivity. These examinations were conducted with the new Tecnai G² F20 STEM to understand the crystallization process that could control coercivity on samples with varying composition and processing

conditions. Ribbon samples of WT165 $\{[\text{Nd}_{0.45}(\text{Y}_2\text{Dy}_1)_{1/3*0.55}]_{10.5}\text{Fe}_{84}\text{B}_{5.5}\}_{1-2x} + \text{Ti}_x\text{C}_x$, $x=0.02$ were melt-spun at 25 m/s and annealed at 750°C for 15 min. for this study. TEM bright-field images exhibited typical microstructures at the inner part of the ribbon samples. The study clearly indicated that the alloy was mostly amorphous after melt spinning at 25 m/s. This was true even though the alloy had a lower B content, 5.5 at.%. After annealing at 750°C for 15 min, the alloy was fully crystallized with a grain size of about 70 nm for the 2-14-1 permanent magnetic phase. Observations with the STEM in a HAADF mode, along with EDS detection, indicated that TiC particles formed along grain boundaries and triple junctions with a grain size of 5 nm. Also, α -Fe was found in the alloy in the HAADF image. Some of the α -Fe grains also were observed in the conventional TEM image with a grain size about 30 nm.

Also, SQUID magnetometer studies of samples that were melt-spun in He and Ar atmospheres were performed to investigate the effect of ambient process cooling on the microstructure and magnetic properties of the ribbons. For the nanocomposite $\text{MRE}_2\text{Fe}_{14}\text{B}/\alpha\text{-Fe}$ sample, WT165, an Ar gas atmosphere increased the coercivity of the as-spun sample slightly above the results using He. On the other hand, for an $\text{MRE}_2\text{Fe}_{14}\text{B}$ alloy with TiC addition, WT096, that was designed for high quench rates, using He or Ar produced minimal change in the coercivity. Alternatively, for an $\text{MRE}_2\text{Fe}_{14}\text{B}$ alloy with Zr substitution and ZrC addition, WT147, that was designed for low quench rates, an Ar gas atmosphere resulted in samples that exhibited a fine and uniform microstructure and enhanced magnetic properties, including coercivity. These studies showed that the role of the quench gas is highly dependent on the alloy design, where the $\text{MRE}_2\text{Fe}_{14}\text{B}/\alpha\text{-Fe}$ nanocomposite alloys are more dependent on quench gas than near-stoichiometric $\text{MRE}_2\text{Fe}_{14}\text{B}$ alloys designed for high quench rates, but similar in sensitivity to near-stoichiometric $\text{MRE}_2\text{Fe}_{14}\text{B}$ alloys designed for low quench rates.

In order to identify more precisely the annealing conditions required to promote an optimal microstructure and thus develop higher quality magnetic properties when crystallizing the amorphous ribbons, detailed studies of ribbon devitrification were performed using differential scanning calorimetry (DSC). In these studies, a Fe rich YDy-based alloy (WT165 $\{[\text{Nd}_{0.45}(\text{Y}_2\text{Dy}_1)_{1/3*0.55}]_{10.5}\text{Fe}_{84}\text{B}_{5.6}\}_{1-2x} + \text{Ti}_x\text{C}_x$, $x=0.02$) was melt spun at a wheel speed of 25 m/s to generate a fully amorphous product phase. A DSC measurement on heating of the ribbon (see Fig. 3a) identified the onset temperature of crystallization for the amorphous phase as 635°C. Isothermal DSC measurement showed that in isothermal heat treatments at 615°C, 20°C lower than the apparent crystallization onset temperature by the standard measurement, crystallization was complete in 6 minutes (see Fig. 3b). To study the crystallization pathway, ribbon samples were isothermally annealed in the DSC for 0, 1, 2, and 6 minutes at 615°C, and then quenched. Afterwards, the magnetic properties and microstructure of these samples were studied (see Fig. 3c).



a)

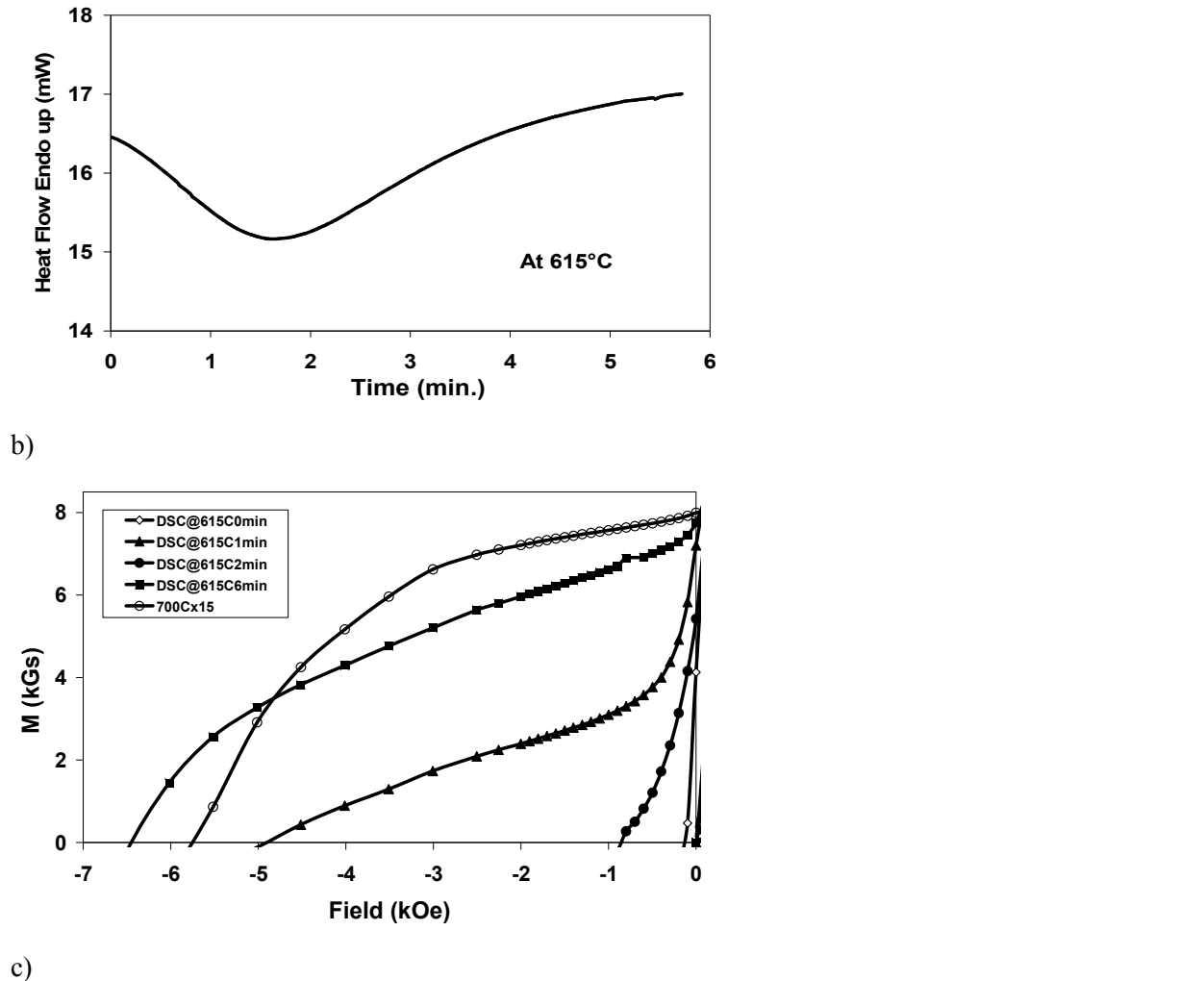


Figure 3. DSC and magnetization measurements of a $\text{MRE}_2\text{Fe}_{14}\text{B}/\alpha\text{-Fe}$ nanocomposite magnet alloy (WT165 $\{[\text{Nd}_{0.45}(\text{Y}_2\text{Dy}_1)_{1/3*0.55}]_{10.5}\text{Fe}_{84}\text{B}_{5.6}\}_{1-2x}+\text{Ti}_x\text{C}_x$, $x=0.02$) showing (a) crystallization enthalpy as a function of temperature on heating, (b) crystallization enthalpy as a function of time during an isothermal anneal at 615 °C, and (c) second quadrant magnetization as a function of annealing time.

The hysteresis loops for ribbons samples with different annealing time at 615°C were characterized to reveal hard and soft magnetic fractions. The hard magnet phase fraction that exhibited good coercivity increased as a function of annealing time, however, even after 6 minutes a "shoulder" remained, indicating retained soft magnetic phase. This shoulder was removed by annealing at 700°C for 15 minutes. This, however, resulted in a decrease in coercivity. A four hour anneal at 615°C produced magnetic properties close to those of the ribbon annealed at 700°C for 15 min. with slightly higher coercivity and lower remanence. The higher annealing temperature and shorter annealing time resulted in hysteresis loops with a better squareness, which usually indicates small and uniform microstructure.

Investigations of the microstructure using the Tecnai G² F20 STEM were performed on samples that had been annealed at 615°C for 0, 1, 2 and 6 min. The samples annealed at 615°C for 0, 1, and 2 minutes showed a similar microstructure with grains embedded in amorphous matrix. The only difference was that the grain size becomes larger with increasing annealing time. EDS analysis indicated that most grains are 2-14-1 hard magnetic phase. Ti was uniformly distributed in the matrix. In contrast, the 6 min sample was totally crystallized, with TiC phase appearing at grain boundaries and triple junctions, as well as grains of

α -Fe (in light contrast). This observation was supported by STEM HAADF images and EDS data. The formation of TiC phase clearly occurred between 2 min and 6 min. during annealing. The TEM images also indicated that the hard phase grain size did not increase much from 2 min. to 6 min., demonstrating the ability of the TiC phase to inhibit grain growth during annealing

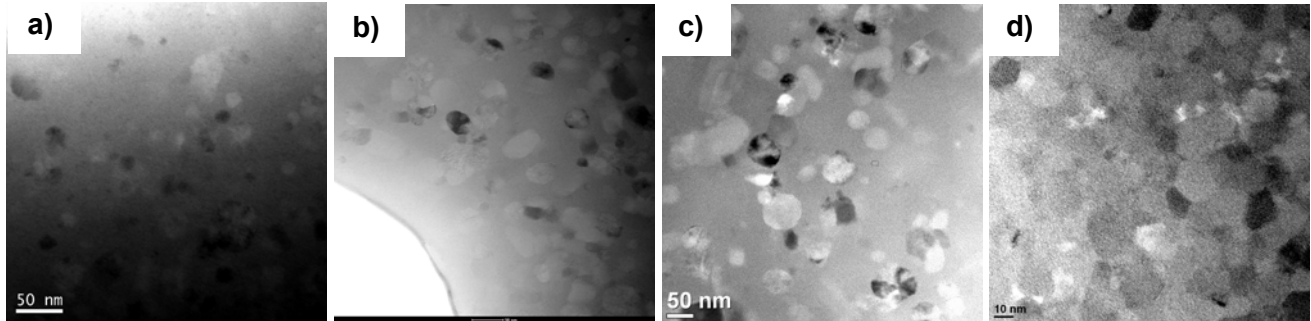


Figure 4. TEM bright-field images of WT165 alloys annealed at 615°C using DSC, showing representative microstructures at (a) 0 min., (b) 1 min., (c) 2 min., and (d) 6 minutes.

In summary, our current hypothesis on the prospects for development of nanocomposite permanent magnets with enhanced exchange coupling is not promising, given that the temperature required to fully crystallize the 2-14-1 phase in the $MRE_2Fe_{14}B/\alpha$ -Fe is too high to retain the soft phase (α -Fe) without coarsening to an unacceptable size, which results in a reduced coercivity and energy product.

Near-stoichiometric magnets: The control of microstructure is key to obtaining optimal magnetic properties in all permanent magnets. This is true for single-phase nanocrystalline magnets and for nanocomposite magnets, as described above. When the microstructure is a result of the crystallization of an amorphous precursor, it is important to understand the crystallization pathway. Thus, for a selected Ames single phase $MRE_2Fe_{14}B$ alloy, detailed studies of the crystallization were performed using extensive DSC and microstructure observations.

The selection of a suitable alloy composition for this study focused on alloy WT147 with a composition of $\{[Nd_{0.45}(Y_2Dy_1)_{1/3*0.55}]_2Zr_{0.3}Co_{1.0}Fe_{13.0}B\}_{(1-2x)} + Zr_xC_x$ ($x=0.01$) that featured Zr+ZrC additions. Melt spinning experiments had demonstrated that enhanced magnetic properties could be produced at low solidification rates for WT147, indicating its ability to adapt for gas atomization which requires this tolerance. For these detailed studies, WT147 was melt spun at a wheel speed of 25 m/s, so that a uniform starting condition, fully amorphous as determined by XRD, was obtained for each sample. The onset temperature of crystallization for the amorphous ribbons was determined by DSC to be 658°C, as seen above in Fig. 3a.

Ribbon samples were isothermally heated for various time intervals at a temperature of 638°C, lower than the onset temperature, and then quenched. Again, as in Fig. 3b, an isothermal DSC experiment showed that full crystallization apparently could be achieved at 638°C after less than 11 minutes of annealing. Using the Tecnai G² F20 STEM, the microstructure of ribbon samples (see Fig. 5) were studied that had been melt-spun at 25 m/s and annealed using the DSC at 638°C for 4.5, 8 and 11 min., respectively. While the as-spun sample was confirmed to be amorphous using XRD, the 4.5 min. annealed sample shows fully crystallized nano-structure with an average grain size of about 25 nm. After annealing for 8 min., the grain size increased to about 40 nm and interesting feature was found along the grain boundaries. Further annealing to 11 min. retained the same microstructure with a larger grain size, over 60 nm. Complimentary STEM HAADF observation clearly indicated a constant darker contrast along grain boundaries in both 8 min. (not shown) and 11 min. annealed samples. This indicated that a lower-mass phase (perhaps ZrC) formed along the grain boundary region in the alloys.

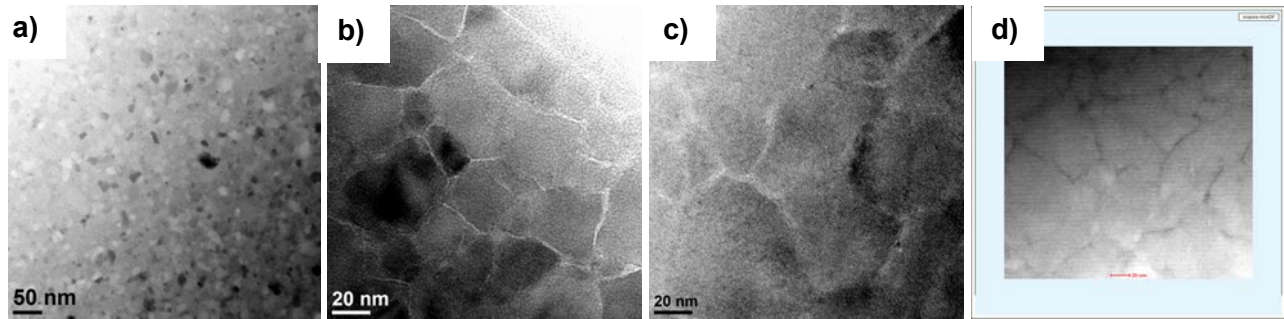


Figure 5. TEM bright-field images of WT147 alloys annealed at 638°C using DSC, showing representative microstructures after annealing for (a) 4.5 min., (b) 8 min, and (c) 11 min., as well as (d) a STEM HAADF image of the 11 min. case.

The magnetic properties of the samples (see Fig. 6) annealed at 638°C for 4.5 and 11 min. exhibited an amorphous (magnetically soft) feature. Ribbons annealed at 638°C for 30 min. and at 625°C for 6, 11, and 60 min. (not shown) exhibited a comparable coercivity with that of ribbons annealed at 750°C for 15 min. However, the hysteresis loops from samples annealed lower than 750°C all exhibit a shoulder close to zero field characteristic of a soft magnetic component. Thus, a higher annealing temperature and a shorter annealing time is helpful to obtain hysteresis loops with a better squareness, perhaps resulting from small and uniform grain size, without a grain boundary amorphous phase.

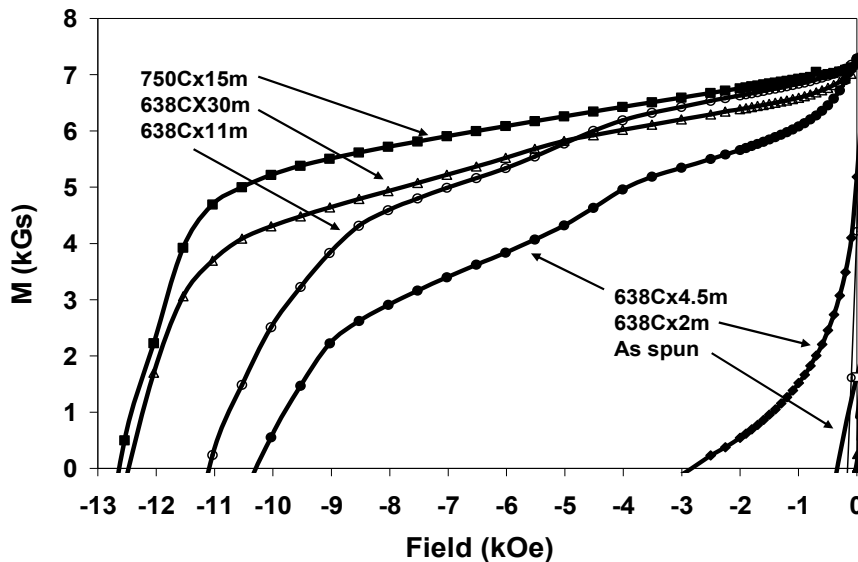


Figure 6. Second quadrant demagnetization curves of WT147 alloy ribbon samples as a function of annealing time at 638°C.

In summary, compared to similar studies on the nanocomposite composition WT165, the WT147 amorphous ribbons require higher temperatures and longer times to be completely crystallized. It is obvious that Zr and ZrC play an important role in stabilizing microstructure.

Verification by gas atomization: Initial verification of alloy compositions that tolerate low solidification rates focused on compositions with Zr+ZrC additions such as $\{[\text{Nd}_{0.45}(\text{Y}_2\text{Dy}_1)_{1/3*0.55}]_{(2.3-y)/17.3}\text{Zr}_{(y/17.3)}\text{Co}_{1.5/17.3}\text{Fe}_{12.5/17.3}\text{B}_{1/17.3}\}_{(1-2x)} + \text{Zr}_x\text{C}_x$ ($x=0.02$). However, the initial run, GA-1-74, using He gas atomization of this alloy was unsuccessful due to the precipitation of ZrC in the pour tube that transports the liquid metal from the crucible to the atomization nozzle, which became blocked resulting in an incomplete run and very low yield. Precipitation of ZrC was attributed to an excessive ZrC content

(supersaturation) at the selected melt pouring temperature. A second He gas atomization run, GA-1-100, that used a $[(Nd_{4.5}(Y_2Dy_1)_{1/3*0.55})_{2.0}Zr_{0.3}Co_1Fe_{13}B]_{1-2x}+Zr_xC_x$, $x=0.01$, magnet alloy (WT147) with lower ZrC content and a higher pouring temperature was successful.

TEM investigations with the Tecnai G² F20 STEM show that the annealed (at 700°C, 15 min.) alloy microstructure of the cross-sectioned spherical powders consisted of very small (5 ~ 10 nm), round shape particles and larger grains (20 ~ 50 nm). EDS analyses indicated that the small particles are ZrC and the larger grains are 2-14-1. The ZrC particles were located at grain boundaries and triple junctions. The formation of ZrC particles apparently inhibited grain growth and controlled microstructure, a favorable characteristic in this alloy system.

While the magnetic properties of GA-1-100 powder were still lower than those of melt spun ribbons with the same composition, energy products (unadjusted) of 7 MGOe and coercivities of 10kOe were obtained over a large range of particle sizes. This compares to 10.4 MGOe and 11kOe for the melt spun ribbon. The decrease of Zr and ZrC did not affect the quenchability of GA-1-100, while improving the coercivity.

In order to investigate the feasibility of gaining a technological advantage by using Ar rather than He as the atomization gas, the prototype alloy of GA-1-100, WT147, was melt spun at a wheel speed of 13m/s in both He (typical for our experiments) and Ar atmospheres. In technological terms, it would be advantageous to make this gas substitution from the perspective of both reduced production cost (for atomization gas) and the possibility of avoiding post-atomization annealing to promote optimum crystallization. The choice of atmosphere is important from the standpoint of the rapidly solidified microstructure that results, because the convective heat transfer coefficient of Ar is significantly lower (about 10X) than that of He, i.e., alloys melt spun (or gas atomized) in Ar will cool significantly slower than those processed in He. For the melt-spun ribbons, the magnetic properties after annealing of the ribbons processed in Ar matched or exceeded those processed in He and a fine and uniform microstructure resulted. With this encouraging result, a gas atomization run, GA-1-114, of this composition was performed using Ar gas and the in situ fluorination coating provisions described above. This run produced powder with a relatively low oxygen content (800ppmw for -45µm) and with exceptional magnetic properties after annealing at 700°C for 15 minutes (see

Table 1), where the magnetic properties of annealed GA-1-114 powders are given as a function of particle size. The magnetic properties of WT147 that was melt spun at 13 m/s and annealed at 700°C for 15 min. are also included in the table. With the exception of the 32-38µm size range (and larger sizes), the BH_{max} for the Ar atomized powder exceeded that of the corresponding He atomized powder. For the finest powders, the difference was about 1.8 MGOe, although post-atomization annealing still was required.

Typical hysteresis loops (not shown) for as-atomized and annealed GA-1-114 powders with different particle size distributions showed that as-atomized GA-1-114 powders exhibited characteristics of both hard and soft magnetic phase fractions indicating that the as-atomized powder consisted of a well-crystallized phase along with an amorphous or very fine-grained phase. After annealing at 700°C for 15 min., the samples exhibited smooth demagnetization curves, indicating that annealed GA-1-114 consists entirely of well crystallized 2-14-1 phase. Phase analysis and microstructural studies are being conducted to confirm this assumption. In summary, the latest near-stoichiometric (2-14-1) composition for gas atomization processing, the WT147 alloy, appears to be well suited for Ar gas atomization, which

Size (µm)	M_s (kG)	M_r (kG)	H_c (kOe)	$(BH)_{max}$ (MGOe)
-20	11.2	6.5	11.2	8.8(10.1)
20-25	11.2	6.4	10.5	8.2
25-32	11.2	6.3	9.6	7.3
32-38	11.2	5.6	7.0	4.8
WT147 (ribbon)	11.1	7.0	11.2	11.0

Table 1. Magnetic properties of GA-1-114 spherical powders, where the $(BH)_m$ for -20 was adjusted by the (conventional) shape factor of 0.33.

is highly desirable for technology transfer purposes since the expense for bulk Ar gas is at least a 3X cost reduction from that of He gas, used for the GA-1-100 powder. Some adjustments of the alloy remain to be tried, however, to promote direct crystallization and avoid the annealing step, if possible.

Magnet Fabrication

Through an extended effort through the later half of FY07, a polymer compounding mixer (twin screw extruder/mixer from Haake) was brought into operation after sitting idle for about 7 years. This effort required equipment operation software to be verified and various sensor and control problems to be fixed. After the unit was functional, a polymer flushing was performed of the "frozen" and contaminated twin-screw extrusion barrel. Unfortunately, unavoidable delays from a lack of parts and information on this early unit (designed and manufactured in 1988) setback the planned examination of the upper limit of loading in polymer for flake and fine spherical particulate. A contraction of the current project in FY08 will not permit this to be completed in FY08, but a new applied research project with GM and AMT will include this objective.

Utilizing the same heated die sets that were used in FY06, a partial set of (5) bonded magnet samples were compression molded from coated magnet flake particulate (MQP-11HTP) for the second stage of industrial environmental testing at AMT. The full sample set of (11) will need to be completed early in FY08 to permit AMT to complete their testing protocol. Processing of the remaining samples requires repair of the fluidized bed coating apparatus that became inoperable at about mid-year.

Industrial Partnerships

By maintaining a dialogue with a network of industrial partners, an opportunity was identified to participate in assembling a proposal entitled "Advanced Electric Traction System" to form an industrial partnership (in a CRADA) with GM and AMT. The overall proposal, with GM as the lead organization, was selected for a new project by the PEEM office. The new project will provide an industrial test of the isotropic (nanocrystalline) bonded magnet technology (with level 1&2 benefits) that was developed in this project for IPM motors.

An industry expert, Dr. Peter Campbell, was selected to conduct an independent analysis of the total manufacturing cost for an advanced electric drive motor with either sintered or bonded permanent magnets in appropriately designed interior PM rotor electric machines.

Conclusion

The current FY07 progress in the four main areas of development, including surface passivation methods, magnet alloy improvements for isotropic nanocrystalline permanent magnets, isotropic bonded magnet fabrication, and industrial partnerships, have provided a significant list of accomplishments for the project. The new efforts for FY08 will include the major challenge of extending the scope of our high temperature magnet alloy design and innovative processing into the arena of anisotropic nanocrystalline bonded magnets and an early exploration of microcrystalline aligned sintered magnets. The potential large gains in magnetic energy product per mass of magnet alloy, without much loss in complex shape forming for the former, serve as the primary driver for this work.

Publications

Wu, Y. Q.; Tang, W.; Miller, M. K.; Anderson, I. E.; McCallum, R. W.; Dennis, K. W.; Kramer, M. J. Microanalytical characterization of multi-rare-earth nanocrystalline magnets by transmission electron microscopy and atom probe tomography. *Journal of Applied Physics* (2006), 99(8, Pt. 2), 08B515/1-08B515/3.

Tang, W.; Wu, Y. Q.; Dennis, K. W.; Kramer, M. J.; Anderson, I. E.; McCallum, R. W.. Comparison of microstructure and magnetic properties of gas-atomized and melt-spun MRE-Fe-Co-M-B (MRE=Y+Dy+Nd, M=Zr+TiC). *Journal of Applied Physics* (2007), 101(9, Pt. 2), 09K510/1-09K510/3.

P.K. Sokolowski, I.E. Anderson, W. Tang, Y.Q. Wu, K.W. Dennis, M.J. Kramer, and R.W. McCallum, "In situ Passivation during High Pressure Gas Atomization of Improved MRE₂Fe₁₄B for High Performance Permanent Magnet Applications," in 8th Global Innovations Symposium: Trends in Materials and Manufacturing Technologies for Energy Production, TMS (The Minerals, Metals, & Materials Society), ISBN: 978-0-87339-677-6 (2007) pp. 7-17.

References

R. W. McCallum, K. W. Dennis, B. K. Lograsso, and I. E. Anderson, "Method of Making Bonded or Sintered Permanent Magnets," U.S. Patent 5,240,513, August 31, 1993.

I. E. Anderson, B. K. Lograsso, and R. L. Terpstra, "Environmentally Stable Reactive Alloy Powders and Method of Making Same," U.S. Patent 5,372,629, December 13, 1994.

R. W. McCallum, K. W. Dennis, B. K. Lograsso, and I. E. Anderson, "Method of Making Bonded or Sintered Permanent Magnets (continuation)," U.S. Patent 5,470,401, November 28, 1995.

I. E. Anderson and R. L. Terpstra, "Apparatus for Making Environmentally Stable Reactive Alloy Powders," U.S. Patent 5,589,199, December 31, 1996.

I. E. Anderson, B. K. Lograsso, and R. L. Terpstra, "Environmentally Stable Reactive Alloy Powders and Method of Making Same," U.S. Patent 5,811,187, September 22, 1998.

R. W. McCallum and D. J. Branagan, "Carbide/Nitride Grain Refined Rare Earth-Iron-Boron Permanent Magnet and Method of Making," U.S. Patent 5,803,992, September 8, 1998.

R. W. McCallum and D. J. Branagan, "Carbide/Nitride Grain Refined Rare Earth-Iron-Boron Permanent Magnet and Method of Making," U.S. Patent 5,486,240, January 23, 1996.

D. J. Branagan and R. W. McCallum, "The Effects of Ti, C, and TiC on the Crystallization of Amorphous Nd₂Fe₁₄B," *J. Alloys and Compds.*, **245** (1996).

D. J. Branagan, T. A. Hyde, C. H. Sellers, and R. W. McCallum, "Developing Rare Earth Permanent Magnet Alloys for Gas Atomization," *J. Phys. D: Appl. Phys.*, **29**, p. 2376 (1996).

M. J. Kramer, C. P. Li, K. W. Dennis, R. W. McCallum, C. H. Sellers, D. J. Branagan, L. H. Lewis, and J. Y. Wang, "Effect of TiC Additions to the Microstructure and Magnetic Properties of Nd_{9.5}Fe_{84.5}B₆ Melt-spun Ribbons," *J. Appl. Phys.*, **83**(11), pt. 2, p. 6631 (1998).

D. J. Branagan and R. W. McCallum, "Changes in Glass Formation and Glass Forming Ability of Nd₂Fe₁₄B by the Addition of TiC," *J. Alloys and Compds.*, **244** (1-2), p. 40 (1996).

Patents

U.S. Patent (PCT) application filed (11-18-02) "Permanent Magnet Alloy with Improved High Temperature Performance."

4. Power Electronics Research and Technology Development

4.1 Wide Bandgap Materials

Principal Investigator: Burak Ozpineci

Oak Ridge National Laboratory

National Transportation Research Center

2360 Cherahala Boulevard

Knoxville, TN 37932

Voice: 865-946-1329; Fax: 865-946-1262; E-mail: ozpinecib@ornl.gov

DOE Technology Development Manager: Susan A. Rogers

Voice: 202-586-8997; Fax: 202-586-1600; E-mail: Susan.Rogers@ee.doe.gov

ORNL Program Manager: Mitch Olszewski

Voice: 865-946-1350; Fax: 865-946-1262; E-mail: olszewskim@ornl.gov

Objectives

- Assess the impact of replacing silicon power devices in transportation applications with devices based on wide bandgap (WBG) semiconductors, especially silicon carbide (SiC).
- Study the impact of SiC devices on plug-in hybrid vehicles.
- Study the possibility of using a thermal boundary in SiC intelligent power modules (IPMs) where silicon gate drivers can be used.
- Study the fault current limiting capability of SiC devices for safety and protection.

Approach

- Develop models of WBG semiconductor devices, junction field-effect transistors (JFETs), and metal oxide semiconductor field-effect transistors (MOSFETs).
- Integrate silicon-based and SiC-based inverter loss models into a drive train using PSAT software to compare the impact of replacing silicon devices with SiC devices.
- Develop a hybrid device package and simulate the model to study the feasibility of using a thermal boundary in SiC-based IPMs.
- Develop circuits to study the fault current limiting capability of SiC devices.

Major Accomplishments

- Acquired several SiC Schottky diodes, JFETs, and SiC MOSFETs.
- Tested, characterized, and modeled SiC Schottky diodes, JFETs, and MOSFETs.
- Developed and modeled a hybrid device package.
- Successfully integrated an inverter loss model into the drive train model in PSAT.

Future Direction

- Acquire, test, and characterize newer technology WBG power devices.
- Study the conceptual changes to inverters/converters and their packaging and thermal management designs to take advantage of WBG devices.

Technical Discussion

I. Device Testing

Several new WBG devices were acquired this year, and these devices were tested, characterized, and modeled. The devices included SiC JFETs, SiC MOSFETs, and SiC Schottky diodes. All the devices obtained were experimental samples. A high-temperature silicon insulated gate bipolar transistor (IGBT) was also tested this year to verify the claims of high temperature. See Tables 1 and 2 for results of some of the WBG devices tested from 2004 to 2007.

Table 1. Power diodes

Device type	Ratings	On-resistance (Ω)	Forward voltage drop (V)	Manufacturer	Year tested
SiC Schottky diode	1200 V, 7.5 A	0.15 Ω at -50°C to 0.32 Ω at 175°C	1.42 V at -50°C to 1.21 V at 175°C	Vendor A	2004
SiC Schottky diode	300 V, 10 A	0.15 Ω at -50°C to 0.16 Ω at 175°C	1.11 V at -50°C to 0.83 V at 175°C	Vendor B	2004
SiC Schottky diode	600 V, 4 A	0.19 Ω at -50°C to 0.39 Ω at 175°C	1.09 V at -50°C to 0.87 V at 175°C	Vendor C	2004
SiC Schottky diode	600 V, 10 A	0.14 Ω at -50°C to 0.25 Ω at 175°C	1.09 V at -50°C to 0.82 V at 175°C	Vendor C	2004
SiC Schottky diode	600 V, 75 A	0.01 Ω at -50°C to 0.03 Ω at 175°C	0.91 V at -50°C to 0.61 V at 175°C	Vendor C	2005
GaN Schottky diode	600 V, 4 A	0.23 Ω at 25°C to 0.47 Ω at 175°C	0.83 V at 25°C to 0.67 V at 175°C	Vendor D	2006
SiC Schottky diode	600 V, 6 A	0.138 Ω at 50°C to 0.359 Ω at 300°C	0.745 V at 50°C to 0.365 V at 300°C	Vendor E	2007

Table 2. Power switches

Device type	Ratings	On-resistance (Ω)	Voltage drop at rated current at room temperature (V)	Manufacturer	Year tested
SiC JFET	1200 V, 2 A	0.36 Ω at -50°C to 1.4 Ω at 175°C	1.3 V at $V_{gs} = 0$ V	Vendor F	2004
SiC JFET	1200 V, 10 A	0.25 Ω at -50°C to 0.58 Ω at 175°C	2.71 V at $V_{gs} = 0$ V	Vendor F	2006
SiC JFET	1200 V, 15 A	0.15 Ω at -50°C to 2.2 Ω at 175°C	3.2 V at $V_{gs} = 3$ V	Vendor A	2006
SiC JFET	600 V, 5 A	0.26 Ω at -50°C to 1.87 Ω at 175°C	2.25 V at $V_{gs} = 3$ V	Vendor G	2006
SiC MOSFET	1200 V, 5 A	(0.48 Ω at -50°C to 0.23 Ω at 50°C) (0.24 Ω at 75°C to 0.29 Ω at 175°C)	1.5 V at $V_g = 20$ V	Vendor C	2005
SiC MOSFET	800 V, 10 A	0.25 Ω at 25°C to 0.09 Ω at 150°C	1.8 V at $V_g = 15$ V	Vendor C	2007
SiC JFET	600 V, 2 A	0.25 Ω at 25°C to 1.07 Ω at 200°C	1.3 V at $V_g = 0$ V	Vendor G	2007

1. SiC Schottky diode

Static characteristics. A 600-V/6-A SiC Schottky diode placed in a high-temperature package was obtained from Sienna Technologies. The main objective was to determine the performance of the diode at higher temperatures, which would not be possible with a standard package. I–V characteristics of the diode were obtained at different temperatures in the 50°C to 300°C temperature range (Figure 1). Figure 2 shows the reverse characteristics of the diode over a wide temperature range. The blocking voltage decreases with increasing temperature. The leakage current increases with increasing temperature (Figure 3).

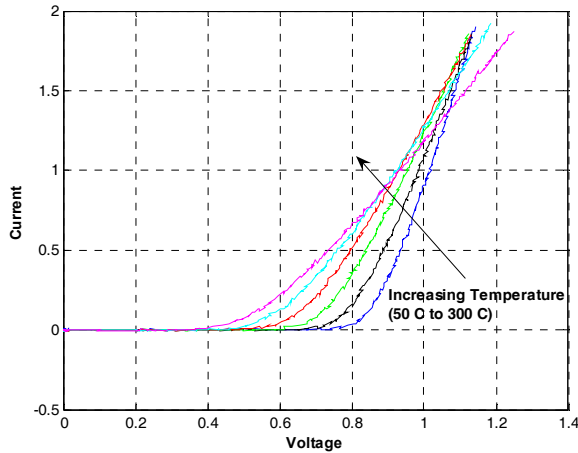


Figure 1. Forward characteristics.

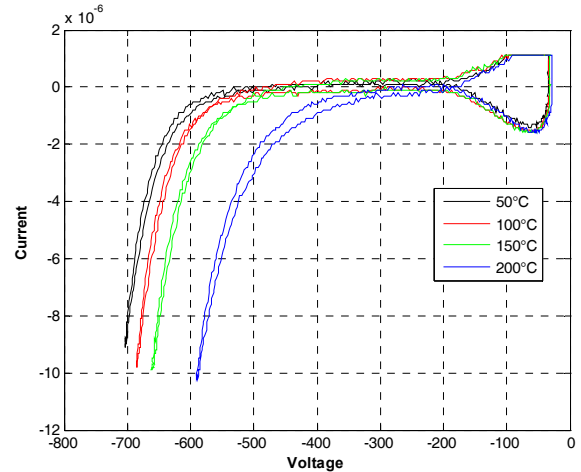


Figure 2. Reverse characteristics.

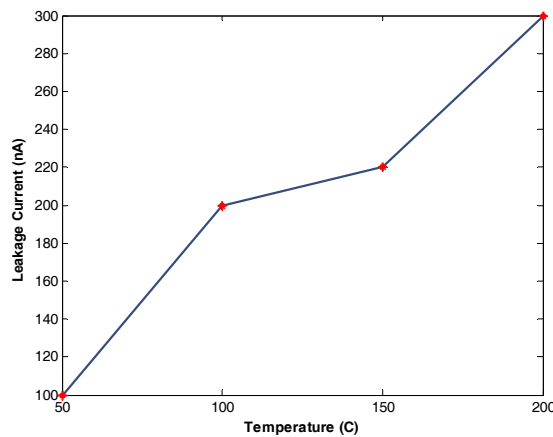


Figure 3. Leakage current of a SiC Schottky diode at different temperatures.

Dynamic characteristics. The SiC Schottky diode was also tested in a chopper circuit, shown in Figure 4 to observe its dynamic characteristics. The IGBT was switched at 1 kHz with a duty cycle of 50% and an R-L load. The reverse recovery tests were performed at different voltages and currents.

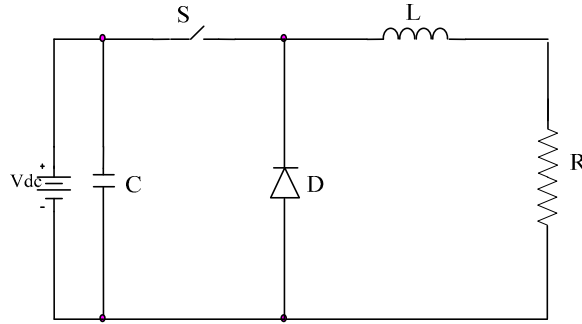


Figure 4. Reverse recovery test circuit.

The reverse recovery current waveforms obtained at different temperatures are shown in Figure 5. As seen in this figure, the reverse recovery current does not change much with temperature. Note that theoretically, Schottky diodes do not display reverse recovery phenomenon because they are majority carrier devices and do not have stored charge. The switching losses obtained at different temperatures are shown in Figure 6.

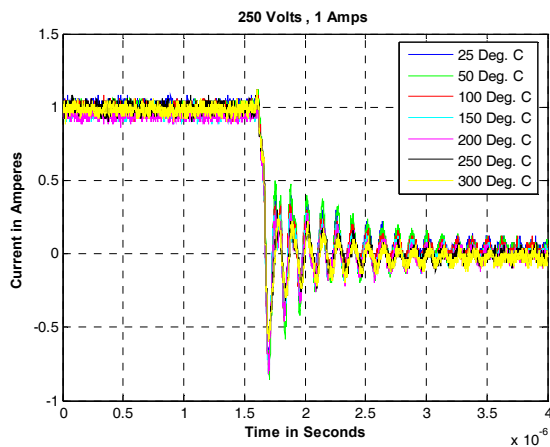


Figure 5. Reverse recovery current waveforms of the SiC Schottky diode at different temperatures.

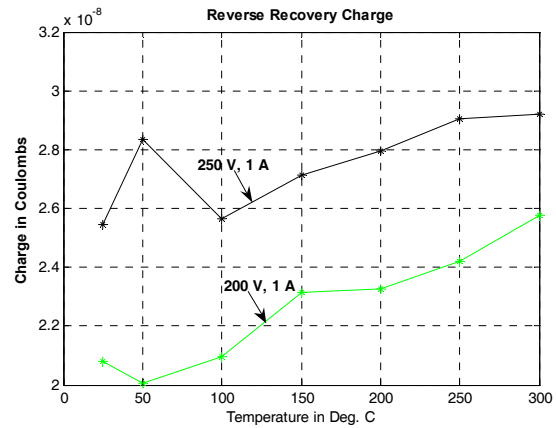


Figure 6. Switching energy losses of SiC diode at different temperatures.

2. SiC MOSFET

The static characteristics of a (800-V, 10-A) SiC MOSFET for different operating temperatures are shown in Figure 7. This experimental device has a negative temperature coefficient, unlike the earlier experimental samples, which had both positive and negative temperature coefficients [1]. The on-resistance of the device decreases from 0.25 Ω at 25°C to 0.09 Ω at 150°C as shown in Figure 8. The transfer characteristics of the MOSFET, obtained for different temperatures, are shown in Figure 9.

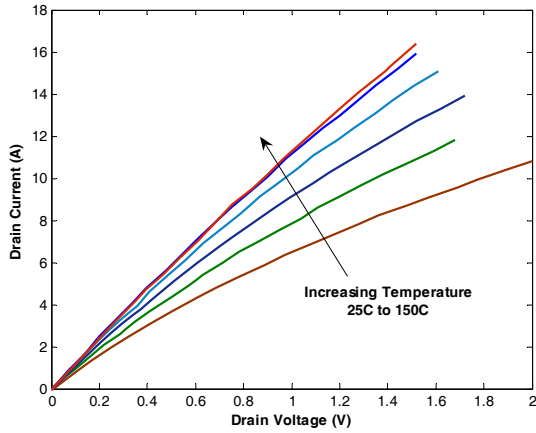


Figure 7. i-v curves of SiC MOSFET.

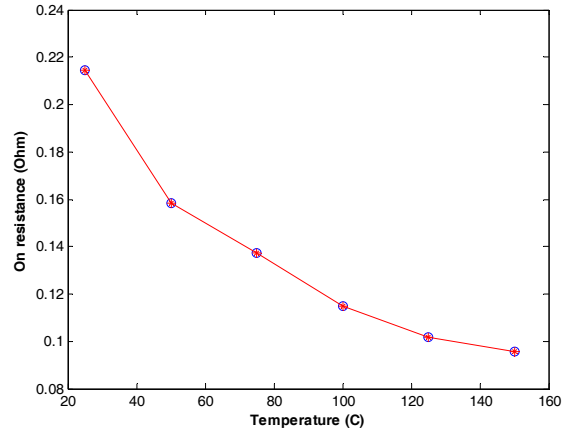


Figure 8. On-resistance of SiC MOSFET.

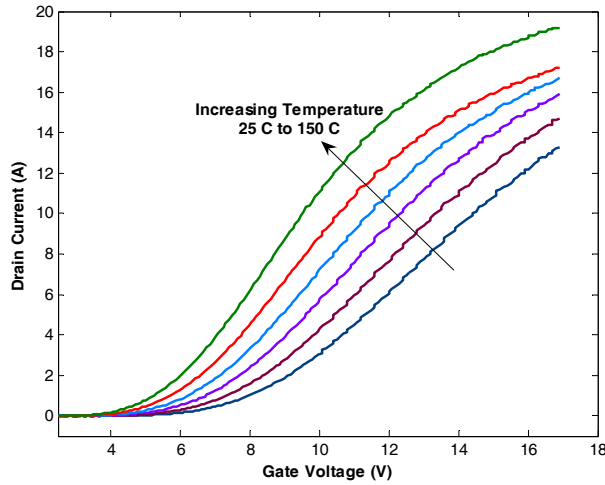


Figure 9. Transfer characteristics of SiC MOSFET.

Dynamic characteristics. The SiC MOSFET was also tested in a chopper circuit with double-pulse switching to observe its dynamic characteristics. The double-pulse circuit enables the use of an inductive load instead of the combined resistive and inductive load. The current through the inductor builds up during the first pulse, and peak forward current is adjusted by changing the width of the first pulse. The switch is turned-off and turned-on for short periods after the first pulse. The turn-on and turn-off energy losses can be obtained during the short pulse intervals.

The turn-on and turn-off switching energy losses of the MOSFET are shown in Figure 10. The turn-off losses do not change much with temperature, but the turn-on losses decrease with increasing temperature.

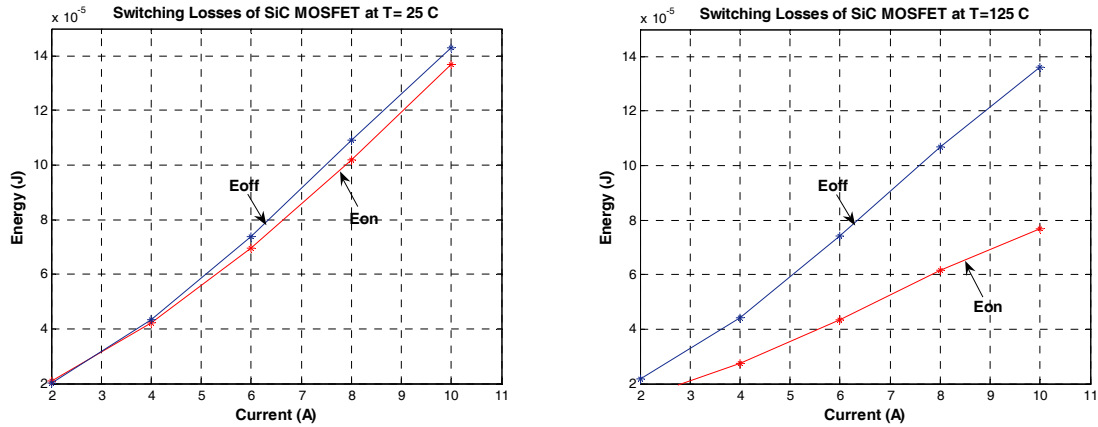


Figure 10. Switching energy losses of SiC MOSFET for different currents and temperatures.

3. SiC JFET

Static characteristics. Static characteristics of a (600-V, 5-A) SiC JFET are shown in Figure 11 for different operating temperatures. SiC JFETs have a positive temperature coefficient, which means that like SiC Schottky diodes, their conduction losses will be higher at higher temperatures. However, a positive temperature coefficient makes it easier to parallel these devices and reduce the overall on-resistance. The on-resistance of the JFET increases from 0.25Ω at 25°C to 1.07Ω at 200°C as shown in Figure 12.

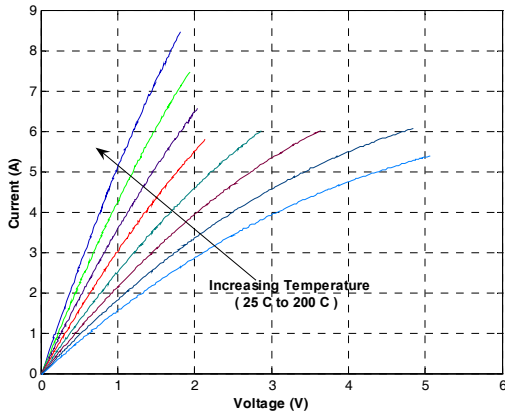


Figure 11. i-v curves of a SiC JFET.

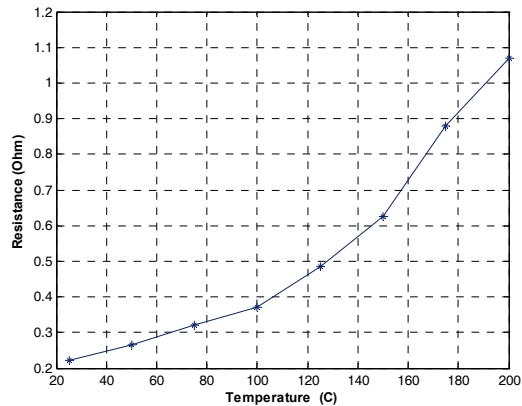


Figure 12. On-resistance of a SiC JFET.

4. High-temperature silicon IGBT

A high-temperature silicon IGBT module (FS30R06W1E3) was obtained from Infineon. These new Infineon Trench technology based IGBTs are designed for operation at 200°C junction temperature. The objective of testing this device is to evaluate the performance of the IGBT over a wide temperature range (25°C to 200°C). The static characteristics of the IGBT at different temperatures are shown in Figure 13. The IGBT has a positive temperature coefficient at rated current.

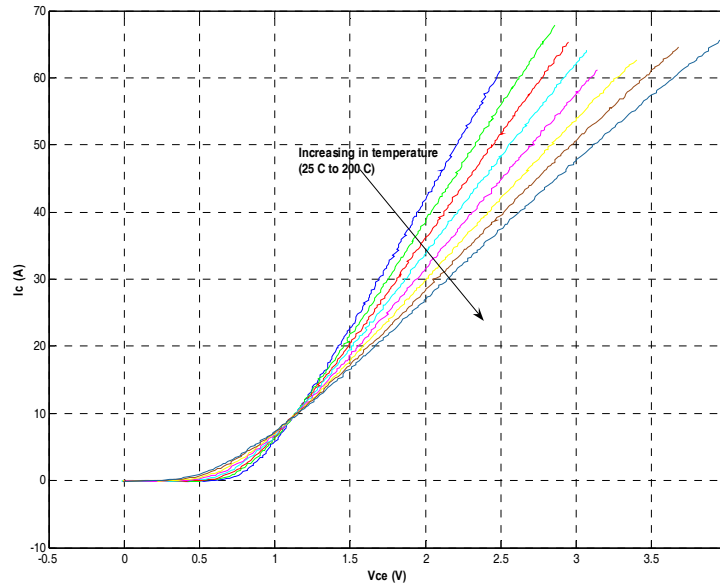


Figure 13. i-v characteristics of IGBT at different temperatures.

Only one leg of the IGBT module was utilized for the test. The other two legs were left “floating.” An R-L load was connected across the upper IGBT. The upper IGBT was kept OFF by supplying -5 V between the gate and the source (schematic, Figure 14).

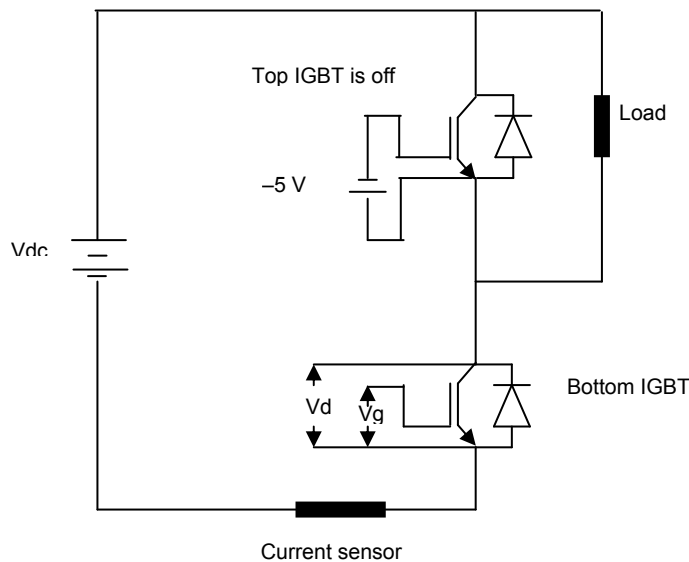


Figure 14. Schematic of the circuit.

A Fuji EXB840 chip was used as the gate driver. The lower IGBT was hard switched; no snubber was utilized. An Agilent 33250A waveform generator was used to generate the 5-kHz switching frequency with a duty cycle of 20%. A hot plate was used to vary the junction temperature of the IGBT. The IGBT module was mounted on a copper plate, which was fixed to the hot plate using thermal grease. The temperature of the hot plate was measured and fed back using a thermocouple to control the desired temperature (Figure 15).

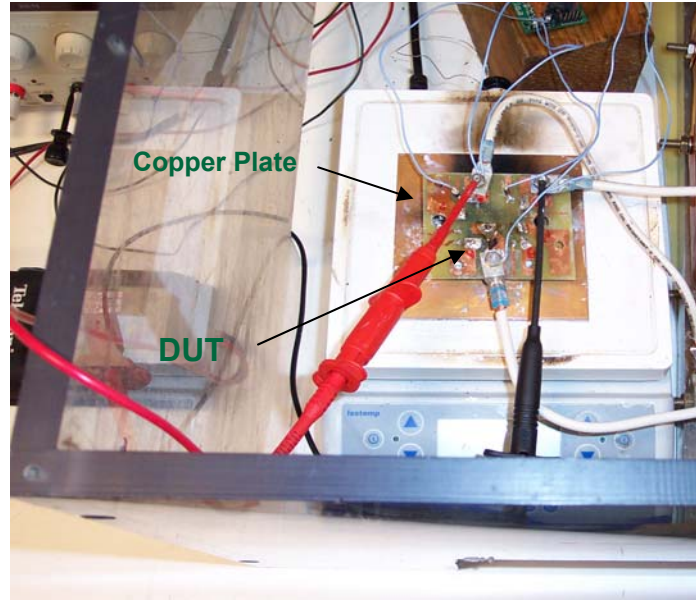


Figure 15. Test setup.

The device performed without a failure up to 175°C junction temperature at different load conditions. The device was switched at 5 kHz, 250 V, 23 A (38 A peak during transient) current, 20% duty cycle, without any problems. The device was operated with different load conditions for at least 15 min for each data point. The IGBT failed at 250-V, 16-A operation at a junction temperature of 200°C after operating for about 10 min. Similar steps were carried out on different legs of the module to confirm the failure. The IGBT failed consistently for operation at 250 V and 200°C at 23 A.

The device was subjected to continuous dc current tests to study the performance of the device close to the rated current. The voltage was increased in steps to obtain 5-, 10-, 15-, 20-, 25-, and 30-A current levels. The tests were carried out at 50, 100, 150, 175, and 200°C junction temperatures.

The device operated without any failure at 30 A (rated current), at 175°C. However, at 200°C junction temperature, the device worked well up to 25 A of current and failed at 30 A. The tests were repeated with another sample to confirm the failure point, and the device failed again at 30 A. It can be concluded that the device is capable of successfully operating at 175°C without any failure. However, at a junction temperature of 200°C, the device fails at higher current levels during both the switching tests and the dc tests.

II. Fault Current Limiting Tests of SiC JFETs

Most SiC power devices proposed for use in traction drives have positive temperature coefficients; this means that as the devices heat up, their resistance increases. In the case of a fault, the fault currents would heat up the device, increasing the device's resistance. The increased resistance reduces the fault current; however, by the time the fault current is limited, damage can be done to the electrical drive system. Another way of limiting fault currents is to increase the device resistance by varying the gate voltage. For this task, ORNL studied the feasibility of including fault-current-limiting feedback to the gate driver of a SiC power switch and studied the temperature response of SiC devices under short-circuit conditions.

Several circuits were built for testing the short-circuit capability of SiC JFETs. The devices were tested for short-circuit current capability by applying short current pulses of different magnitudes. Figure 16 shows the pulse current test waveforms at different current values for a (1200-V, 5-A) JFET.

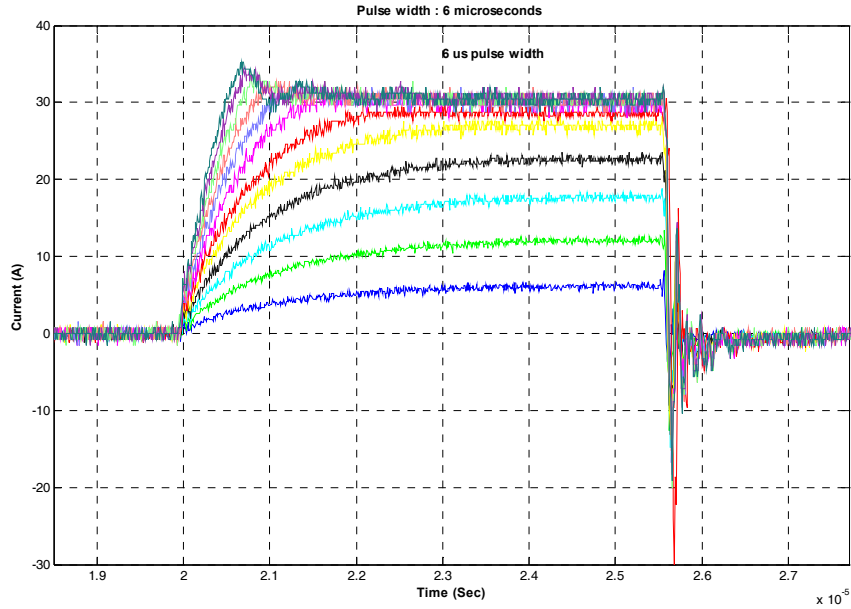


Figure 16. Short-circuit pulse test waveforms of a SiC JFET.

The current through the device was controlled by varying the pulse width and magnitude. The JFET exhibited self-current limiting capability at zero gate voltage. The current saturated at 35 A for a (1200-V, 5-A) device. The current saturation value corresponds to the value in the device characteristic curve obtained at room temperature.

The temperature response of the device was also studied by applying continuous dc current to the device to see the rate of change in resistance with temperature. The temperature response of the SiC JFET is shown in Figure 17. The tests showed that the positive temperature coefficient property of the device

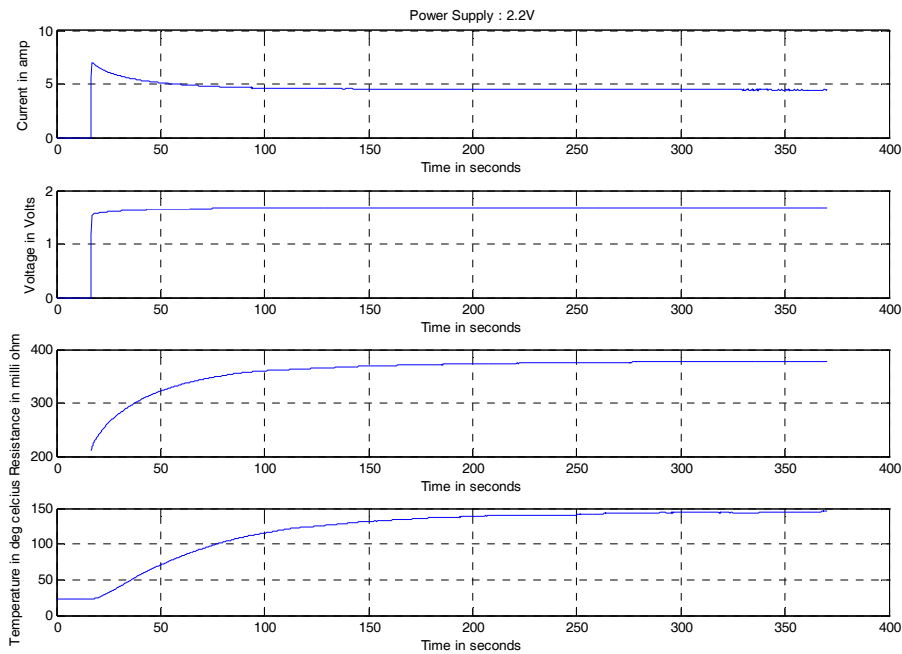


Figure 17. Temperature response profile of a SiC JFET.

limited the current. However, as predicted, the time it takes for the device to limit the current is long because of the slow change in resistance with temperature. The time is on the order of several seconds and is too long for the device to withstand the short-circuit current. It should be noted that the thermal time constant of the device package is also included in the total time.

To protect the device under fault conditions, a fault-current-limiting circuit is required. As mentioned earlier, the fault current can also be limited by varying the gate voltage. The variation in gate current with gate voltage can be obtained from the transfer characteristics. The gain (defined as change in current with change in gate voltage) of the JFET is an important parameter of the device for fault current limiting. A fault-current-limiting circuit was developed and integrated into the gate driver circuit. Figure 18 shows the schematic of the fault-current-detection and fault-current-limiting circuit under short circuit fault. The circuit was built using commercially available IC chips. The fault current detection is achieved by sensing the drain-source voltage across the device. The circuit has a blanking time capability that can be adjusted by varying the RC time constant between the gate turn-on signal and the detection signal. The blanking time prevents nuisance trips because of transient currents. The circuit has the flexibility to be adjusted for a particular on-state voltage drop between (0–7 V). The output stage of the gate driver circuit is capable of handling 14 A of peak current. The circuit can be adapted for higher gate currents by implementing a complementary transistor pair at the output stage of the gate driver.

The waveforms in Figure 19 show the fault detection signal, the gate voltage waveform, and the fault signal feedback to the controller. The fault across the device is simulated using a preset voltage across the

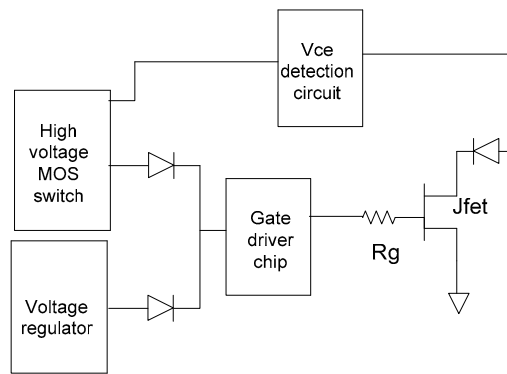


Figure 18. Schematic of the protection circuit for fault protection.

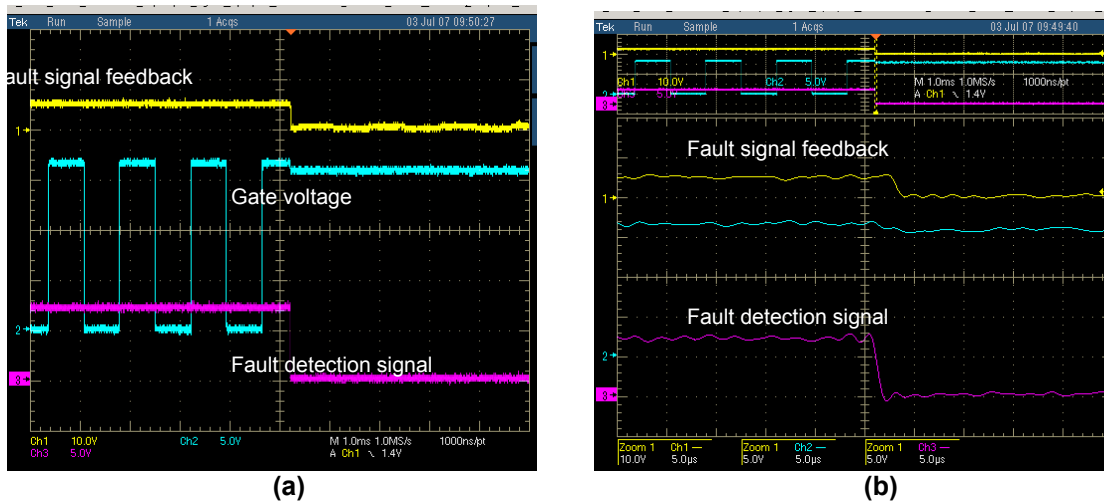


Figure 19. Test results of the protection circuit: (a) normal view and (b) zoomed view.

fault detection circuit, which in the actual device is the on-state voltage drop corresponding to the short circuit current. The gate voltage is clamped to a desired preset voltage as soon as the fault is detected. There is a delay between the fault detection signal and the fault signal output. However, the gate voltage starts to decrease even before the fault signal is active. This change in the gate voltage reduces the peak fault current immediately after the fault. The gate voltage is clamped to the preset voltage until the controller commands the turn-off the gate signal. The time needed for the gate voltage to be clamped is determined by the amount of time the device can withstand a short circuit. The protection circuit also has the undervoltage gate protection feature that will protect the device from damaging itself because of excessive losses.

The circuit was tested with the device operating to verify the functionality of the circuit. The circuit was able to limit the current by changing the gate voltage. Figure 20 shows the waveforms of gate voltage, drain current and, and drain voltage.

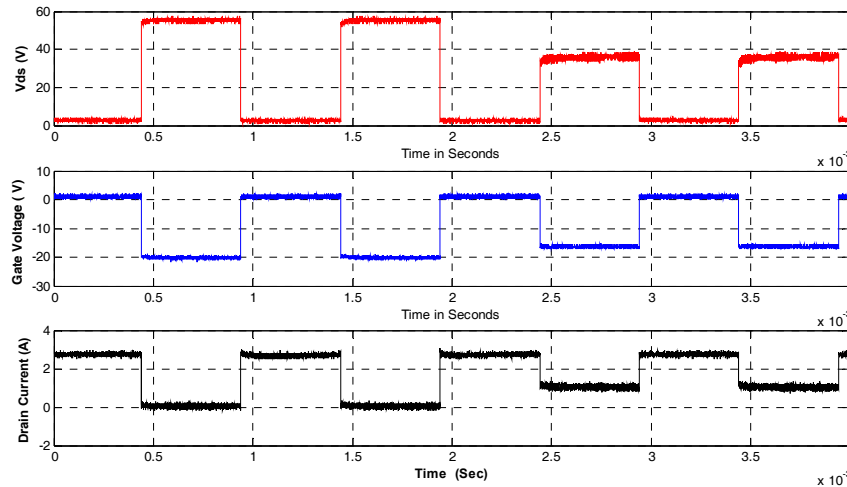


Figure 20. Gate voltage, drain voltage and, drain current waveforms of a SiC JFET.

III. Hybrid Packaging

To take advantage of the high-temperature operation capability of WBG devices, device packages that can withstand high temperatures are required. Various organizations are working toward high-temperature packaging. Several high-temperature packages that include discrete device packages to power modules have been reported in the past several years. However, even though the packages and devices can handle high temperatures, the low-power electronics that drive the power devices are limited to maximum temperatures of 200°C. Silicon-on-insulator (SOI) based technology and silicon-based electronics are limited to 125°C. Additionally, SOI-based electronics are expensive. High-temperature (more than 200°C) electronics have been reported as being feasible; however, they have not been built or designed. It could be many years before a logic level high-temperature transistor will be developed. This creates a void in the power module industry, especially with the IPM products, which include the electronics inside the module.

This proposed idea focuses on developing a hybrid package that includes high-temperature WBG devices and low-temperature silicon electronics. The developed package will provide an intermediate solution before complete high-temperature modules can be built. The innovative concept in this hybrid package is a thermal boundary layer separating the high-temperature zone from the low-temperature zone. This concept enables the use of low-temperature electronics in close proximity with high-temperature power devices in IPMs.

The SiC power device zone (high temperature) is allowed to operate at or below 300°C, and the silicon control circuit zone (low temperature and low power) is kept at or below 125°C. The structure was

modeled using the PRO-E CAD tool. To prove the concept, a feasibility study was done by modeling the package with different ambient conditions. The design concept was compared to a silicon-based IPM for physical sizing and heat flux requirements. The ambient temperature was fixed at 100°C, and it was assumed that fan-driven convection cooling was used on the heat transfer surfaces of the modules. This ambient temperature allows a 25°C temperature gradient between the junction of the silicon electronic devices and the ambient. The boundaries of the package were assumed to be insulated.

A comparison of the resulting module sizes is shown in Figure 21, indicating about a 75% reduction in volume when utilizing SiC for the power devices. The size reduction is mainly accomplished by the reduced volume of the heat sink/fins and reduced need for the typical heat spreading copper base in the conventional IPM. The results clearly indicate that the concept functions as expected.

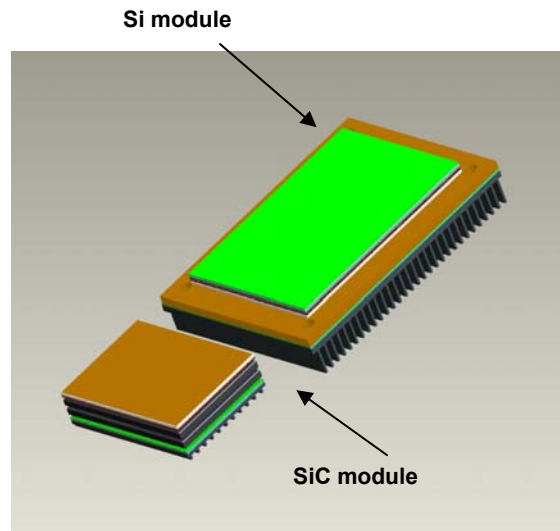


Figure 21. Comparison of sizes between hybrid package and silicon IPM.

IV. PSAT Traction Drive Model for a Plug-in HEV

PSAT HEV models use one integrated block that contains experimental data for the motor and the inverter, called a “motor controller.” The power loss of the inverter cannot be changed for different inverters because the data include the motor’s contribution. Therefore, new models were created to separate the motor and the inverter to be able to simulate all-silicon and all-SiC inverters.

The inverter model computes the inverter average power loss based on device characteristics and motor performance and uses an equivalent thermal circuit to estimate the rise of the device junction temperatures.

The motor model computes the ac current, voltage, and power factor of the motor and modulation index of PWM control that is used to calculate the losses in the inverter. The newly developed PSAT library block for the motor controller uses the above inverter and motor models to form a new motor controller model that uses the original block’s inputs and outputs (Figure 22).

The model was simulated for an Urban Driving Scheme cycle with both silicon-based and SiC-based inverters (assuming cooling conditions are the same). The results showed that the fuel economy is improved from 71.43 to 71.69 mpg (increased by 0.36%). The overall system efficiency is improved from 39.205% to 39.342% (increased by 0.35%).

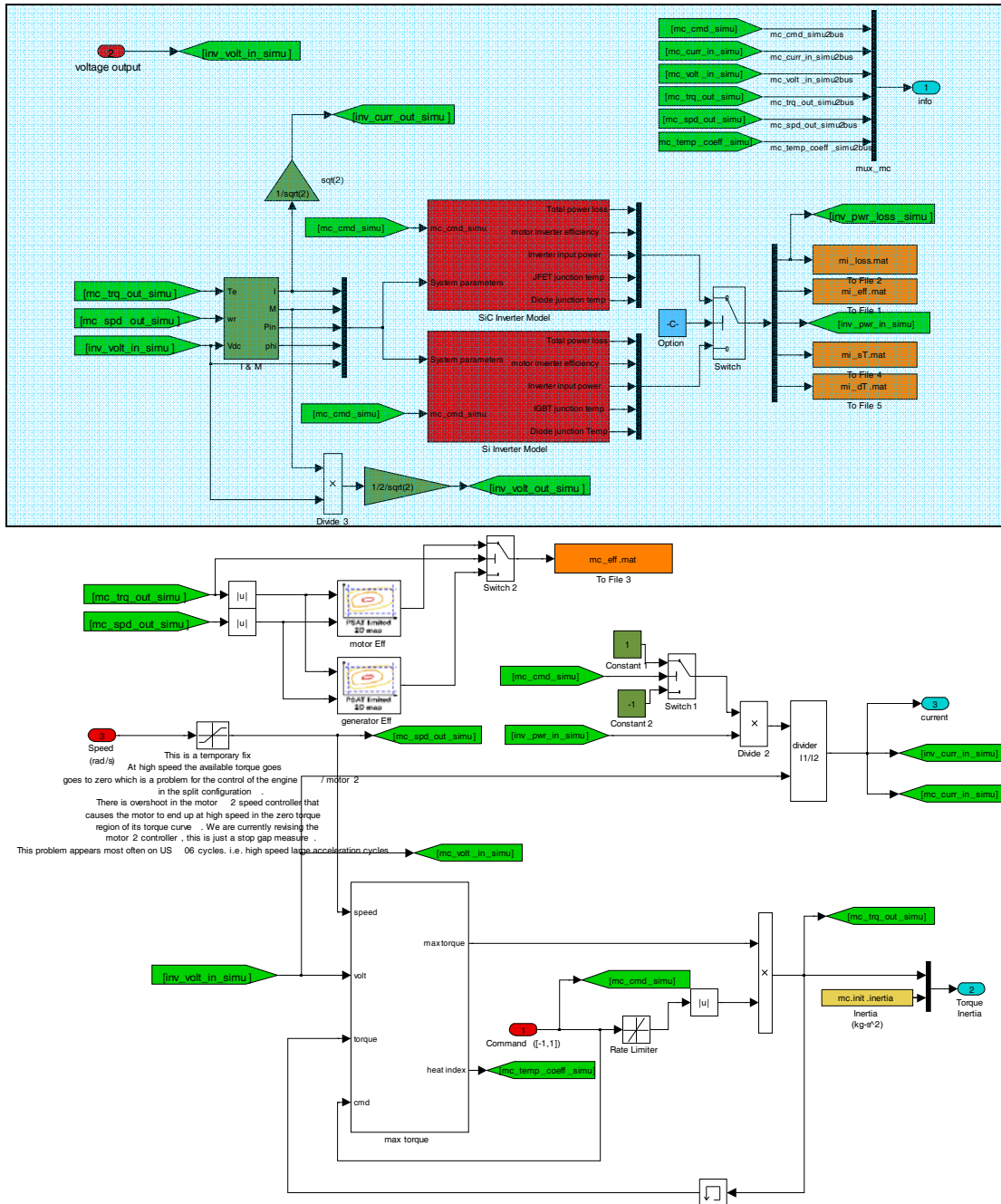


Figure 22. New motor controller model. The shaded portion shows the inverter models added to the block.

Conclusion

Several new devices (SiC Schottky diodes, JFET, and MOSFET) were acquired, tested, and modeled. A high-temperature hybrid package was developed and modeled. The simulation results showed that the package was feasible. An inverter loss model was successfully integrated into the drive train model in PSAT. The motor drive block in PSAT had one integrated unit. The motor drive in the drive train was split it into a motor and inverter block. A fault-current-limiting circuit for a SiC JFET was developed and tested.

Publications

H. Zhang, L. M. Tolbert, B. Ozpineci, and M. Chinthavali, "A SiC-based converter as a utility interface for a battery system," *IEEE Industry Applications Society Annual Meeting, October 8–12, 2006, Tampa, Florida*.

L. M. Tolbert, H. Zhang, M. Chinthavali, and B. Ozpineci, "SiC-based power converters for high temperature applications," *European Conference on Silicon Carbide and Related Materials, September 3–7, 2006, Newcastle, UK*.

Reference

1. M. Chinthavali, B. Ozpineci, L. M. Tolbert, and A. S. Kashyap, *Wide Bandgap Semiconductors*, ORNL/TM-2005-214, Oak Ridge National Laboratory, November 2005.

4.2 dc/dc Converters for HEVs and FCVs

Principal Investigator: Gui-Jia Su

Oak Ridge National Laboratory

National Transportation Research Center

2360 Cherahala Boulevard

Knoxville, TN 37932

Voice: 865-946-1330; Fax: 865-946-1262; E-mail: sugj@ornl.gov

DOE Technology Development Manager: Susan A. Rogers

Voice: 202-586-8997; Fax: 202-586-1600; E-mail: Susan.Rogers@ee.doe.gov

ORNL Program Manager: Mitch Olszewski

Voice: 865-946-1350; Fax: 865-946-1262; E-mail: olszewskim@ornl.gov

Objectives

- Overall project objective is to produce flexible converter topologies that
 - integrate the functions of power management in triple-voltage bus systems in electric vehicles(EVs)/hybrid electric vehicles (HEVs) to reduce component count, size, and cost;
 - is applicable to triple-voltage and dual-voltage systems; and
 - provides easy power scaling capability.
- The objective for the FY 2007 effort is to design, fabricate, and test a 6-kW prototype with
 - higher efficiency (>95%),
 - higher power density and specific power (exceeds the FreedomCAR 2015 targets), and
 - fast dynamic response.

Approach

- Employ a three-phase configuration to
 - reduce dc bus capacitor requirements,
 - increase dynamic response, and
 - Increase power density by spreading heat sources.

Major Accomplishments

- Developed two converter topologies:
 - one with an LC filter on the 14-V bus for 14-V dominant systems, and
 - one without the LC filter for 42-V dominant systems.
- Built and successfully tested a 6.4-kW prototype that met all technical goals:
 - greater than 95% efficiency across a wide load range,
 - high power density of 2.6 kW/L, and
 - fast dynamic response time (<30-ms settling time).

Technical Discussion

Background

The 42-V power net has been proposed to cope with the ever increasing vehicle electrical loads in automobiles. Although the anticipated widespread deployment of the 42-V systems has not materialized yet, as the automotive industry moves to drive-by-wire through the electrification of power steering, **braking, suspension, and other engine control actuators, the 42-V net will likely be needed**

to handle these heavy loads. This is because the existing 14-V system cannot efficiently power those loads and with the higher voltage (>200-V) (HV) bus for traction drive in full HEVs and fuel cell vehicles, it will be very difficult to meet the safety requirements and to suppress electromagnetic interference (EMI) by running high-voltage cables throughout the vehicle. While this is especially needed for fuel cell vehicles, which have no internal combustion (IC) engines to assist those mechanisms, drive-by-wire technology has already been employed in luxury vehicles. For instance, the Toyota RX400h SUV uses dc-dc converters to transform the traction battery voltage to 14 V for onboard electronics and to 42 V for electric power steering. In addition, the 42-V power system could be used for traction drives in mild hybrid vehicles. To date, some 42-V-based start/stop functions along with limited power assist capability have been implemented in pickup trucks and other vehicles on the market.

While full hybrids offer an option to eliminate the conventional starter/alternator, it may be kept as a backup for the motor/generator in the hybrid system. In HEVs with a 42-V alternator, a dc-dc converter supplied from the 42-V bus may be used to charge the high-voltage battery as shown in Figure 1(a). On the other hand, for HEVs having a generator directly connected on the HV bus, a dc-dc converter is typically required to charge the 14-V and/or 42-V batteries.

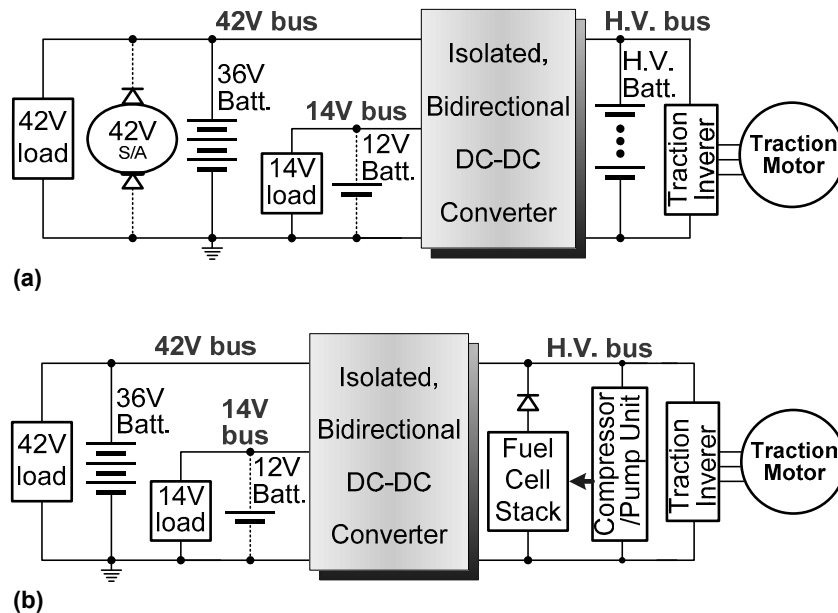


Figure 1. A dc-dc converter interconnecting 14-V/42-V/HV bus nets in hybrid and fuel-cell-powered vehicles.

Furthermore, when the HV bus is powered by a fuel cell, a bidirectional dc-dc converter is required to interconnect it to the low-voltage buses for vehicle auxiliary loads as shown in Figure 1(b). An energy storage device is also required for startup of the fuel cell and for storage of the energy captured by regenerative braking. One way to is to utilize the vehicle 12-V (on the 14-V bus) or 36-V (on the 42-V bus) battery with the bidirectional dc-dc converter. During vehicle starting, the HV bus is raised up to around 300 V by the dc-dc converter, drawing power from the 14-V or 42-V battery. This HV bus then supplies power for the fuel cell compressor motor expanding unit controller and brings up the fuel cell voltage, which in turn feeds back to the HV bus to release the loading from the battery. Kinetic energy, captured by regenerative braking, can also be stored in the battery by operating the converter in the buck mode.

In summary, a triple-voltage bus (14-V/42-V/HV) system will likely be employed in future HEVs and fuel-cell-powered vehicles. Dc-dc converters are already available to interconnect any two of the buses; however, to reduce component count, size, cost, and volume, it is desirable to employ an integrated dc-dc

converter to interconnect the three voltage buses instead of using two separate converters. Aside from bidirectional power control capability, the converter needs to provide galvanic isolation between the low- and high-voltage buses to meet safety requirements. Further, soft switching is preferred over hard switching because of the reduced level of EMI and switching losses.

The overall project objective is to produce flexible converter topologies that (1) can integrate the power management functions of two converters to reduce component count, size, and cost; (2) are applicable to triple-voltage and dual-voltage systems; and (3) can provide easy power scaling capability to meet power requirements of different size vehicles. To this end, two low-cost, soft-switched, isolated bidirectional dc-dc converter topologies have been developed and are shown in Figure 2. The topology in Figure 2(a) is suited for 14-V dominant systems, where most of the traditional vehicle loads remain in the 14-V net, while the 42-V net supports newly added functions such as electrical power steering. After a majority of the 14-V vehicle loads have transitioned to the 42-V net and the power requirement for the 14-V net decreases, the 12-V battery can be eliminated. For such systems, the dc-dc converter does not need to transfer power out of the 14-V bus. Figure 2(b) presents a dc-dc converter topology for power management in such triple-voltage vehicle power systems with a further reduced-part count. Both topologies consist of dual half-bridges and a high-frequency transformer. The transformer provides the required galvanic isolation and voltage level matching between the low-voltage buses and the HV bus, while the 14-V and 42-V buses share a common ground. In the topology shown in Figure 2(b), the 14-V bus is derived by tapping the capacitor leg at the midpoint, eliminating the buck/boost inductor, L_f and the filter capacitor, C_f on the 14-V bus in the topology shown in Figure 2(a).

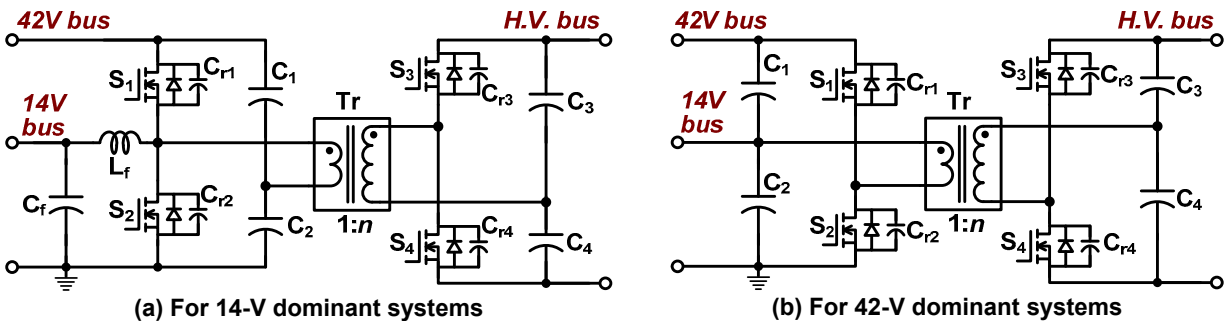


Figure 2. Schematic of the soft-switched, bidirectional dc-dc converters for triple-voltage bus systems.

The use of dual half-bridges in both proposed topologies offers several advantages. It minimizes the number of switching devices—only four—and their associated gate driver components. This saving in part counts becomes more significant in multiphase configurations, which are preferred for high-power applications due to reduced ripple current and ease of packaging. The half-bridge converters are well suited for multiphase arrangements because all the phases can share the two capacitor legs, and the required capacitances do not necessarily increase with the number of phases. On the contrary, they can be reduced because the currents flowing into the midpoints of the capacitor legs decrease while their frequency multiplies. This leads to further reduction in component count and volume.

Another advantage of the proposed converters arises from the fact that no dedicated active switches are needed for soft-switching. The leakage inductance of the transformer together with the snubber capacitors, including the parasitic capacitance of the switches, $C_{r1} \sim C_{r4}$, are utilized to provide soft-switching for the switches. The resonance between the capacitors and the inductor after each switching operation enables the switches to turn on under zero current and voltage, while the snubber capacitors allow them to turn off at zero voltage. It is worth noting that external snubber capacitors can be eliminated if the switches' parasitic capacitance is sufficient to ensure soft-switching operations over a desired range of load current, which is often the case with high-current metal oxide semiconductor field-effect transistors (MOSFETs) due to their large silicon areas. The inherent soft-switching capability and

the low component count of the converter allow high power density, efficient power conversion, and compact packaging.

The objective for the FY 2007 effort was to design, fabricate, and test a 6-kW prototype using a three-phase configuration with these goals: (1) higher efficiency (>95%), (2) higher power density and specific power (exceed FreedomCAR 2015 targets), and (3) fast dynamic response

Description of the Reduced-Part dc-dc Converter

Figure 3 shows a schematic of the reduced-part, triple-voltage dc-dc converter in a three-phase configuration. It consists of three converter building blocks connected in parallel and two capacitor legs shared by all the blocks. The phase angles of the transformer voltages and currents of the converter blocks are shifted by 120 electrical degrees by interleaving the switching patterns to reduce the ripple currents flowing into the capacitors, thus reducing the capacitor volume and size.

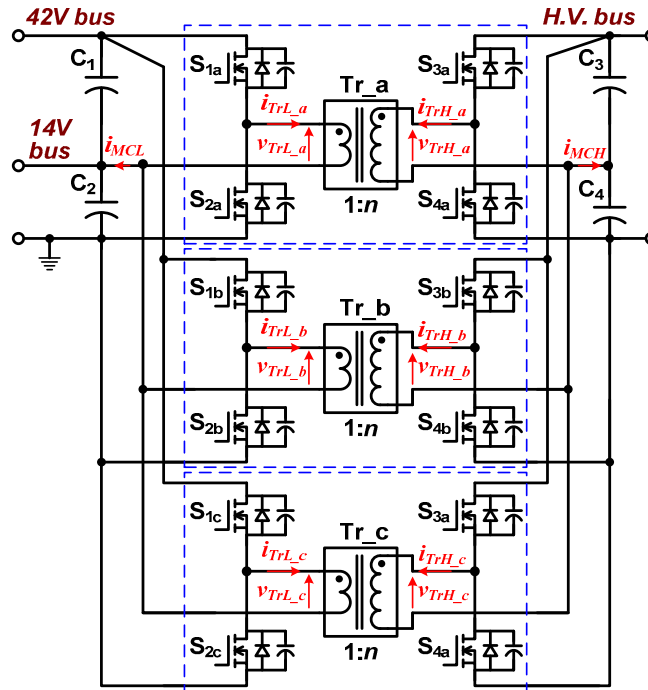


Figure 3. Schematic of the reduced-part, triple-voltage dc-dc converter in a three-phase configuration.

Control of power flow among the three busses is based on a combined duty ratio and phase shift angle control. At steady state, the voltages across the capacitors, C_1 and C_2 , C_3 , and C_4 , are determined by the duty ratio, d , as follows:

$$\begin{cases} V_{C1} = (1-d) \cdot V_{42V} \\ V_{C2} = d \cdot V_{42V} \\ V_{C3} = (1-d) \cdot V_{HV} \\ V_{C4} = d \cdot V_{HV} \end{cases}, \quad (1)$$

where $V_{C1} \sim V_{C4}$ represents the voltage across the capacitors and $C_1 \sim C_4$, and V_{42V} and V_{HV} represent the voltage of the 42-V and HV busses, respectively. This is due to the fact that the products of volt × second of the transformer primary and secondary voltages over the positive half cycles must be equal to those

over the negative half cycles. Therefore, duty ratio adjustment can be utilized for making the 14-V bus voltage, V_{14V} , track the 14-V bus voltage by

$$V_{14V} = d \cdot V_{42V} \quad (2)$$

For 14-V/42-V systems, the duty ratio is fixed at $d = 1/3$ for normal operation and can be changed to regulate the bus voltage during load transients.

Control of the power flow between the low-voltage and HV sides can be achieved by adjusting the switching frequency and the phase shift angle between the transformer terminal voltages. A phase shift angle, ϕ , is employed for the power flow control as shown in Figure 4. Power flows from the 42-V bus to the HV bus when the phase of the transformer primary voltages, v_{TrL} , supplied by the 42-V half-bridges is leading the secondary voltages, v_{TrH} , supplied by the HV half-bridges. The converter thus works in the boost mode to power the HV bus. By making the phase of the secondary voltage lead the primary voltage, power flow is reversed.

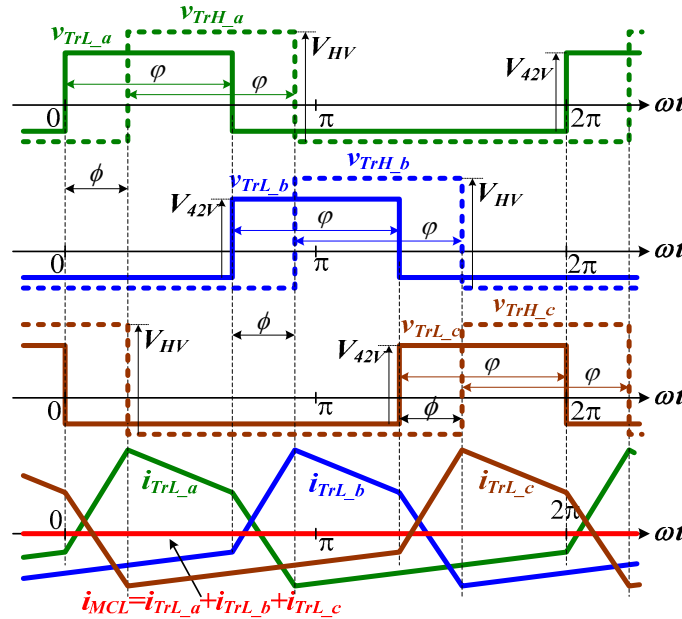


Figure 4. Operating waveforms showing interleaved voltages and currents and phase angle between the transformer low- and high-side terminal voltages for power flow control.

A power flow equation can be derived from the relationships of the transformer voltages and currents. Assuming the duty ratio is fixed at 1/3, that is, $\phi = 2\pi/3$ at steady state, the power transferred across the transformers can be expressed by

$$P = \frac{V_{42V} V_{HV}}{n} \cdot \frac{\phi}{\pi f_{sw} L_s} \cdot \left[\frac{1}{3} - \frac{3\phi}{8\pi} \right] \quad (6)$$

where n is the transformer turns ratio, L_s is the transformer leakage inductance, and f_{sw} is the switching frequency. For a given design, the maximum power that can be transferred is determined by

$$P_{\max} = \frac{V_{42V} V_{HV}}{n} \cdot \frac{2}{81 f_{sw} L_s} \dots, \text{ at } \phi_{P_{\max}} = \frac{4\pi}{9} \quad (7)$$

Equation (6) indicates that, for a fixed duty cycle and switching frequency, the power is related to the phase shift angle and transformer leakage inductance. For a given amount of power, a smaller leakage inductance results in a smaller phase shift angle. To reduce the circulating current and to improve the efficiency, the phase shift angle should be kept as small as possible. Therefore, the leakage inductance needs to be minimized. On the other hand, a higher leakage inductance provides soft-switching operation over a wider range of load current. Automotive applications usually require a higher peak power for a short period of time, typically in a few tens of seconds. Equation (7) can be used to help a design meet the peak power requirement.

For a given low-side bus voltage, V_{42V} , and switching frequency, f_{sw} , varying the duty ratio, d , will change the voltage distribution between the two capacitors, C_1 and C_2 , and thus the peak flux linkage, Ψ_{peak} , of the transformer. Assuming the voltage drops across the switches can be ignored, the positive transformer primary voltage is equal to the capacitor voltage, V_{C1} , and this voltage is applied for an interval of $t_p = d/f_{sw}$, which corresponds to a phase angle of $\phi = d \cdot 2\pi$. Similarly, the negative primary voltage, V_{C2} , is imposed over an interval of $t_n = (1-d)/f_{sw}$. At steady state, the products of voltage and time over the positive and negative cycles must be equal; that is, $V_{C1} \cdot t_p = V_{C2} \cdot t_n$, which also holds for the secondary voltage. This leads to

$$\frac{V_{C1}}{V_{C2}} = \frac{V_{C3}}{V_{C4}} = \frac{1-d}{d} \quad (8)$$

The peak flux linkage, Ψ_{peak} is then determined by

$$\Psi_{peak} = \frac{d \cdot (1-d) \cdot V_{42V}}{2 f_{sw}} \quad (9)$$

It is worth noting that operating at a duty ratio other than the typical value of 0.5 for the half-bridge converters will decrease the peak flux and thereby transformer core size. Figure 5 plots peak flux normalized by the flux at a 50% duty cycle against the duty ratio. The maximum value at $d = 0.5$, λ_{peak} , is given by

$$\lambda_{peak(d=0.5)} = \frac{V_{42V}}{8 n_p f_{sw}} \quad (10)$$

where n_p is the number of turns of the primary winding. However, at $d = 1/3$ for the proposed converter, the peak flux is reduced to

$$\lambda_{peak(d=1/3)} = \frac{V_{42V}}{9 n_p f_{sw}} \quad (11)$$

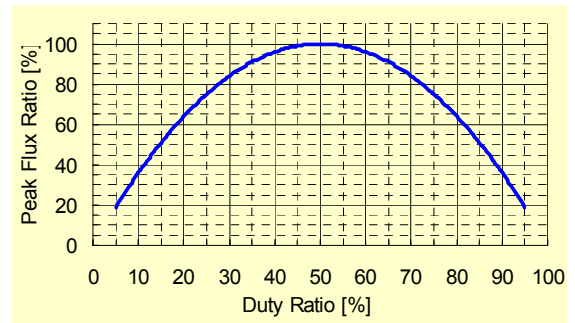


Figure 5. Normalized transformer peak flux vs duty ratio.

Comparing Eqs. (10) and (11) reveals that the cross-sectional area of the transformer core can be reduced by 11% at the same switching frequency and number of turns.

Simulation, Prototype Build, and Experimental Results

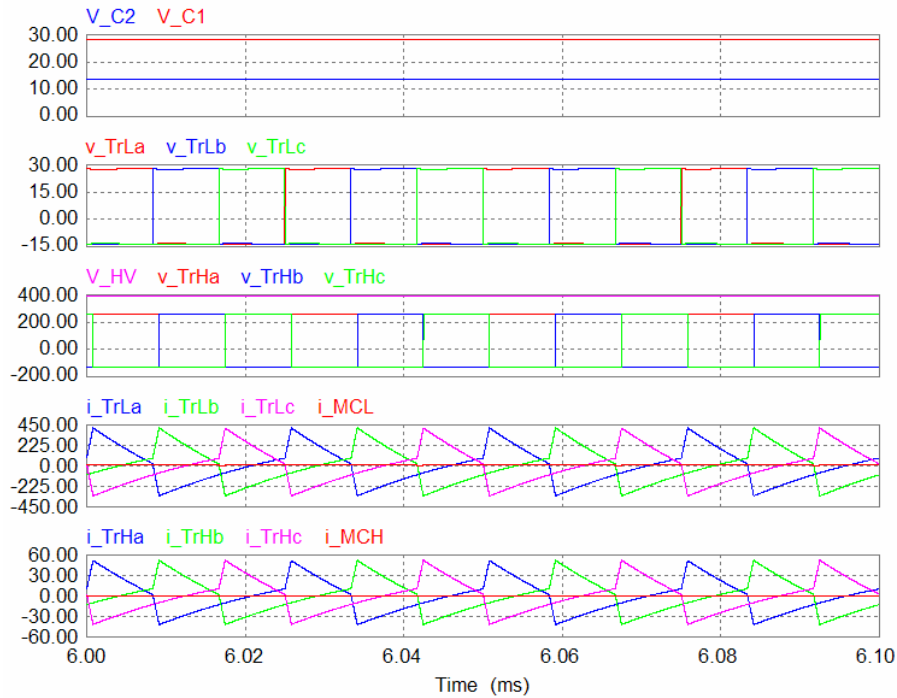
The converter is required to transfer a rated power of at least 6 kW from the 42-V bus to the 14-V and high-voltage busses or from the high-voltage bus to the other two busses. To meet this requirement, transformer parameters were designed as follows: $n = 8$, $L_s = 0.15 \mu\text{H}$. The switching frequency was selected at $f_{sw} = 40 \text{ kHz}$. A detailed circuit simulation was first performed to verify the design goal. Figure 6 gives simulation results showing bidirectional power flows. In Figure 6(a), 6.1 kW is provided from the 42-V bus to the 14-V and HV busses (boost mode), while in Figure 6(b) the same amount of power is transferred from the HV bus to the 42-V and 14-V nets (buck mode). The simulation results confirm the design goals. It is also confirmed that currents flowing into the midpoint of the low- and high-voltage side capacitor legs, i_{MCL} and i_{MCH} , are significantly lower than each individual transformer current. These significantly reduced capacitor currents enable a substantial reduction of the capacitance requirements.

Incorporating the modeling results, a 6.4-kW reduced-part-count converter prototype was designed and fabricated. Figure 7 shows a photo of the prototype, which is laid on a liquid-cooled heat sink with a footprint of 11 by 7.8 in. Planar transformers were designed for use in the prototype due to the advantages of tight control of the leakage inductance and easy assembly. To meet the requirement of transferring a rated continuous power of at least 6 kW over a HV bus voltage range of 250 V ~ 400 V, the ferrite E core, E64/10/50-3C92 made by Ferroxcube, was selected, which has an effective cross-sectional area of 519 mm^2 . With a two-turn primary winding, the nominal peak flux density is calculated as $B = 0.25 \text{ T}$ at $f_{sw} = 40 \text{ kHz}$. Other parameters were designed as follows: $n = 8$, $L_s = 0.15 \mu\text{H}$. The HV switches are implemented with CoolMOS MOSFETs (IXYS IXKN 75N60C), and the low-voltage switches are standard MOSFETs. The power flow control is implemented with a digital signal processor, TI TMS320F1808, which has high-resolution PWM generators and operates at 100 MHz. Power density is calculated at 2.6 kW/L, which is 30% higher than that of the prototype developed in FY 2006.

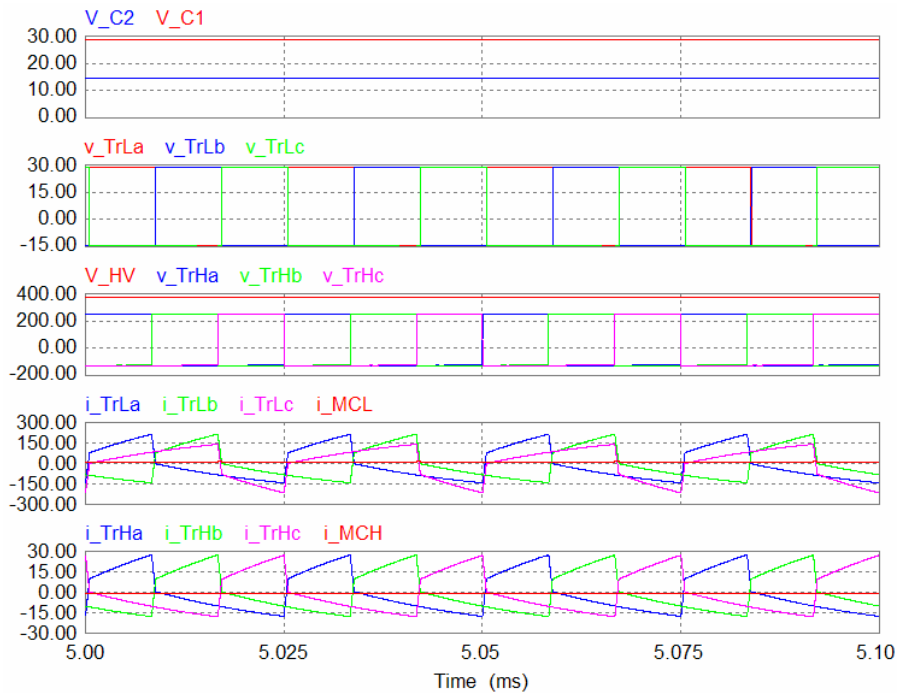
To verify the combined duty ratio and phase shift angle control scheme for power flow management, a test setup was assembled with voltage and current probes connected at various points on the prototype to monitor the operating waveforms and measure the input and output power. Oscilloscopes and a Yokogawa digital power analyzer were used to take measurements. Figure 8 shows a photo of the test setup. The converter was tested for characterizing efficiency and dynamic response in both the buck and boost modes by connecting a dc power source at the 42 V or HV bus for powering resistive loads on the other two busses.

Figure 9 shows typical experimental transformer voltage and current waveforms in the buck mode with 6.05 kW (left) and in the boost mode with 6.01 kW (right). Three-phase HV side currents and the HV and LV side voltages of phase A were recorded (refer to Figure 3 for the trace labels). The fact that little ringing appeared on the voltage and current waveforms indicates soft-switching operation.

Figure 10 plots efficiency against the combined load power for both high to low (buck) and low to high (boost) conversion. The measured efficiency is between 95.0% and 96.9% over a wide output power range from 1 kW to the maximum power. Improvements of 2 ~ 3 percentage points are achieved over the two-phase prototype developed in FY 2006. Under light load conditions, zero-voltage switching was not achievable, which resulted in lower efficiency. The recorded maximum output power was 6.4 kW in the boost mode.



(a) Boost mode: power transfer from 42 V to the 14-V and HV busses



(b) Buck mode: power transfer from the HV bus to the 14-V and 42-V busses

Figure 6. Simulation results showing bidirectional power flow. V_{C1} and V_{C2} : voltage across respective capacitor C1 or C2; V_{TrLa} , V_{TrLb} , V_{TrLc} : primary voltage of the respective transformer; V_{TrHa} , V_{TrHb} , V_{TrHc} : secondary voltage of the respective transformer; i_{TrLa} , i_{TrLb} , i_{TrLc} : primary current of the respective transformer; i_{TrHa} , i_{TrHb} , i_{TrHc} : secondary current of the respective transformer; i_{MCL} , i_{MCH} : current flowing into the midpoint of the low- and high-voltage side capacitor legs, respectively.

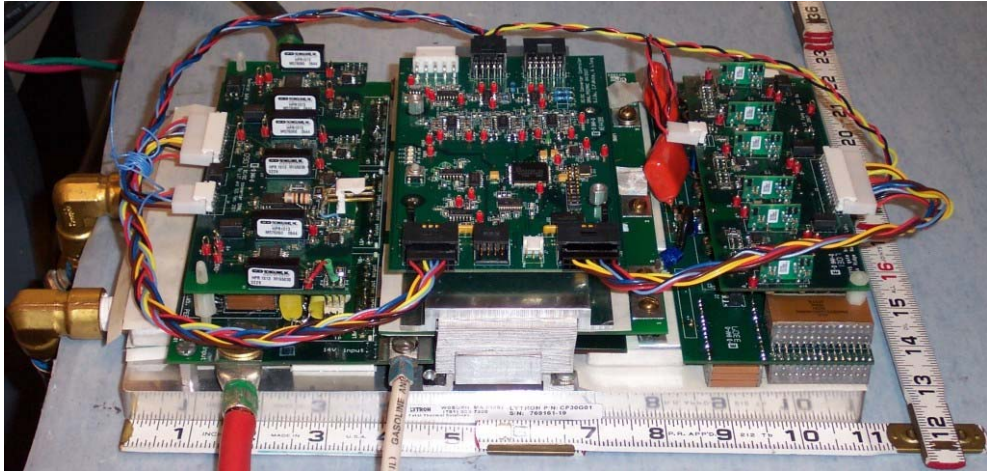


Figure 7. Photo of the 6.4-kW prototype. Footprint: 11 in. wide \times 7.8 in. deep, and maximum height: 2.5 in.

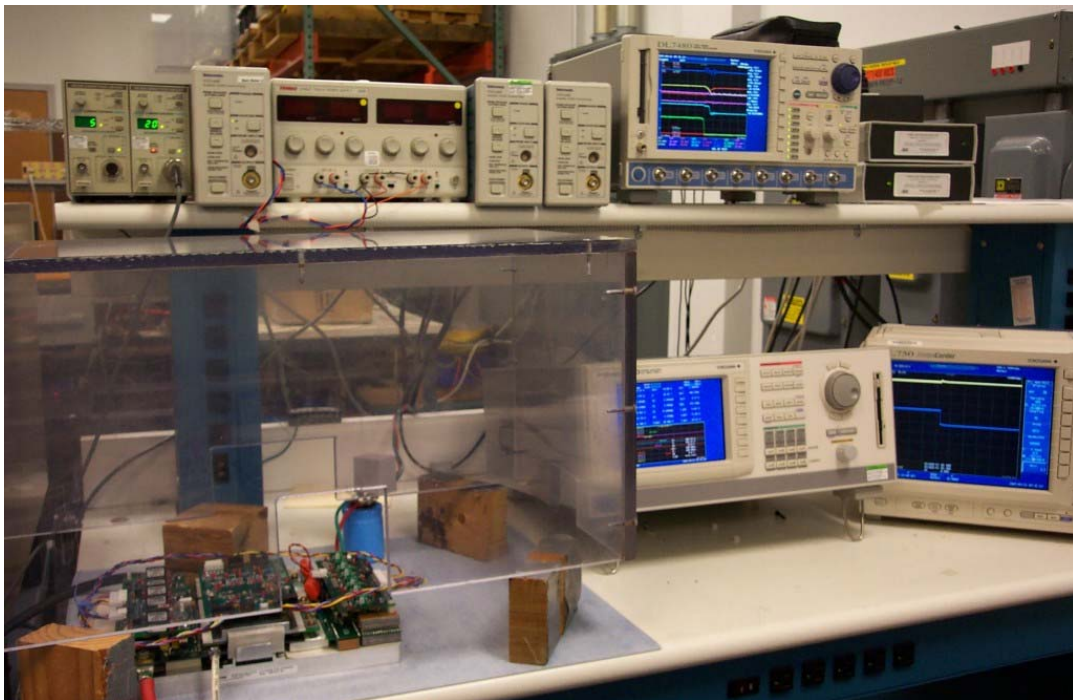


Figure 8. Photo of the test setup.

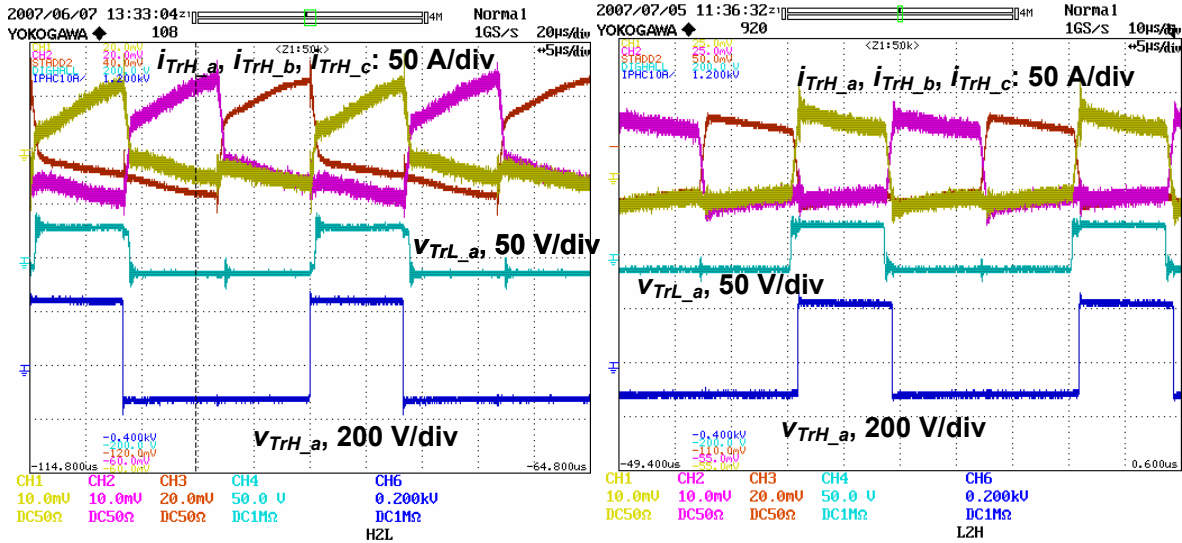


Figure 9. Experimental results of the converter in the buck mode with a combined load power of 6.05 kW (left) and in the boost mode at 6.01 kW (right), respectively.

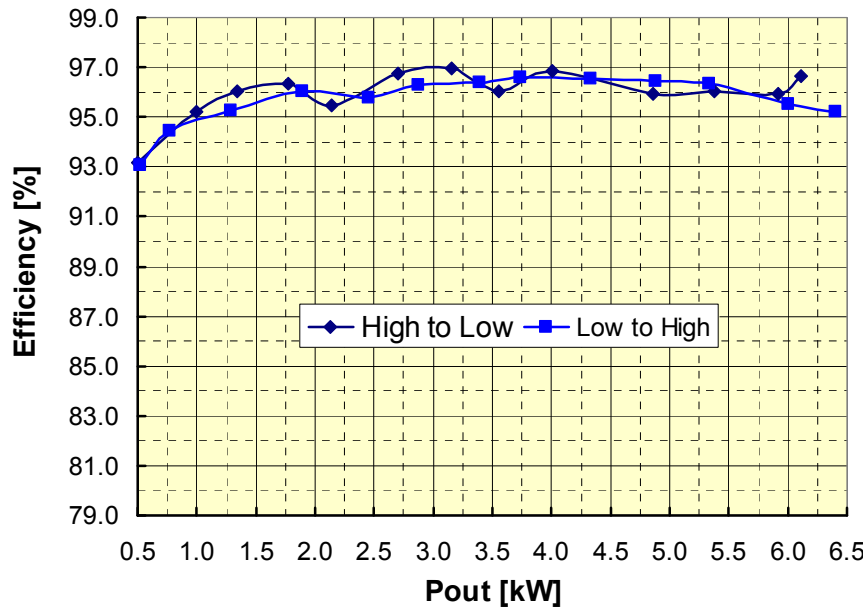


Figure 10. Measured conversion efficiency in both the boost and buck modes.

To evaluate dynamic response of the 42-V and HV bus voltages to step changes in the load current, tests were conducted by switching on and then off a resistor on the 42-V and then HV busses. Figure 11 shows the 42-V bus voltage and load current waveforms during a step change of 1.2 kW at the 42-V bus. A settling time of less than 20 ms was measured. Similarly, Figure 12 shows the bus voltage and load current waveforms during a step change of 1.1 kW at the HV side. A settling time of less than 3 ms was measured. The measured settling times were well within our target of 50 ms.

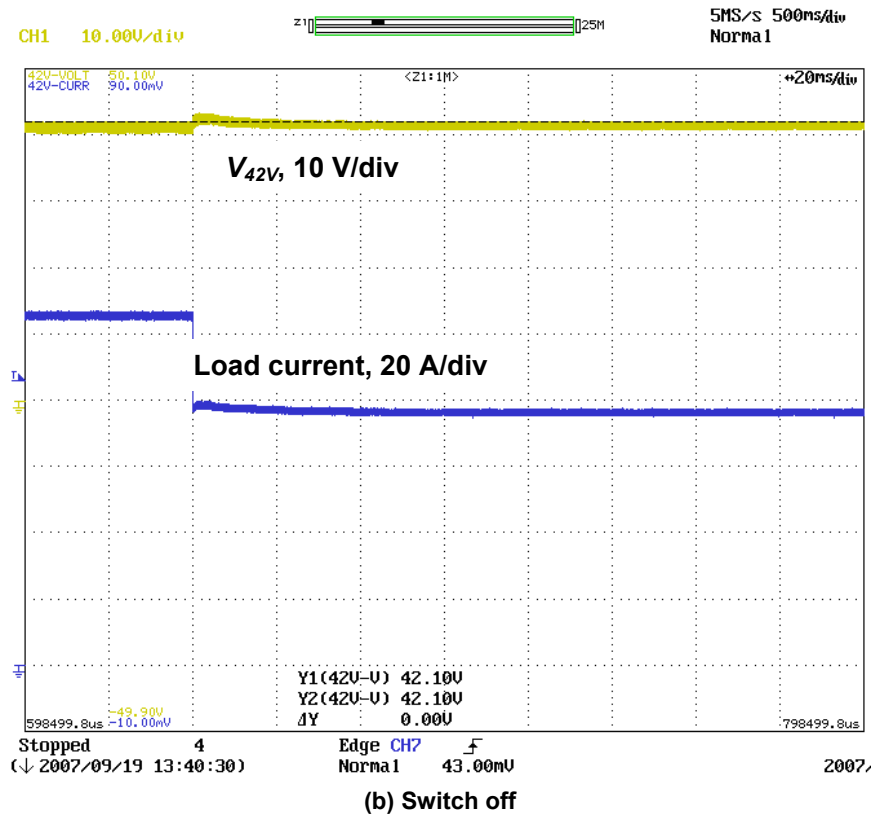
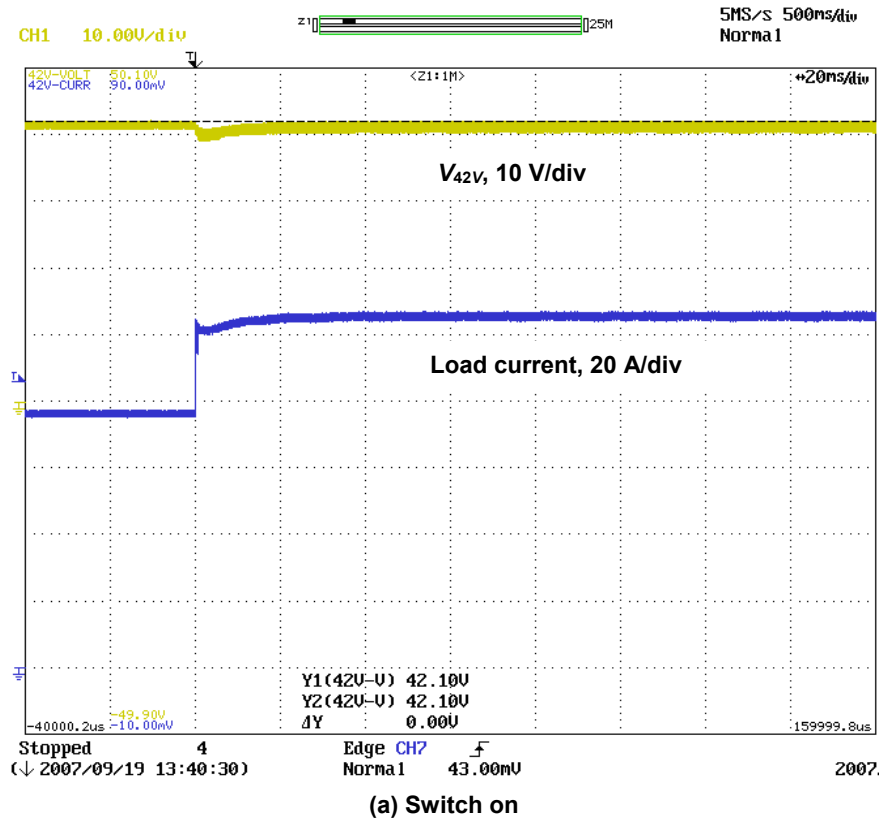


Figure 11. Response to switching on and then off a 1-kW resistor on the 42-V bus.

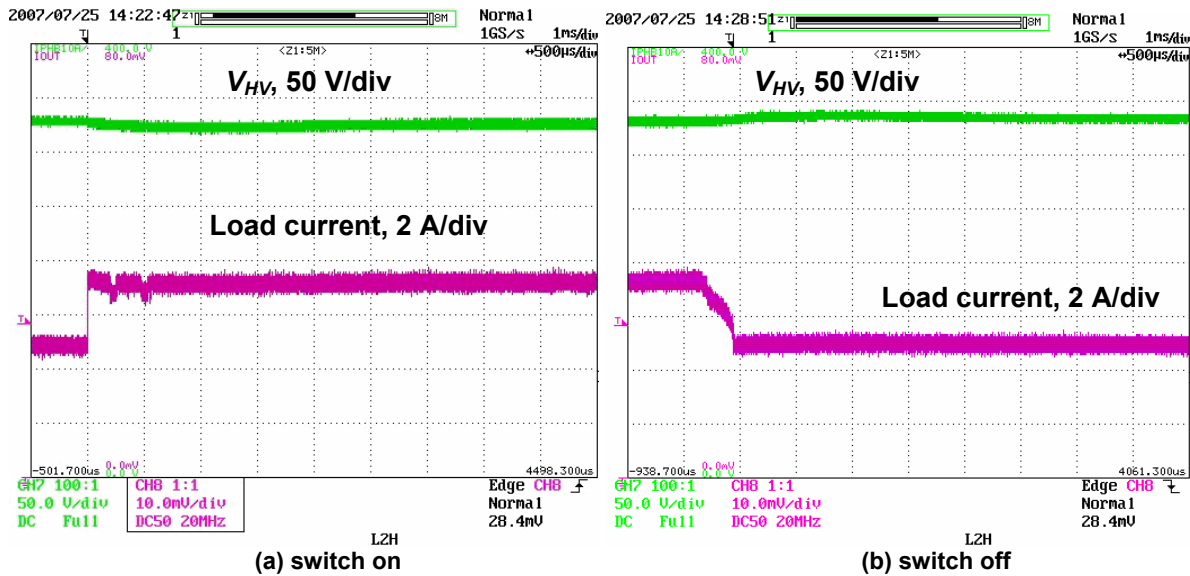


Figure 12. Response to switching on and then off a 1-kW resistor on the HV side.

Conclusion

This project generated two dc-dc converter topologies for power management in triple-voltage-bus (14-V/42-V/HV) systems in electric and hybrid vehicles. The converters offer many advantages: (1) use only four switching devices, leading to significant cost savings and higher power density; (2) require no auxiliary circuit or complex control dedicated for soft switching; (3) provide galvanic isolation between the low- and high-voltage nets; (4) achieve flexible power flow management with bidirectional power transfer between the low-voltage buses and the HV bus by employing the combined duty ratio and phase shift angle control schemes; and (5) are suitable for modular, power-scalable configurations.

The reduced-part dc-dc converter eliminates the buck/boost inductor and filter capacitor from the first topology while retaining its favorable features. Simulation and experimental results on a 6- to 4-kW prototype confirmed the operating principle and high efficiency, high power density, and fast dynamic response.

Publications

L. Tang and G. J. Su, "An interleaved, reduced component count, multi-voltage bus dc/dc converter for fuel cell powered electric vehicle applications," in *Proceeding of 2007 IEEE IAS Annual Meeting (IAS'07)*, September 23–27, 2007, New Orleans, Louisiana.

G. J. Su, J. Cunningham, and L. Tang, "A reduced-part, triple-voltage dc-dc converter for electric vehicle power management," in *Proceeding of IEEE 38th Annual Power Electronics Specialists Conference (PESC'07)*, June 17–21, 2007, Orlando, Florida, pp. 1989–1994.

G. J. Su and L. Tang, "A bidirectional, triple-voltage dc-dc converter for hybrid and fuel cell vehicle power systems," *IEEE Applied Power Electronics Conference and Exposition 2007 (APEC'07)*, February 25–March 1, 2007, Anaheim, California, **2**, 1043–1049.

Patent

"Triple Voltage dc-to-dc Converter and Method," pending.

References

1. J. G. Kassakian, H. Wolf, J. M. Miller, and C. J. Hurton, "The future of automotive electrical systems," *Proc. of IEEE Workshop on Power Electronics in Transportation*, Dearborn, Michigan, October 1996, pp. 3–12.
2. J. G. Kassakian, "Future automotive electrical systems—the power electronics market of the future," *Proc. of the IEEE Applied Power Electronics Conference*, New Orleans, February 2000, pp. 3–9.
3. S. Murthy, T. Sebastian, and B. Liu, "Implications of 42V battery power on the design of motors for electric power steering system," *SAE Future Transportation Technology Conference*, Costa Mesa, California, August 21–23, 2000, Paper 2000-00-3068.
4. R. W. Stence, "Digital by-wire replaces mechanical systems in cars," *SAE Powertrain & Fluid Systems Conference and Exhibition, Tampa, Florida, October 25–28, 2004*, Paper 2004-01-2926.
5. M. Naidu, R. Henry, and N. Boules, "A 3.4 kW, 42 V, high efficiency automotive power generation system," *SAE Future Transportation Technology Conference, Costa Mesa, California, August 21–23, 2000*, Paper 2000-01-3064.
6. R. W. Stence, "Shifting to 42 volt hybrid systems," *SAE Powertrain & Fluid Systems Conference and Exhibition, Tampa, Florida, October 25–28, 2004*, Paper 2004-01-3067.
7. F. Z. Peng, H. Li, G. J. Su, and J. S. Lawler, "A new ZVS bi-directional dc-dc converter for fuel cell and battery applications," *IEEE Trans. on Power Electronics* **19**(1), 54–65 (January 2004).
8. G. J. Su and F. Z. Peng, "A low cost, triple-voltage bus dc/dc converter for automotive applications," *the IEEE Applied Power Electronics Conference and Exposition (APEC)*, March 6–10, 2005, Austin, Texas, **2**, 1015–1021.
9. G. J. Su and L. Tang, "A bidirectional, triple-voltage dc-dc converter for hybrid and fuel cell vehicle power systems," in *Conf. Rec. IEEE Applied Power Electronics Conference and Exposition 2007 (APEC'07)*, February 25–March 1, 2007, Anaheim, California, **2**, 1043–1049.

4.3 Cascade Multilevel Inverter for Fuel-Cell-Based HEV

Principal Investigator: Burak Ozpineci

Oak Ridge National Laboratory

National Transportation Research Center

2360 Cherahala Boulevard

Knoxville, TN 37932

Voice: 865-946-1329; Fax: 865-946-1262; E-mail: ozpinecib@ornl.gov

DOE Technology Development Manager: Susan A. Rogers

Voice: 202-586-8997; Fax: 202-586-1600; E-mail: Susan.Rogers@ee.doe.gov

ORNL Program Manager: Mitch Olszewski

Voice: 865-946-1350; Fax: 865-946-1262; E-mail: olszewskim@ornl.gov

Objectives

- To produce a cascade multilevel inverter that combines inverter and converter functions.
- To eliminate the magnetics required for the direct current (dc)-dc boost converter, therefore reducing the weight, volume, and cost of the system while increasing its efficiency.

Approach

- Assess the performance and cost trade-offs to come up with a viable design.
- Simulate the inverter/converter in PSpice for circuit operation.
- Develop a model of the electric traction drive system (inverter/converter/motor) in Simulink.
- Design, build, and test a 1.2-kW unit.
- Test the unit with a fuel-cell power source.
- Develop a plug-in hybrid electric vehicle (HEV) version of the converter and simulate it.

Major Accomplishments

- Developed a control algorithm to keep the capacitors charged.
- Simulated the inverter/converter in PSpice and Simulink.
- Developed a model of an electrical drive system with the inverter/converter.
- Designed, built, and tested a 1.2-kW prototype.
- Tested the unit with a fuel-cell power source.
- Developed a plug-in HEV version of the converter and simulated it.

Future Direction

- Develop new control algorithms to increase the boost ratio to three.
- Implement and test the new control algorithms.

Technical Discussion

A cascade multilevel inverter is a power electronic device built to synthesize a desired alternating current (ac) voltage from several levels of dc voltages. Such inverters have been the subject of research in the last several years [1–4], where the dc levels were considered to be identical because all of them were batteries, solar cells, etc. In Ref. 5, a multilevel converter was presented in which the two separate dc sources were the secondaries of two transformers coupled to the utility ac power. Corzine et al. [6] have proposed using a single dc power source and capacitors for the other dc sources. A method was given to

transfer power from the dc power source to the capacitor to regulate the capacitor voltage. A similar approach was later (but independently) proposed by Du et al. [7]. These approaches required a dc power source for each phase. Similar methods have also been proposed by Veenstar and Rufer [8,9]. The approach here is very similar to that of Corzine et al. [6] and Du et al. [7] with the important exception that only a single standard three-leg inverter is required as the power source (one leg for each phase) for the three-phase multilevel inverter.

Specifically, the interest here is in using a single dc power source connected to a standard three-leg inverter, which in turn is connected to capacitors to form a three-phase five-level cascade multilevel inverter to be used as a drive for a permanent magnet (PM) traction motor or induction motor. The five-level inverter consists of a standard three-leg inverter (one leg for each phase) and an H-bridge in series with each inverter leg, using a capacitor as a dc source. It is shown that one can simultaneously maintain the regulation of the capacitor voltage while achieving an output voltage waveform that will be higher than that obtained using a standard three-leg inverter by itself.

Inductor-less cascaded multilevel inverter architecture

The topology of the proposed inductor-less dc-ac cascaded H-bridge multilevel boost inverter is shown in Figure 1. The inverter uses a standard three-leg inverter (one leg for each phase) and an H-bridge with a capacitor as its dc source in series with each phase leg.

To see how the system works, a simplified single-phase topology is shown in Figure 2. The output voltage v_1 of this leg of the bottom inverter (with respect to the ground) is either $+V_{dc}/2$ (S_5 closed) or $-V_{dc}/2$ (S_6 closed). This leg is connected in series with a full H-bridge, which in turn is supplied by a capacitor voltage. If the capacitor is kept charged to $V_{dc}/2$, then the output voltage of the H-bridge can take on the values $+V_{dc}/2$ (S_1, S_4 closed), 0 (S_1, S_2 closed or S_3, S_4 closed), or $-V_{dc}/2$ (S_2, S_3 closed). An example output waveform that this topology can achieve is shown in Figure 3(a). When the output voltage $v = v_1 + v_2$ is required to be zero, one can either set $v_1 = +V_{dc}/2$ and $v_2 = -V_{dc}/2$ or $v_1 = -V_{dc}/2$ and $v_2 = +V_{dc}/2$.

Further detail about the capacitor's voltage regulation is illustrated in Figure 3. During $\theta_1 \leq \theta \leq \pi$, the output voltage in Figure 3(a) is zero, and the current $i > 0$. If S_1, S_4 are closed (so that $v_2 = +V_{dc}/2$) along with S_6 closed (so that $v_1 = -V_{dc}/2$), then the capacitor is discharging [$i_c = -i < 0$ see Figure 3(b)] and $v = v_1 + v_2 = 0$. On the other hand, if S_2, S_3 are closed (so that $v_2 = -V_{dc}/2$) and S_5 is also closed (so that $v_1 = +V_{dc}/2$), then the capacitor is charging [$i_c = i > 0$ see Figure 3(c)] and $v = v_1 + v_2 = 0$. The case $I < 0$ is accomplished by simply reversing the switch positions of the $i > 0$ case for charging and discharging of the capacitor. Consequently, the method consists of monitoring the output current and

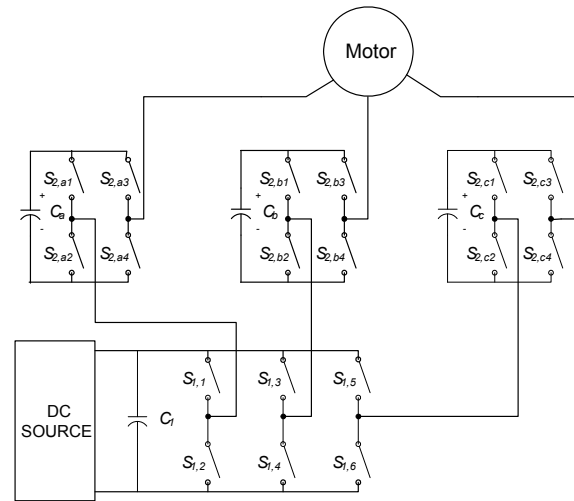


Figure 1. Topology of the proposed inductor-less dc-ac cascaded H-bridge multilevel boost inverter.

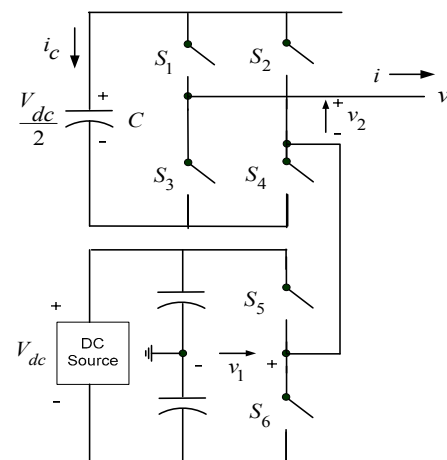


Figure 2. Single phase of the proposed inductor-less dc-ac cascaded H-bridge multilevel boost inverter.

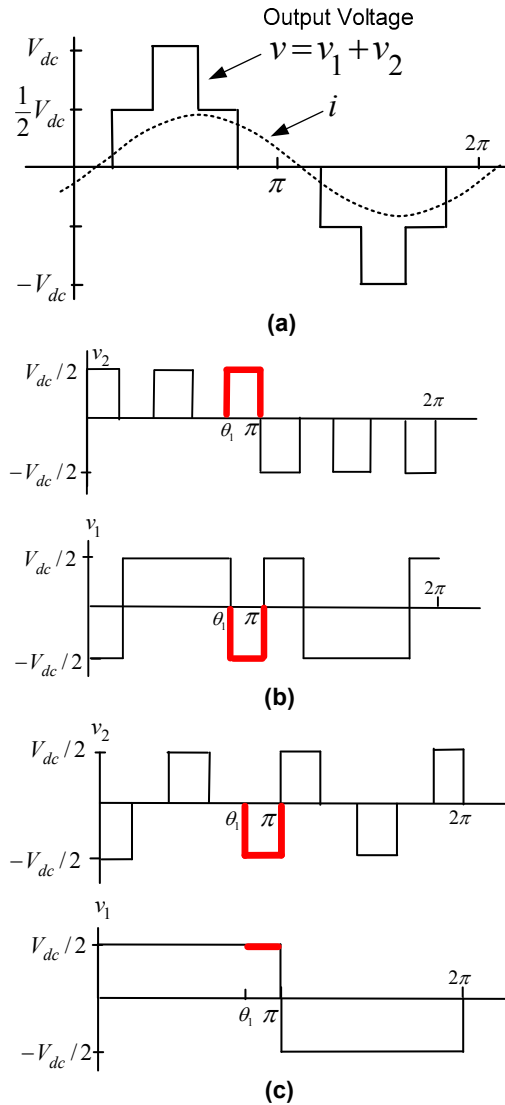


Figure 3. Capacitor voltage regulation with capacitor charging and discharging (a) overall output voltage and load current; (b) capacitor discharging; (c) capacitor charging.

the capacitor voltage so that during periods of zero voltage output, either the switches S_1 , S_4 , and S_6 are closed or the switches S_2 , S_3 , and S_5 are closed, depending on whether it is necessary to charge or discharge the capacitor. It is this flexibility in choosing how to make that output voltage zero that is exploited to regulate the capacitor voltage.

If fundamental frequency switching modulation control is used, the goal of the switching control is to output a five-level voltage waveform, and the load current is a sinusoidal waveform that is shown in Figure 3(a). If the capacitor's voltage is higher than $V_{dc}/2$, the switches S_5 and S_6 are controlled to output voltage waveform v_1 , and the switches S_1 , S_2 , S_3 , and S_4 are controlled to output voltage waveform v_2 , as shown in Figure 3(b). The highlighted portions of the waveform in Figure 3(b) are the capacitor discharging periods, during which the inverter's output voltage is 0. If the capacitor's voltage is lower than $V_{dc}/2$, the switches S_5 and S_6 are controlled to output voltage waveform v_1 , and the switches S_1 , S_2 , S_3 , and S_4 are controlled to output voltage waveform v_2 , shown in Figure 3(c). The highlighted trace in Figure 3(c) is the capacitor charging period when the inverter's output voltage is 0. Therefore, the capacitor's voltage can be regulated by alternating the capacitor's charging and discharging control when the inverter output is 0.

This method of regulating the capacitor voltage depends on the voltage and current not being in phase. That is, one needs positive (or negative) current when the voltage is passing through zero to charge or discharge the capacitor. Consequently, the amount of capacitor voltage the scheme can regulate depends on the phase angle difference of output voltage and current. In other words, the

highest output ac voltage of the inverter depends on the displacement power factor of the load.

Five-level fundamental frequency control

There are several kinds of modulation control methods such as the traditional sinusoidal pulse width modulation method (SPWM), space vector PWM method, selective harmonic elimination method, and active harmonic elimination method, and they all can be used for inverter modulation control. For the proposed inductor-less dc-ac boost inverter control, a practical modulation control method is the fundamental frequency switching control for high-output voltage and SPWM control, which only uses the bottom inverter, for low-output voltage.

The key issue of the fundamental frequency modulation control is the selection of the two switching angles. The goal is to output the desired fundamental frequency voltage and to eliminate the fifth harmonic. Mathematically, this can be formulated as the solution to the following equations:

$$\begin{aligned}\cos(\theta_1) + \cos(\theta_2) &= m_a \\ \cos(5\theta_1) + \cos(5\theta_2) &= 0\end{aligned}\quad (1)$$

This is a system of two transcendental equations with two unknowns θ_1 and θ_2 , and m_a is the output voltage index. Traditionally, the modulation index is defined as

$$m = \frac{V_1}{V_{dc}/2} \quad (2)$$

Therefore, the relationship between the modulation index m and the output voltage index m_a is

$$m = \frac{4}{\pi} m_a \quad (3)$$

There are many ways one can solve Eq. (1) for the angles. Here, the resultant method [10] is used to find the switching angles. A practical solution set is shown in Figure 4, which is continuous from modulation index 0.75 to 2.42.

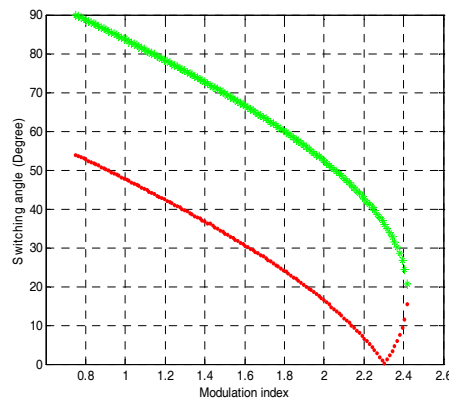


Figure 4. Switching angle solutions for proposed inductor-less dc-ac cascaded H-bridge multilevel boost inverter control.

Although it can be seen from Figure 4 that the modulation index range for the five-level fundamental frequency switching control method can reach 2.42, which is double that of the traditional power inverter, it requires the capacitors' voltage to be kept constant at $V_{dc}/2$.

Traditionally, the maximum modulation index for linear operation of a traditional full-bridge bilevel inverter using SPWM control method is 1 (without third harmonic compensation) and 1.15 (with third harmonic compensation, and the inverter output voltage waveform an SPWM waveform, not square waveform). With the cascaded H-bridge multilevel inverter, the maximum modulation index for linear operation can be as high as 2.42; however, the maximum modulation in dex depends on the displacement power factor, as will be shown below.

As previously mentioned, the cascaded H-bridge multilevel inverter can output a boosted ac voltage to increase the output power, and the output ac voltage depends on the displacement power factor of the load. Here, the relationship of boosted ac voltage and the displacement power factor is discussed.

It is assumed that the load current displacement angle is φ as shown in Figure 5. To balance the capacitor voltage, the pure capacitor charge needs to be greater than the pure discharge amount. That is, to

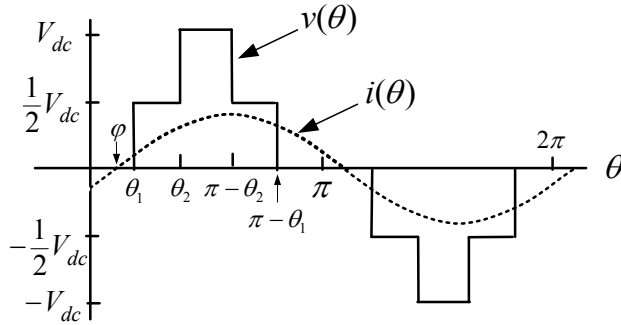


Figure 5. Capacitor charging and discharging cases.

regulate the capacitor’s voltage with a fundamental frequency switching scheme, the following equation must be satisfied,

$$\int i_{charging} d\theta - \int i_{discharging} d\theta > 0 . \tag{4}$$

The current charging and discharging with an inductive load can be classified into three cases. For convenience and practicality of discussion, it is reasonable to assume the inductance load current as

$$i = I \sin(\omega t - \varphi) , \tag{5}$$

and the displacement power factor

$$pf = \cos(\varphi) . \tag{6}$$

The three cases are

(1) $0 \leq \varphi \leq \theta_1$

$$\int_0^\varphi |i| d\theta + \int_\varphi^{\theta_1} i d\theta + \int_{\pi-\theta_1}^\pi i d\theta - \int_{\theta_2}^{\pi-\theta_2} i d\theta > 0 . \tag{7}$$

(2) $\theta_1 < \varphi \leq \theta_2$

$$\int_0^{\theta_1} |i| d\theta + \int_{\pi-\theta_1}^\pi i d\theta - \int_{\theta_2}^{\pi-\theta_2} i d\theta > 0 . \tag{8}$$

(3) $\theta_2 < \varphi \leq \pi/2$

$$\int_0^{\theta_1} |i| d\theta + \int_{\pi-\theta_1}^\pi i d\theta - \int_{\theta_2}^{\pi-\theta_2} i d\theta > 0 . \tag{9}$$

Combining Eqs. (5)–(9), it can be concluded that for $0 \leq \varphi \leq \theta_1$,

$$pf \leq \frac{\pi}{4m} , \tag{10}$$

and for $\theta_1 < \varphi \leq \pi/2$,

$$pf \leq \cos \left\{ \tan^{-1} \left[\frac{\cos(\theta_2)}{\sin(\theta_1)} \right] \right\} . \tag{11}$$

Therefore, the conditions for the fundamental frequency switching scheme to eliminate the fifth harmonic and to regulate the capacitor’s voltage are Eqs. (10) and (11).

For practical applications, direct use of Eqs. (10) and (11) is not convenient. A more convenient way to use Eqs. (10) and (11) is to use minimum phase displacement angles. That means if the phase displacement angle is greater than the minimum angle, the voltage can be regulated anyway.

Figure 6 shows the minimum phase displacement angle computed by Eqs. (4)–(11). From the figure, it can be seen that for a modulation index range $m < 1.27$ (the inverter output is a five-level waveform, not bilevel waveform or square waveform), the minimum phase angle displacement is 0, which means the capacitor’s voltage can be regulated for all displacement power factors in this modulation index range. For modulation index range $m > 1.27$, the required minimum phase displacement angle is shown in Figure 6. Figure 6 also shows the two switching angles.

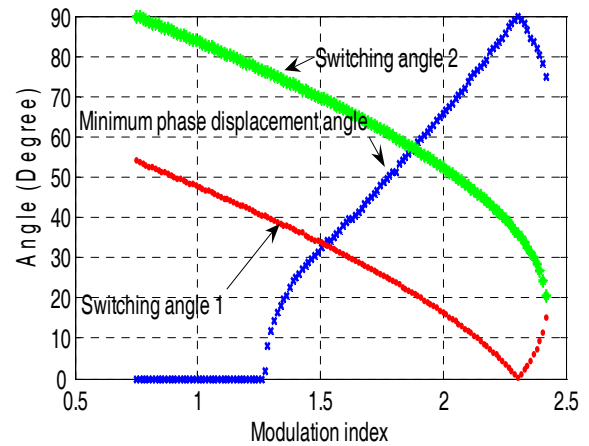


Figure 6. Minimum phase displacement angle.

The phase displacement power factor vs the output voltage modulation index is shown in Figure 7.

It can be derived from Figure 7 that the highest output voltage modulation index depends on the displacement power factor. The inverter can regulate the capacitor’s voltage with a displacement power factor 1 if the modulation index is below 1.27; if the modulation index is above 1.27, the displacement power factor must be lower than a specified amount.

Unipolar PWM control

A unipolar output voltage waveform is shown in Figure 8. For this switching scheme, the inverter needs to output $-V_{dc}/2$, 0, and $V_{dc}/2$ phase voltages. For a traditional inverter, one phase leg can only

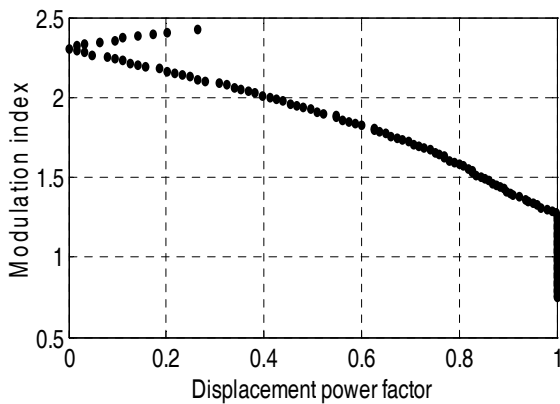


Figure 7. Displacement power factor and output voltage modulation index.

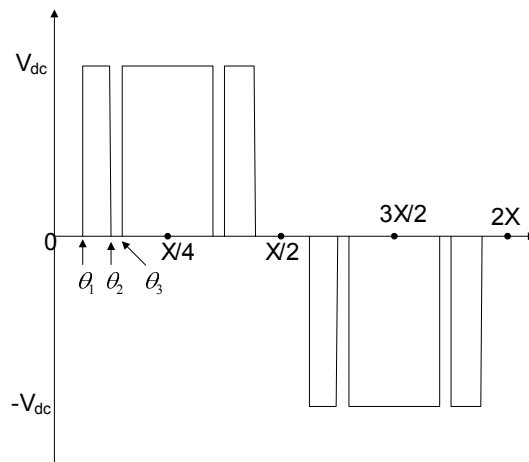


Figure 8. Unipolar switching scheme output voltage waveform.

output $-V_{dc}/2$ and $V_{dc}/2$ phase voltage, and no 0 voltage level. Therefore, traditional inverters cannot use a unipolar switching scheme. For the hybrid cascaded H-bridge multilevel inverter, the combinations of the bottom inverter output and the top H-bridge are possible for a unipolar switching scheme control because it can generate 0 voltages.

Here, to realize the proposed unipolar switching scheme control, one key issue is to regulate the capacitor's voltage to $V_{dc}/2$. To regulate the capacitor's voltage, if $i > 0$ and $V_c < V_{dc}/2$, the inverter controls the bottom inverter to output $V_{dc}/2$ and the top H-bridge to output $-V_{dc}/2$ for the inverter's 0 voltage output; if $i > 0$ and $V_c > V_{dc}/2$, the inverter controls the bottom inverter to output $-V_{dc}/2$ and the top H-bridge to output $V_{dc}/2$ for the inverter's 0 voltage output. The $i < 0$ situation is similar to the $i > 0$ situation; the controller just needs to reverse its switching signals.

It can be seen that the key issue of the unipolar switching control is to choose suitable switching angles. In this paper, the goal is to output the desired fundamental frequency voltage and to eliminate the low order fifth, seventh, eleventh, and thirteenth harmonics. Mathematically, this can be formulated as the solution to the following equations:

$$\begin{aligned}
 \cos(\theta_1) - \cos(\theta_2) + \cos(\theta_3) - \cos(\theta_4) + \cos(\theta_5) &= m \\
 \cos(5\theta_1) - \cos(5\theta_2) + \cos(5\theta_3) - \cos(5\theta_4) + \cos(5\theta_5) &= 0 \\
 \cos(7\theta_1) - \cos(7\theta_2) + \cos(7\theta_3) - \cos(7\theta_4) + \cos(7\theta_5) &= 0 \\
 \cos(11\theta_1) - \cos(11\theta_2) + \cos(11\theta_3) - \cos(11\theta_4) + \cos(11\theta_5) &= 0 \\
 \cos(13\theta_1) - \cos(13\theta_2) + \cos(13\theta_3) - \cos(13\theta_4) + \cos(13\theta_5) &= 0
 \end{aligned} \tag{12}$$

This is a system of five transcendental equations in the five unknowns $\theta_1, \theta_2, \theta_3, \theta_4,$ and θ_5 . There are many ways one can solve for the angles. Here the resultant method is used to find the switching angles. Here, the modulation index m is defined as

$$m = \frac{\pi V_1}{2V_{dc}} \tag{13}$$

The solutions are shown in Figure 9, which is continuous from modulation index up to 1.15.

Prototype building and test setup

To experimentally validate the proposed inductor-less dc-ac cascaded H-bridge multilevel boost inverter control scheme, a prototype 5-kW three-phase cascaded H-bridge multilevel converter has been built using 100-V, 180-A MOSFETs as the switching devices. The prototype is shown in Figure 10(a). A real-time variable output voltage, variable frequency three-phase motor drive controller based on an Altera FLEX 10K field programmable gate array (FPGA) is used to implement the control algorithm. For convenience of operation, the FPGA controller is designed as a card to be plugged into a personal computer, shown in Figure 10(b), which uses a peripheral component interconnect (PCI) bus to communicate with the microcomputer. To maintain the capacitors' voltage balance, a voltage sensor is used to detect the capacitors' voltage and feed the voltage signal to the FPGA controller; the FPGA controller then outputs the corresponding switching signals according to the capacitor's voltage. A 15-hp induction motor was used as the load of the inverter, and the motor was

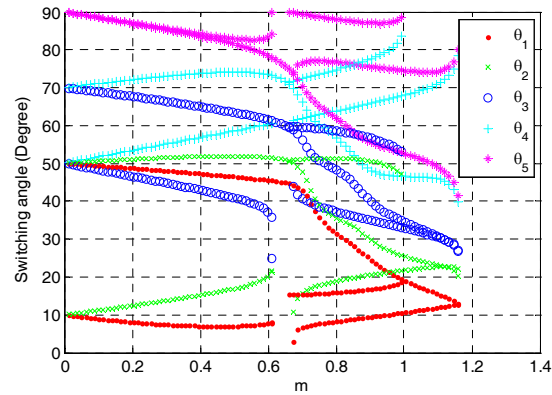
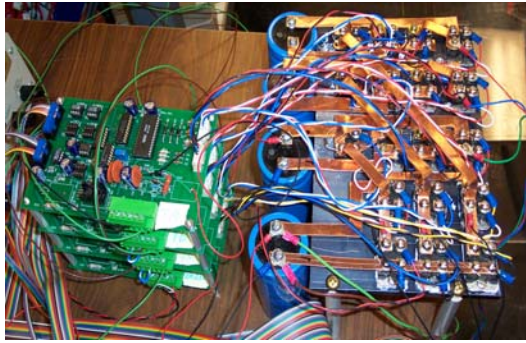


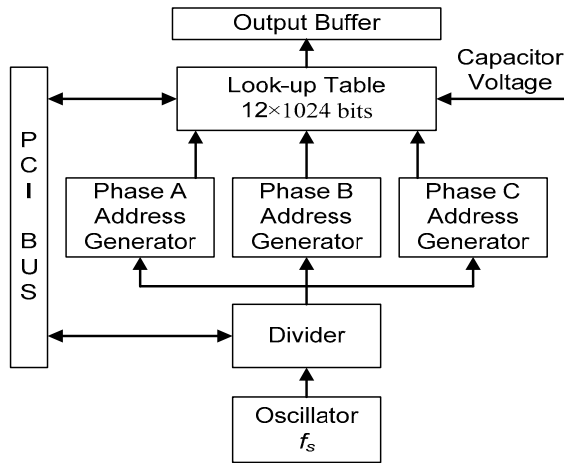
Figure 9. Switching angle solutions for five-angle unipolar switching scheme.



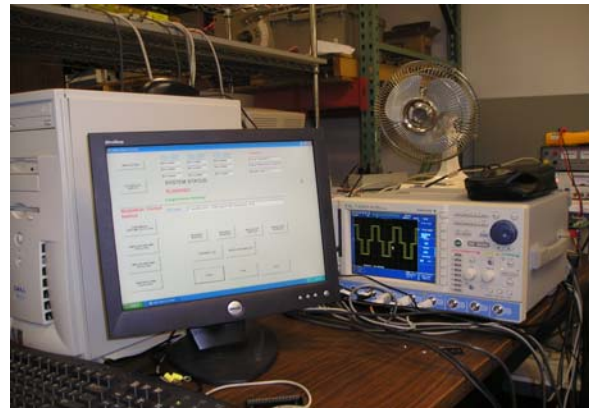
(a)



(b)



(c)



(d)

Figure 10. (a) 5-kW inductor-less dc-ac cascaded H-bridge multilevel boost inverter prototype, (b) FPGA controller, (c) block diagram of FPGA controller, and (d) bench setup.

loaded to less than 5 kW in the experiments. The block diagram of the FPGA controller is shown in Figure 10(c). The whole bench setup is shown in Figure 10(d).

The switching signal data are stored in a 12×1024 on-chip RAM. An oscillator generates a fixed frequency clock signal, and a divider is used to generate the specified control clock signal corresponding to the converter output frequency. Three-phase address generators share a public switching data RAM because they have the same switching data with only a different phase angle. (The switching data are only for one-half cycle because the switching data are symmetric.) For each step, the three-phase signal controller controls the address selector to fetch the corresponding switching data from the RAM to the output buffer according to the capacitor's voltage.

Bench test

(1) Fundamental frequency switching control test with power supply. Figure 11 shows the output phase voltage waveform, line-line voltage waveform, and phase current waveform with the output frequency at 60 Hz. The modulation index of the output voltage is 2.03, and the capacitors' voltage is regulated to $V_{ac}/2$. The phase voltage waveform

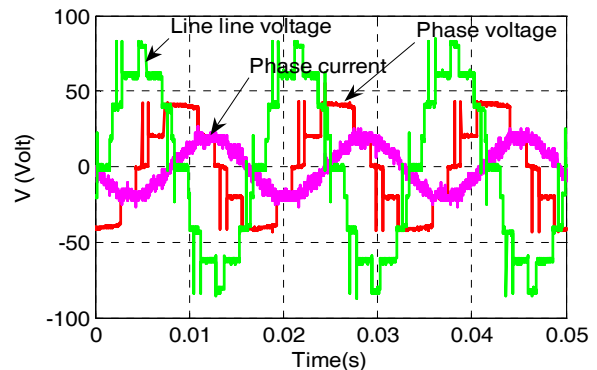


Figure 11. Phase voltage waveform, line-line voltage waveform, and current waveform with 15-hp induction motor load ($m = 2.03$, and $f = 60$ Hz).

shows that the output voltage is five level, the line-line voltage is nine level, and the phase current is a near-sinusoidal waveform.

The experimental results and their FFT analysis all verified the fundamental frequency switching control. The modulation index in this experiment is from 0 to 2.03, which is much wider than the normal modulation index range 0 ~ 1.15 for a traditional standard three-leg inverter.

Further tests were conducted to ascertain the load current vs modulation index with different fundamental frequencies to determine the highest output voltages for both the inductor-less cascaded multilevel boost inverter and a traditional inverter by using an R-L load bank.

For the load current vs modulation index testing, the R-L load is fixed, the modulation index is changed under different fundamental frequencies, and the load currents are recorded. The load current curves for frequencies 60 Hz, 100 Hz, 150 Hz, and 200 Hz are shown in Figure 12.

Figure 12 shows that in the working range of the inductor-less cascaded multilevel boost inverter, the load current and the modulation index are linear. This feature is similar to the traditional inverter and allows easy use in practical applications.

For this experiment, to obtain the highest output voltages for the inductor-less cascaded multilevel boost inverter and the traditional inverter, two steps were involved. First, the load was connected to the bottom traditional inverter to output its highest voltage; second, the load was connected to the cascaded H-bridge multilevel inverter with the same dc power supply voltage. The output voltages for the two cases are shown in Table 1.

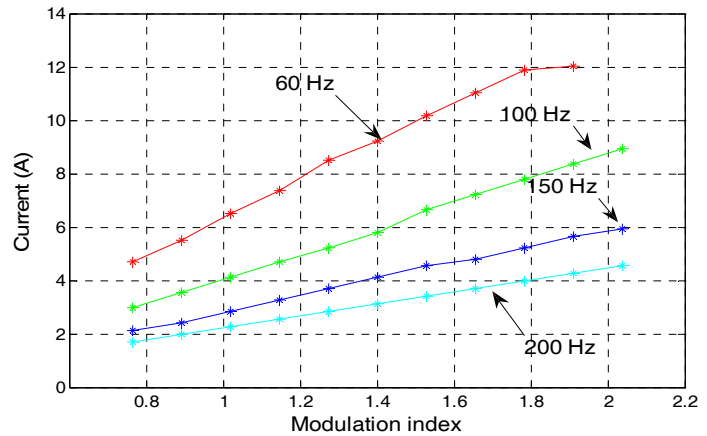


Figure 12. Load current vs modulation index with different fundamental frequency.

Table 1. Highest output voltage for traditional inverter and cascaded H-bridge multilevel inverter (dc bus is 40 V)

Test frequency (Hz)	Traditional inverter output voltage (V)	CMLI (V)	Experimental boost ratio
200	23.1	42.8	1.85
150	23.1	42.2	1.82
100	23.1	41.2	1.78
60	23.1	37.7	1.63
40	23.1	33.1	1.43

Table 1 shows that the highest output voltage of the cascaded H-bridge multilevel inverter is much higher than that of the traditional inverter. The voltage boost ratio is higher than 1.4 for the entire testing frequency range.

Table 1 also shows that the highest output voltage of the inverter is decreasing when the frequency is decreasing; this is because the impedance of the inductor is decreasing. Another issue is that the boost voltage ratio is decreasing when the frequency is decreasing; this is because the power factor is increasing for a fixed R-L load.

(2) Fundamental frequency switching control test with fuel cell dc source. The converter was also tested with a fuel cell dc source. The test procedure was similar to the power supply test. Figure 13 shows the test case using a 24-kW R-L load bank (rating power 24 kW), $m = 2.037$, and $f = 200$ Hz.

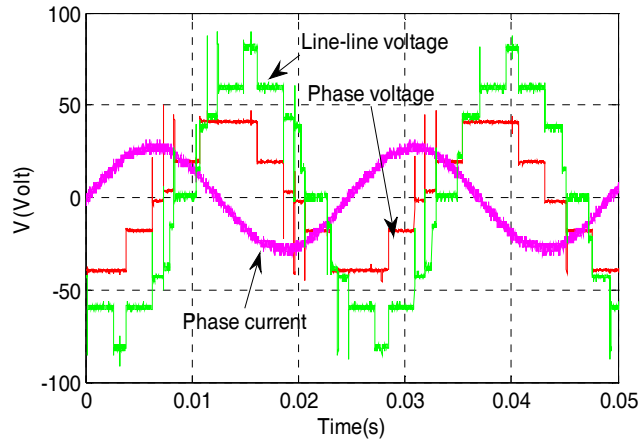


Figure 13. Phase voltage, line-line voltage, and phase current waveforms.

Figures 14 and 15 show the fuel cell voltage vs modulation index and current vs modulation index, respectively, for different output fundamental frequencies. These waveforms show that the converter functions properly with a fuel cell dc source, boosting voltage as required.

(3) Simulation of the plug-in HEV version of the converter. The plug-in HEV version of the converter can be connected to the grid to charge the on-board batteries without any extra components. The idea here is to use one H-bridge as a rectifier and use the other two phase legs of the bottom inverter as a boost converter to charge the batteries. Figure 16 shows the grid voltage when the charging current is 20 A (peak value). Figure 17 shows grid voltage and source current for the same condition.

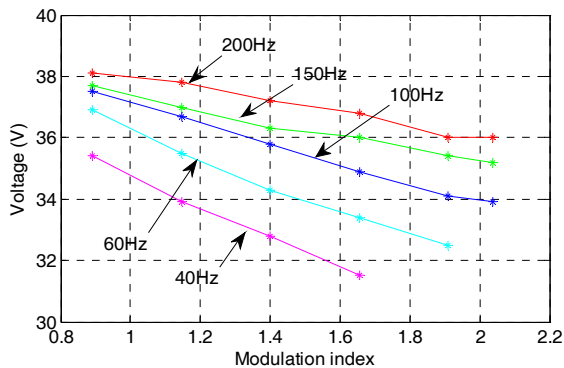


Figure 14. Fuel cell voltage vs modulation index with different fundamental frequency.

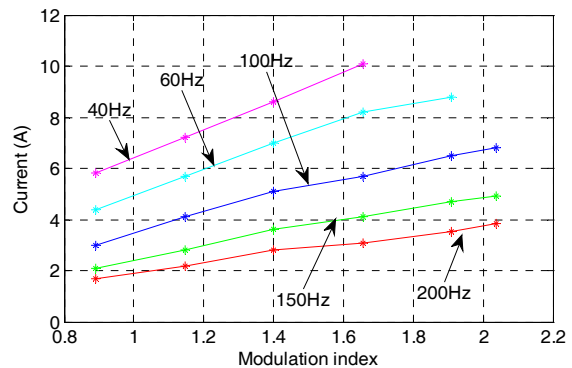


Figure 15. Load current vs modulation index with different fundamental frequency.

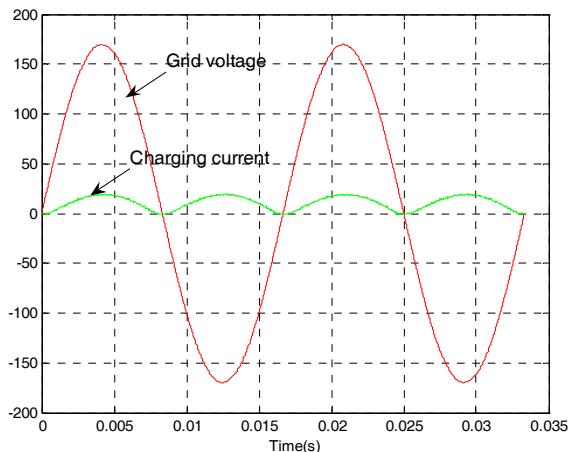


Figure 16. Grid voltage and charge current is 20 A (peak value).

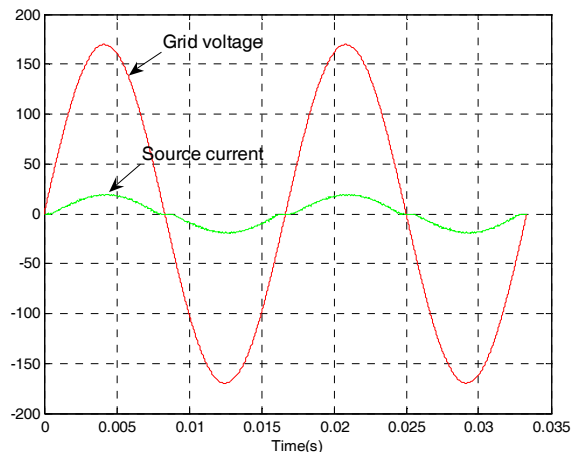


Figure 17. Grid voltage and source current.

Conclusion

The inductor-less cascaded H-bridge multilevel boost inverter uses a standard three-leg inverter (one leg for each phase) and an H-bridge in series with each inverter leg. A fundamental switching scheme can be used for modulation control and to output a five-level phase voltage. Experiments show that the proposed inductor-less dc-ac cascaded H-bridge multilevel boost inverter can output a boosted ac voltage with the same dc power supply that has a wider modulation index range than a traditional inverter. The application of this dc-ac boost inverter on HEV and EV applications can eliminate the bulky inductor of the present dc-dc boost converter, increasing the power density.

Patents

N/A

Publications

Z. Du, L. M. Tolbert, J. Chiasson, and B. Ozpineci, "Inductorless dc-ac cascaded h-bridge multilevel boost inverter for electric/hybrid electric vehicle applications," Industrial Applied Power Electronics Conference, APEC 2007, Anaheim, California.

Z. Du, L. M. Tolbert, J. Chiasson, and B. Ozpineci, "A cascade multilevel inverter using a single dc source," Applied Power Electronics Conference, APEC 2006, Dallas, Texas.

Z. Du, L. M. Tolbert, J. Chiasson, B. Ozpineci, H. Li, and A. Q. Huang, "Hybrid Cascaded H-bridges Multilevel Motor Drive Control for Electric Vehicles," Power Electronics Specialists Conference, PESC, 2006, Jeju Korea.

References

1. L. M. Tolbert, F. Z. Peng, and T. G. Habetler, "Multilevel converters for large electric drives," *IEEE Transactions on Industry Applications* **35**(1), January/February 1999, pp. 36–44.
2. J. S. Lai and F. Z. Peng, "Multilevel converters—A new breed of power converters," *IEEE Transactions on Industry Applications* **32**(3), May/June 1996, pp. 509–517.
3. J. Rodríguez, J. Lai, and F. Peng, "Multilevel inverters: a survey of topologies, controls and applications," *IEEE Transactions on Industry Applications* **49**(4), August 2002, pp. 724–738.
4. Z. Du, L. M. Tolbert, and J. N. Chiasson, "A cascade multilevel inverter using a single dc source," *IEEE Applied Power Electronics Conference*, March 19–23, 2006, Dallas, Texas, pp. 426–430.

5. K. A. Corzine, F. A. Hardrick, and Y. L. Familiant, "A cascaded multi-level h-bridge inverter utilizing capacitor voltages sources," *Proceedings of the IASTED International Conference, Power and Energy Systems*, February 24–26, 2003, Palm Springs, California, pp. 290–295.
6. J. N. Chiasson, B. Özpıneci, and L. M. Tolbert, "Five-level three-phase hybrid cascade multilevel inverter using a single dc source," *IEEE Applied Power Electronics Conference*, February 25–March 1, 2007, Anaheim California, pp. 1504–1507.
7. J. N. Chiasson, B. Özpıneci, Z. Du, and L. M. Tolbert, "Conditions for capacitor voltage regulation in a five-level cascade multilevel inverter: application to voltage-boost in a PM drive," *IEEE International Electric Machines and Drives Conference*, May 3–5, 2007, Antalya, Turkey, pp. 731–735.
8. J. K. Steinke, "Control strategy for a three phase AC traction drive with a 3-level GTO PWM inverter," *IEEE PESC, 1988*, pp. 431–438.
9. P. Hammond, "A new approach to enhance power quality for medium voltage ac drives," *IEEE Trans. Industry Applications* **33**, January/February 1997, pp. 202–208.
10. J. N. Chiasson, L. M. Tolbert, K. J. McKenzie, and Z. Du, "Control of a multilevel converter using resultant theory," *IEEE Transactions on Control System Theory* **11**(3), May 2003, pp. 345–354.
11. W. A. Hill and C. D. Harbourt, "Performance of medium voltage multilevel inverters," *IEEE Industry Applications Society Annual Meeting*, October 1999, Phoenix, Arizona, pp. 1186–1192.
12. G. Carrara, S. Gardella, M. Marchesoni, R. Salutati, and G. Sciuotto, "A new multilevel PWM method: A theoretical analysis," *IEEE Trans. Power Electronics* **7**(3), July 1992, pp. 497–505.
13. L. M. Tolbert, F. Z. Peng, and T. G. Habetler, "Multilevel PWM methods at low modulation indices," *IEEE Trans. Power Electronics* **15**(4), July 2000, pp. 719–725.
14. D. G. Holmes, "The significance of zero space vector placement for carrier based PWM schemes," *IEEE IAS Annual Meeting, 1995*, pp. 2451–2458.
15. J. Vassallo, J. C. Clare, and P. W. Wheeler, "A power-equalized harmonic-elimination scheme for utility-connected cascaded H-bridge multilevel converters," *IEEE Industrial Electronics Society Annual Conference*, November 2–6, 2003, pp. 1185–1190.
16. S. Sirisukprasert, J.-S. Lai, and T.-H. Liu, "Optimum harmonic reduction with a wide range of modulation indexes for multilevel converters," *IEEE Trans. Ind. Electronics* **49**(4), August 2002, pp. 875–881.
17. P. C. Loh, D. G. Holmes, and T. A. Lipo, "Implementation and control of distributed PWM cascaded multilevel inverters with minimum harmonic distortion and common-mode voltages," *IEEE Trans. on Power Electronics* **20**(1), January 2005, pp. 90–99.
18. Z. Du, L. M. Tolbert, and J. N. Chiasson, "Modulation extension control for multilevel converters using triplen harmonic injection with low switching frequency," *IEEE Applied Power Electronics Conference*, March 6–10, 2005, Austin, Texas, pp. 419–423.
19. H. S. Patel and R. G. Hoft, "Generalized harmonic elimination and voltage control in thyristor inverters: Part I—harmonic elimination," *IEEE Trans. Industry Applications* (9), May/June 1973, pp. 310–317.
20. H. S. Patel and R. G. Hoft, "Generalized harmonic elimination and voltage control in thyristor inverters: Part II—voltage control technique," *IEEE Trans. Ind. Applications* **10**, September/October 1974, pp. 666–673.
21. P. N. Enjeti, P. D. Ziogas, and J. F. Lindsay, "Programmed PWM techniques to eliminate harmonics: A critical evaluation," *IEEE Transactions on Industry Applications* **26**(2), March/April 1990, p. 302–316.
22. T. Kato, "Sequential homotopy-based computation of multiple solutions for selected harmonic elimination in PWM inverters," *IEEE Trans. Circuits and Systems I* **46**(5), May 1999, pp. 586–593.
23. Z. Du, L. M., Tolbert, and J. N. Chiasson, "Active harmonic elimination for multilevel converters," *IEEE Trans. Power Electron.* **21**(2), March 2006, pp. 459–469.

4.4 Advanced Converter Systems for High-Temperature HEV Environments

Principal Investigator: Leon M. Tolbert

Oak Ridge National Laboratory

National Transportation Research Center

2360 Cherahala Boulevard

Knoxville, TN 37932

Voice: 865-946-1332; Fax: 865-946-1262; E-mail: tolbertlm@ornl.gov

DOE Technology Development Manager: Susan A. Rogers

Voice: 202-586-8997; Fax: 202-586-1600; E-mail: Susan.Rogers@ee.doe.gov

ORNL Program Manager: Mitch Olszewski

Voice: 865-946-1350; Fax: 865-946-1262; E-mail: olszewskim@ornl.gov

Objective

- Develop a high-efficiency bidirectional dc-dc power converter.
- Incorporate high-temperature power devices and capacitors with a high-temperature packaging technology and gate drives that will enable the converters to operate in high ambient temperature conditions.

Approach

- Maximize utilization of available high-temperature SiC power electronics devices, high-temperature capacitors, and packaging.
- Use integrated, high-temperature gate drives using a silicon-on-insulator (SOI) process.
- Design, fabricate, and test two different low-temperature multilevel dc-dc converter topologies then down-select to one design for high-temperature fabrication.

Major Accomplishments

- A 5-kW 50-V/250-V multilevel modular capacitor clamped dc-dc converter was fabricated and tested. The converter has demonstrated the ability to transfer power in either direction over a wide voltage range with an efficiency in the range of 94 to 96%.
- An SOI gate drive chip with dimensions of 2.2 mm² was fabricated and tested at temperatures of up to 200°C.
- A 55-kW 200-V/600-V multilevel dc-dc converter has been designed.
- High-temperature packaging of SiC junction field effect transistors (JFETs) has been accomplished.

Future Direction

- A second-generation high-temperature gate drive will be designed, fabricated, and tested at ambient temperatures of up to 200°C. The new chip will have two gate drives per chip and an on-chip voltage regulator circuit in addition to a redesigned level-shifting block.
- A high-temperature 55-kW 200-V/600-V bidirectional multilevel dc-dc converter will be fabricated and tested.
- High-temperature packaging of SiC JFETs into modules for use in the converter will be conducted.

Technical Discussion

3X dc-dc Converter Development

After comparison of several topologies, the topology in Figure 1 was selected for 3X dc/dc applications [1] by Michigan State University and Oak Ridge National Laboratory (ORNL). With this structure, the output voltage can be the input voltage itself, twice the input voltage, or three times the battery voltage, say 200, 400, and 600 V. Therefore, the converter has three steady state operation modes, which are shown in Figures 1, 2, and 3, respectively. In the $3*V_{in}$ output mode for instance, the converter operates in switching States I, II, and III with 1/3 duty ratio for every state. In State I, $V_{c1} = V_{in}$; in state II, $V_{c2} = V_{c1} + V_{in}$; in State III, C_2 is in series with V_{in} to charge C_{out} to $3*V_{in}$. The capacitor voltages will be balanced automatically after these three states.

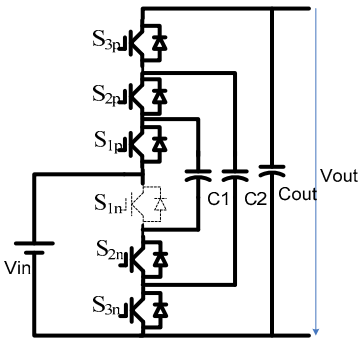
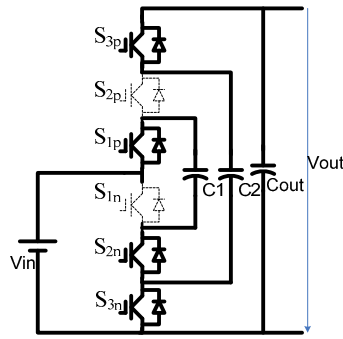
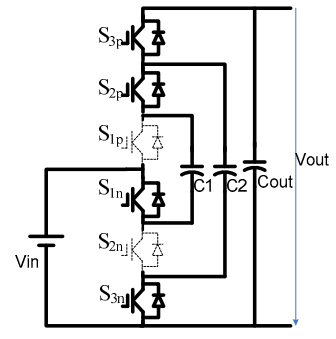


Figure 1. 3X dc/dc topology showing principle of $1V_{in}$ voltage output.

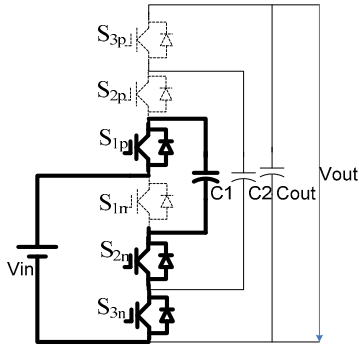


(a) State I

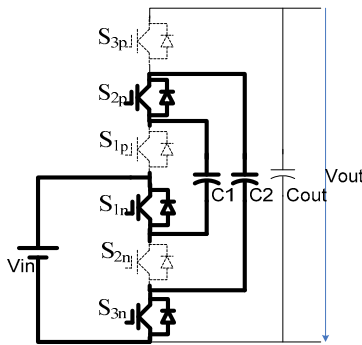


(b) State II

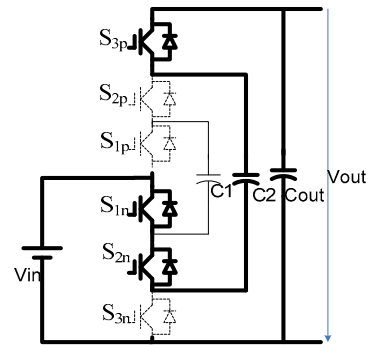
Figure 2. Steady state operation with $2V_{in}$ voltage output.



(a) State I



(b) State II



(c) State III

Figure 3. Steady state operation with $3V_{in}$ voltage output.

The 3X converter is designed to be able to output 30 kW continuous and 55 kW for 18 s. Device ratings were selected on the basis of the above specifications. IGBT module CM600DU-5F was chosen as the main switch (Table 1). The maximum operation voltage with no load is 200 V. The peak current through the switches occurs at 55-kW peak power, during the 3X operation shown in Figure 3. Given 120-V input voltage for 55 kW, the maximum current through each switch can reach 458 A.

Table 1. Characteristics of selected module

Module	Voltage rating	Current rating	Specification
CM600DU-5F	$V_{CES} = 250 \text{ V}$	$I_{e25} = 600 \text{ A}$	Dual IGBT module in half bridge

Capacitor parameters were specified according to the operating voltage and current ratings and voltage ripple limit (10% ~ 20%) (Table 2).

Table 2. Required capacitance, voltage, and current

Capacitor	Required capacitance (μF)		Maximum operation voltage (V)	RMS current @120V 30kW (A)
	10% ripple	20% ripple		
C ₁	694	347	200	204
C ₂	347	174	400	204

Several different capacitors and their corresponding three-dimensional (3-D) layout were investigated, and several design iterations were used. Figure 4 shows the 3-D design of the 3X converter using multilayer ceramic (MLC) capacitors from AVX. Table 3 shows the capacitor parameters and dimensions. The overall size of the converter is around 8 in. \times 7 in. \times 3.4 in. Another design was based on film capacitors, Figure 5 shows the design, and Table 4 shows the capacitor parameters. The overall size of the converter-using film capacitor is 8.6 in. \times 9 in. \times 3.6 in. Table 5 summarizes the pros and cons

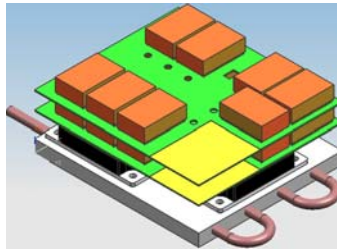


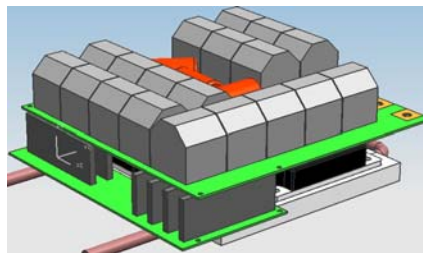
Figure 4. 3-D design of the 3X converter using MLC capacitors.

Table 3. MLC capacitor parameters

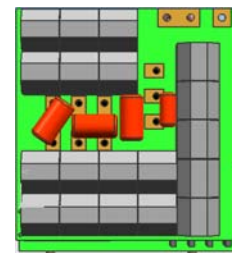
Capacitor	Available capacitance (μF)	WVDC (V)	Permissible RMS current @ 85°C (A)	Type	Configuration	Dimension per piece	Price per piece
						Length \times width \times height (inch \times inch \times inch)	
C1	720 (120 μ \times 6)	200	287.4 (47.9 \times 6)	MLC	6 pieces SM062C127KHN650	2.05 \times 1.35 \times 0.658	\$257
C2	470 (47 μ \times 10)	500	282 (28.2 \times 10)	MLC	10 pieces SM067C476KBN650	2.05 \times 1.35 \times 0.658	\$625



(a) IGBT modules on heat sink



(b) Trimetric view of 3-D model



(c) Top view of 3-D model

Figure 5. 3-D layout.

Table 4. Film capacitor parameters

Capacitor	Available capacitance (μF)	WVDC (V)	Permissible RMS current @ 25°C (A)	Type	Configuration	Dimension per piece	Price per piece
						Length \times width \times height (inch \times inch \times inch)	
C1	500 (50 \times 10)	300	260 (26 \times 10)	Polyester film	10 FFV34H0506K in parallel	1.575 \times 1.418 \times 1.575	\$26.34
C2	160 (20 \times 8)	700	240 (30 \times 8)	Polypropylene film	8 FFV36A0206K in parallel	1.575 \times 1.418 \times 1.575	\$23.44
C3	20	700	30	Polypropylene film	FFV36A0206K	1.575 \times 1.418 \times 1.575	

Table 5. Pros and cons of MLC vs film capacitors

	MLC	Film
Pros	<ul style="list-style-type: none"> • Small size • Extremely high current • Negative temperature coefficient. • High-temperature operation • Low ESR 	<ul style="list-style-type: none"> • Low cost • Benign failure • High current
Cons	<ul style="list-style-type: none"> • Too expensive • Nonbenign failure 	<ul style="list-style-type: none"> • Large size • Relatively high ESR • Medium temperature • Smaller capacitance than MLC

of MLC vs film capacitors. The required MLC capacitors and printed circuit board (PCB) were quoted at about \$10.6K, much higher than the film capacitor's \$4.4K. Film capacitors were selected and finally purchased. To minimize the effect from stray inductance in the output current path, one decoupling capacitor (FFV36A0206K) is used in parallel with the load capacitor C_{out} .

The calculated power loss at 55 kW is about 1818 W. The estimated efficiency is approximately 97%; the efficiency at 30 kW is expected to be higher than 98%. Based on current density calculations and PCB manufacturers' production capability, a 9-layer PCB was designed to hold and connect the film capacitors to the IGBT modules. Underneath the capacitor board, the gate drive circuit is placed. Control and power supply circuits share the same board with the gate drive. Figure 5(b) and (c) show the overall 3-D layout.

A self-powered gate drive board was designed. The power is supplied from the input or the 200-V battery. The 200-V battery is stepped down to 15 V that feeds each gate drive circuit where a gate driver chip (VLA500k-01r) is used. From the 15-V power, the gate driver generates +15 V/-10 V bias voltages for its gate signal. As for control, a complex programmable logic device (CPLD) circuit is used to generate PWM signals to the IGBTs. If a fault happens, the short circuit protection would be activated, and it will block the gate signal; at the same time, fault protection signals are fed back to the CPLD.

5-kW 7X dc-dc Converter (MMCCC)

Figure 6 shows the circuit topology for a multilevel modular capacitor clamped converter (MMCCC) [7] designed by the University of Tennessee and ORNL personnel. Figure 7 shows the experimental prototype of a 5-kW MMCCC converter [2]. This converter is designed to achieve any conversion ratio up to 7. Thus, the converter has six modules, and each module has its own gate drive circuit on board. A control circuit, using a Parallax Stamp BS2P40 microcontroller development kit, has been programmed to generate the proper gate signals for the various transistors in each module. Each module has three pairs

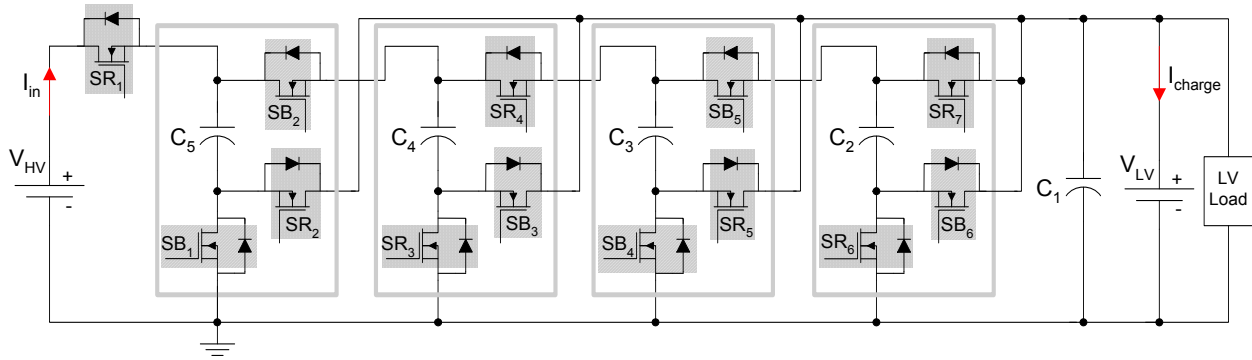


Figure 6. Six-level 5-kW version of the MMCCC.



Figure 7. The six-level 5-kW version of the MMCCC with six modules. The sixth module (first one from right) is bypassed for normal operation.

of MOSFETs, and they were used in pairs to enhance the current handling capability. For normal operation with a conversion ratio of 5, the last two modules from the right are used as bypass modules. As explained earlier, to implement the bidirectional power management, one additional module is required. In addition, to introduce some level of redundancy and fault bypass capability in the system, one module is used as a reserve. This is why the converter was fabricated with six modules.

To test the efficiency and performance of the 5-kW converter, it was loaded at different voltages and conversion ratios (CRs). As the first step, the CR was set to 4, a fixed load of 1.76 Ω was connected to the low-voltage (LV) side, and the input (HV side) high voltage was varied from 0 to 250 V. The corresponding efficiency of a four-level converter is shown in Figure 8(a). Figure 8(b) shows the

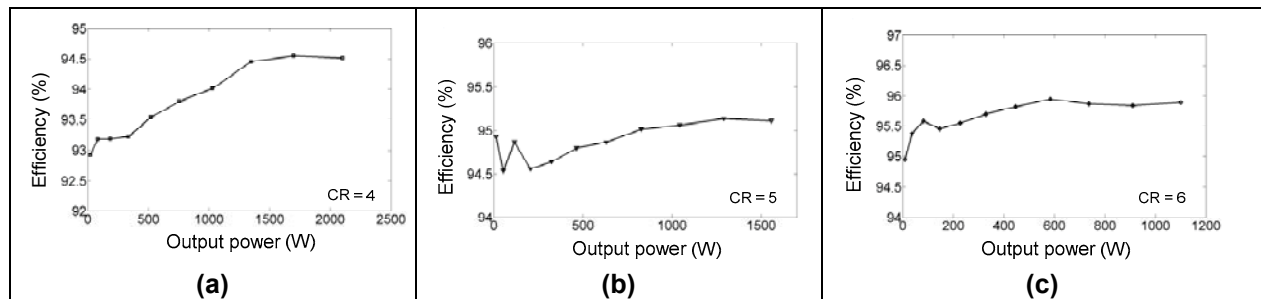


Figure 8. The efficiency of the 5-kW MMCCC converter at different conversion ratio and output power: (a) four-level converter, (b) five-level converter, and (c) six-level converter.

efficiency of the MMCCC in a five-level configuration, and Figure 8(c) shows it for six levels. After observing these three figures, two conclusions can be made: (1) the converter has almost flat efficiency characteristics that means that the efficiency is very high even at zero or partial loads, and (2) the best possible efficiency is achieved when the CR is high. Thus, when the converter operates in a six-level configuration, the efficiency is higher than four- or five-level configurations for the same output power.

High-Temperature Gate Drive Integrated Circuit

The high-temperature gate driver integrated circuit (IC) was designed by The University of Tennessee and fabricated by ATMEL using 0.8- μm , 3-metal and 2-poly-bipolar CMOS and DMOS (BCD) in an SOI process. Figure 9 shows the fabricated chip's microphotograph. This circuit occupies an area of 3.6 mm^2 ($2,240 \mu\text{m} \times 1,600 \mu\text{m}$) including pads and electric static discharge (ESD) protections. The two high-voltage NMOS devices of the half-bridge output stage occupy a major portion of the die area. They are sized ($W/L = 24,000 \mu\text{m}/1.6 \mu\text{m}$) to provide as large peak current as needed to minimize the switching loss of the power FET. Each of these NMOS transistors is comprised of six hundred 45-V NMOS devices ($W = 40 \mu\text{m}$) connected in parallel. The high-voltage devices are well-isolated from the low-voltage devices through a thick dielectric layer. Multiple pad connections are used for the power supply and output nodes to minimize the bond wire's parasitic inductances. All critical metal interconnects are made thick to avoid electromigration, which is a potential failure mechanism at higher temperatures. Figure 10 shows three gate driver chips in a QFN44 package placed next to a dime for visual comparison of the size of the chip.

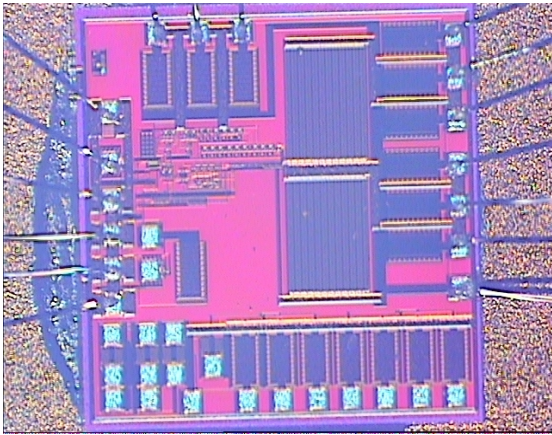


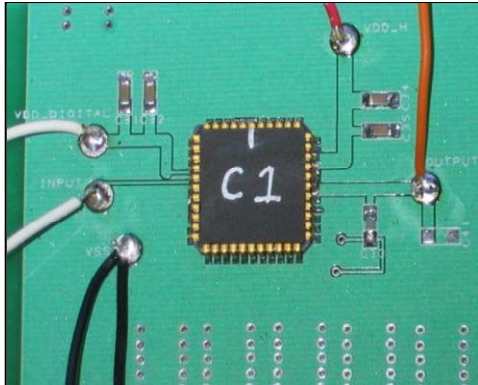
Figure 9. Micrograph of the gate driver IC with bond wires.



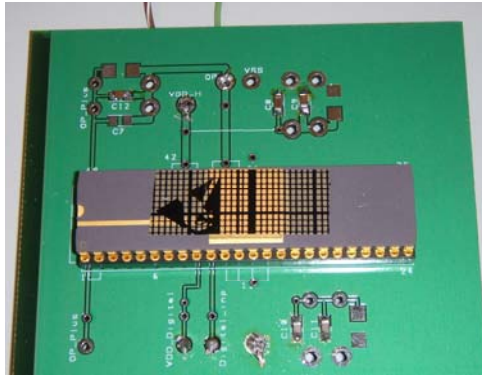
Figure 10. Gate driver IC in CDIL44 package in comparison with a dime.

The bare dies received from ATMEL were bonded in LDCC44 ceramic packages using the K & S 4500 manual wire bonder at ORNL. A double-layer PCB was designed to house the chip, bootstrap capacitor, and power supply filter networks [Figure 11(a)]. The board was fabricated using polyimide material, which can withstand temperatures higher than 200°C . A second PCB was designed and fabricated using the same polyimide material for the gate driver chip in a CDIL48 ceramic package [Figure 11(b)].

High-temperature solders were used to connect all the components in the PCBs. All the wires used for testing have insulation made of Teflon so that they do not melt at 200°C . One major challenge was to find high-temperature capacitors. We could not find any commercially available capacitors (in low quantity) that can operate to 200°C . For our testing we have used MURATA's X7R type capacitors (operating temperature range -55°C to 125°C). Because the tests were successful at temperatures higher than 125°C ,



(a) PCB for LDCC44 package



(b) PCB for LDCC44 package

Figure 11. Polyimide printed circuit boards for testing the gate driver IC.

we believe these capacitors can operate at temperatures higher than the specified range. In the second PCB, we have used sockets from Mill-Max Manufacturing Corp. to place the gate driver IC in the board. This socket also operates successfully at 200°C.

The first functionality check was performed for the gate driver IC at room temperature with small capacitive loads [5]. Once it passed those tests, then it was tested with a 10-nF capacitive load in series with a 10-Ω resistor at room temperature and at high ambient temperatures (up to 175°C). These tests were conducted at ORNL using a Delta Design 9023 model temperature chamber. Figure 12 shows the gate signal generated by the chip at 175°C ambient temperature with the load condition specified above. Rising and falling edges are also magnified in Figure 12. Table 6 shows the 10% to 90% rise-time and 90% to 10% fall-time of the generated gate signals at different temperatures. Readings were taken 15 min after the temperature of the chamber reached the desired level to ensure that the die temperature had reached the chamber temperature. The chip was also tested with the same load for different duty cycle (20% to 80%) input signals at room temperature.

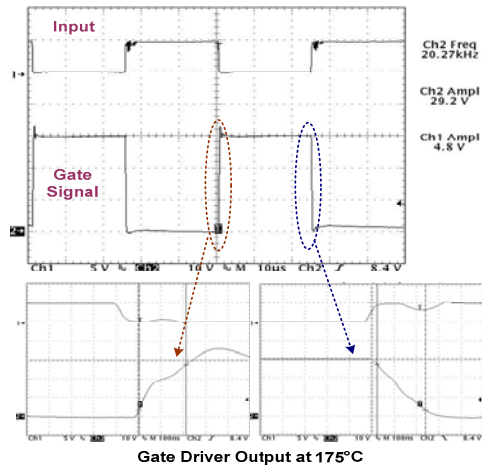


Figure 12. Gate signal generated by the IC at 175°C with 10-nF capacitive load in series with 10-Ω resistor.

Table 6. Experimental rise-time and fall-time with R-C load, 10-nF capacitor and 10-Ω resistor

Ambient temperature (°C)	$t_{\text{rise-time}}$ (10%–90%) (ns)	$t_{\text{fall-time}}$ (90%–10%) (ns)
27	200	78
85	204	90
150	208	158
175	210	216

A SiC power MOSFET developed by Cree has been used to test the gate driver chip. A 10-Ω resistive load was connected between the 50-V power supply and the drain terminal of the MOSFET.

Approximately 5-A load current was flowing through the load and the MOSFET when it was turned ON by the gate driver chip. The test board was placed inside the temperature chamber, and the SiC MOSFET was kept outside the chamber because it was not packaged for the high-temperature operation. Starting from room temperature, the chip was tested up to 200°C.

One chip was successfully tested up to 175°C at 40-kHz switching frequency (Figure 13). Another IC successfully switched ON/OFF the MOSFET up to 200°C (Figure 14). Figures 13 and 14 show the digital input signal (blue), gate signal generated by the gate driver circuit (red), and voltage wave shape at the drain terminal of the MOSFET (green). The PCB was placed inside the temperature chamber without any cooling facility, and the temperature was raised from room temperature to 200°C in five steps (85°C, 125°C, 150°C, 175°C, and 200°C) ; at each temperature step it was kept for 15 min before taking any readings. At 200°C it was tested for more than 30 min. In this way the chip successfully operated over 150°C for more than 90 min without any cooling mechanism.

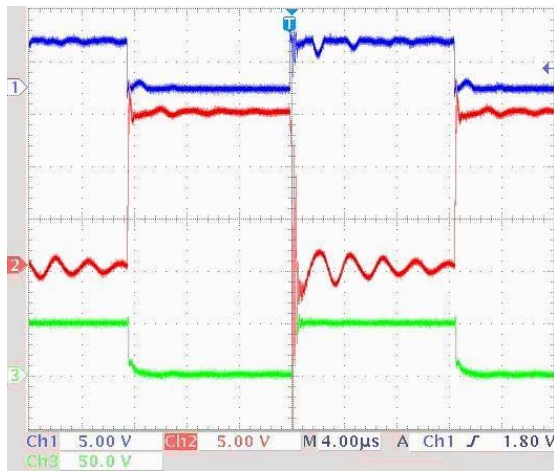


Figure 13. Test waveforms for 175°C, 40 kHz.

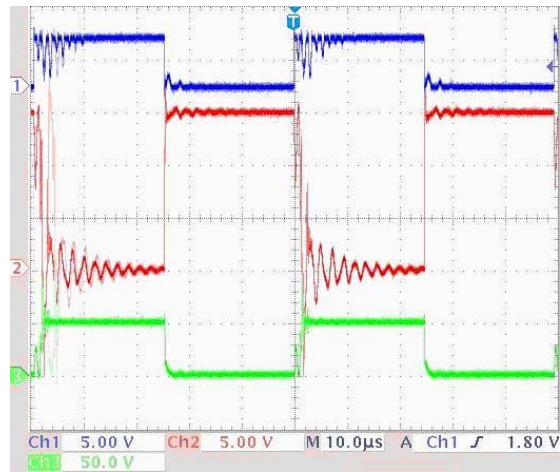


Figure 14. Test waveforms for 200°C, 20 kHz with bond wires.

Table 7 shows the targets that were set for the first version of the gate driver chip and the performance achieved with this version.

Table 7. Actual performance comparison with goals

Specifications	Goal	Achieved	Comments
Output voltage swing	35 V	35 V	
Maximum operating ambient temperature	175°C	200°C	
Capacitive load driving	10 nF	10 nF	Also successfully drove the SiC Power MOSFET
Switching frequency	20 kHz	40 kHz	
Rise-time and fall-time	≤100 ns with 10-nF load	≤216 ns with 10-nF load	Need to increase the peak charging current capacity of the chip
Driving SiC FET switch	JFET/MOSFET	MOSFET	The MOSFET was successfully driven by the gate driver IC up to 200°C

High-Temperature Packaging

The University of Idaho packaged two SiC JFETs in a parallel configuration. The SiC devices were supplied through ORNL by SemiSouth Inc. These devices, one of which is shown in Figure 15, are rated to 600 V and 5 A of current. The small pad on the left-hand side of the device is the gate contact, while most of the rest of the surface of the die is the source contact. The drain contact is the backside of the die in this case. The gate contact for this device is 150 μm wide and 100 μm tall, and the much larger source contact for this device is 1055 μm wide by 911 μm tall. Both the top surface of the die and the bottom surface of these dice are composed of layers of titanium (Ti), platinum (Pt), and gold (Au). The metal thicknesses on the bottom surface of the die are 1000 \AA Ti, 1000 \AA Pt, followed by the final finish of 5000 \AA of Au, while the top surface of the die is coated with 1000 \AA Ti, 1000 \AA Pt, followed by the final finish of 20,000 \AA of Au. The thin gold on the bottom surface of the devices is designed to be compatible with die attachment processes that utilize solder or conductive adhesive. In contrast, the much thicker gold on the top surface is required for wire bonding.

The strategy employed to package these devices is the use of a high-temperature metal housing with glass electrical seals. The surfaces of this package were specified with a finish of electroless nickel, and the housing itself is made from a steel frame with a copper base. As shown in Figure 16, the selected package has six pins as well as a metal tab; this package was selected for ease of testing rather than for its overall size. However, a number of key criteria were used to evaluate the possible package options:

- Continuous operation at 200°C ambient was the minimum temperature requirement.
- The package must be able to handle the 600-V voltage stress.
- A minimum current rating of 10 A was required.
- A minimum of four pins are required.
- The packages should be in a through-hole configuration to facilitate testing.

The selected TO-257 package was one of only a few available on the tight timeline of this project, but it meets or exceeds these requirements with the inclusion of six 30-mil-diam alloy 52 copper-cored pins. Each of these pins is rated to 9 A at room temperature, and four of them have been used to carry the 10 A of current for the two JFETs in parallel. In addition, this package has a metal tab that can be bolted to a heat sink and was used to provide an electrical connection to the common drains of the JFET devices.

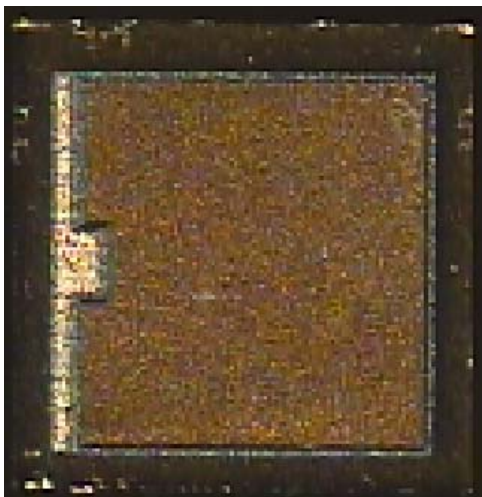


Figure 15. 600-V, 5-A SiC JFET.

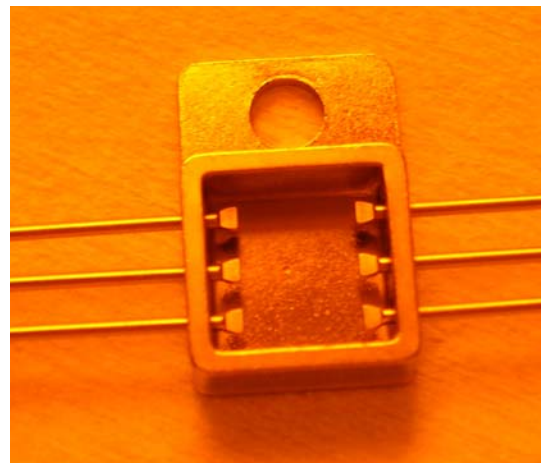


Figure 16. Example of the package housing as received from a vendor. Orange color is an artifact of the clean room lighting.

Another key question regarding the package housing was the breakdown capability and current carrying capability of the package at 200°C. University of Idaho has used and tested identical configurations of packages in the past, and it has been demonstrated that this configuration is capable of voltage and current levels in excess of those required for this project. An example of those data is shown in Figure 17. The top figure is the result of several voltage stress tests applied to a similar package at 200°C. Clearly even the worst-case breakdown of 1250 V far exceeds the requirements of the present package. The bottom figure illustrates high current testing of the same package configuration as used in this work, but with three 60-mil-diam pins. During this test the current flowed through three pins in parallel that the manufacturer rates to 35 A each. At 200°C and 90 A of current, the wire bonds inside the package failed, while there was no change or damage to the pins of the package. This clearly demonstrates that little if any derating is required for these pins at 200°C and that the four pins used in the current work are more than adequate.

In addition to the package housings, the internal interconnect structures between the JFETs and housing were carefully considered. Key questions include

- What is the most suitable die attachment material?
- How large should the wire bonds be in order to handle the current?
- What type of wire bond material should be used?

Based on past work, MIL-H-3534B standard is a reasonable guide for wire bond sizing even at 200°C. Therefore, this standard was used as a guide for bond sizing and dictates no more than 5.3 A for 5-mil-diam aluminum wire bonds that are longer than 40 mils in length. Therefore, two 5-mil wire bonds were selected for each device to ensure adequate current carrying capability. In contrast the gate contacts for these JFETs carry very little current, and the pads on the die are too small for a 5-mil-diam wire. Therefore, a 1-mil-diam aluminum wire was selected for the gate connections. In practice two 1-mil wires were applied to many of the dice simply to provide some level of redundancy.

Figure 18 illustrates the internal view of one of the packages produced in this work. The blue material is a ceramic substrate fabricated by the authors for this package design. The substrate allows the thin gate wires to be bonded to a common gate point on the substrate, which keeps their length very short. This approach is ideal because the small-diameter wires can become weak when formed into long bonds. Two-mil-diam aluminum wires are then used to attach this common gate point to two separate pins of the package.

Throughout this work, aluminum wires have been used exclusively to interconnect the die. The principal driver behind this selection is the fact that fundamentally larger wires can be used with aluminum rather than gold, and it has been documented that aluminum wires bonded to nickel surfaces, such as that used on the package pins, are very reliable at high temperatures. In addition, aluminum wires are the current industry standard for power modules and the infrastructure for that technology is well

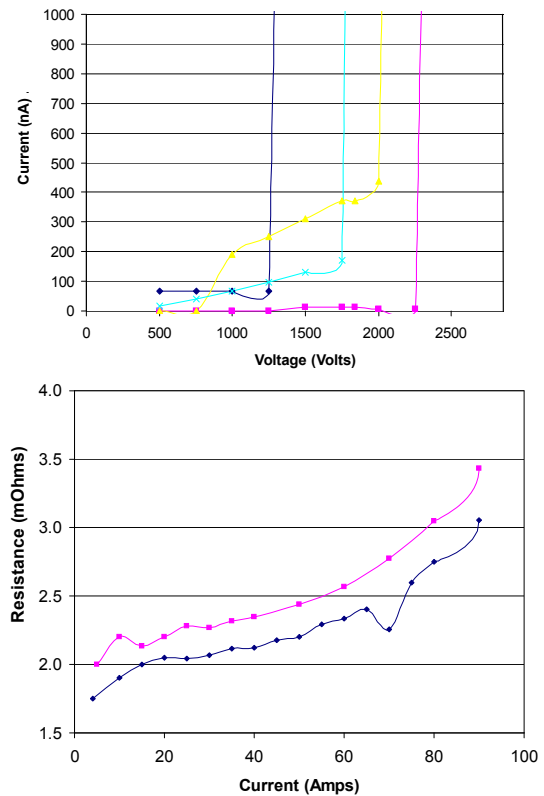


Figure 17. Voltage breakdown (top) and current testing (bottom) of a similar package at 200°C.

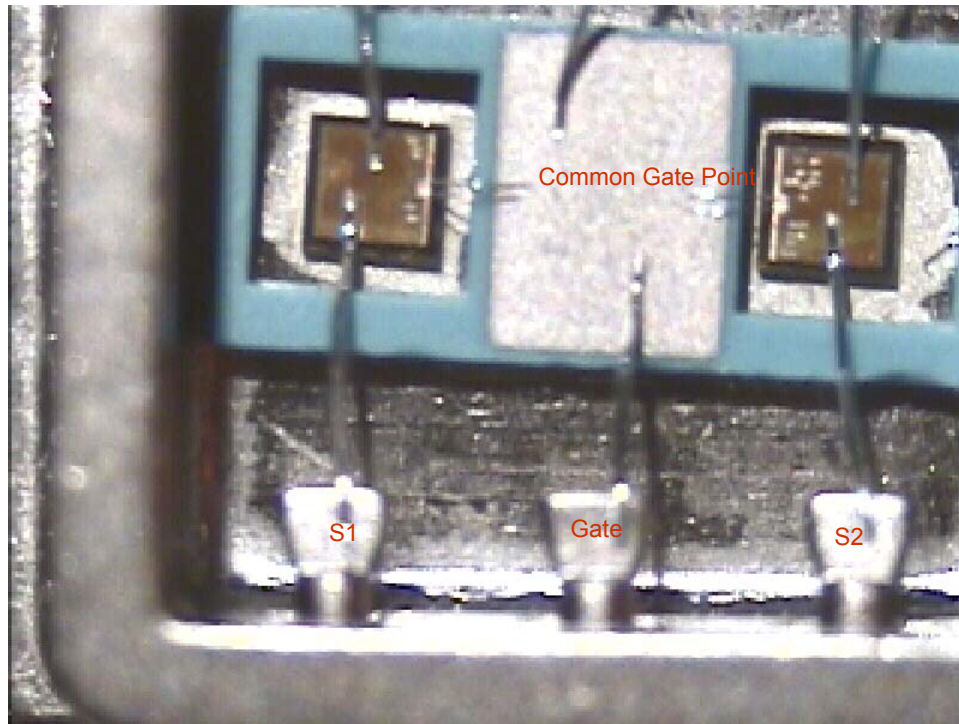


Figure 18. Micrograph of internal structure of the developed JFET packages.

established [8]. However, the die regrettably has a gold finish, which opens the possibility for a gold aluminum intermetallic to form that can lead to bond failure over time. The only viable alternative for volume production with the current existing technology would be the use of gold wires, which are limited in current-carrying capability and size. In addition, the use of gold in long-term products would adversely affect the cost of those products. Therefore, the authors have selected aluminum wire for all of the internal interconnects in these packages.

The final question to address is the die attachment material. Because the minimum ambient operating temperature of these devices is presumed to be 200°C, the die attachment material must have a solidus temperature much higher than this value. This requirement rules out most commonly used solder materials such as lead tin eutectic, which is generally processed at just over 200°C. While there are a number of solders, brazes, and other materials with solidus temperature in excess of 250°C, another possibility is a modified silver-filled polyimide adhesive. This adhesive material is stable to 350°C, which is higher than most of the available solder materials and offers adequate thermal and electrical conductivity for this application. For a very high current device, a solder or a braze material would be more appropriate; however, the devices used in this project are relatively low in current, and as a result this adhesive material is an ideal choice. In this case, a small quantity of adhesive was dispensed into the package housing, and both the substrate and the two dice were bonded into the housing at the same time.

Conclusion

This challenging project involves the development and demonstration of several novel technologies in order to achieve a converter that can operate at high ambient temperatures. Novel magnetic-less or small magnetic dc-dc converter topologies will result in reduced volume and weight compared to conventional topologies. The multilevel design of these converters will also allow segregation of the battery pack into multiple modules. This will allow only a portion of the battery pack to be replaced if there is a failure. It may also result in an increase in reliability and availability of the battery power, as the converter designs will allow for a damaged or failed battery module or power electronics module to be bypassed.

A high-temperature gate drive has been fabricated in SOI and tested at high temperatures. This design shows great promise for allowing gate drives to be located near high-temperature power electronics with no cooling. Slow progress in SiC switching transistors (JFETs) and high-temperature capacitors has hampered this project, but still this project has demonstrated several valuable technologies for future HEVs [2]. Gains made from this project will likely impact other power electronics projects that need high-temperature packaging, gate drives, or modular conceptual designs.

Publications

F. Khan and L. M. Tolbert, "A 5-kW multilevel dc-dc converter for hybrid electric and fuel cell automotive applications," IEEE Industry Applications Society Annual Meeting, September 23–27, 2007, New Orleans, Louisiana.

F. Khan and L. M. Tolbert, "A 5 kW bi-directional multilevel modular dc-dc converter (MMCCC) featuring built in power management for fuel cell and hybrid electric automobiles," *IEEE Vehicular Power and Propulsion Conference*, September 9–12, 2007, Arlington, Texas.

M. Huque, R. Vijayaraghavan, M. Zhang, B. Blalock, L. Tolbert, and S. Islam, "An SOI-based high-voltage, high-temperature gate-driver for SiC JFET," *IEEE Power Electronics Specialists Conference*, June 17–21, 2007, Orlando, Florida, pp. 1491–1495.

F. H. Khan and L. M. Tolbert, "A multilevel modular capacitor clamped dc-dc converter with fault tolerant capability," *IEEE Applied Power Electronics Conference*, February 25–March 1, 2007, Anaheim, California, pp. 361–367.

F. H. Khan and L. M. Tolbert, "A multilevel modular capacitor clamped dc-dc converter," *IEEE Industry Applications Society Annual Meeting*, October 8–12, 2006, Tampa, Florida, pp. 966–973.

F. Barlow and A. Elshabini, *High-Temperature High-Power Packaging Techniques for HEV Traction Applications*, ORNL/TM-2006/515, UT-Battelle, LLC, Oak Ridge National Laboratory, Oak Ridge, Tennessee, November 2006

References

1. M. Shen, F. Z. Peng, and L. M. Tolbert, "Multi-level dc/dc power conversion system with multiple dc sources," *IEEE Power Electronics Specialist Conference*, Orlando, Florida, June 17–21, 2007, pp. 2008–2014.
2. L. M. Tolbert, H. Zhang, M. S. Chinthavali, and B. Ozpineci, "SiC-based power converters for high temperature applications," *Materials Science Forum* **556–557**, 965–970 (September 2007).

4.5 Current Source Inverter

Principal Investigator: Gui-Jia Su

Oak Ridge National Laboratory

National Transportation Research Center

2360 Cherahala Boulevard

Knoxville, TN 37932

Voice: 865-946-1330; Fax: 865-946-1262; E-mail: sugj@ornl.gov

DOE Technology Development Manager: Susan A. Rogers

Voice: 202-586-8997; Fax: 202-586-1600; E-mail: Susan.Rogers@ee.doe.gov

ORNL Program Manager: Mitch Olszewski

Voice: 865-946-1350; Fax: 865-946-1262; E-mail: olszewskim@ornl.gov

Objectives

- Overall project objectives are to
 - eliminate the drawbacks of the voltage-source inverter by switching to a current-source-based topology,
 - reduce cost and volume by 25% compared to voltage source inverter designs,
 - improve inverter and motor lifetime,
 - increase motor efficiency (10% loss reduction),
 - increase constant-power-speed-range,
 - reduce the cost and size of batteries in plug-in hybrid electric vehicles (HEVs), and
 - serve as an enabler for silicon carbide (SiC)-based inverters to operate in elevated temperature environments.
- The objective for the FY 2007 effort is to
 - prove the concept by a simulation study,
 - develop pulse width modulation (PWM) schemes and inverter control strategies designed for maximum torque per ampere for internal permanent magnet (IPM) motors, and
 - conduct a conceptual design of a 55-kW prototype.

Approach

- Perform detailed circuit simulation in PSIM using the Prius motor as the target motor to
 - study carrier-based and space vector modulation schemes for minimizing switching loss,
 - study algorithms for maximum torque per unit current control of the Prius motor,
 - study circuit models for determining the voltage boost capability,
 - study system performance, and
 - establish voltage and current ratings of major components for a 55-kW prototype.

Major Accomplishments

- Completed simulation study and proved the concept.
- Investigated both carrier-based and space vector PWM schemes and designed an optimum PWM method for future prototype development.
- Developed a strategy for maximum torque per amp control of IPM motors.
- Completed a conceptual design of a 55-kW prototype and downselected major components.

Future Direction

- Design, fabricate, and test a 55-kW inverter prototype.

Technical Discussion

Background

Current electric vehicles (EVs)/HEVs use inverters that operate from a voltage source and thus are called voltage-source inverters (VSIs) [Figure 1(a)] because the most readily available and efficient energy storage devices, batteries, are inherently voltage sources. These devices can easily be incorporated into VSIs. The VSI, however, possesses several drawbacks that make it difficult to meet the requirements of the FreedomCAR goals in terms of volume, lifetime, and cost for the inverter operating with a high-temperature (105°C) coolant. It requires a very high-performance direct-current (dc) bus capacitor to maintain a near ideal voltage source. Also, currently available capacitors that can meet the demanding requirements are costly and bulky, taking up one-third of the inverter volume and cost. The reliability of the inverter is also limited by the capacitors and further hampered by possible shoot-through of the phase legs making up a VSI [S_1 - S_2 , S_3 - S_4 , and S_5 - S_6 in Figure 1(a)]. In addition, steep rising and falling edges of the output voltage in a form of pulse trains generate high electromagnetic-interference (EMI) noises, impose high stress on the motor insulations, and produce high-frequency losses in the copper windings and iron cores of the motor as well as generate bearing-leakage currents that erode the bearings over time.

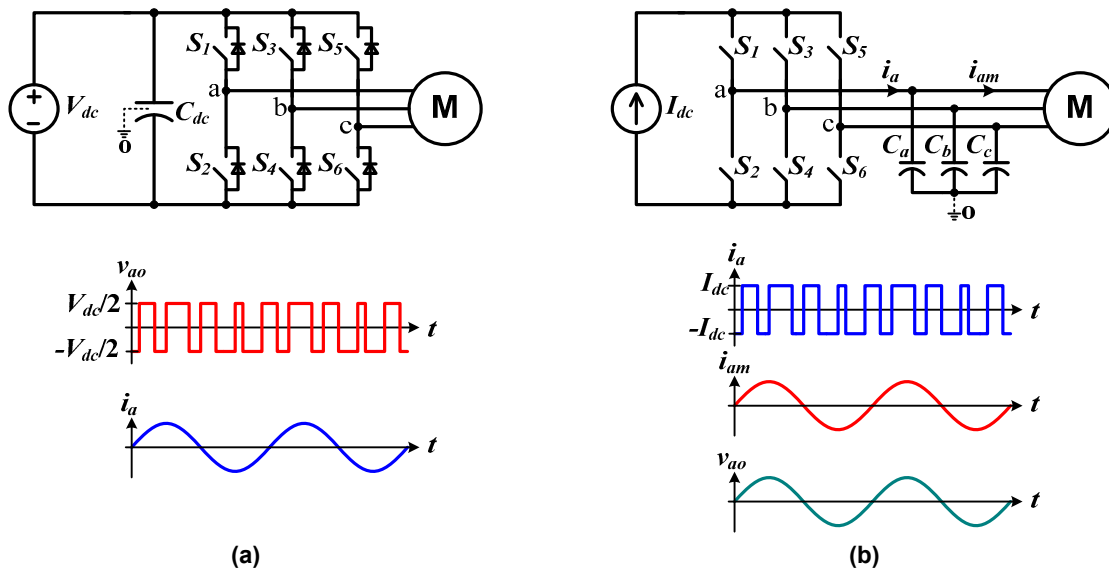


Figure 1. Schematics of the two types of inverters and typical output voltage and current waveforms: (a) the voltage-source inverter; (b) the current-source inverter.

As the maximum operating junction temperature of the latest silicon insulated gate bipolar transistors (IGBTs) increases, the capacitor, in fact, presents the most difficult hurdle to operating a VSI in the automotive high-temperature environments. The function of the dc bus capacitor is twofold: (1) to maintain a near-ideal voltage source and (2) to absorb the ripple current generated by the switching actions of the inverter. The root mean square value of the ripple current is proportional to the motor current with a maximum ratio of $50 \sim 60\%$ depending on the PWM schemes. Currently, two types of dielectrics, polymer film and ceramics, are being pursued for use in high-temperature environments. Polymer film capacitors are the capacitor of choice for HEVs currently on the market due to their benign failure mode and adequate ripple-current handling capability at lower coolant temperatures (about 70°C). However, their ripple-current handling capability rapidly diminishes as the temperature increases. As a result, a significantly larger capacitor would be required in higher operating temperature environments.

On the other hand, while the ceramic capacitors can still provide adequate ripple-current capability even at the higher temperatures, their tendency to produce catastrophic failures and their higher cost has made them unacceptable for HEV applications.

In addition, for the VSI to operate from a low-voltage battery, a bidirectional dc-dc converter is needed. Figure 2 shows a widely used inverter topology with such a converter, where two additional IGBTs and an inductor are used for interfacing to a low-voltage battery.

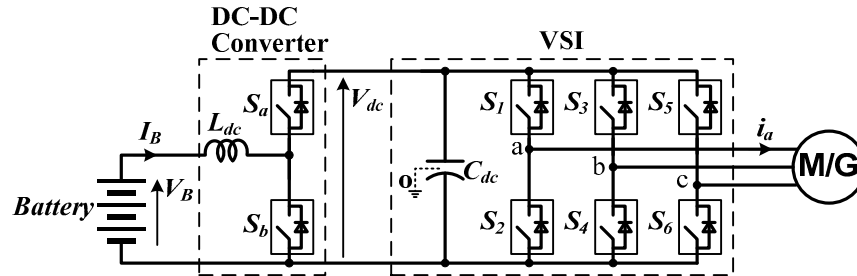


Figure 2. A voltage source inverter with a bidirectional dc-dc converter for interfacing to a low-voltage battery.

All these problems can be eliminated or significantly reduced by the use of another type of inverter, the current source inverter (CSI) [shown in Figure 1(b)]. The CSI does not require any dc bus capacitors and uses only three alternating-current (ac) filter capacitors of a much smaller capacitance; the total capacitance of the ac filter capacitors is estimated at approximately one-fifth of the dc bus capacitance in the VSI. In addition, the CSI offers many other advantages important for EV applications, including that (1) it does not need antiparallel diodes in the switches, (2) it can tolerate phase-leg shoot-throughs, (3) it provides a sinusoid-shaped voltage output to the motor, and (4) it can boost the output voltage to a higher level than the source voltage to enable the motor to operate at higher speeds. These advantages could translate into a significant reduction in inverter cost and volume with increased reliability, a much higher constant-power-speed-range, and improved motor efficiency and lifetime.

Two factors, however, have so far prevented the application of CSIs in HEVs. The first is the difficulty of incorporating batteries into a CSI as energy storage devices, and the second is the limited availability of power switches that can block voltages in both forward and reverse directions. Now that IGBTs with reverse-blocking capability are being offered as engineering samples and the technology is rapidly reaching the maturity needed for commercial production, this research aims to remove the remaining hurdles and bring the advantageous CSI to HEV applications. This project examines a new inverter topology based on the CSI, but with a novel scheme to incorporate energy-storage devices. By significantly reducing the amount of capacitance required, the CSI-based inverter with silicon IGBTs will be able to substantially decrease the requirements for cooling systems and, further, could enable air-cooled power inverters in the future when SiC-based switches become commercially viable.

The overall objective of the research is to design, fabricate, test, and evaluate a 55-kW inverter prototype based on the novel CSI topology to replace the VSI for EV applications. Three major tasks will be carried out over 3 years: (1) modeling and simulation, (2) design and fabrication of a 55-kW prototype, and (3) testing and evaluation. In FY 2007, computer modeling and simulation has been conducted to downselect an optimal interface circuit, followed by production of a conceptual design of a 55-kW inverter system. Building on the FY 2007 activities, a 55-kW prototype will be designed, fabricated, and tested in FY 2008 to provide data for performance analysis.

Description of the Proposed Current Source Inverter

Figure 3 shows a schematic of the proposed CSI with a battery interface circuit. The interface circuit—with the help of the dc choke, L_{dc} —transforms the voltage source of the battery into a current source to the inverter bridge by providing the capability to control and maintain a constant dc bus current,

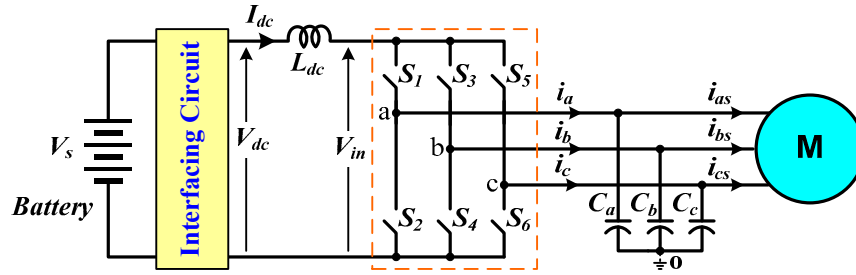


Figure 3. Schematic of the proposed current-source based inverter.

I_{dc} . More important, the interface circuit also enables the inverter to charge the battery during dynamic braking without the need for reversing the direction of the dc bus current.

Whereas the VSI produces a voltage pulse train, the CSI generates a current pulse train in each phase output by turning on and off the switches, $S_1 \sim S_6$, in the bridge according to a PWM strategy. The pulsed phase currents are then filtered by a simple filter network utilizing the three capacitors, C_a , C_b , and C_c , which provide sinusoidal currents as well as sinusoidal voltages to the electrical motor. The sinusoidal voltages are desirable for the motor because they eliminate the problems of the VSI output voltages, which are in the form of pulse trains with steep rising and falling edges and thus generate high EMI noises, impose high stress on the motor insulation, and produce high-frequency losses in the copper windings and iron cores of the motor as well as generate bearing-leakage currents.

An ac generator driven by an internal combustion engine could also be incorporated into the inverter system for hybrid vehicles.

Generally, modulation schemes can be categorized into two main groups: carrier-based and space vector schemes. Because of the duality between the VSI and CSI, it is possible to translate the modulation schemes between the two types of inverters. Switching tables of the VSI and the CSI are given in Table 1 and Table 2, respectively. The space vector diagrams are given in Figure 4.

Table 1. Switching table of the VSI

	Top devices			Bottom devices			Phase voltages		
	S_1	S_3	S_5	S_2	S_4	S_6	V_{ao}	V_{bo}	V_{co}
V_0	0	0	0	1	1	1	0	0	0
V_1	1	0	0	0	1	1	V_{dc}	0	0
V_2	1	1	0	0	0	1	V_{dc}	V_{dc}	0
V_3	0	1	0	1	0	1	0	V_{dc}	0
V_4	0	1	1	1	0	0	0	V_{dc}	V_{dc}
V_5	0	0	1	1	1	0	0	0	V_{dc}
V_6	1	0	1	0	1	0	V_{dc}	0	V_{dc}
V_7	1	1	1	0	0	0	V_{dc}	V_{dc}	V_{dc}

Table 2. Switching table of the CSI

	Top devices			Bottom devices			Phase currents		
	S_1	S_3	S_5	S_2	S_4	S_6	i_a	i_b	i_c
I_1	1	0	0	0	0	1	I_{dc}	0	$-I_{dc}$
I_2	0	1	0	0	0	1	0	I_{dc}	$-I_{dc}$
I_3	0	1	0	1	0	0	$-I_{dc}$	I_{dc}	0
I_4	0	0	1	1	0	0	$-I_{dc}$	0	I_{dc}
I_5	0	0	1	0	1	0	0	$-I_{dc}$	I_{dc}
I_6	1	0	0	0	1	0	I_{dc}	$-I_{dc}$	0
I_7	1	0	0	1	0	0	0	0	0
I_8	0	1	0	0	1	0	0	0	0
I_9	0	0	1	0	0	1	0	0	0

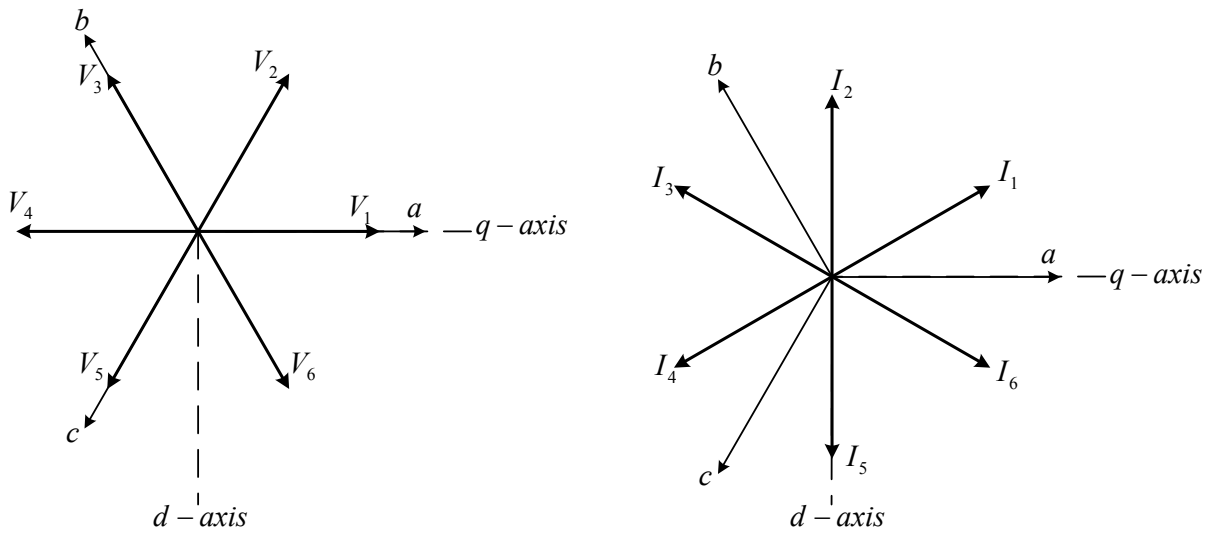


Figure 4. Space vector diagrams for the VSI (left) and CSI (right).

The voltage vector of the VSI is mapped to the current vector of the CSI according to the following rules,

$$\begin{aligned}
 V_1 &\rightarrow I_6 & V_2 &\rightarrow I_1 \\
 V_3 &\rightarrow I_2 & V_4 &\rightarrow I_3 \\
 V_5 &\rightarrow I_4 & V_6 &\rightarrow I_5
 \end{aligned} \tag{1}$$

The switching functions of the CSI can then be mapped from that of the VSI by

$$\begin{aligned}
 S_{1i} &= S_{1v} \cdot S_{6v} + S_{0i} & S_{3i} &= S_{3v} \cdot S_{2v} + S_{0i} \\
 S_{5i} &= S_{5v} \cdot S_{4v} + S_{0i} & S_{2i} &= S_{2v} \cdot S_{5v} + S_{0i} \\
 S_{4i} &= S_{4v} \cdot S_{1v} + S_{0i} & S_{6i} &= S_{6v} \cdot S_{3v} + S_{0i}
 \end{aligned} \tag{2}$$

where the subscript “v” represents the switching function of the VSI, while the subscript “i” represents that of the CSI; S_{0i} represents the zero sequence states of the CSI, I_7 , I_8 , and I_9 . The zero sequence signals are there to balance the on time intervals for the switches and will not affect the fundamental component; however, they can be used to minimize the switching losses. Table 3 gives the optimal zero sequence for each switching state.

Table 3. Optimal zero sequence

Current active vector	Next active vector	Sector	Optimal zero sequence
I_6	I_1	I	I_7
I_1	I_2	II	I_9
I_2	I_3	III	I_8
I_3	I_4	IV	I_7
I_4	I_5	V	I_9
I_5	I_6	VI	I_8

Note that because of the phase angle difference between the voltage vectors and the current vectors, the direct mapping of the space vectors of the VSI to those of the CSI produces a 30° phase shift between the output current and the reference current.

The triangle carrier-based modulation produces two active zones, in which each active zone is composed of two active states arranged with different sequences. The zero states are located at both the beginning and the end of each active zone. On the other hand, the sawtooth carrier-based modulation removes the zero state between the two active zones and combines the two active zones into one. Therefore, the latter may further reduce the number of device switchings over a switching cycle.

The space vector PWM technique is another attractive method for digital control because of its inherent advantages of direct calculation in qd reference frame and straightforward implementation in digital controllers. The space vector modulation methodology of VSIs can also be adapted to the CSIs. The goal is to optimally use the three variables—two active vectors “a” and “b” and zero vector—to generate the desired current vector. The process of implementation can be divided into three steps: (1) transformation of the commands from the abc stationary reference frame to the q-d stationary reference frame, (2) calculation of the time intervals of the vector “a” and vector “b,” and (3) generation of modulation signals based on the time intervals. Table 4 gives the normalized time interval for the two active and zero vectors for each sector.

Simulation results of the three PWM schemes at a frequency of 5 kHz are given in Figure 5, where (a) is for the triangle carrier, (b) for the sawtooth carrier, and (c) for the space vector modulation schemes, respectively. While all three schemes generate smooth sinusoidal load currents, at the same carrier frequency, the sawtooth-based PWM produces greater harmonics around the switching frequency and smaller harmonics at the multiples of the switching frequency. Given equal switching losses, the frequency of the sawtooth carrier can be doubled, thus significantly reducing the total harmonic distortion.

Table 4. Normalized time intervals for the two active and zero vectors for each sector

Sector	First active vector (t_α)	Second active vector (t_β)	Zero vector (t_0)
I	$-\frac{i_c}{I_{dc}}$	$-\frac{i_b}{I_{dc}}$	$1 - \frac{i_a}{I_{dc}}$
II	$\frac{i_b}{I_{dc}}$	$\frac{i_a}{I_{dc}}$	$1 + \frac{i_c}{I_{dc}}$
III	$-\frac{i_a}{I_{dc}}$	$-\frac{i_c}{I_{dc}}$	$1 - \frac{i_b}{I_{dc}}$
IV	$\frac{i_c}{I_{dc}}$	$\frac{i_b}{I_{dc}}$	$1 + \frac{i_a}{I_{dc}}$
V	$-\frac{i_b}{I_{dc}}$	$-\frac{i_a}{I_{dc}}$	$1 - \frac{i_c}{I_{dc}}$
VI	$\frac{i_a}{I_{dc}}$	$\frac{i_c}{I_{dc}}$	$1 + \frac{i_b}{I_{dc}}$

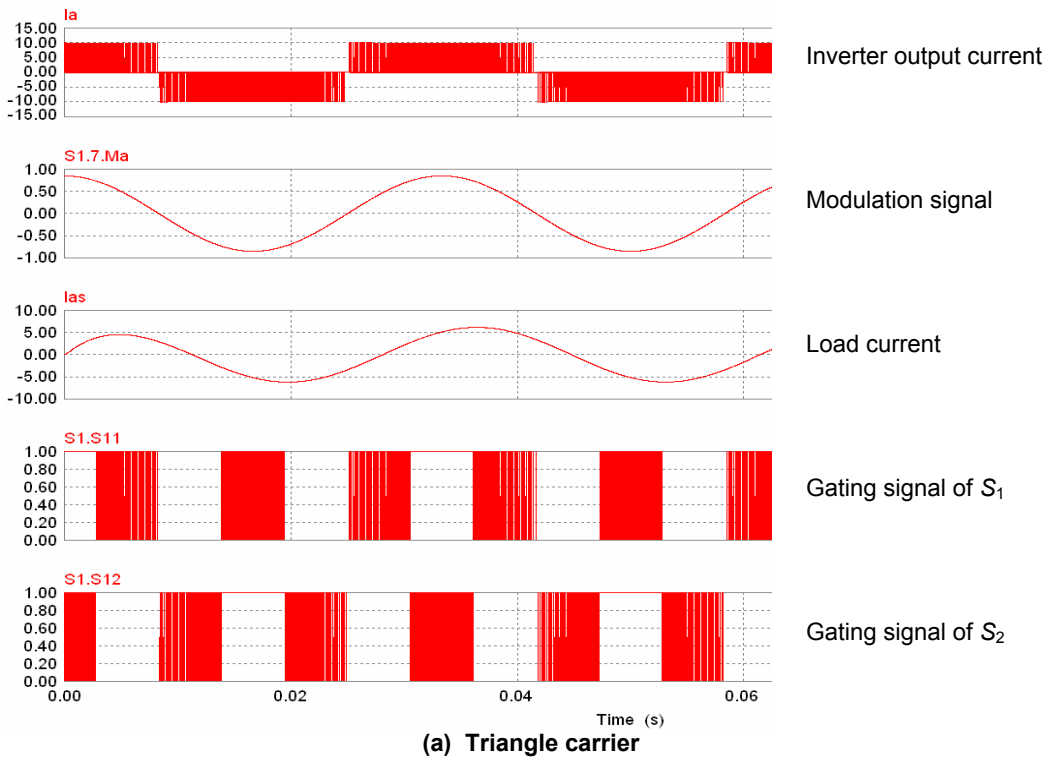
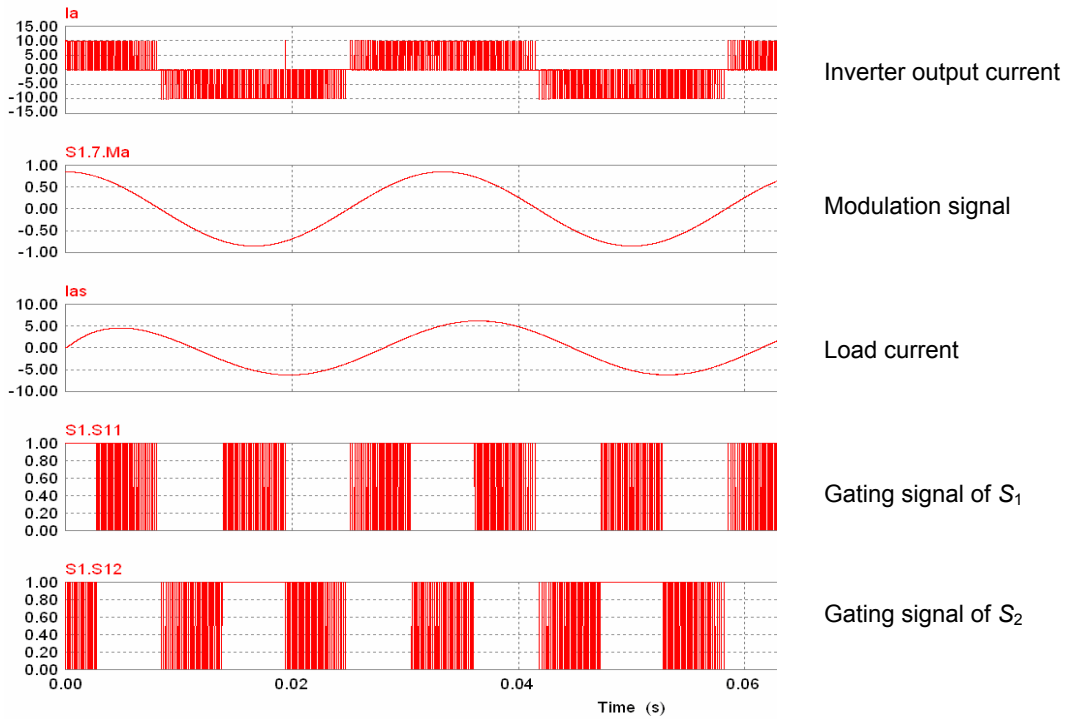
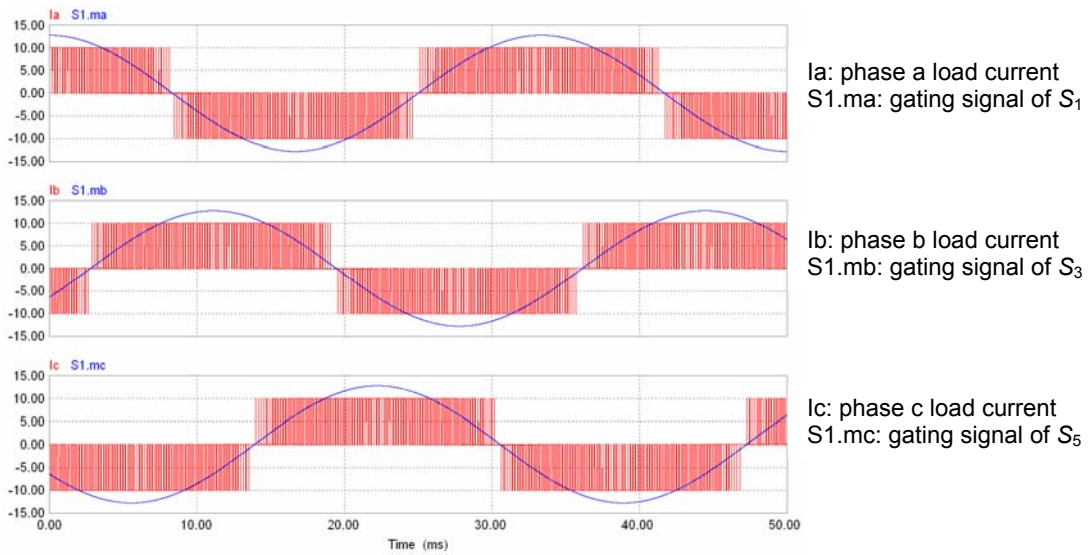


Figure 5. Simulation results of the PWM schemes.



(b) Sawtooth carrier



(c) Space vector

Figure 5. Simulation results of the PWM schemes (continued).

The carrier-based PWM schemes can be realized by direct mapping from the VSI counterparts and are thus simple and easy to implement with analog circuits. While the active state intervals are calculated indirectly and the sequence and ordering of the active states are implicit for the carrier-based PWM schemes, with the space vector PWM algorithm, the sequence, ordering, and the period of the active states are all explicitly computed. Moreover, the sequence of the active states and null state can be arranged arbitrarily as long as the total time period for each switching cycle meets the desired value. The space vector PWM algorithm is therefore good for digital control and will be used in the prototype development.

Modeling and Control of IPM Machines with the CSI

Assuming the interface circuit generates the output voltage, V_{dc} , proportional to the input voltage, V_s , that is,

$$V_{dc} = M_{dc} \cdot V_s \quad (3)$$

where M_{dc} is a control signal. The CSI switch network can be modeled by

$$i_a = S_1 \cdot I_{dc} - S_2 \cdot I_{dc}, \quad i_b = S_3 \cdot I_{dc} - S_4 \cdot I_{dc}, \quad i_c = S_5 \cdot I_{dc} - S_6 \cdot I_{dc} \quad (4)$$

The ac filter capacitors and dc link inductor can be described by Eqs. (5) and (6), respectively.

$$Cdv_{ao} / dt = i_a - i_{as}, \quad Cdv_{bo} / dt = i_b - i_{bs}, \quad Cdv_{co} / dt = i_c - i_{cs} \quad (5)$$

$$L_{dc} pI_{dc} = V_{dc} - V_{in} \quad (6)$$

The input voltage, V_{in} can be calculated from the switching functions and the ac capacitor voltages as

$$V_{in} = v_{ao} (S_1 - S_2) + v_{bo} (S_3 - S_4) + v_{co} (S_5 - S_6) \quad (7)$$

The equivalent circuit of the CSI, which is essentially a boost converter, is shown in Figure 6, in which the switching device G represents the switches of the CSI while the RL load represents an IPM machine. The input and output voltages of the boost converter are related by

$$\frac{V_{load}}{V_{dc}} = \frac{1}{1 - D_{on}} \quad (8)$$

where D_{on} is the duty ratio of the switching device G . The duty ratio is equal to the shoot-through ratio and can be found for balanced three-phase stator currents by

$$D_{on} = 1 - \frac{3}{\pi} M \quad (9)$$

where M is the modulation index for the CSI. Equation (8) can be expressed as

$$V_{load} = \frac{\pi}{3M} V_{dc} \quad (10)$$

It is now apparent from the above equation that the load voltage increases when the magnitude of the modulation index decreases. When the desired output currents are given, the multiplication of the dc link current and the modulation signals are fixed. Hence if the modulation signals decrease, the dc link current needs to be increased to track the desired output phase current.

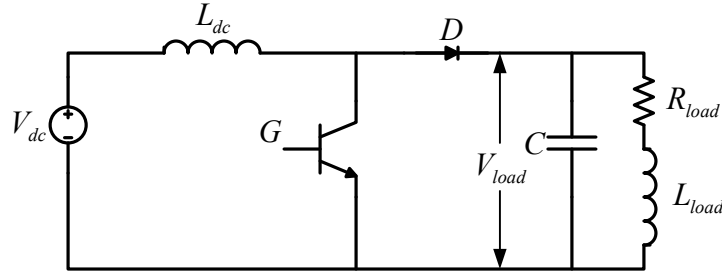


Figure 6. Equivalent circuit of the CSI for voltage boosting.

The ac capacitors, which are connected in parallel with the IPM machine, function as a filter in the CSI. The reactive currents generated by these capacitors are proportional to the square of the phase voltages. Hence these filter capacitors must be included in the analysis to accurately predict the inverter current, which is especially important when the motor is running at high speeds. The core-loss of an IPM machine can be accounted for by a resistor. Including the core-loss resistor in the modeling can reduce the predicted current error. By including the ac capacitors and core-loss resistor, q- and d-axis equivalent circuits of the IPM machine are given in Figure 7, where L_{ls} is the stator leakage inductance; L_{mq} and L_{md} the q- and d-axis mutual inductances, respectively; R_c the stator core loss resistor; C the filter capacitor per phase; i_{qs} and i_{ds} the q- and d-axis torque producing currents; and i_{qst} and i_{dst} the total currents from the CSI, including the capacitor current component.

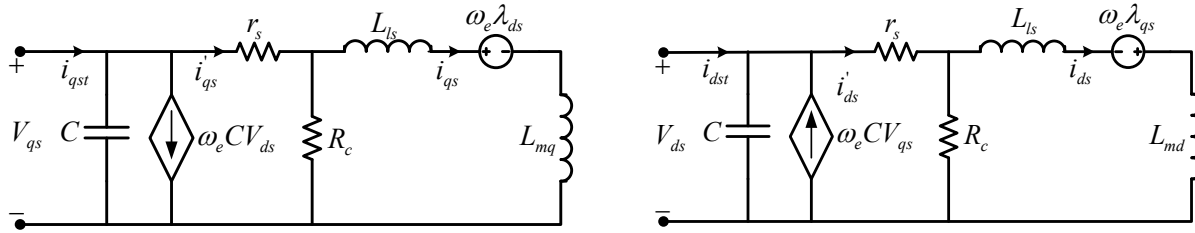


Figure 7. The q- and d-axis equivalent circuits of an IPM machine.

At steady state, the total q- and d-axis currents, including the core-loss resistor and ac capacitors, are given as

$$i_{qst} = \omega_e \left(Cr_s + \frac{L_{ds}}{R_c} \right) i_{ds} + \left[1 - \omega_e^2 CL_{qs} \left(1 + \frac{r_s}{R_c} \right) \right] i_{qs} + \frac{\omega_e \lambda_m}{R_c}, \quad (11)$$

$$i_{dst} = -\omega_e \left(Cr_s + \frac{L_{qs}}{R_c} \right) i_{qs} + \left[1 - \omega_e^2 CL_{ds} \left(1 + \frac{r_s}{R_c} \right) \right] i_{ds} - \omega_e^2 C \lambda_m \left(1 + \frac{r_s}{R_c} \right). \quad (12)$$

Once the torque-producing currents are obtained, the current commands of the CSI can be calculated using Eqs. (11) and (12).

If only the torque-producing currents are considered, the IPM machine model becomes

$$V_{qs} = \omega_e L_{ds} i_{ds} + \omega_e \lambda_m, \quad V_{ds} = -\omega_e L_{qs} i_{qs}, \quad T_e = \frac{3P}{4} \left[\lambda_m i_{qs} + (L_{ds} - L_{qs}) i_{ds} i_{qs} \right]. \quad (13)$$

The goal of this steady state analysis is to find the optimal stator currents within the constraints imposed by the inverter to produce the maximum output torque per unit of current. Without going into a detailed derivation, the resultant optimal current expressions are given as follows.

Region I and II:

$$i_{qs_op} = \frac{\sqrt{-2\lambda_m^2 + 8L_{qs}^2 I_m^2 - 16L_{qs} L_{ds} I_m^2 + 8L_{ds}^2 I_m^2 + 2\lambda_m \sqrt{\lambda_m^2 + 8L_{qs}^2 I_m^2 - 16L_{qs} L_{ds} I_m^2 + 8L_{ds}^2 I_m^2}}{4(L_{qs} - L_{ds})}$$

$$i_{ds_op} = -\sqrt{I_m^2 - i_{qs_op}^2}$$
(14)

Region III:

$$i_{qs} = \frac{\sqrt{-L_{ds}^2 \lambda_m^2 \omega_e^2 + 2L_{ds} \lambda_m \omega_e \sqrt{L_{ds}^2 V_m^2 - L_{ds}^2 \omega_e^2 L_{qs}^2 I_m^2 - L_{qs}^2 V_m^2} + L_{qs}^2 \omega_e^2 \lambda_m^2 + L_{qs}^4 \omega_e^2 I_m^2}}{\omega_e (L_{qs}^2 - L_{ds}^2)}$$

$$i_{ds} = -\sqrt{I_m^2 - i_{qs}^2}$$
(15)

Region IV:

$$i_{ds} = \frac{-4\omega_e \lambda_m L_{ds} + 3\omega_e L_{qs} \lambda_m + \sqrt{\omega_e^2 \lambda_m^2 L_{qs}^2 + 8L_{ds}^2 V_m^2 - 16L_{qs} L_{ds} V_m^2 + 8L_{qs}^2 V_m^2}}{4\omega_e L_{ds} (L_{ds} - L_{qs})}$$

$$i_{qs} = \frac{\sqrt{(V_m / \omega_e)^2 + (\lambda_m + L_{ds} i_{ds})^2}}{L_{qs}}$$
(16)

Simulation results for steady states are given in Figures 8–10. Different working regions are represented by different colors; the boost region (Region II) is in red. The simulation results validate the boost functionality of the CSI. The constant torque region is extended, greatly enhancing the drive performance.

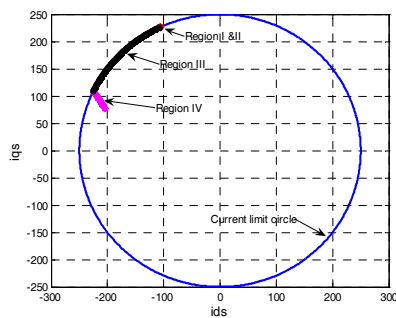


Figure 8. Optimal q- and d-axis currents for IPM machine.

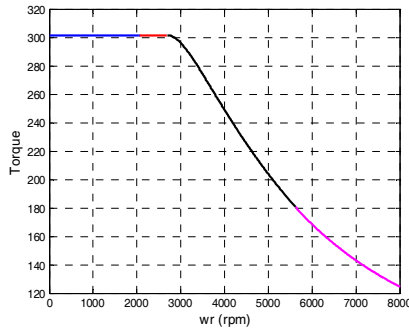


Figure 9. Electromagnetic torque of the IPM machine.

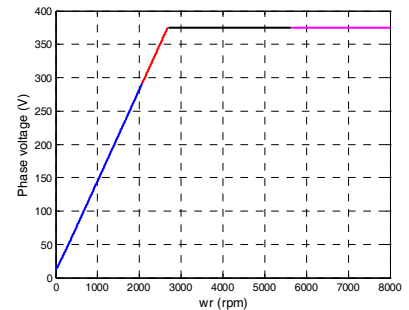


Figure 10. Peak value of the phase voltage.

The control of the IPM drive system can be divided into two regions. In Region I, the motor speed is relatively low so that the boost function of the CSI is not needed. Instead, it operates under a constant

modulation index, while the interface circuit is responsible for the dc current control. In Region II, the interface circuit is effectively bypassed to enhance the boost function of the CSI when the measured dc current is less than the commanded dc current. When the actual dc current is greater than the command, the interface circuit will be activated to maintain the dc current.

Simulation results for control of the Prius motor with the proposed control scheme are shown in Figures 11 and 12. The optimal q- and d-axis currents according to the steady-state analysis results are used to drive the IPM machine under the maximum torque control scheme. The inverter switching frequency is 5 kHz. The dc source voltage is 250 V. It is observed from the simulation results that the maximum torque per amp control can operate from 0 to well over the rated speed of the Prius motor and that the actual q- and d-axis currents track their respective commands very well.

Conceptual Design of a 55-kW Prototype

Based on the simulation results, a conceptual design of a 55-kW CSI was carried out, and major components were selected. Table 5 gives a list of the components. The CSI requires IGBTs that can block voltages in both forward and reverse directions, and because those IGBTs will not likely be available for our prototype development, we have designed custom modules and will ask a power device manufacturer to produce small quantities needed for the prototype development.

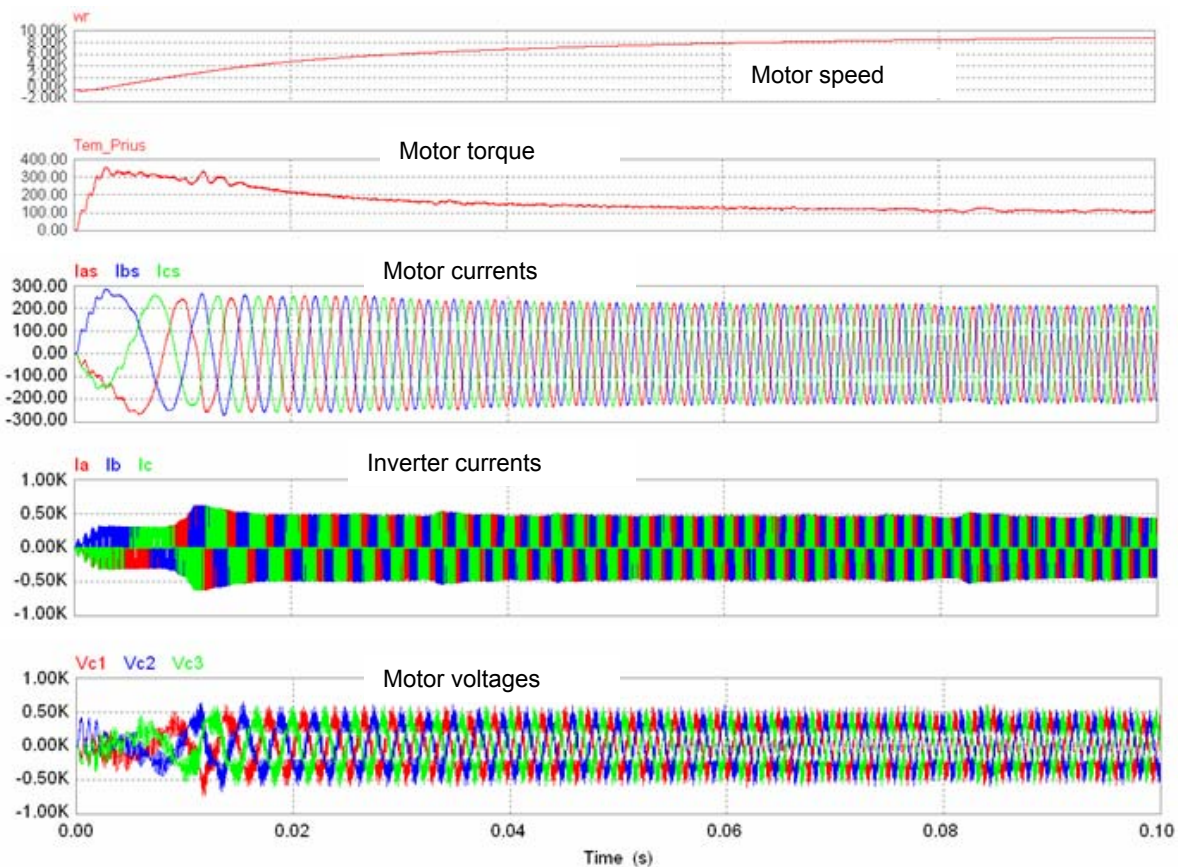


Figure 11. Simulation waveforms showing that maximum torque per amp control can operate from 0 to well over the rated speed of the Prius motor; maximum speed: 8500 rpm.

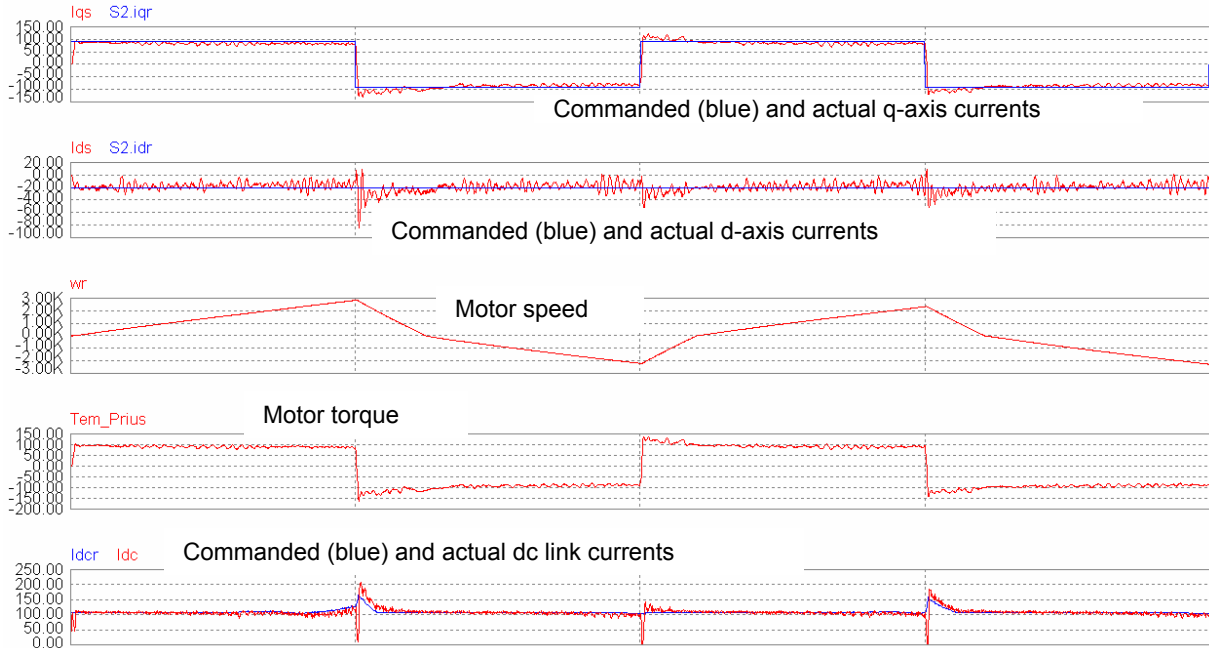


Figure 12. Simulation results for dynamic torque control of the IPM machine.

Table 5. A list of the major components

Component description	Part number	Specifications	Quantity
Inverter IGBT module	Custom	Dual pack, 1200 V, 450 A	3
Converter IGBT module	APTGT300DH60G	Dual pack, 600 V, 300 A	1
ac filter capacitor	5MPA2306J	530 Vac, 30 μ F	3
dc inductor	AMCC 630	200 μ H, 300 A	1
Heat sink	CP30G01	Mounting surface: 8 in. \times 11 in.	1

Conclusion

A high-performance IPM machine drive using a current-source-based inverter has been proposed for HEV applications. The CSI offers many advantages including (1) high reliability due to elimination of dc bus capacitors and endurance of phase-leg shoot-through, (2) improved motor efficiency and lifetime by providing sinusoid-shaped voltage and current to the motor, (3) increased constant-power-speed-range due to the voltage boosting capability, and (4) reduced requirements for battery storage capacity in plug-in HEVs.

Modeling and simulation has been performed with regard to (1) the boost function of the CSI and its effectiveness in extending the constant torque operation region, (2) the equivalent circuit model of the IPM machine, including the effects of the ac filter capacitors and the core-loss resistor, and (3) a high-performance control scheme ensuring the maximum output torque across the entire operating range, including the field-weakening region. The simulation results have validated the functionality of the boost mechanism, the effectiveness of the equivalent circuit model, and the proposed control scheme.

A conceptual design of a 55-kW CSI has been carried out, and major components have been selected.

References

1. B. Wu, G. R. Slemon, and S. B. Dewan, "PWM-CIS induction motor drive with phase angle control," *IEEE Transactions on Industry Applications* **27**(5), 970–976 (September/October 1991).
2. B. Wu, S. B. Dewan, and G. R. Slemon, "PWM-CIS inverter for induction motor drives," *IEEE Transactions on Industry Applications* **28**(1), 64–71 (January/February 1992).
3. G. Joos, G. Moschopoulos, and P. D. Ziogas, "A high performance current source inverter," *IEEE Transactions on Power Electronics* **8**(4), 571–579 (October 1993).
4. M. Takei, Y. Harada, and K. Ueno, "600V-IGBT with reverse blocking capability," *Proceedings of IEEE ISPSD '2001*, pp. 413–416, 2001.
5. E. R. Motto, J. F. Donlon, M. Tabata, H. Takahashi, Y. Yu, and G. Majumdar, "Application characteristics of an experimental RB-IGBT (reverse blocking IGBT) module," *Proceedings of IEEE IAS 2004 Annual Meeting*, pp. 1504–1544, 2004.

4.6 Utilizing the Traction Drive Power Electronics System to Provide Plug-in Capability for HEVs

Principal Investigator: Gui-Jia Su

Oak Ridge National Laboratory

National Transportation Research Center

2360 Cherahala Boulevard

Knoxville, TN 37932

Voice: 865-946-1330; Fax: 865-946-1262; E-mail: sugj@ornl.gov

DOE Technology Development Manager: Susan A. Rogers

Voice: 202-586-8997; Fax: 202-586-1600; E-mail: Susan.Rogers@ee.doe.gov

ORNL Program Manager: Mitch Olszewski

Voice: 865-946-1350; Fax: 865-946-1262; E-mail: olszewskim@ornl.gov

Objectives

- Overall project objectives are to
 - reduce cost and volume by 90% compared to standalone battery chargers,
 - provide rapid charging capability for use at high-power charging stations,
 - enable plug-in hybrid electric vehicles (PHEVs) as mobile power generators, and
 - investigate hardware and software requirements for implementing smart charging and vehicle-to-grid capabilities.
- Objectives for FY 2007 effort are to
 - prove the concepts by circuit simulation studies,
 - develop battery charging and mobile power generation control strategies, and
 - develop a conceptual design of a 55-kW prototype traction drive with charging and generation functions.

Approach

- Utilize the onboard traction drive inverter(s) and motor(s) to eliminate the requirement for a separate battery charger.
- Perform detailed circuit simulation in PSIM to
 - study control algorithms for battery charging,
 - study control algorithms for mobile power generation,
 - study system performance and thermal implications, and
 - establish voltage and current ratings of major components for a 55-kW prototype.

Major Accomplishments

- Completed simulation study and proved the concept.
- Developed control strategies for charging the battery and operating a PHEV as a generator.
- Completed a conceptual design of a 55-kW prototype and selected major components.

Future Direction

- Design, fabricate, and test a 55-kW inverter prototype with plug-in charging and mobile generation capabilities.

Technical Discussion

Background

Plug-in hybrids are emerging as a pre-fuel-cell technology that offers a greater potential than those hybrid vehicles currently available on the market to reduce oil consumption and carbon dioxide pollutants. In plug-in hybrids, the battery's energy storage capacity needs to be increased significantly to enable a driving distance of at least 40 miles in the all-electric mode needed for a substantial reduction of oil consumption for daily commuting. A charger is also required to replenish the battery after being depleted, which is typically done overnight to leverage energy costs by taking advantage of off-peak electricity rates.

Standalone battery chargers, however, impose extra cost to the already expensive HEVs and possess other limitations. A typical standalone battery charger for plug-in hybrids consists of a diode rectifier and a unidirectional (can only charge the battery) dc-dc converter that uses power semiconductor switches, diodes, inductors, and capacitors, as shown in Figure 1. The cost of a charger with a low charging capability of 1 ~ 3 kW can reach almost 30% of the electric traction system costs for a midsize PHEV-20 car (\$690) [1]. The limited charging capability results in a long charging time (6 ~ 8 h), which could negatively impact the acceptance of PHEVs.

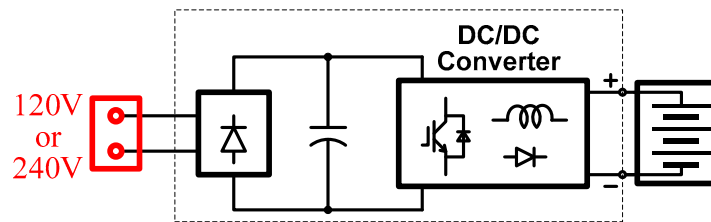


Figure 1. A schematic showing major components in a standalone battery charger.

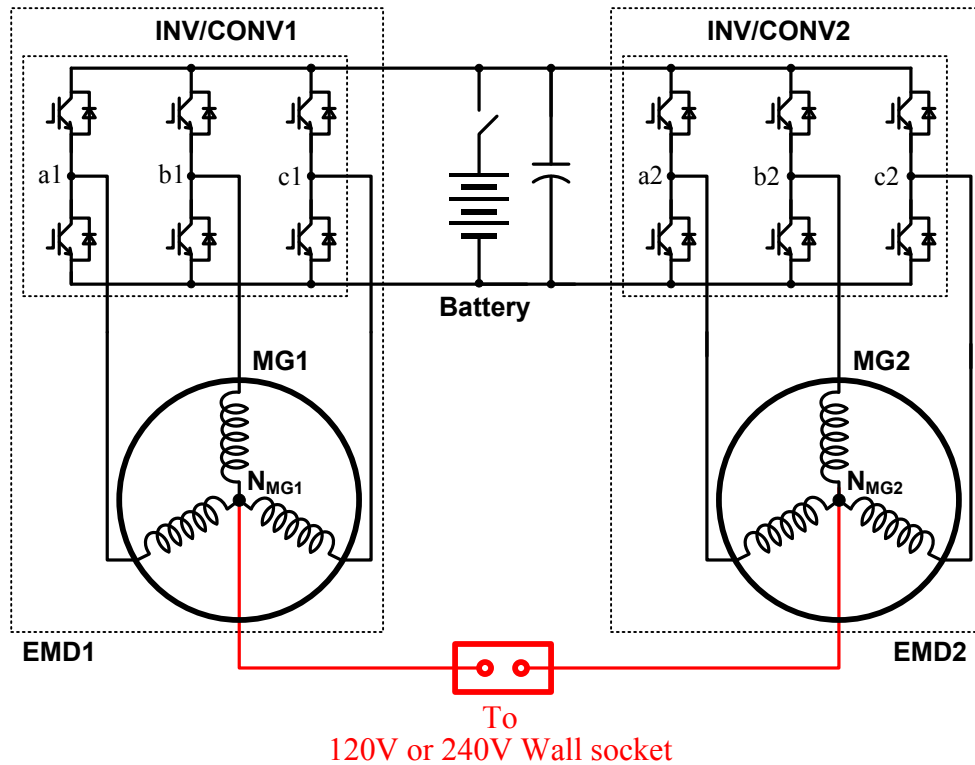
To minimize the cost of the charger, this project aims at investigating the utilization of the already onboard power electronics and motors for fulfilling the charging requirements. It is expected that, compared to a standalone battery charger, the proposed approach will impose virtually no additional cost or significantly reduce it, depending on the configuration of the onboard traction drive system. The proposed approach is to integrate the battery charging function into the traction drive system and to eliminate or minimize the number of additional components. Because traction power inverters have a greater current-carrying capability, the integrated charger can reduce the charging time significantly. Another added benefit with this approach is the capability of making the PHEVs function as mobile generators at no additional or minimum extra cost. During this project Oak Ridge National Laboratory (ORNL) will also investigate hardware and software requirements for implementing smart charging and vehicle-to-grid capabilities.

Description of the Reduced-Part dc/dc Converter

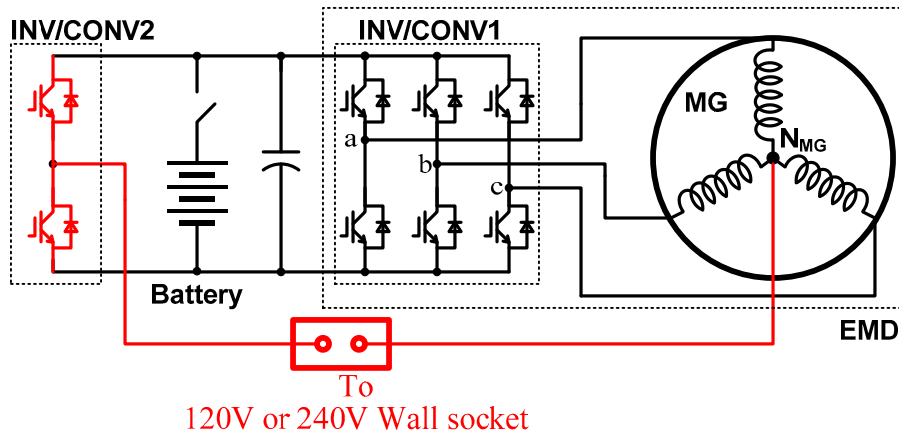
Figure 2 shows two topologies for utilizing the onboard electrical drive system to provide plug-in charging and mobile generation capabilities for HEVs. The onboard electrical drive system may consist of one or more electrical motor drive (EMD) units, all connected to a common dc bus. Each motor drive unit typically employs a three-phase inverter/converter (INV/CONV) and a three-phase motor/generator (MG) of Y-connection with a neutral point (N_{MG}). At least one drive unit is coupled to the engine shaft through a mechanical transmission. The basic idea is to use the motor/generators as inductors by connecting their neutral points to an external source for charging the battery, or external loads for supplying power to them. The external charging source can be a dc, single or multiphase ac power supply depending on the number of onboard drive units. Figure 2(a) illustrates an arrangement for a series of HEVs, where two inverter/converters and two motor/generators are employed. For such vehicles, virtually no additional

components, except some wiring and connectors are required. For parallel HEVs, where only one inverter/converter and motor/generator are used, two switches need to be added, as shown in Figure 2(b).

All the switch legs in each inverter/converter collectively function as a single switch leg and the motor/generator as an inductor. Together, the drive units form a single-phase or multiphase converter, when operating in the charging mode, to regulate the dc bus voltage. When operating in the generation mode, the drive units form a single or multiphase inverter to supply external loads. In this mode, the



(a) For HEVs using two inverters and motors



(b) For HEVs using a single inverter and motor

Figure 2. Topologies for utilizing the onboard electrical drive system to provide plug-in charging and mobile generation capabilities for HEVs. (Red denotes added components.)

motor/generator of the drive unit coupled to the engine shaft is driven by an engine to generate power for supplying the dc bus and ultimately the external loads, or power can be drawn from the battery for short time interval operations.

Figure 3 shows an equivalent circuit of Figure 2(a), when operating in the charging mode. All the three switch-legs (a1, b1, c1 and a2, b2, c2) in each of the two inverters/converters, INV/CONV1 and INV/CONV2, collectively function as a single switch leg, and the motors/generators as two impedance networks [stator zero sequence impedance networks (ZSIN1 and ZSIN2)]. Each of the ZSINs consists of three branches, and each branch comprises the stator winding phase resistance (R_{ms1} or R_{ms2}) and the stator phase leakage inductance (l_{m0s1} or l_{m0s2}). Together, the two drive units form a single-phase converter to regulate the battery voltage, V_{bat} , or the charging current, I_{bat} . Normally, the single-phase converter is controlled in such a way as to maintain a unity power factor by keeping the source current, i_s , in phase with the source voltage, v_s . An additional benefit of operating the three-phase converters as single leg converters is the reduced harmonic current components resulted from interleaving the gating signals of the three legs.

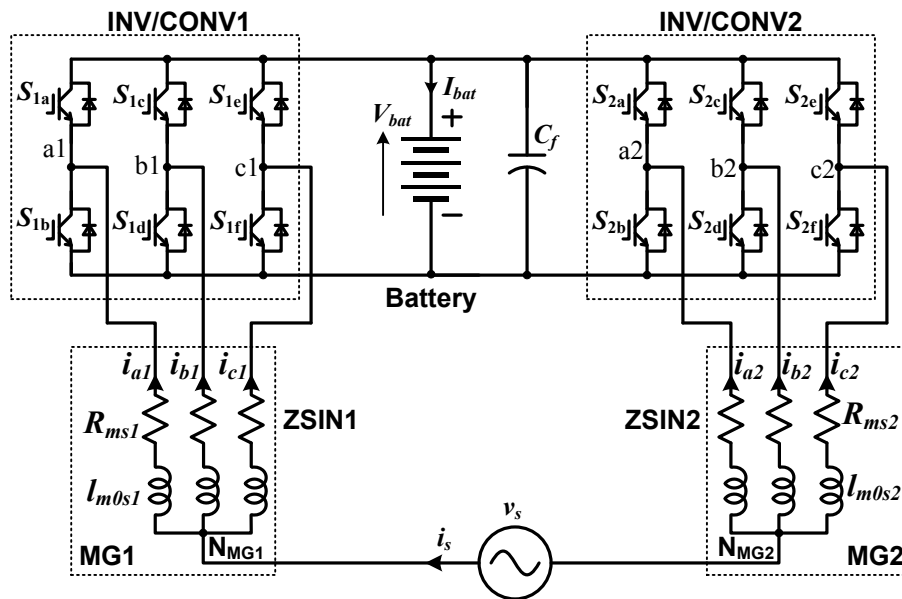
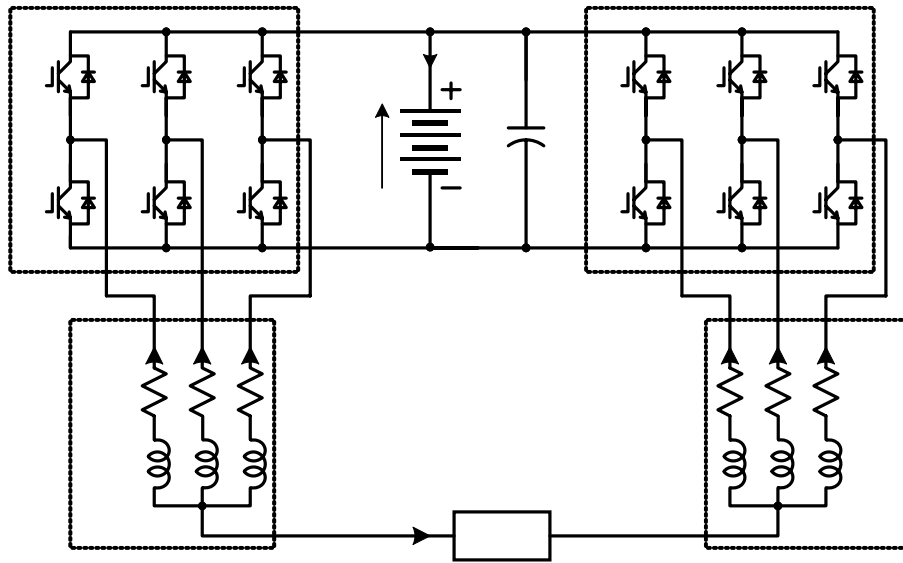


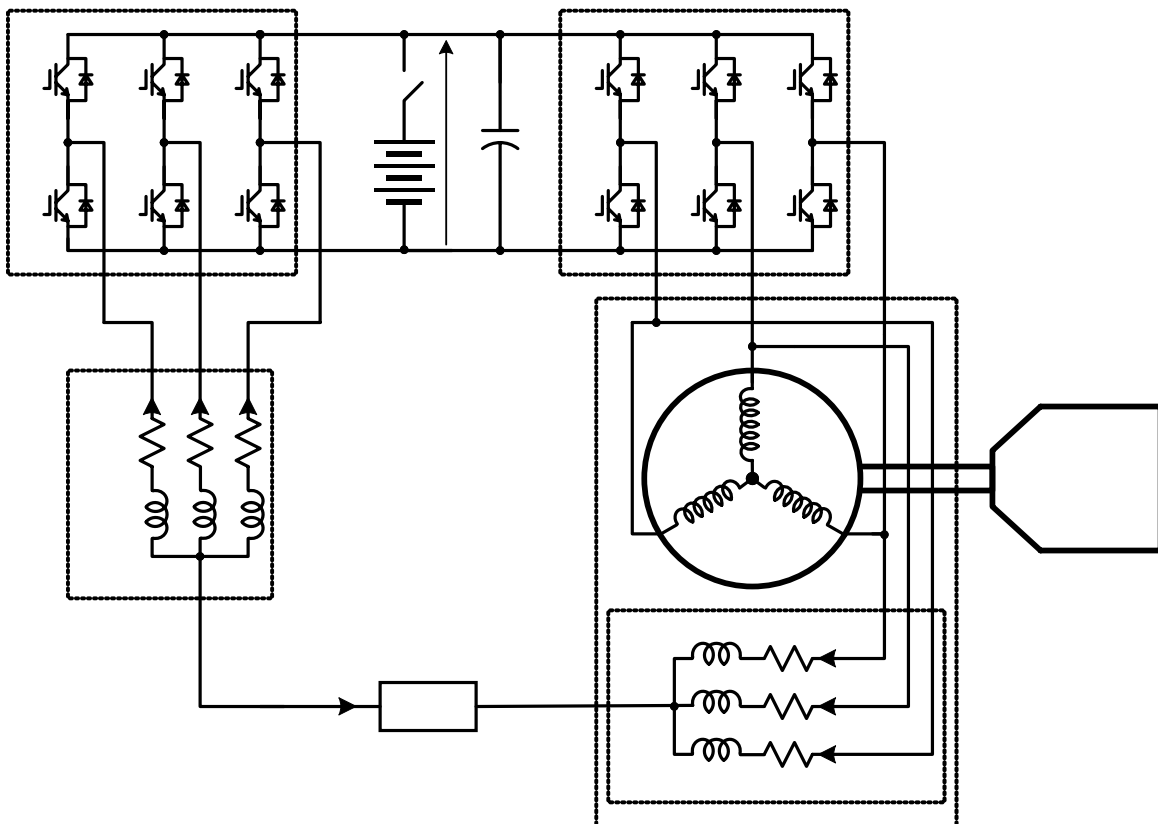
Figure 3. An equivalent circuit for the battery charging mode.

Figure 4 shows equivalent circuits of Figure 2(a), when operating in the mobile generation mode. There are two available power sources, the battery and the engine. Figure 4(a) illustrates the case where the battery is the source. In this case, all the three switch-legs in each of the two inverters/converters collectively function as a single switch leg and the motors/generators as two impedance networks. Together, the two drive units form a single-phase inverter to regulate the load voltage, v_{Load} .

Figure 4(b) illustrates the case where power is generated by the MG2 driven by the engine. In this case, the three switch-legs in INV/CONV1 collectively function as the first single switch leg of a single-phase inverter and the MG1 as an impedance network. The other inverter/converter, INV/CONV2, has dual functions. It first operates as a three-phase converter to regulate the dc bus voltage V_{dc} by drawing power from the generator; at the same time, its three-phase legs collectively form the second switch leg of the single-phase inverter to regulate the load voltage, v_{Load} .



(a) Using the battery as the power source



(b) Using the motor MG2 driven by the engine as the power source

Figure 4. Equivalent circuits for mobile generator mode.

Simulation Results

Detailed circuit simulations were performed in PSIM to prove the concepts and provide circuit design data for use in the prototype design of a 55-kW drive system with plug-in charging function. Figure 5 gives simulation results showing the system is operating in the charging mode when the battery is charged at 20 kW from a 240-V source. Figure 6 plots simulation results for operating in the charging mode, but the charging power is reduced to 10 kW from a 120-V source. In both cases, the charger is operating at a unity power factor as indicated by the fact that the source current, i_s is in phase with the source voltage, v_s .

Figures 7 and 8 show simulation results when the system is operating in the generating mode. The first figure is for the case where the system is supplying 2-kW power at 120 V to a resistive load, and power is drawn from the battery as indicated by the negative battery current. The second figure is for the system drawing power from the generator and supplying 5 kW to a resistive load at 120 V.

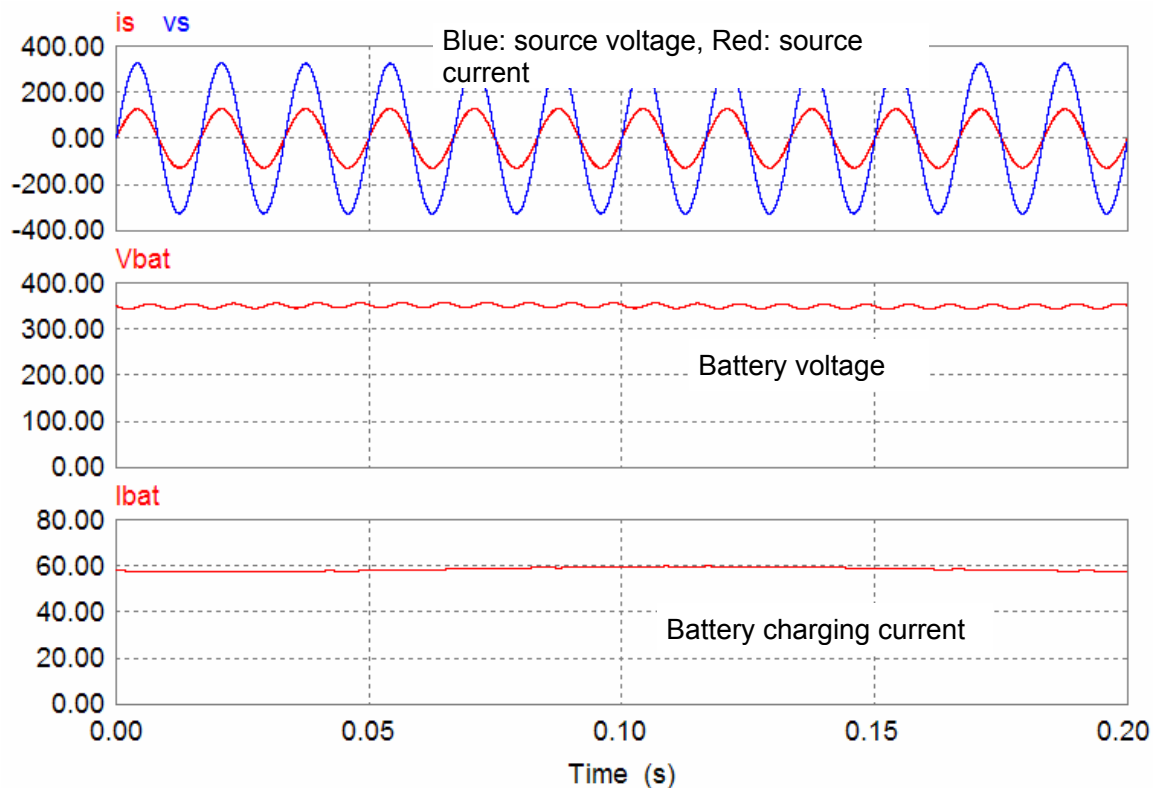


Figure 5. Simulation results showing operation in the charging mode at 20 kW from a 240-V source.

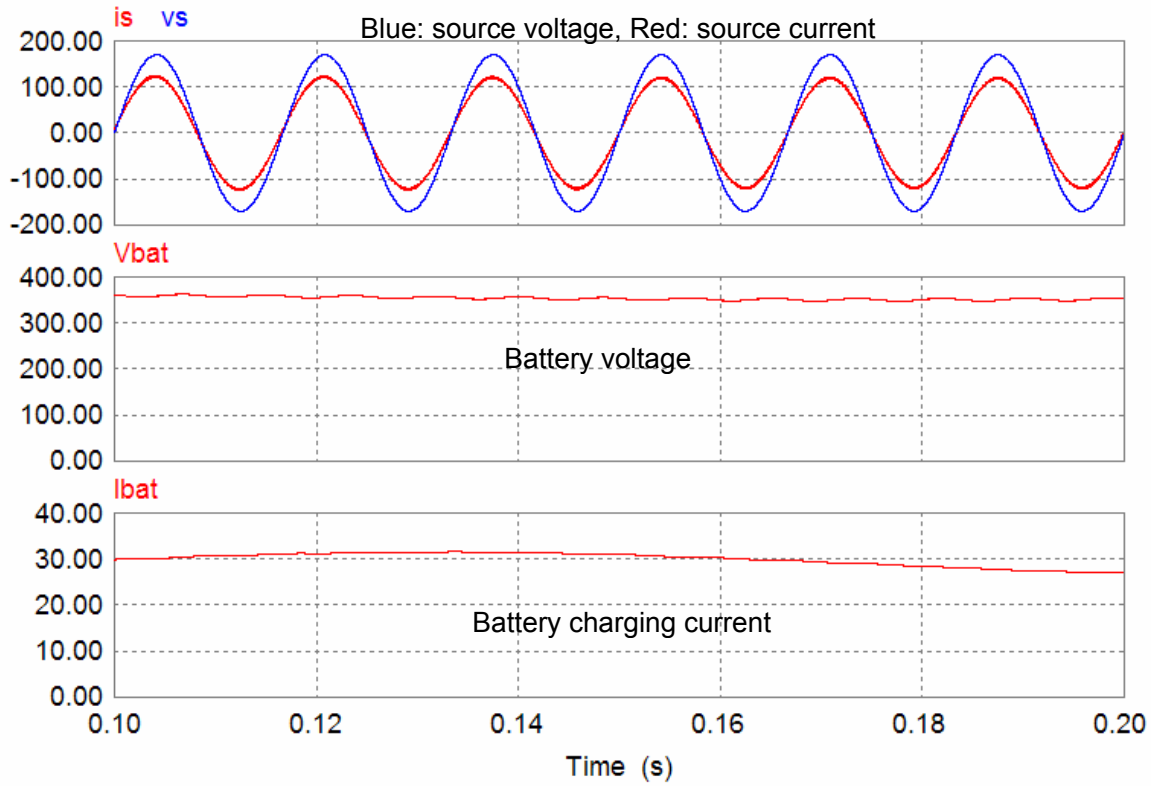


Figure 6. Simulation results showing operation in the charging mode at 10 kW from a 120-V source.

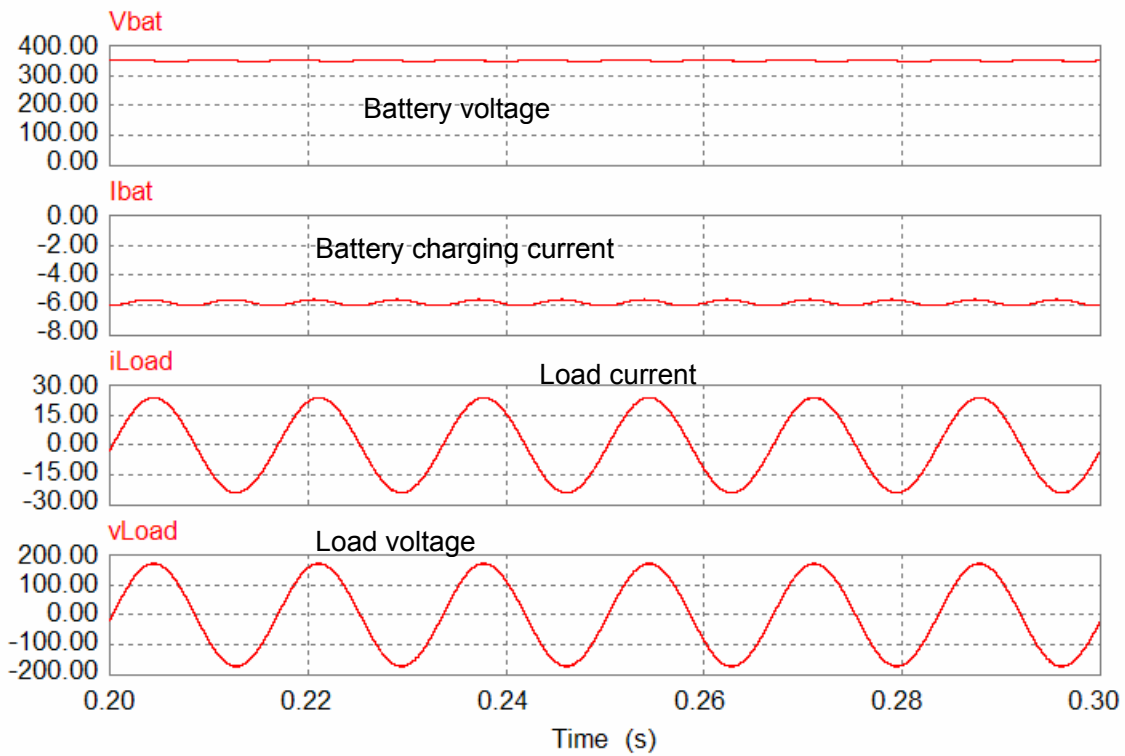


Figure 7. Simulation results showing operation in the generating mode, supplying 2 kW at 120 V.

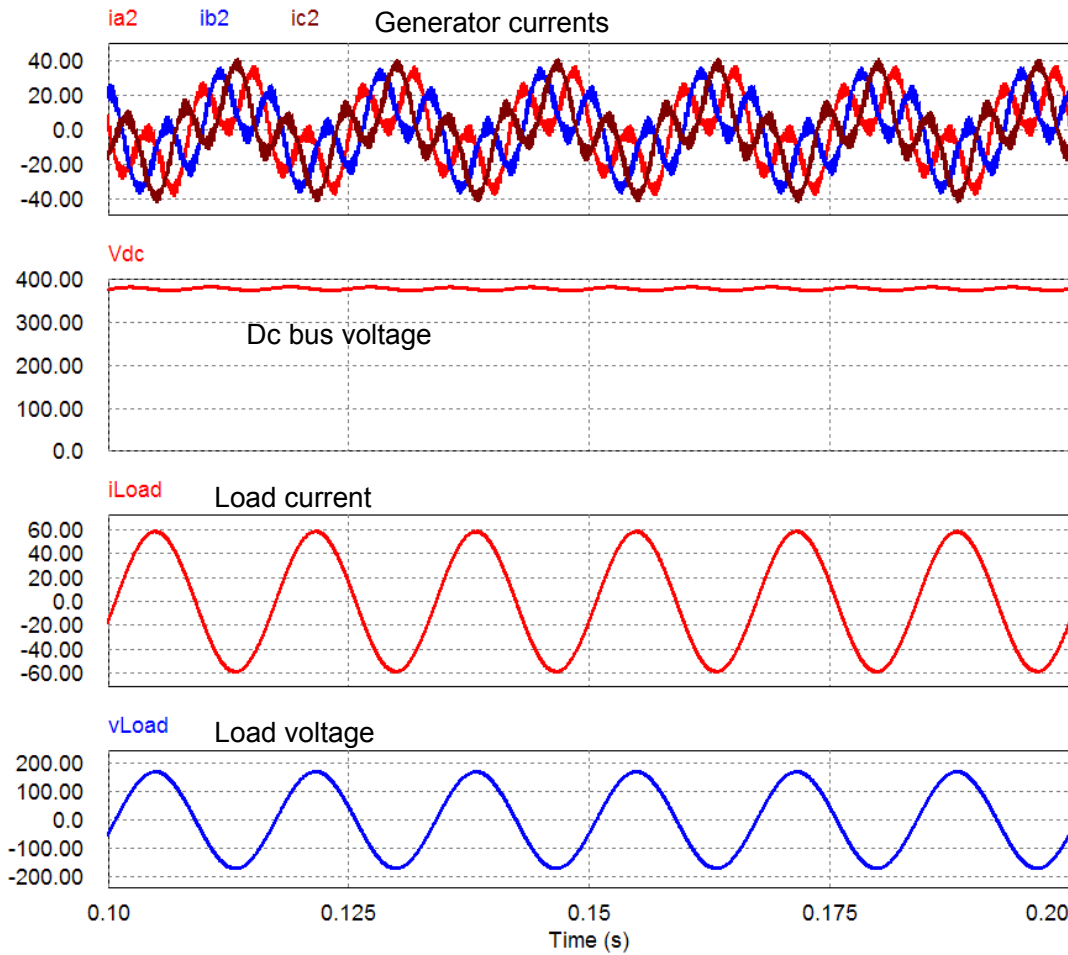


Figure 8. Simulation results showing operation in the generating mode, supplying 5 kW at 120 V.

Conceptual Design of a 55-kW Prototype

Based on the simulation results, a preliminary prototype design of a 55-kW drive system with plug-in charging and mobile generation capabilities was carried out and major components selected. Table 1 gives a list of the components, and Figure 9 shows a 3-D layout of the drive system.

Table 1. A list of major components

Component description	Part No.	Specifications	Quantity
Inverter IGBT module	PM600CLA060	6 pack, 600 V, 600 A	1
Converter IGBT module	PM300CLA060	6 pack, 600 V, 300 A	1
Bus capacitor	UP33BC0375	600 VDC, 375 μ F	4
Heat sink	416201U - 305	Mounting surface: 12 in. \times 7 in.	1

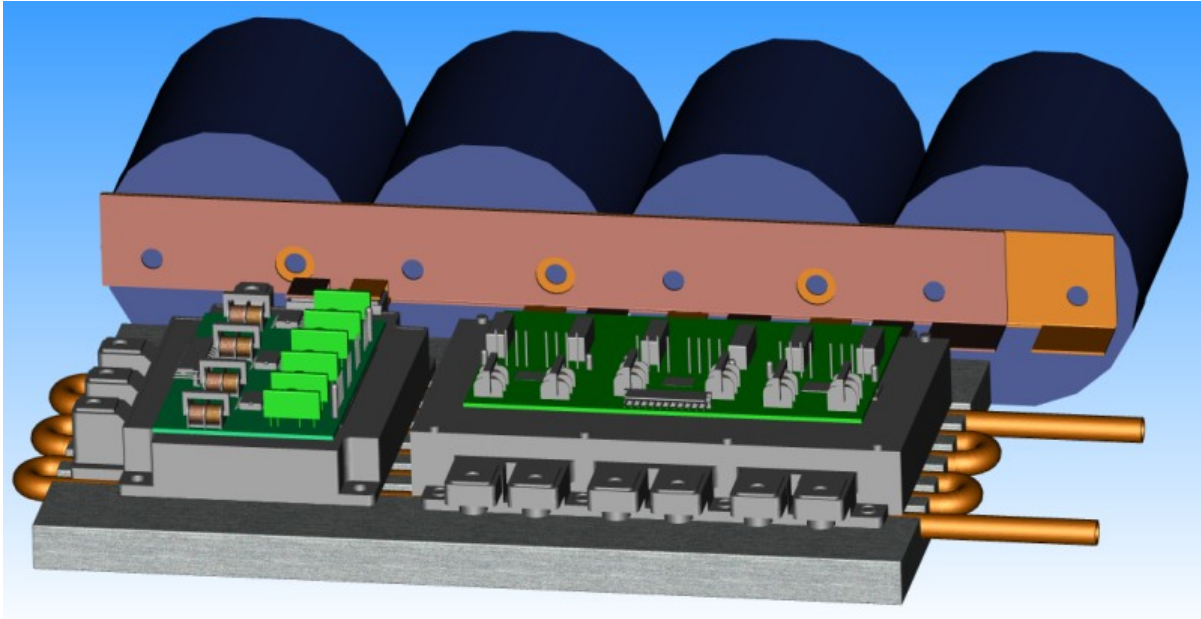


Figure 9. A 3-D drawing of a 55-kW inverter layout design with plug-in charging capability. Heat sink footprint: 12 in. W \times 7 in. D.

Conclusion

In this project, several ways have been proposed to utilize the onboard electrical drive system in different HEV configurations to provide plug-in charging capability. The proposed charging schemes offer many benefits including (1) significantly reducing the cost and volume of battery chargers in plug-in PHEVs, (2) providing rapid charging capability, and (3) enabling PHEVs to function as mobile generators. Detailed circuit simulation has been carried out, and the simulation results have proved the concepts and validated the rapid charging capability.

A preliminary design of a 55-kW drive system with plug-in charging and mobile generation capabilities has been carried out, and major components have been selected.

Patent

“Electric Vehicle System for Charging and Supplying Electrical Power,” pending.

Reference

1. EPRI report 1009299, *Advanced Batteries for Electric-Drive Vehicles*, May 2004.

4.7 dc/dc Converter for Fuel Cell and Hybrid Vehicle

Principal Investigator: Laura Marlino

Oak Ridge National Laboratory

National Transportation Research Center

2360 Cherahala Boulevard

Knoxville, TN 37932

Voice: 865-946-1245; Fax: 865-946-1262; E-mail: marlinold@ornl.gov

DOE Technology Development Manager: Susan A. Rogers

Voice: 202-586-8997; Fax: 202-586-1600; E-mail: susan.rogers@ee.doe.gov

ORNL Program Manager: Mitch Olszewski

Voice: 865-946-1350; Fax: 865-946-1262; E-mail: olszewskim@ornl.gov

Objectives

The objective of this project was to develop and fabricate a 5-kW dc/dc converter with a baseline 14-V output capability for fuel cell and hybrid vehicles. The major objectives for this dc-dc converter technology are to meet

- higher efficiency (92%),
- high coolant temperature capability (105°C),
- high reliability (15 years/150,000 miles),
- smaller volume (5 L),
- lower weight (6 kg), and
- lower cost (\$75 kW).

Approach

The key technical challenge for this converter design was the 105°C coolant temperature. The power switches and magnetics had to be designed to sustain these operating temperatures reliably, without a large cost/mass/volume penalty. The following key technologies were proposed to break through technical barriers to achieve the project goals.

Topology

A novel interleaved dc/dc converter topology was proposed for this high power conversion, as shown in Figure 1. The key merits of this topology are

- lower root mean square current stresses on components due to interleaving,
- reduced ripple current on capacitors due to interleaving,
- lower power losses due to low R_{ds_on} and soft-switching,
- smaller magnetics due to high switching frequency, and
- low electromagnetic interference (EMI) due to integrated power devices and magnetics.

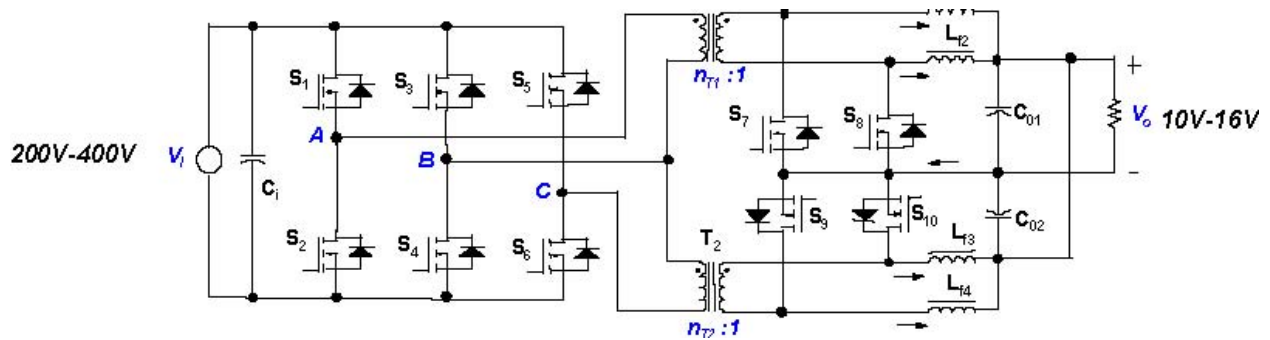
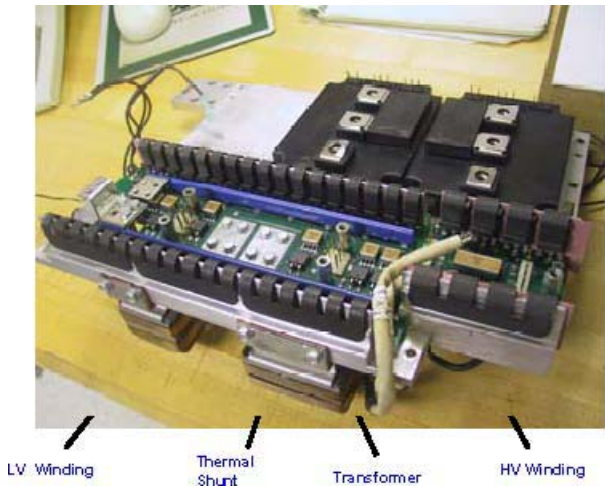


Figure 1. The novel interleaved dc-dc converter topology.

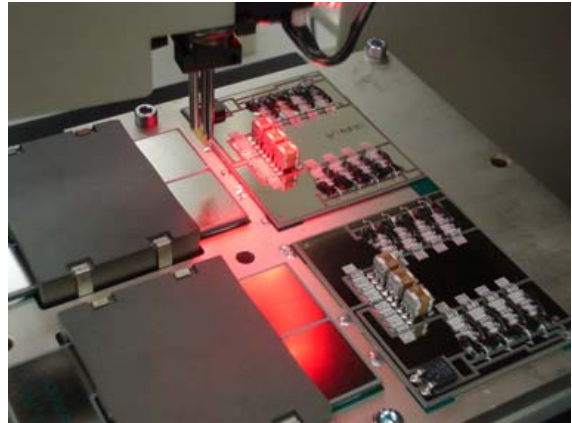
Integrated Module-Based dc/dc Converter

A power module-based integration technology was employed in this design. The 105°C coolant temperature was technically challenging. To meet the design criterion of junction temperature of 125°C, the thermal impedance has to be very small. Power module integration simplifies thermal stack-up layers, obtaining smaller thermal resistance. Furthermore, the customized power module design enhanced the high current interconnection path, reducing the conduction losses. The bolt connections in the transformer winding and the busbars were replaced with using wire bonds that improved reliability. Figure 2 shows a traditional dc/dc converter packaging and the power module-based design approach adopted by this project. The major advantages of the power module based dc/dc converters are

- enhanced thermal performance,
- reduced number of devices,
- increased reliability, and
- higher level of integration.



(a) Conventional design



(b) Power module based design

Figure 2. A traditional dc/dc converter packaging vs power module based packaging.

Planar Magnetics with Enhanced Cooling

This converter was also designed using planar magnetics, a technology that is thought to be critical for reliable and cost-effective high-volume production of such products. The benefits from this technology are

- lower leakage inductance due to shorter winding termination and smaller circuit paths,
- elimination of discrete contacts' ohmic loss,

- reduction of ohmic loss due to shorter conduction paths,
- lower ac loss due to flat winding structure,
- higher core window utilization ratio,
- smaller core volume and weight,
- higher surface-to-volume ratio for improved heat conduction,
- direct cooling of core by direct contact to heat sink, and
- higher power density.

The planar transformer winding structure is shown in Figure 3:

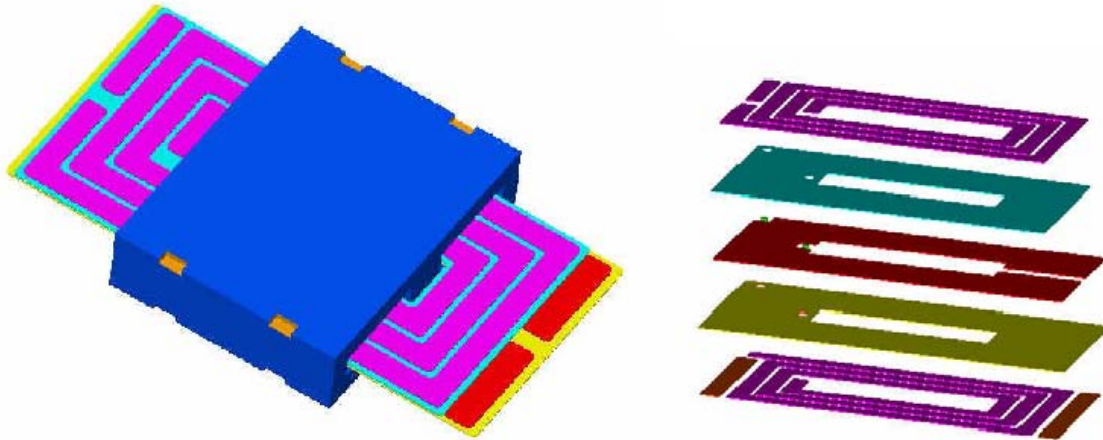


Figure 3. A planar transformer winding structure.

Major Accomplishments

During the year the focus of the FY 2007 work was on the manufacturing issues and testing of the Beta prototype. Table 1 summarizes the final test results vs the Department of Energy (DOE) goals and highlights the percentage of the goals achieved or missed.

Table 1. Final test results and DOE goal achieved

	Parameters	DOE goal	Beta final test result (3/15/2007)	Percent goal achieved
1	Output power	5 kW	5.1 kW	102%
2	Efficiency	92%	93%	101%
3	Cost estimation	\$375 total (\$75/kW)	\$458	82%
3	Coolant temperature	105 °C	105°C	100%
5	Volume	5 L	5.1 L	98%
6	Weight	6 kg	8.33 kg	72%
7	Coolant pressure drop	0.73 psi (5 kPa)	0.25 psi	292%

Future Direction

This project was completed in FY 2007.

Technical Discussion

Manufacturing Process Development—Power Module Process

The power module process includes solder paste printing, die attachment, reflow wire bonding, intermediate testing, and end of line testing. Figure 4 shows the wire bond operation on the power module baseplate. There were many multiple iterations before realizing an appropriate temperature profile for the reflow and wire bond program for the bonding machine.

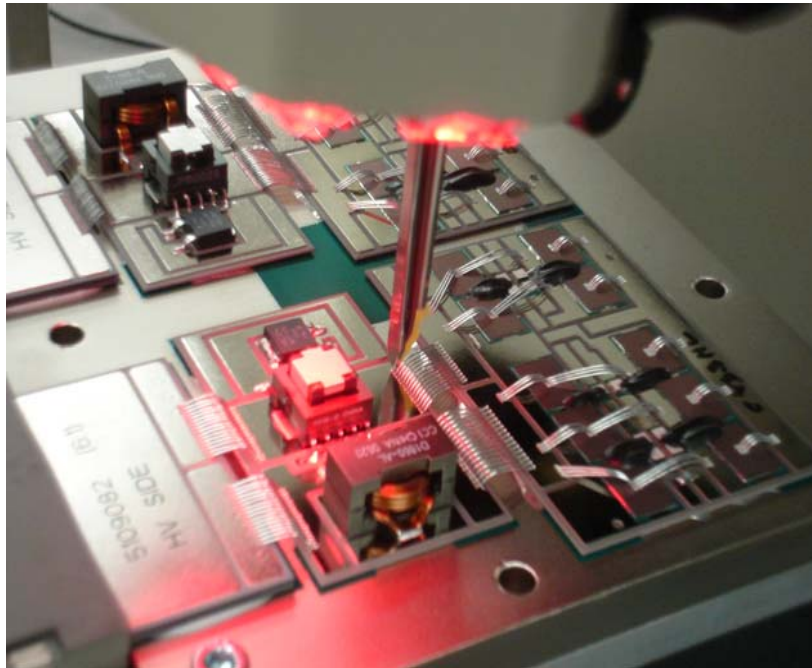


Figure 4. Wire bonding operation.

Manufacturing Process Development—Pilot Plant Process

The manufacturing process is an operation sequence that assembles parts from the bill of materials (BOM) into a finished dc/dc converter. Figure 5 shows a screen shot of one assembly step. The parts to be assembled are listed. The torque values are specified. After completion, the actual torque value is recorded. Figure 6 shows the flow of three representative sequences of three steps in the process.

Beta Prototype Fabrication

It had originally been planned to construct 20 of the power modules, which included units for qualification testing. Budgetary constraints limited the number of builds to nine power modules and five finished dc/dc converters. Figure 7 shows the finished power modules in the clean room.

Beta dc/dc Converter Prototype Final Testing

Four units of the Beta dc/dc converters were tested at the Ballard facility to verify the final design. Oak Ridge National Laboratory (ORNL) representatives later witnessed electrical testing of the unit. The test results among units were consistent. Figure 8 shows the efficiency test setup. It includes the chiller that can provide up to 105°C coolant, a high-voltage power supply with a 200-V to 400-V adjustable range, and 5-kW low-voltage electronic loads and meters.

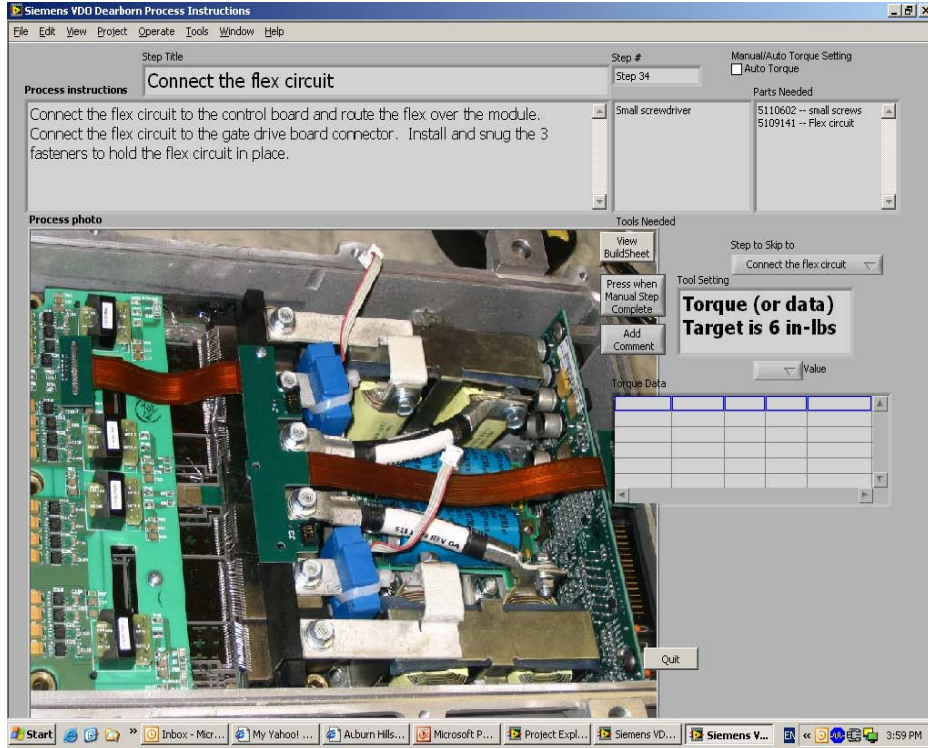


Figure 5. An example of an assembly step.



Figure 6. Assembly process flow diagram.



Figure 7. Completed ORNL Beta power modules.



Figure 8. Engineering test setup for up to 105°C operation.

Figures 9–12 shows the test efficiency mapping. The test conditions are

- four input voltages: 200 V, 300 V, 350 V, 400 V;
- two output voltages: 13.3 V, 15 V;
- two coolant temperatures: 25°C, 105°C; and
- load varies from 0–5 kW.

From the test results, it can be seen that the peak efficiency reaches 94%. The most efficiency curves are 92% or better. At 105°C coolant, the efficiency drops about 1% compared to operation with 25°C coolant. Efficiency at 15-V output is about 1% higher than at a lower output like 13.3 V, because the load current is lower at the higher voltage. The lower current yields lower conduction losses.

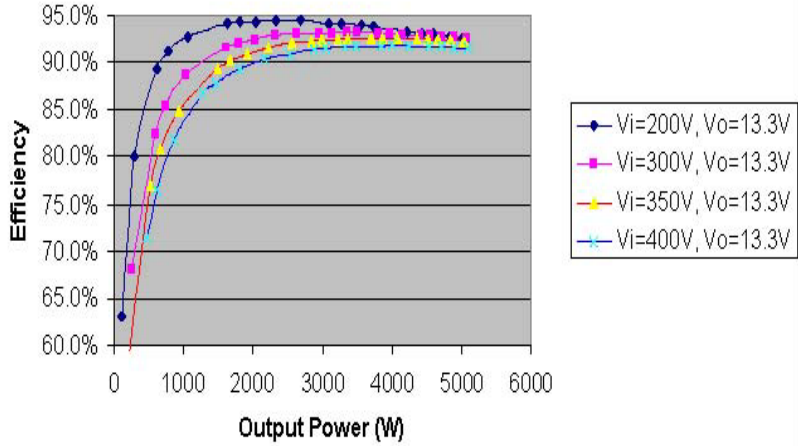


Figure 9. Efficiency test results at $V_o = 13.3$ V, coolant temperature = 25°C .

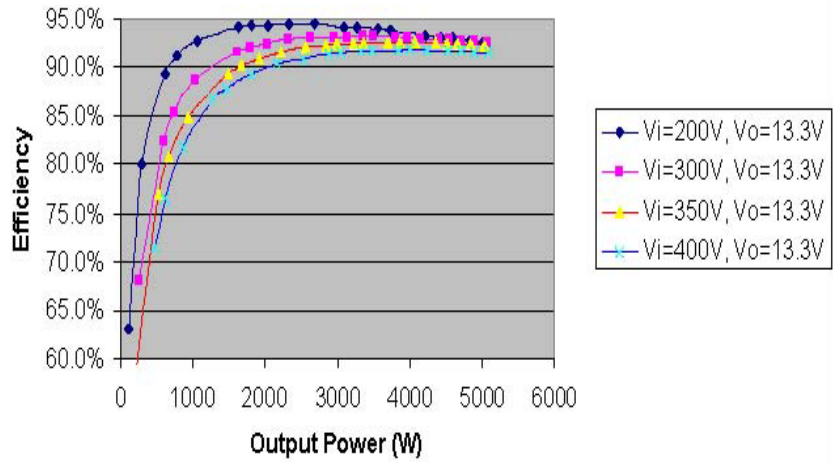


Figure 10. Efficiency test results at $V_o = 13.3$ V and coolant temperature = 150°C .

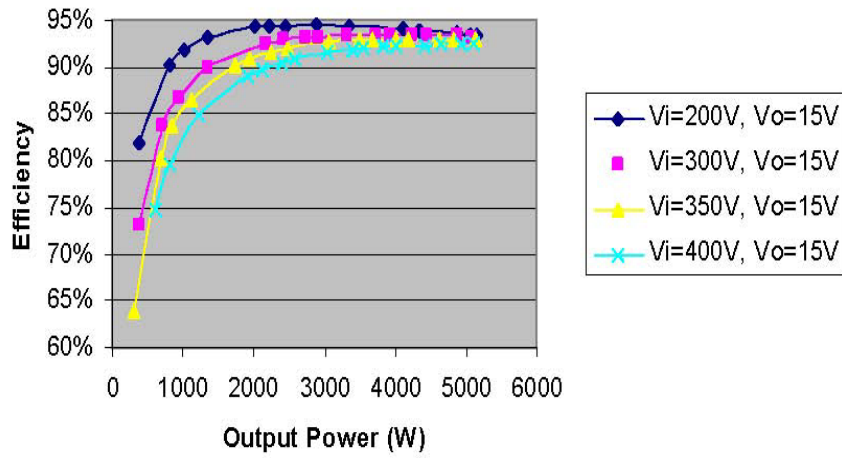


Figure 11. Efficiency test results at $V_o = 15\text{ V}$ and coolant temperature = 25°C .

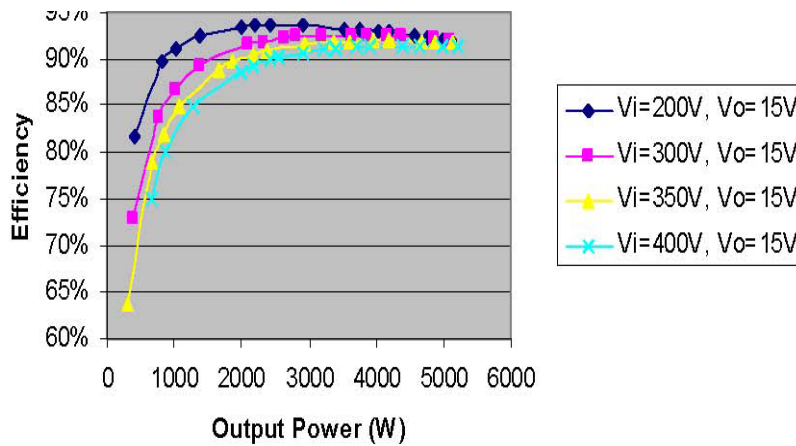
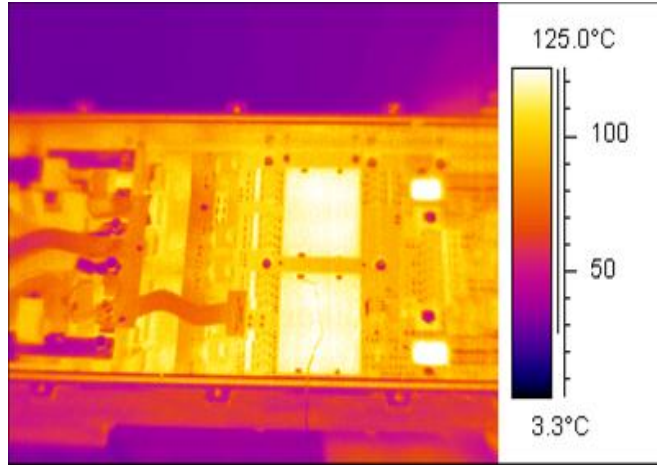


Figure 12. Efficiency test results at $V_o = 15\text{ V}$ and coolant temperature = 150°C .

Figure 13 shows an infrared photo taken when the dc/dc converter operated at 5 kW continuously at 105°C . From the photo it can be seen that some areas in the floor reached 125°C , which was consistent with the design.



**Figure 13. An infrared photo for dc-dc converter test condition:
 $V_i = 300\text{ V}$, $P_o = 5\text{ kW}$, and coolant temperature = 105°C .**

Detailed test results are contained in the TM report listed under “Publications.”

Beta Prototype Size and Weight

The final design had a total volume of 5.1 L, which is slightly over the DOE target of 5 L. Figure 14 depicts the dimensions of the Beta prototype. The total weight ended up at 8.33 kg, slightly higher than the DOE target.

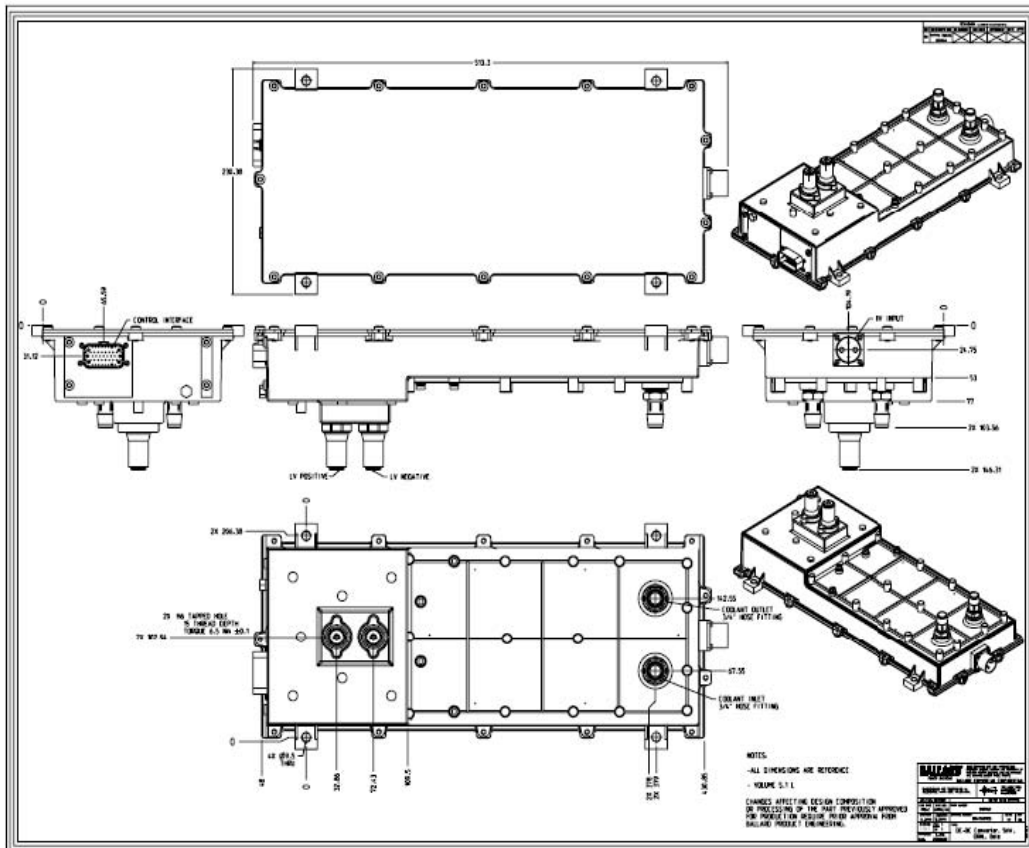


Figure 14. The Beta dc/dc mechanical dimensions.

Conclusions

Table 1 is a summary of the results achieved for this program. The module achieved five out of seven goals. It is thought that the weight target can be achieved in a high-volume production design and the cost can also be reduced. The coolant pressure exceeds the goal by 192% because of the extreme effort made in the thermal and coolant channel design.

The DOE weight target was 6 kg. The Beta design result is 8.33 kg, above the target by 2.33 kg. There are three potential opportunities to meet the weight target:

1. The power module currently occupies 2.8 kg; moving the coolant channel to the housing will reduce the thickness of the baseplate, resulting in 45% weight reduction.
2. The housing and cover currently weigh 2.83 kg. This part was done with sand casting. In high-volume production, it would be die cast, which allows the wall thickness to be reduced from 4 mm to 2 mm–2.5mm, resulting in 35% weight reduction. The cover is over-designed for the beta design and can be reduced 30% in high-volume production.
3. The low-voltage output studs occupy 0.29 kg. This was an existing motor feedthrough part previously used in another E-drive product. The length is more than needed for the dc-dc converter. With a custom design for high-volume production, the weight can be reduced 60% by redesigning around a smaller length.

With these three weight reduction plans, it is estimated that the weight can be reduced by 2.39 kg, which would achieve the DOE goal of 6 kg.

The DOE cost target for this project was \$375. The Beta design result came in at an estimated cost of \$458, which is 82% of the DOE target. The usage of two expensive materials in this design can be revisited to reduce the cost in high-volume production. They are

1. AlSiC power module baseplate, and
2. silicon nitride planar transformer windings.

Further opportunities for cost reduction include

1. improve the material utilization factor,
2. work with supplier to identify major cost driver, and
3. improve the yield.

Publications

L. Zhu (Ballard), L. D. Marlino, and G. J. Su, *DC-DC Converter for Fuel Cell and Hybrid Vehicles Subcontract Report*, ORNL/TM-2007/110, Oak Ridge National Laboratory, 2007.

Presentation on Industrial Power Converter Products and Services Session in IEEE IAS 2006, Tampa, Florida, October 12, 2006.

Patents

“An Interleaved High Power DC/DC Converter,” U.S. Patent Application No. 20050270806.

“Integration of Planar Magnetics Transformer and Power Switching Devices in a Liquid Cooled High Power DC/DC Converter,” Patent Application No. 20050270745.

References

None.

4.8 High Performance Embedded Capacitors for (P)HEV Power Electronic Systems

U. (Balu) Balachandran, B. Ma, D. K. Kwon, and M. Narayanan

Energy Systems Division

Argonne National Laboratory

9700 S. Cass Ave.

Argonne, IL 60439

Voice: 630-252-4250; Fax: 630-252-3604; E-mail: balu@anl.gov

DOE Technology Development Manager: Susan A. Rogers and Steven Boyd

Voice: 202-586-8997; Fax: 202-586-1600; E-mail: susan.rogers@ee.doe.gov; steven.boyd@ee.doe.gov

Argonne Program Manager: U. (Balu) Balachandran

Voice: 630-252-4250; Fax: 630-252-3604; E-mail: balu@anl.gov

Objectives

The goal of this R&D program is to develop high performance and economical DC bus capacitor technologies that will meet the APEEM specifications for (P)HEV power electronic systems. Current DC bus capacitors occupy a large fraction of the volume and weight of the inverter module, cannot tolerate temperatures up to 120°C, and suffer from poor packaging, inadequate reliability, and deleterious failure modes. Traditional capacitor architectures with conventional dielectrics cannot adequately meet all of the performance goals for capacitance density, weight, volume, and cost. Meeting these goals requires a dielectric with high permittivity that tolerates operating at high temperature, is packaged in an architecture with high volumetric efficiency, and exhibits benign failure features.

Approach

Argonne National Laboratory's (Argonne) capacitor R&D program addresses the technology gap in an innovative manner. We are developing high performance, low cost capacitors that are embedded directly into the printed wire board (PWB). In these "embedded film-on-foil capacitors", a base-metal foil (nickel or copper) is coated with a high permittivity ferroelectric material, (Pb,La)(Zr,Ti)O₃ (abbreviated as PLZT). Ferroelectrics possess high permittivity, breakdown electric fields, and insulation resistance. They can withstand high temperatures such that high ripple currents can be tolerated at under-the-hood temperatures. Use of base-metals and solution-based deposition techniques reduce the cost. An embedded capacitors approach significantly reduces component footprint, improves device performance, provides greater design flexibility, and offers an economic advantage for commercialization. This technology will achieve the high degree of packaging volumetric efficiency with less weight.

Our R&D efforts focus on examining the issues that underpin the performance of film-on-foil embedded capacitors, developing low cost capacitor designs, establishing fabrication protocols that are commercially robust and economically viable, and transferring the technology to industry for manufacturing.

Major Accomplishments

- Set up dielectric property characterization system.
- Refined chemical solution deposition technique to fabricate PLZT on nickel foils.
- Optimized LaNiO₃ (LNO) buffer layer processing conditions to eliminate deleterious effects of a parasitic low capacitance interfacial oxide layer and thereby improve dielectric performance of the ferroelectric films.

- Demonstrated excellent dielectric properties on 1" x 1" PLZT/LNO/Ni film-on-foil capacitors with dielectric constant, k , ≈ 1300 at room temperature and $k \approx 1800$ at 150°C .
- PLZT/LNO/Ni film-on-foil capacitors were thermally cycled ≈ 1000 times between -50°C and 150°C with no measurable degradation in k .
- Evaluated mechanical properties of PLZT/LNO/Ni film-on-foil capacitors (measured at ORNL).
- Developed PWB-compatible PLZT/Cu film-on-foil capacitors with $k > 450$ and loss factor $\tan(\delta) \leq 0.04$.
- Initiated an alliance with a PWB manufacturer and an automotive electronics company to embed the 'film-on-foil' dielectrics and fabricate embedded (P)HEV capacitor prototypes.
- Designed electrode architectures for embedding film-on-foil capacitors.
- Submitted a proposal with Delphi Automotive Electronics and other partners in response to DOE/NETL funding opportunity announcement DE-PS26-06NT43001-01, Development of power electronics and electric motor technology for plug-in hybrid electric vehicles.
- Presented program status and future direction to EE Tech Team.
- Submitted three manuscripts for publication in peer reviewed journals.
- Presented the results at two scientific conferences.
- Acquired a commercial ultrasonic coater to fabricate large area dielectric films suitable for APEEM applications.

Future Direction

The R&D effort has demonstrated feasibility of using ferroelectric film-on-foil dielectrics for power electronics operating at under-the-hood temperatures. Progress achieved thus far sets the stage to begin development of prototype PWBs with embedded (P)HEV capacitors. This will require our technology to be refined and aligned with PWB fabrication routines. In terms of compatibility with PWB processing, fabrication of PLZT dielectric films on large area Cu foils is the most desirable. Building upon our current success with PLZT/Cu film-on-foil capacitors, we will investigate the issues that underpin dielectric performance, and use that knowledge to refine processing conditions. The ferroelectric film fabrication process will be optimized for (P)HEV specific applications. Robust processing conditions will be developed to crystallize the film without forming a parasitic interfacial capacitance. We will evaluate the high voltage and high temperature behavior of the film-on-foil capacitors with a perspective on reliability. We will also investigate the microstructural aspects of dielectric breakdown and degradation, and will tailor devices based on those findings. At the same time, we will develop the fabrication methodology for coating large size film-on-foil sheets with the desired thickness for power electronic systems.

These ferroelectric film-on-foil sheets will be integrated into a PWB manufacturing process and embedded into the wire boards. Working with our alliance partners, we will address the challenges posed by embedding, imaging the inner-layers, metallization, and circuit design. We will build prototype embedded capacitor components, test the device's performance and benchmark it against APEEM goals. These initial prototypes will be evaluated by ORNL as well as other research institutions. We will continue our effort in developing dielectric materials with improved performance.

Technical Discussion

The replacement of bulky inefficient discrete capacitors with capacitors embedded within the layers of a printed wire board is an innovative and highly desirable solution for applications that require high capacitance density and volumetric efficiency. Embedded capacitors can be located directly underneath the active devices, significantly reducing component footprint and greatly improving reliability. While this technology has primarily received attention for low voltage, high frequency decoupling capacitors, it

can potentially be extended to the higher voltages of (P)HEV systems. The vision of embedded DC bus capacitors is compelling and offers US automotive companies a substantial technological advantage over their foreign counterparts. The bulky coke-can-like banks of capacitors can be replaced by lengths of capacitors tucked flat and neatly underneath the active components and bus structure. Reducing the number of solder joints and decreasing the length of electrical leads will improve reliability.

The key provision is the integration of high-k ferroelectric layers within a printed wire board. Because high temperature ($\sim 650^\circ\text{C}$) processing is required to obtain dense crystalline ferroelectric materials with high-k, direct deposition on a polymeric printed wire board is not possible. Instead, a pre-fabricated 'film-on-foil' approach is adopted, whereby the ferroelectrics are first deposited via chemical solution deposition (CSD) on a thin base metal foil, then crystallized at high temperatures, and the coated foils subsequently embedded within the printed wire boards.

Due to the high-temperature processing condition required for the fabrication of 'film-on-foil' capacitors, a principal concern is eliminating deleterious effects from the formation of a low-k parasitic oxide at the metal-ceramic interface. This low-k oxide would act as a series capacitor and reduce the overall capacitance. To negate the influence of an interfacial oxide, two approaches have been investigated: (1) A conductive oxide buffer layer is interposed between the ferroelectric and the metal foil, and acts as an effective bottom electrode. Any discontinuous secondary oxide that may form below the buffer layer at the metal interface is inconsequential to the parallel plate capacitor. (2) Crystallization of the ferroelectric ceramic layer is conducted in a controlled atmosphere whose $p\text{O}_2$ is low enough to prevent formation of an interfacial oxide but not so low that the dielectric decomposes.

1 – PLZT/LNO/Ni Capacitors

We have developed a core technology for fabricating CSD PLZT on Ni film-on-foil capacitors with LaNiO_3 (LNO) buffer layers. CSD solutions were synthesized at Argonne, and films were deposited by spin coating. All pyrolyses and crystallizations were done in air and repeated to build up layers of sufficient thickness.

The conductive LNO can obviate the parasitic influence of any interfacial NiO formation during the high temperature processing that is required for crystallization of PLZT on a Ni substrate in air. We have fabricated 1" x 1" PLZT/LNO/Ni film-on-foil capacitors with $k > 1300$ and dissipation factor ≈ 0.06 , as shown in Fig. 1. Capacitance density of 1.6 microfarads/cm² was achieved on a 0.7 micron thick PLZT/LNO/Ni capacitor, which is nearly equivalent to on the capacitance density of platinized Si substrates. Coating of larger samples is currently being investigated using a newly acquired Prism large area coating system from Ultrasonic Coating Systems.

2 – PLZT/Cu Capacitors

Cu is the primary material for PWB interconnects and metallization. We have initiated development of PLZT on bare Cu foils. In this process, a controlled environment with reduced $p\text{O}_2$ is used to prevent formation of a parasitic interfacial oxide layer. The $p\text{O}_2$ must be low enough to prevent oxidation of the Cu-PLZT interface, yet not too low to induce decomposition of the PLZT film. Thermodynamic models aid in determining the appropriate $p\text{O}_2$ for the heating, crystallization, and cooling cycles.

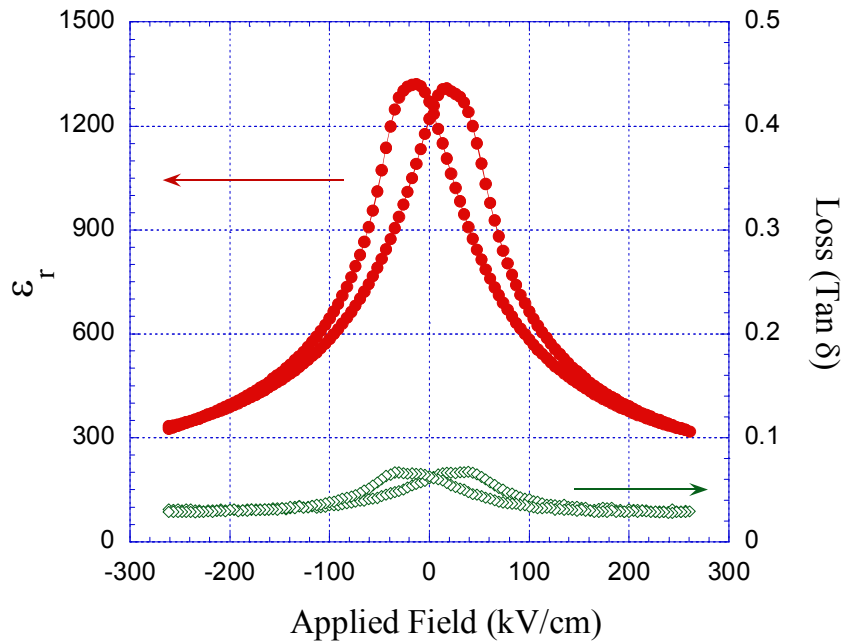


Figure 1. Relative permittivity and dielectric loss measured at room temperature as a function of applied bias field for a 1” x 1” PLZT/LNO/Ni film-on-foil capacitor.

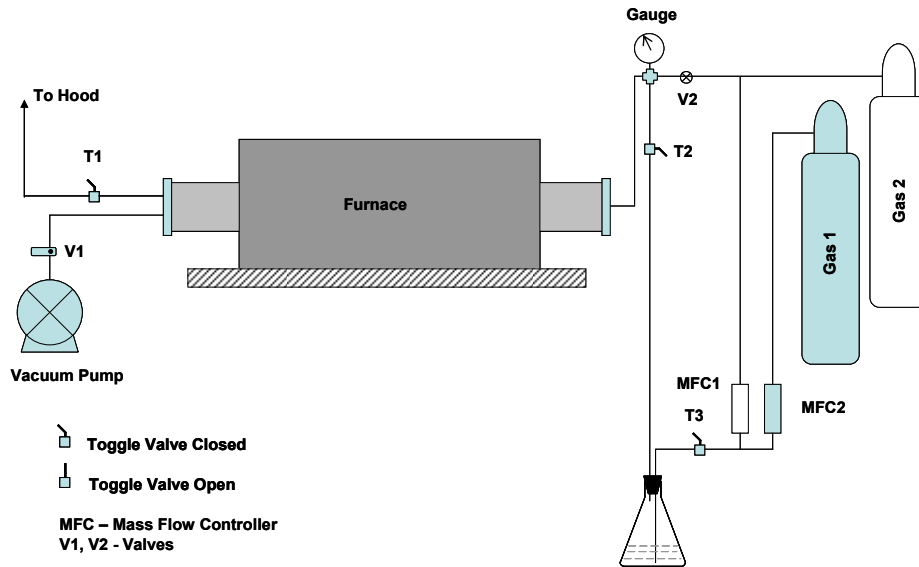


Figure 2. Schematic illustration of experimental setup for processing PLZT on copper foils in controlled atmosphere.

Figure 2 shows a schematic illustration of the experimental setup for heat treating samples in controlled atmospheres. Hydrogen-containing reducing gas (Gas 1) is mixed with inert gas (Gas 2) in the appropriate ratio using mass flow controllers (MFCs). Before entering the furnace, the gas mixture flows through a water bubbler to pick up moisture for achieving the desired pO₂ in the heat treatment furnace, which is determined by the relative concentrations of hydrogen and water and the Gibbs free energy for the following reaction [1] at the particular heat treatment temperature.



The pO_2 level inside the heat treatment furnace must be controlled so that the copper substrate is not oxidized and yet the oxides in PLZT material are not reduced. Thermodynamic phase boundaries for reduction of lead oxide (PbO) and oxidation of Cu are plotted in Fig. 3. A suitable pO_2 level for crystallizing PLZT on Cu foil lies below the boundary for Cu oxidation and above the boundary for lead reduction reaction boundary, as highlighted in the plot. For example, the pO_2 must be in the range $-14.5 \leq \log(pO_2) [\text{atm}] \leq -11.5$ in order to crystallize PLZT on Cu foil at 650°C . This pO_2 level is achieved by flowing ≈ 1 ppm H_2 balanced with inert gas through a water bubbler at room temperature.

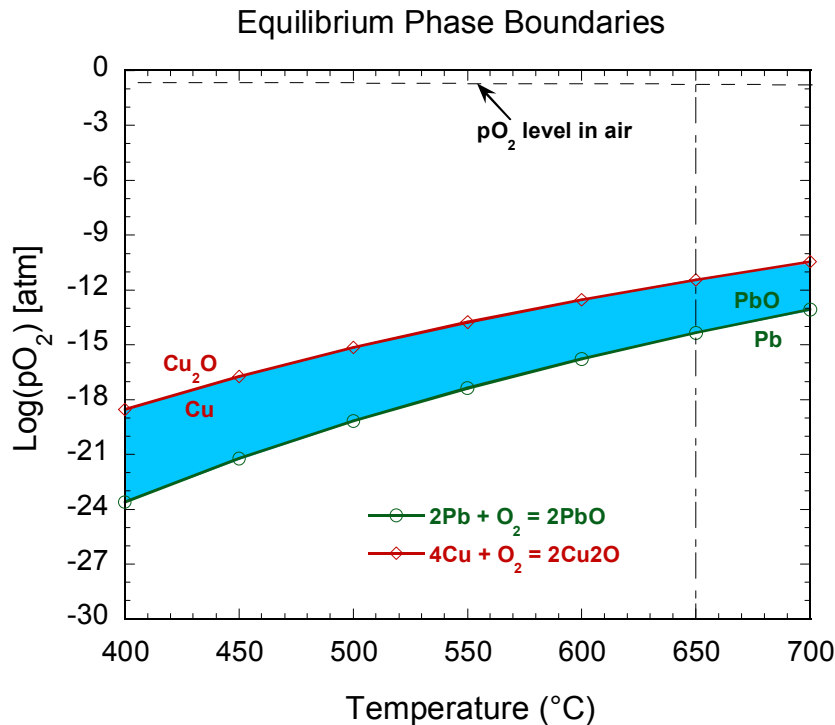


Figure 3. Equilibrium phase boundaries for oxidation of Cu and Pb.

Encouraging initial results were obtained on PLZT/Cu film-on-foil capacitor samples. Figure 4 shows the dielectric property of 3 coatings of PLZT on a $0.5'' \times 0.5''$ Cu substrate by chemical solution deposition. Relative permittivity of 450 and dielectric loss of 0.04 were measured at room temperature.

3 – Temperature Dependent Characterization of Dielectric Properties

With the newly constructed dielectric testing system, we tested $1'' \times 1''$ PLZT/LNO/Ni film-on-foil capacitor samples as a function of temperature. Figure 5 shows the dielectric constant measured with zero bias for PLZT grown on LNO-buffered Ni foil in comparison with that grown on a platinumized Si substrate. The Curie temperature for the PLZT/Pt/Si sample is $\approx 150^\circ\text{C}$, whereas the Curie temperature for PLZT/LNO/Ni is slightly higher. The temperature variation of capacitance is within 20% for the PLZT/Pt/Si sample.

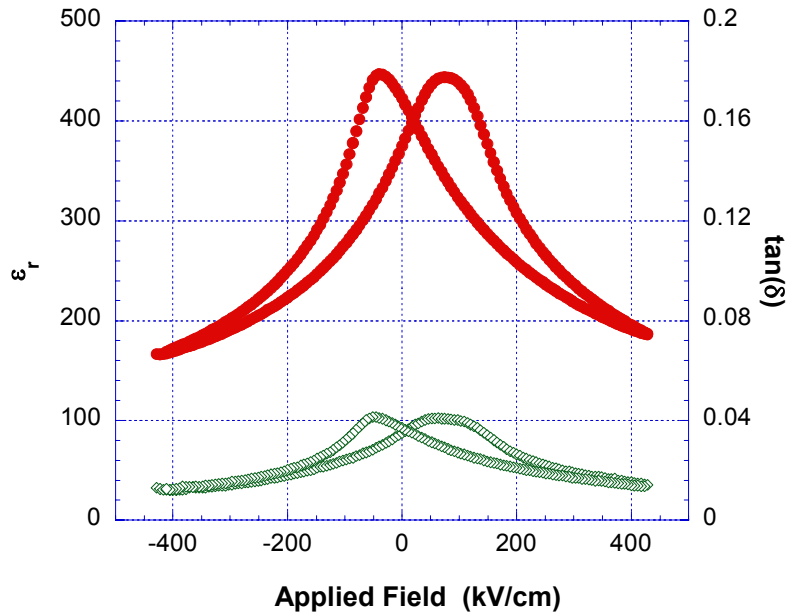


Figure 4. Relative permittivity and dielectric loss measured at room temperature as a function of applied bias field for a 0.5” x 0.5” PLZT/Cu film-on-foil capacitor.

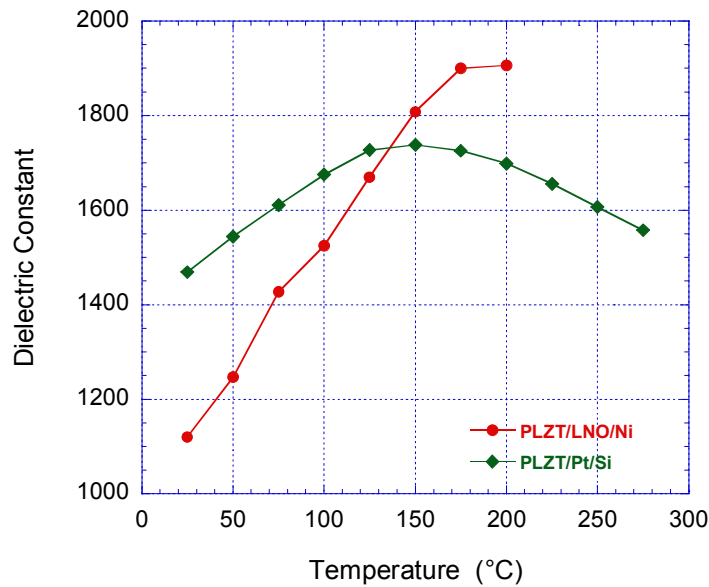


Figure 5. Temperature dependent dielectric constant of a 1” x 1” PLZT/LNO/Ni film-on-foil capacitor in comparison with a PLZT grown on a platinized silicon substrate.

A PLZT/LNO/Ni film-on-foil capacitor with platinum top electrode has been thermally cycled at temperature between -50°C and 150°C for ≈ 1000 times at Delphi Electronics and Safety. Dielectric properties of the PLZT/LNO/Ni film-on-foil capacitor were measured before and after the thermal cycling

experiments. No measurable degradation in dielectric properties or aging effect was detected after thermal cycling.

Time relaxation current density was measured on a 1" x 1" PLZT/LNO/Ni film-on-foil capacitor at 25°C and 150°C with an applied voltage of 10 V and a delay of 1 sec (Fig. 6). A 100-nm-thick platinum top electrode film was deposited by electron-beam evaporation on the surface of PLZT. Nickel foil acts as the bottom electrode for the testing. The current density measured at 150°C is roughly a factor of two higher than the value measured at room temperature. A leakage current density of $\approx 10^{-8}$ A/cm² was measured at 150°C, which corresponds to an insulation resistance of $\approx 10^9$ Ω/cm².

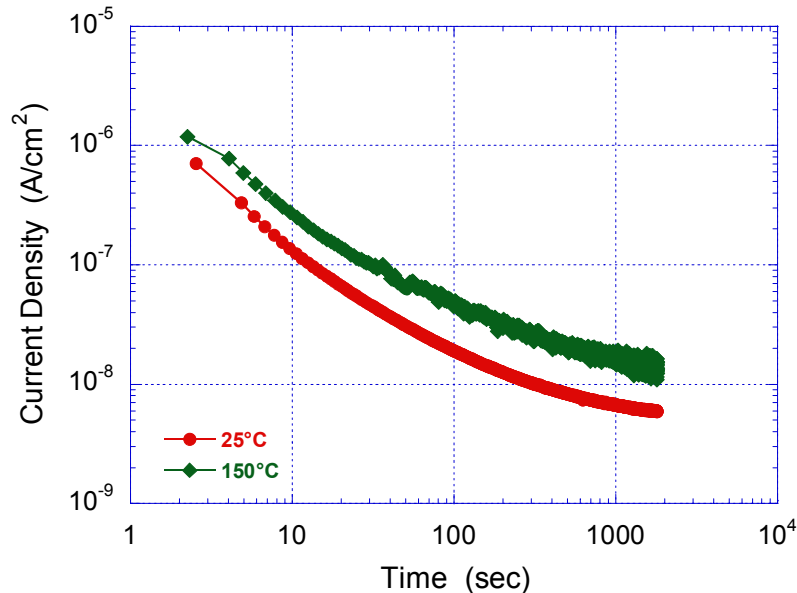


Figure 6. Time relaxation current density measured on a 1" x 1" PLZT/LNO/Ni film-on-foil capacitor at room temperature and 150°C.

4 – Graceful Failure

We have developed film-on-foil capacitors that exhibit graceful failure – a gradual loss in capacitance during localized breakdown events. Following a breakdown occurrence, the capacitor continues to function and is considered to have failed only after a defined leakage current or dielectric loss is reached. At sufficiently high voltages, dielectric breakdown occurs at a discrete faulted area. This discharges the stored energy of the dielectric in that localized spot. In a matter of microseconds the discharge heats the immediate area, which physically “clears” away the dielectric from the defect site, and vaporizes the metal top electrode in a small region surrounding the defect. By this process the breakdown site becomes electrically isolated and removed from the remainder of the capacitor structure. The capacitor continues to operate to even higher voltages. Self-clearing capacitors can sustain many breakdown events during their lifetime and can tolerate higher voltages. A small loss in capacitance is observed only after several breakdown/clearing events occur. Indeed, it usually takes hundred to thousands of such clearings to cause a few percent loss in capacitance. In such a manner, instead of shorting, the capacitor effectively “self-heals”, and failure occurs gracefully. Such self-clearing failure modes are the same as those in metallized polymer capacitors. A U.S. Patent has been issued to Argonne for developing graceful failure by self-clearing method.

5 – Prototype Development

We have demonstrated a proof-of-concept for film-on-foil capacitors. To proceed towards the next step of prototype embedded capacitors, we have teamed with Delphi Electronics and Safety, a leading

automotive electronics supplier, and Diversified Systems, Inc., a PWB manufacturer. Together with these partners, we will begin to develop technologies for integrating film-on-foils into PWB fabrication. This will include embedding, imaging and etching, and interconnects and terminations. Novel PWB circuit designs will be conceived to maximize the capacitance and voltage in the smallest possible volume. The embedded capacitors will be assembled and analyzed under (P)HEV inverter conditions.

Conclusion

We have developed a core technology for fabricating high capacitance density PLZT film capacitors on base metal foils. PLZT film-on-foil capacitors have been fabricated with LNO buffer layers atop Ni foils, allowing the capacitors to be processed in air. Low pO_2 processing has been used to fabricate PLZT capacitors on Cu foils without the need for a buffer layer. An alliance with a PWB manufacturer and an automotive electronics company was initialized to embed our film-on-foil dielectric elements and fabricate embedded (P)HEV capacitor prototypes. Top electrode metallization design and connection layout for a prototype embedded capacitor were studied. This film-on-foil technology will be used to fabricate (P)HEV embedded DC bus capacitors with significantly reduced size and weight, and improved performance and reliability.

Publications

1. B. Ma, D. K. Kwon, M. Narayanan, U. Balachandran, *Chemical Solution Deposition of Ferroelectric Lead Lanthanum Zirconate Titanate Films on Base-Metal Foils*, submitted to Journal of Electroceramics, 2007.
2. K. K. Uprety, D. Y. Kaufman, *Chemical solution deposition of $LaNiO_3$ on Ni metallic substrate for ferroelectric $(Pb_{0.92}La_{0.08})(Zr_{0.52}Ti_{0.48})O_3$ thin film capacitors*, submitted to Thin Solid Film, 2007.
3. B. Ma, U. Balachandran, D. Y. Kaufman, K. K. Uprety, *Strategy for the integration of PLZT thin films on base-metal foils for high voltage embedded passives*, to be published in Mater. Res. Soc. 2006 Fall Meeting Symp. Proc., Boston, MA, Nov 27 - Dec 1, 2006.
4. D. Y. Kaufman, S. Saha, K. K. Uprety, *PLZT film-on-foil capacitors for embedded passives*, the Proceedings of the 12th US-Japan Seminar on Dielectric and Piezoelectric Ceramics, Annapolis, MD, Nov 6-9, 2005.
5. D. J. Kim, D. Y. Kaufman, S. K. Streiffer, T. H. Lee, R. Erck, O. Auciello, *Chemical solution deposition of PLZT films on base metal foils*, Mat. Res. Soc. Symp. Proc., Vol. 748, pp. 457-62 (2003).

References

1. See for example, R. C. Weast, et al., *Handbook of Chemistry and Physics*, 67th Ed., pp. D-35, CRC Press, Boca Raton, FL, 1987.

Patents

1. D. K. Kaufman, S. Saha, *Ceramic capacitor exhibiting graceful failure by self-clearing method for fabricating self-clearing capacitor*, US Patent #7,009,141, August, 2006.

4.9 Glass Ceramic Dielectrics for DC Bus Capacitors

Principal Investigator: Michael Lanagan

Penn State University

278 Materials Research Laboratory

University Park, PA 16903

Voice: 814-865-6992 ; Fax: 814-865-2326; E-mail: mlanagan@psu.edu

DOE Technology Development Manager: Susan A. Rogers

Voice: 202-586-8997; Fax: 202-586-1600; E-mail: Susan.Rogers@ee.doe.gov

Objectives

Commercial capacitors do not meet FreedomCAR specifications for high temperature operation, cost and reliability. The goals of this project are to create glass and glass-ceramic capacitors that are low cost and fulfill the power electronic performance criteria at high temperature. In addition, there are promising new glass fabrication methods for consumer electronics that may be transitioned to capacitors for hybrid electric vehicle converters.

- Increase energy density beyond 1 J/cm³ in a fully packaged capacitor (related to overall power electronic converter volume).
- Demonstrate graceful failure mechanisms in glass ceramic capacitors (related to long-term converter performance).
- Adapt commercial materials and fabrication processes from large-scale production processes (i.e. flat panel displays) which are related to converter cost.

Approach

- Adapt low-cost production methods and materials, already developed for flat panel displays, to high temperature capacitors.
- Characterize glass and glass-ceramic materials at high temperature to project reliability of capacitors that are made from these materials.
- Develop benign failure modes in glass capacitor to avoid catastrophic failure.
- Manufacture prototype capacitors in collaboration with industrial partners

Major Accomplishments

- Collaborated with commercial glass manufacturers (Schott Glass USA and Corning) to establish flat panel display glass as a viable capacitor material.
- Synthesized glass-ceramic materials and fabricate prototype capacitors in collaboration with TRS Technologies.
- Developed conducting coatings to enhance benign failure in glass capacitors and to increase reliability.

Future Direction

- Scale-up capacitors made from glass to 10 μ F 1,000 V levels
- Highly accelerated life testing of commercial glass to ensure these materials will withstand 600 V at 150 C for 10,000 hrs.

Technical Discussion

Collaboration with commercial glass manufacturers:

New plasma displays rely on the fabrication of large-area glass sheets that are 400 microns thick. These same glass sheets are applicable to high-temperature power capacitors for hybrid electric vehicles. A feasibility study was carried out to determine if these materials are viable candidates for power electronic capacitors. In addition, the plasma display production road map will be studied to determine if thinner glass sheets are planned for this industry. Scientists from Schott Glass and Corning Inc. have visited Penn State are developing new processes for making continuous sheets of glass less than 30 μm in thickness. An example of the flexibility of these glass sheets is shown in the Figure 1.

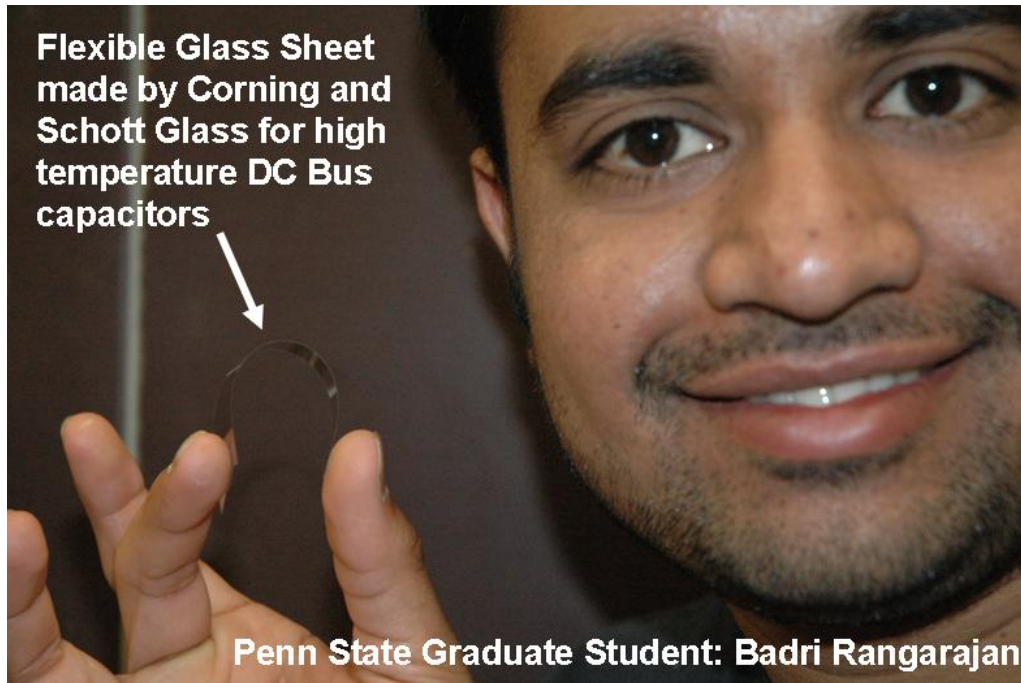


Figure 1. Demonstration of the excellent flexibility of thin glass sheet (45 microns) currently being manufactured by Corning and Schott glass companies. The high temperature electrical properties have been reported in previous monthly reports and show that these materials can be used in DC bus capacitors up to 250°C.

Scale up glass-ceramic manufacturing with TRS Technologies:

Penn State researchers are also exploring glass-ceramic materials which have a higher dielectric constant than commercial glass. In order to meet FreedomCar capacitor size requirements for DC bus capacitors, the dielectric constant must be increased. Figure 2 shows the glass ceramic casting process that was developed at Penn State. Penn State has successfully made 100 μm glass-ceramic layers with high energy density (Figure 3).



Figure 2. Glass ceramic sheet formation by pouring molten glass on a roller. The sheets made by this process were provided to TRS Technologies for incorporation into a multilayer capacitor.

The dielectric energy density is an intrinsic material parameter that allows engineers to project capacitor size for a given application. Larger energy densities result in more volume efficient capacitors. The energy density of the glass ceramic is close to 4 Joules/cm^3 , which is substantially higher than commercial capacitors. The operating field of the glass ceramic is lower than 600 kV/cm , which decreases the energy density. Glass ceramic materials made at Penn State were delivered to TRS Technologies for incorporation into a prototype capacitor (Fig. 3b).

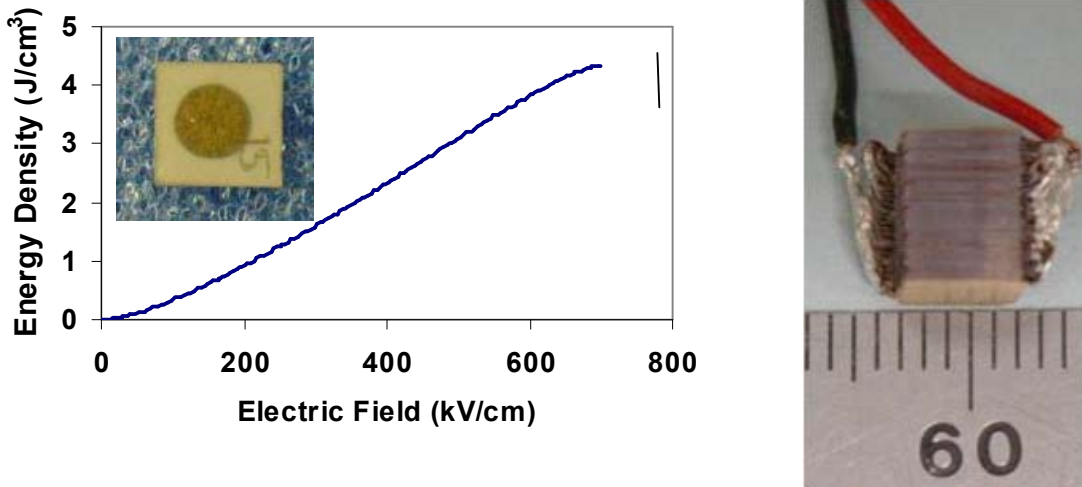


Figure 3. (a) Energy density and photo of a $100 \mu\text{m}$ glass-ceramic layer. The breakdown voltage for this individual layer approaches 7000 V , which is substantially higher than the DOE FreedomCar capacitor requirement of 600 V . (b) 50 nF multilayer ceramic capacitor, materials made by Penn State University, capacitor made by TRS Technologies (60 nF).

Develop benign failure in glass capacitors:

Penn State has successfully applied manganese oxide coatings to silicon oxide substrates which has the first step in creating a graceful failure mechanism in ceramic capacitors. A publication based on this work is currently being reviewed by the Journal of the American Ceramic Society and the Department of Energy FreedomCar program is acknowledged.

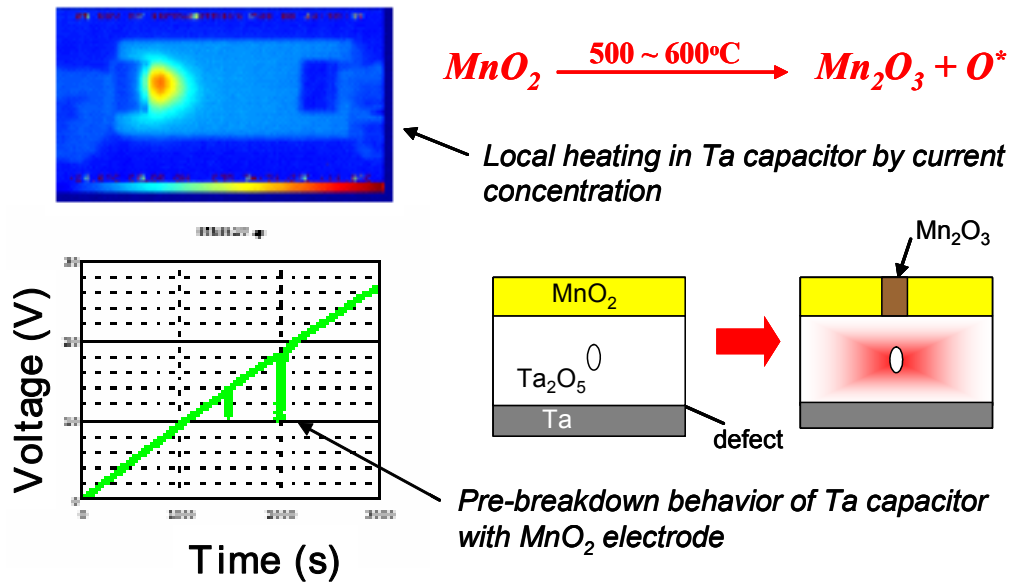


Figure 4. Graceful failure mode in a commercial tantalum electrolytic capacitor. Upper left: the hot spot is shown as a red region on a blue background. The hot spot is generally a weak spot in the dielectric that conducts and heats. **Upper right:** Manganese oxide undergoes a phase transition between 500 and 600°C. The conducting MnO₂ electrode converts to an insulating Mn₂O₃ phase, limiting the shorting current in the capacitor. **Lower right:** schematic of a capacitor cross section in which a defect in the dielectric film causes a hot spot which converts the MnO₂ film to Mn₂O₃. **Lower left:** breakdown events are recorded as the capacitor voltage increases. The capacitor is still operational (i.e. holds voltage) after breakdown. This is graceful failure.

Conclusion

The outcome of this project is a cost effective manufacturing process for high temperature capacitors that will meet the FreedomCAR Specifications. Penn State has collaborated with several industrial partners including large raw materials manufacturers (Corning Inc. and Schott Glass USA) and small capacitor manufacturers (TRS Technologies) to investigate reliable prototype capacitors from glass-ceramic materials.

Publications and Presentations:

B. Rangarajan*, B. Jones, T. Shrout and M.T. Lanagan, "Barium/Lead Based Invert Glasses for High Energy Density Capacitor Applications," J. Amer. Ceram. Soc., 90(3):784-788, 2007.

D. Kwon, T. Akiyoshi and M.T. Lanagan, "(ICACC-S10-049-2007) Synthesis of Manganese Oxide Thin Films for Capacitor Electrodes," 31st International Cocoa Beach Conference & Exposition on Advanced Ceramics & Composites, Daytona Beach, Florida. January, 2007.

M.T. Lanagan (Primary Presenter), D. Kwon and E. Semouchkina, "(ICACC-S10-056-2007) Dielectric Materials Development for Low Temperature Co-Fired Ceramics ," 31st International Cocoa Beach Conference & Exposition on Advanced Ceramics & Composites, Daytona Beach, Florida. January, 2007. (Invited Presentation).

M. T. Lanagan, Workshop Organizer, "High Energy and Temperature Capacitor for Advanced Power Systems (HEATCAPS) Workshop," State College, PA October, 2007.

M. T. Lanagan, "Electronic Applications of Glass," 1st International Workshop on Scientific Challenges of New Functionalities in Glass, Washington DC, April 2007 (Invited Presentation).

B. Rangarajan, B. Jones, T. Shrouf and M. Lanagan, "Glass ceramics from invert glasses for high energy density capacitor applications, GOMD Meeting, Greenville, SC, May 15-19, 2006.

B. Rangarajan, "Glass capacitors with high energy densities as energy sources in hybrid vehicles," Global Roadmap for Ceramics, International Congress on Ceramics, Toronto, June 25-29, 2006.

B. Rangarajan, B. Jones, C. Wang, T. Shrouf and M.T. Lanagan, "Barium/Lead Based Invert Glasses for High Energy Density Capacitor Applications," 8th International Symposium on Crystallization in Glasses and Liquids, Jackson Hole, Wyoming. September, 2006.

5. Systems Research and Technology Development

5.1 Benchmarking of Competitive Technologies

Principal Investigator: Tim Burress

Oak Ridge National Laboratory

National Transportation Research Center

2360 Cherahala Boulevard

Knoxville, TN 37932

Voice: 865-946-1216; Fax: 865-946-1262; E-mail: burreستا@ornl.gov

DOE Technology Development Manager: Susan A. Rogers

Voice: 202-586-8997; Fax: 202-586-1600; E-mail: Susan.Rogers@ee.doe.gov

ORNL Program Manager: Mitch Olszewski

Voice: 865-946-1350; Fax: 865-946-1262; E-mail: olszewskim@ornl.gov

Objectives

- Provide status of nondomestic hybrid electric vehicle (HEV) technologies through assessment of design, packaging, fabrication, and performance during comprehensive evaluations
 - Compare results with other HEV technologies
 - Distribute findings in open literature
- Support FreedomCAR program planning and assist in guiding research efforts
 - Confirm validity of the program technology targets
 - Provide insight for program direction
- Produce a technical basis that aids in modeling/designing
- Foster collaborations with EETT and VSATT
 - Identify unique permanent magnet synchronous motor (PMSM)/inverter/converter/drive-train technologies
 - Ascertain what additional testing is needed to support R&D

Approach

- Choose vehicle subsystem
 - Evaluate potential benchmarking value of various HEVs
 - Consult with original equipment manufacturers (OEMs) as to which system is most beneficial
- Teardown power converter unit (PCU) and transaxle
 - Determine volume, weight, specific power, and power density
 - Assess design and packaging improvements
 - Conduct tests on magnets and capacitors
- Prepare secondary components for experimental evaluation
 - Develop interface and control algorithm
 - Design and fabricate hardware necessary to conduct tests
 - Instrument subsystems with measurement devices
- Evaluate hybrid subsystems
 - Determine peak and continuous operation capabilities
 - Evaluate efficiencies of subsystems
 - Analyze thermal data to determine assorted characteristics

Major Accomplishments

- The Camry HEV was selected for benchmarking based on its consumer appeal.
- Design/packing studies of the Camry PCU revealed significant improvements when compared to the Prius design.
- The PCU motor inverter controls were bypassed to allow full control over testing conditions.
- Intensive efforts were made to disassemble and evaluate key components within the PCU/transaxle.
- Mass, volume, power density, and specific power of various PCU/transaxle components were assessed.
- Efficiency, performance, and continuous capabilities of the Camry subsystems were evaluated.

Future Direction

- Discussions will be conducted with EETT and VSATT to determine the appropriate system to study in FY 2008.
- Focus will likely be placed upon a new high-power system of the hybrid Lexus product line, such as the GS-600h.
- Approaches similar to that of previous benchmarking studies will be taken while working to suit the universal need for standardized testing conditions.

Technical Discussion

The subsystems of the 2007 Hybrid Toyota Camry Synergy Drive were obtained in order to conduct thorough studies of design, packaging, efficiency, performance, and operational characteristics. Two separate systems were obtained, because some of the studies are destructive by nature. Additionally, a parallel effort was made as the system that was not disassembled was prepared for experimental evaluation.

The hybrid Camry drive system is similar to the Prius in design and function. A key modification of the design is an increase of the maximum motor speed from 6,000 rpm to 14,000 rpm. Torque is directly proportional to current, and power is directly proportional to torque; generally speaking, the amount of torque and current required to maintain a consistent power level decreases as rotor speed increases. This is accomplished by rearranging the winding configuration from series to parallel. Although this reduces the low-speed torque capability of the motor, the torque output is increased through the high-speed reduction gear, and thus the Camry peak torque of about 667 Nm is greater than the 400-Nm torque rating of the Prius. Hence, the increase of rotor speed has allowed for an increase in power rating while also increasing the low-speed torque capabilities. Specifications published by Toyota state that the peak power capability of a primary Camry drive motor has increased to 105 kW from the Prius drive motor rating of 50 kW. The published power rating of the Prius was verified in previous tests, but the power rating of the Camry motor was found to be much lower.

Teardown—Power Converter Unit

The PCU shown in Figure 1 includes a heat sink, boost converter, motor inverter, generator inverter, and their associated components such as capacitors, drivers, and controllers. While the overall function of the Camry PCU is similar to that of the Prius PCU, there is a significant difference between the two in terms of architecture. The surface area of the heat sink is utilized more efficiently, and the amount of null space is reduced drastically. In the Prius PCU, there is a large amount of null space above the integrated power module (IPM) and boost converter. A different type of power connector and bus bar design for the dc link and motor/generator leads also facilitated an increase in volumetric efficiency. Only small portions of the underside of the Prius cold plate were used to dissipate heat. The Camry PCU design makes use of nearly all the available heat sink surface area. The boost converter section is located in the upper portion of the PCU, and the IPM is mounted upside down to the bottom side of the cold plate.

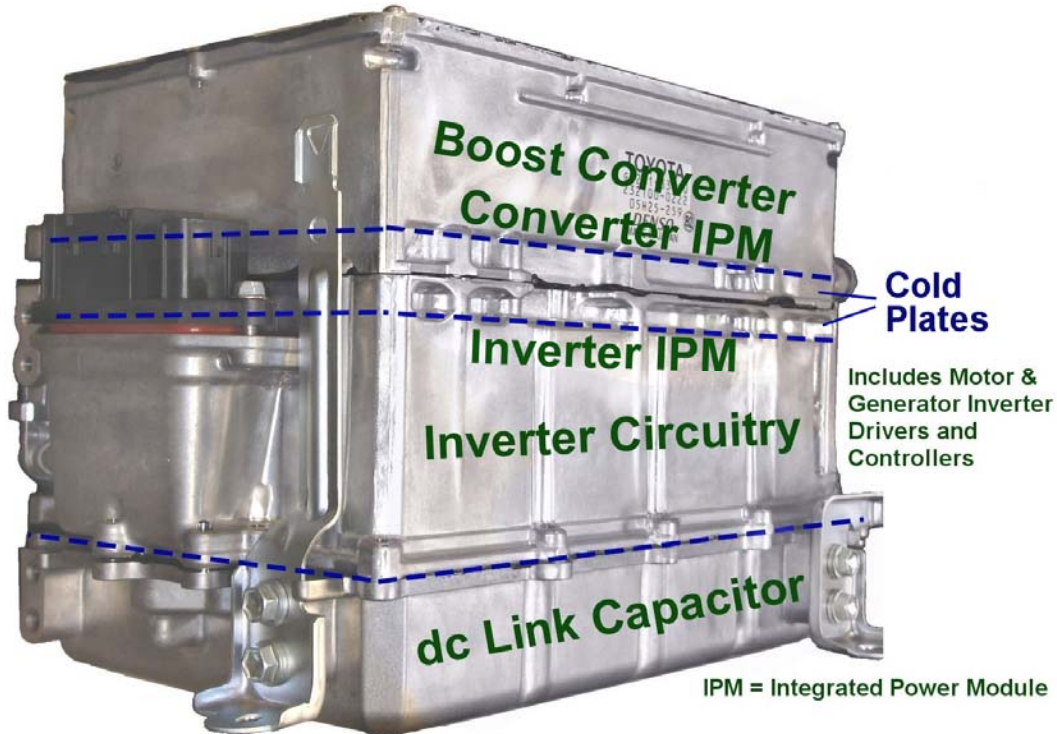


Figure 1. Power converter unit.

Along with the IPM driver board and controller board, the dc link capacitor is located on the very bottom of the PCU.

All components of the PCU except for the dc link capacitor are shown in Figure 2. Shown in the upper segment of Figure 2 is the IPM, which includes a three-phase motor and generator inverter along with a driver board that incorporates protection features. There are six IGBTs per each phase of the Camry motor inverter, where the Prius has four IGBTs per phase. Similar to the Prius generator inverter, the Camry generator inverter includes two IGBTs per phase. The area of silicon for each IGBT has decreased from about 133 mm^2 to 117 mm^2 for the Prius and Camry, respectively. A comparison of the inverter layouts in Figure 3 indicates significant distinctions between the designs. Overall, the Camry IPM is slightly smaller than the Prius IPM even though the peak power capability has increased by at least 30%. Note that the amount of heat sink area per silicon area is less than half of that of the Prius, and although the peak power is approximately proportional to the silicon area, the continuous duration is not proportional, but it does increase as the heat is now distributed among more devices. Just as in the Prius PCU, the motor and generator inverters share the same direct current (dc) link, which allows power to be supplied to the primary drive motor from the battery and the internal combustion engine (ICE).

A controller board for the boost converter and motor/generator is mounted to the driver board. Various feedback signals, such as motor and generator current, rotor position, speed, and temperature, are obtained from an assortment of sensors. The same Tamagawa speed and position resolver and AU6802N1 integrated chip are used for feedback from the generator and motor. The controller communicates with the vehicle control unit via a controller area network (CAN) interface system. Commands and information such as desired motor traction effort, regenerative braking torque, and enable signals are transmitted over the network. This differs from the controller layout of the Prius, which is mostly controlled externally of the PCU.

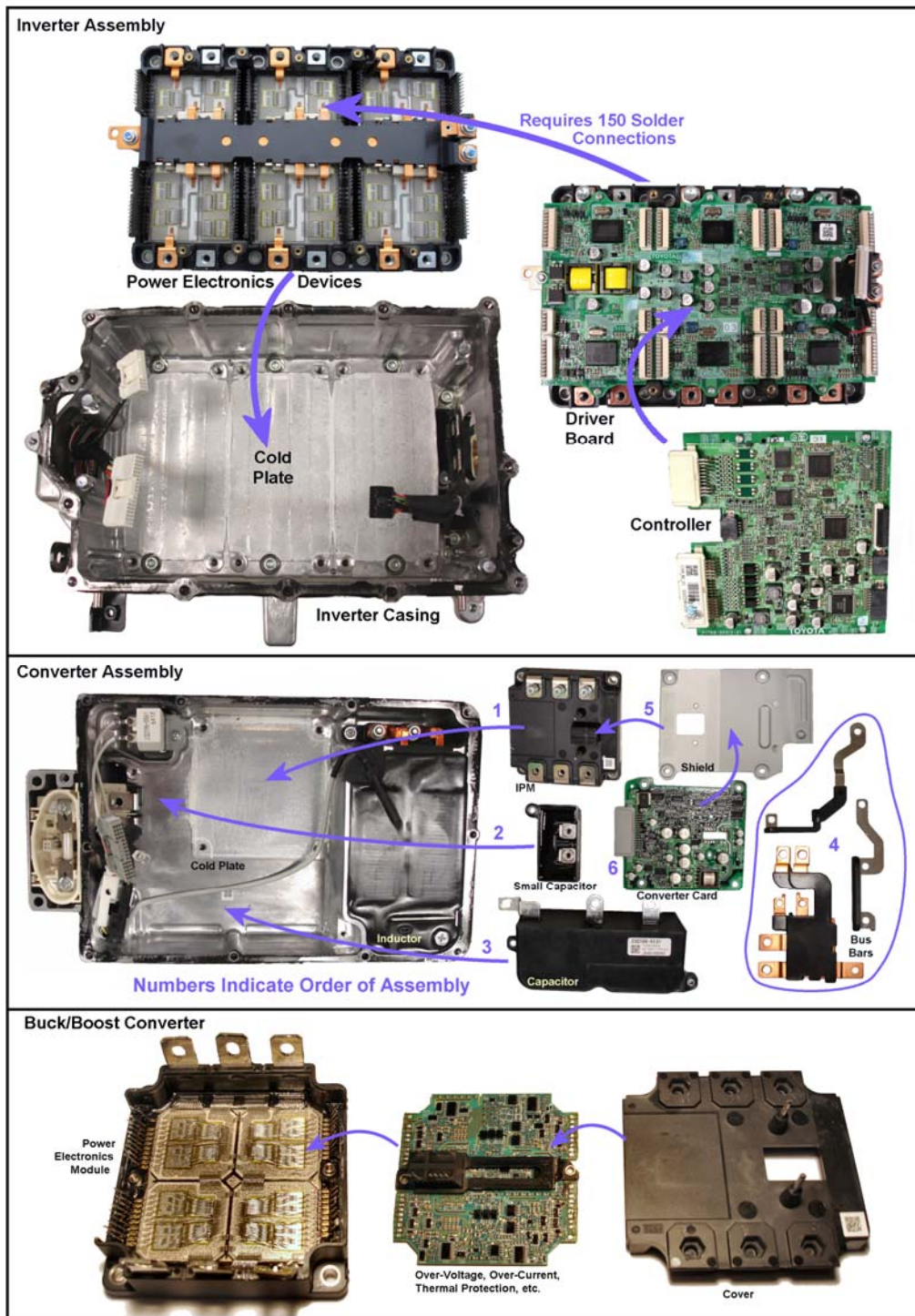


Figure 2. PCU teardown.

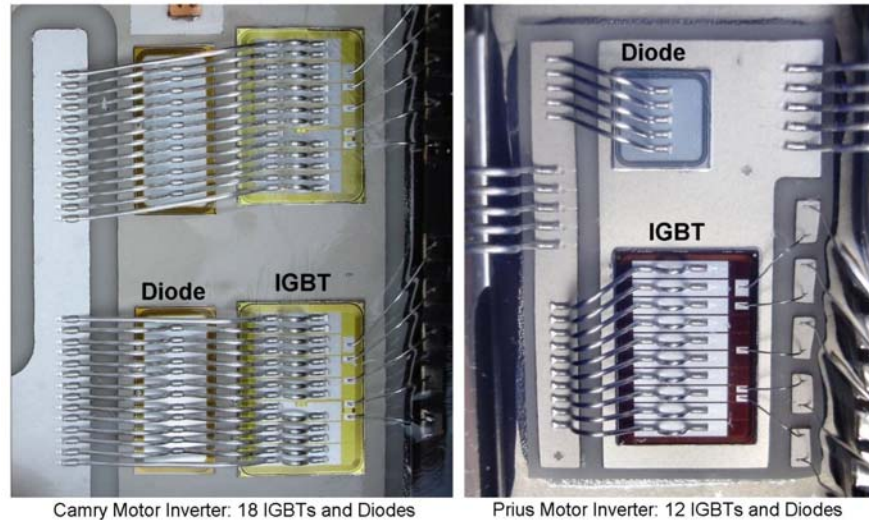


Figure 3. Camry and Prius inverter layout.

The middle segment of Figure 2 shows the components of the boost converter, which includes a large inductor, low-side capacitor, small filter capacitor, small resistor, power electronics, and driver circuitry. The Camry boost converter power rating has been increased to about 30 kW from the 20 kW rating of the Prius. Input voltage from the battery pack to the boost converter has been increased from about 202 V to 245 V, and the boosted voltage output has been increased from 500 V to 650 V. The boost converter circuit topology is that of a traditional bidirectional converter, which allows regenerative energy to flow to the battery. There are four individual IGBTs in parallel, forming the upper switching device, and four IGBTs in parallel to form the lower switching device, as shown in the lower segment of Figure 2.

The dc link capacitor is connected to the high-voltage output of the boost converter, and its size has increased considerably from the Prius. The volume associated with the dc link capacitor of the Camry is larger than the volume of all three Prius capacitors together. All three capacitors were packaged as one unit in the Prius PCU, but all three are separated in the Camry PCU. The large capacitor on the dc link has a capacitance of 2,098 μF rated at 750 V vs the Prius capacitance of 1,130 μF rated at 600 V. The Camry and Prius both have an additional small 750-V capacitor on the high-voltage dc link with capacitances of 0.9 μF and 0.1 μF , respectively. Also common to both systems is a capacitor on the low voltage side of the boost converter. The size of this capacitor was increased slightly from the Prius at 282 μF rated at 600 V to 278 μF rated at 500 V.

According to X-ray images of the large, 2,098- μF capacitor, it contains 24 discrete capacitor modules. One of the capacitor modules was removed to be tested and compared with a capacitor module from the Prius. The single Prius capacitor equivalent series resistance (ESR) values are lower, but they vary more with frequency. Note that the Prius only has 8 in parallel instead of 24, and the combined effect is much different. The capacitance of the large Prius capacitor varies much more than the Camry capacitance does with frequency. The dissipation factor for the Camry capacitor is much lower than that for the Prius.

The permanent magnets were obtained from the rotor through destructive removal in order to perform hysteresis tests. During hysteresis tests, a magnet is subjected to an intense positive magnetic field, and then the magnetic field intensity is slowly decreased until it eventually becomes negative. The strength of the negative magnetic field is increased until demagnetization occurs, and then a positive field is applied until the magnet is fully magnetized again. During this cycle, the strength of the magnet is measured to reveal important characteristics such as the remanent flux density and coercivity. These tests are conducted at various temperatures, as the properties of a magnet are influenced greatly by thermal conditions, as indicated in Figure 4. The remanent flux density correlates with the strength of the magnet; the Camry permanent magnet is about 4.2% weaker than the Prius magnet. However, at all temperatures,

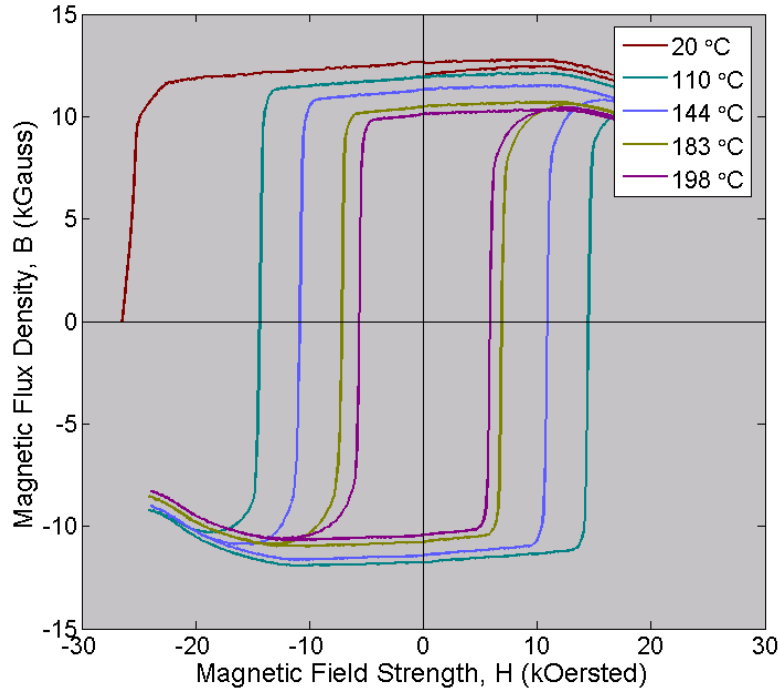


Figure 4. Hysteresis graphs for Camry PMSM magnet.

the coercivity of the Camry magnet is about 70% of the Prius magnet coercivity. This means that the Camry magnets are more easily demagnetized when opposing fields are applied to the magnet. In automotive applications, permanent magnet motors will often run at high temperatures. Additionally, these characteristics are especially important in reluctance PMSMs, wherein not only field weakening control methods are used, but reluctance torque is utilized, which also entails field weakening. The high-temperature operation with strong field weakening control methods greatly increases the chance of permanently demagnetizing or weakening the strength of the rotor magnets.

Teardown-transaxle

The overall functionality of the 2007 Camry transaxle is similar to that of the Prius, yet there are slight differences. A high-speed reduction gear was added to convert the output of the 14,000-rpm primary drive motor. A planetary gear is used as a compact solution for the conversion. The high-speed rotor is connected to the sun of the reduction planetary gear, and the planetary carrier is fixed to the transaxle housing. The planets mesh with the ring of the power split planetary gear, giving a total gear ratio of 2.47. The drive portion of the transaxle was also modified, in which a drive gear is used in the Camry transaxle as a replacement of a drive chain in the Prius transaxle.

Shown in Figure 5 are various perspectives of the transaxle, and the volume associated with the primary motor is indicated. The volume was reduced to about 77% of the volume devoted to the primary Prius motor. This was primarily done by reducing the rotor length, while the motor actually increased in power capability by increasing the rotor speed. Although the Camry rotor lamination stack is about 0.85 in., or about 26% shorter, the rotor weight is only about 1.2 kg, or 12% lighter than that of the Prius rotor. The lack of weight improvement is mostly due to the addition of a spline to the Camry rotor, which is needed to interface with the high-speed reduction gear. The stator lamination stack has a matching reduction in length, and the weight was reduced by about 30%. The Camry stator fabrication techniques appear to be more articulate. For example, the amount of wasted copper at the end turns is lower. This is a benefit from having a parallel winding configuration, which is used to extend the speed range. However, with parallel windings, the low-speed torque capability decreases if the total phase current is constant.

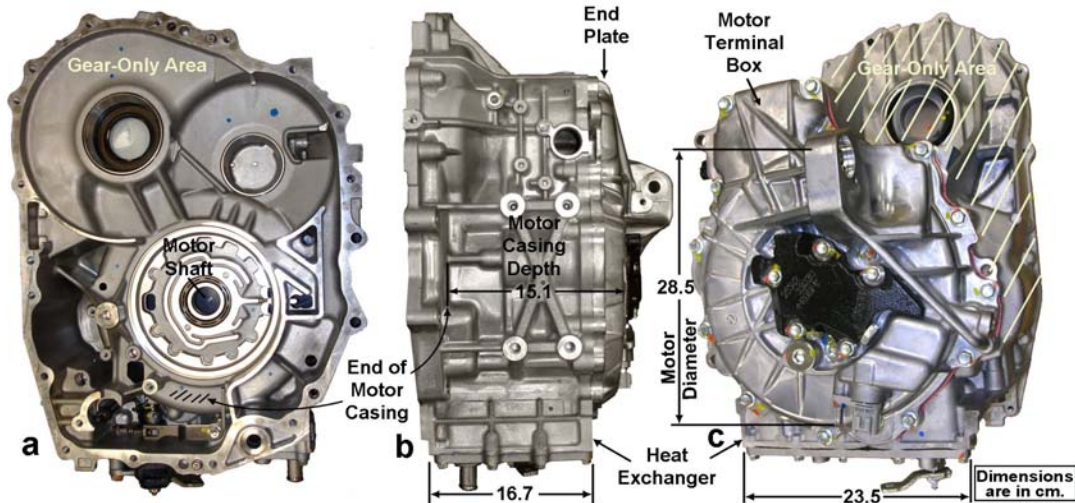


Figure 5. Various perspectives of 2007 Camry transaxle.

Even though the Camry inverter current rating has increased to about 300 A rms from the Prius inverter current rating of about 225 A rms, the peak torque of the Camry is only 270 Nm compared with 400 Nm for the Prius. However, a speed reduction gear with a ratio of 2.47 increases the 270-Nm rating to about 667 Nm. The Camry has 14 turns of a 9-strand bundle of copper per pole, where the Prius has 9 turns of a 13-strand bundle of copper per pole. The Camry stator contains a total of 12.5 lb of copper, while the Prius stator contains 15 lb.

More focus must be placed on the mechanical integrity of the rotor as the speed range of the motor is expanded. The rotor lamination design, shown in Figure 6, was modified to suit the mechanical stress demands of retaining the permanent magnets during high-speed operation. Notably, a bridge was added between each pair of magnets, which are oriented in a “V” arrangement. Interestingly, the rotor diameter of the Camry and Prius are the same. The stator laminations are quite similar, with the Camry winding slots being slightly shorter, yet wider than those of the Prius. Just as the stator and rotor lamination stack length was reduced, the magnet length was reduced by about 0.88 in. The Camry magnets are 0.004 in. thicker and 0.006 in. wider. Therefore the reduction of magnet weight is approximately directly proportional to length reduction, which is 58 g vs 77 g for the Prius individual magnet weight. This 25% reduction is also observed in the total magnet weight, which was reduced from 1,232 g to 928 g.

A comparison of the specific power and power density of three HEV systems, the Accord, Prius, and the Camry is provided in Table 1. To provide an accurate comparison with single motor systems such as

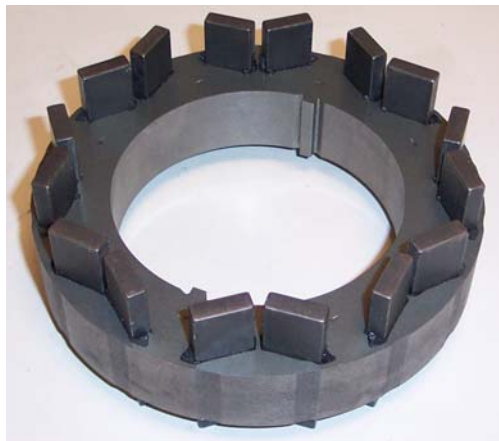


Figure 6. Partially disassembled 2007 Camry rotor.

Table 1. Comparison of specific power and power densities for various HEV components

Component and parameter	Accord (12 kW)	Prius (50 kW)	Camry (70 kW)
<i>Motor</i>			
Peak power density, kW/L	1.15	3.3	~5.9
Peak specific power, kW/kg	0.53	1.11	~1.7
<i>Inverter (excluding generator inverter and buck/boost converter)</i>			
Peak power density, kW/L	2.89	5.7	~11.7
Peak specific power, kW/kg	2.37	5.7	~9.3

the Accord, the mass and volume associated with only the primary drive motor and inverter were used in these calculations. The results indicate that the peak power density of the inverter was more than doubled from the Prius to the Camry. Additionally, the peak specific power of the motor and inverter and the peak power density of the motor were almost doubled. Both the Camry and the Prius systems significantly surpass the Accord system. Note that peak power capabilities were used in these calculations, and the used of continuous ratings may yield closer results. However, it is difficult to generalize continuous power ratings because they are based upon a variety of conditions such as coolant temperature, stator temperature limit, and motor speed.

Experimental evaluation

Various evaluations were conducted upon the PCU and transaxle to determine operational characteristics such as efficiency, continuous capability, and performance. Initial tests include measurement of back-emf voltage, no load losses, and locked rotor torque. These tests provide parameters and characteristics of the motor that are useful for approximating the capabilities of the motor. Secondary evaluations include efficiency, performance, and continuous analyses upon the subsystems. Before any tests could be conducted, the transaxle had to be modified to provide access to the motor shaft. The only shafts externally accessible are the engine input shaft and the differential gear output shafts. Although the differential gear is indirectly connected to the motor through several drive and planetary gears, power measurements through these gears would not be accurate.

Two separate approaches were taken to access the motor shaft. The first approach, similar to the approach taken with the Prius, involved welding the planetary gear so that the motor output was accessible from the engine input shaft. Although no-load loss tests were conducted to obtain losses associated with the high-speed gear, these evaluations do not portray how the gear behaves under load and varying power levels. While the first approach was an efficient method to initiate testing, there were still uncertainties associated with high-speed gear losses, which could potentially skew the efficiency and performance analysis of the motor. Therefore a second, more rigorous approach was developed but could not be initiated until a previously ordered commercial gear-box arrived to suit the speed range of our newly installed dynamometer, shown in Figure 7. The rotor shaft was modified with a spline, which is fed directly to a speed and torque transducer. The other side of the torque transducer was coupled to the speed reduction gear box, as shown in Figure 7. The gear box is capable of handling speed up to 18,000 rpm, and the new dynamometer can operate at power levels of up to 400 hp. All hardware on the high-speed portion of the shaft was designed to have face mount couplings, which provides extra safety since the shafts are shorter and are not exposed. Additionally, shaft alignment issues are avoided with this

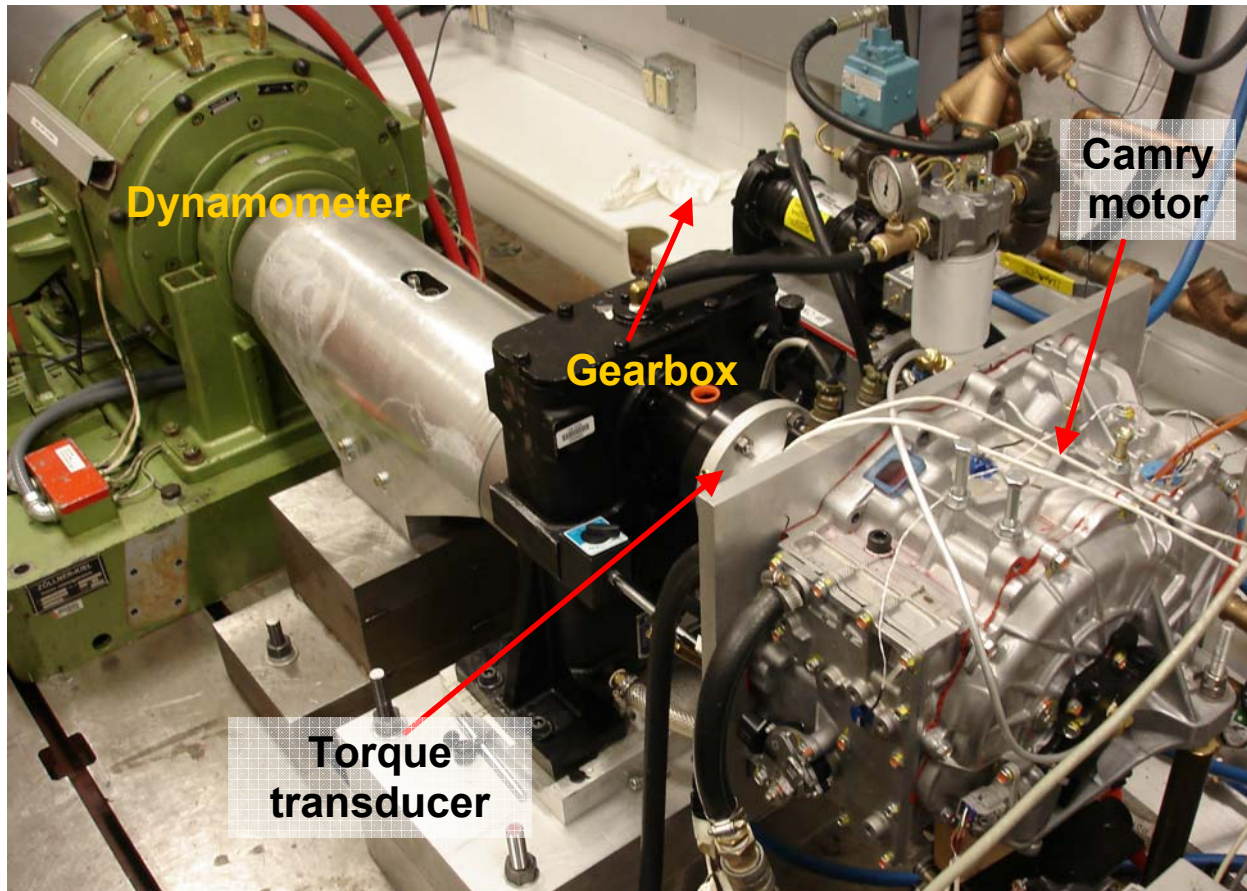


Figure 7. Newly installed 400-hp dynamometer, high-speed reduction gear, and Camry setup.

approach. A comparison of results from the two test setups yields very few discrepancies, indicating that the high-speed reduction gear losses do not vary significantly as the amount of load changes.

During the design and fabrication process of the transaxle modification, a lot of effort was devoted to ensuring that the cooling system was not hindered or enhanced in any way. The system depends greatly on proper oil circulation for heat conduction and lubrication. Oil is circulated via slinging action of the gears and is also circulated with a mechanically driven trochoid oil pump. Reservoirs are located in the upper portion of the transaxle to catch oil that is slung by the gears. Channels distribute the oil throughout the transaxle to the motor, generator, gears, and bearings. Windows were strategically placed in the transaxle housing to monitor the behavior of the oil flow and to ensure that any modifications did not affect the flow behavior. A large reservoir is adjacent to the heat exchanger and is nearly full when the ring of the planetary gear rotates at about 1000 rpm. The heat exchanger is in series with the inverter, and according to the Camry service manual, under normal conditions, the ethylene glycol and water coolant temperature is near 65°C at a flow rate about 10 L/in. Therefore, these conditions were used throughout most of the tests. Thermocouples were tactically placed to monitor stator, inner/outer case, and oil temperatures both near and far from the heat exchanger.

Additional instrumentation was added to the transaxle and PCU and a data acquisition system was developed to collect thermal, mechanical, and electrical data such as coolant temperatures, heat sink temperatures, torque, speed, currents, and voltages. These data were collected and fed into an immense spreadsheet and saved for future use. An optimal control scheme was developed to ensure the most efficient operation of the motor throughout the entire operation range. The controller uses speed, position, and current feedback to regulate the output conditions supplied by the inverter. The OEM motor inverter

controls were bypassed to allow full control over the inverter, enabling uninhibited testing of the system over various operation conditions.

Back-electromotive force (emf) tests were conducted by spinning the PMSM rotor with a secondary motor as the voltages across the open motor leads were measured. These tests provide information about the air gap flux due to the permanent magnets, as the induced back-emf voltage is proportional to speed and permanent magnet flux. Because the windings of the Camry are connected in parallel instead of being connected in series like the Prius, the back-emf voltage induced by the permanent magnets is lower for a given speed. The RMS line-to-neutral voltage of the Camry motor at 14,000 rpm is about 400 V vs about 550 V for the maximum Prius speed of 6,000 rpm. The low back-emf voltage of the Camry allows for operation at higher speeds, because the supply voltage limit is not reached until a much higher speed than for the Prius.

No-load loss tests were conducted with a similar setup, and the torque generated by the rotor and various gears was determined as the motor was spun at various speeds. With only the motor rotor installed, these loss tests provide information about core and friction losses associated with rotational movement. Losses of each gear in the gear train were also determined by removing one gear after each loss test is conducted. These tests were also conducted with various oil temperatures that drastically affect losses due to varying oil viscosity. For example, at 3,500 rpm, gear losses dropped from 1,600 W with an oil temperature of 30°C to 900 W with an oil temperature of 90°C.

Locked rotor torques were measured as a positive dc current was fed to phase “a” and returned through phases “b” and “c” connected in parallel, and the rotor position was swept through an entire electrical cycle. The torque measurements for stator currents of 25 A, 50 A, 150 A, and 200 A are shown in Figure 8. To avoid extreme stator temperatures and possible stator damage, measurements were only taken during the peak torque region for the higher dc currents of 250 A, 300 A, 350 A, and 400 A. A stator dc current of about 440 A is required to create the rated torque of 270 Nm, and this dc current corresponds with a phase current of about 310 A-rms.

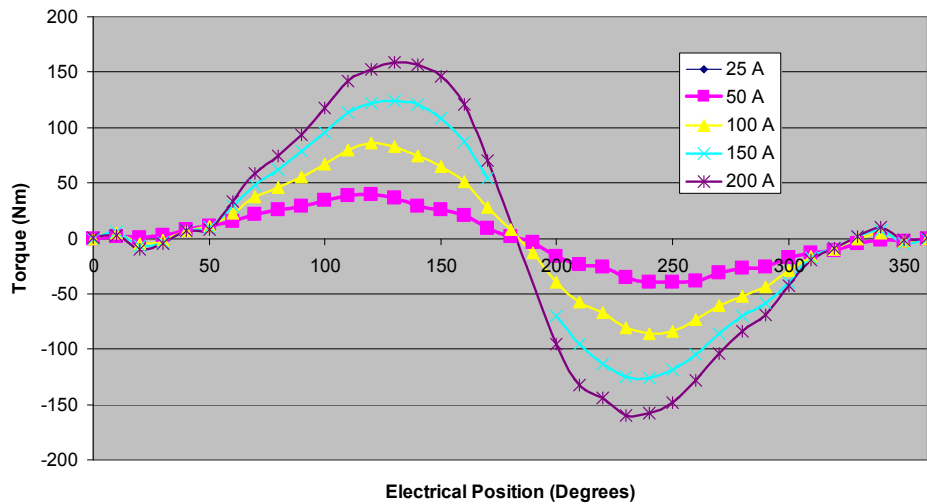


Figure 8. 2007 Camry locked rotor test results.

Efficiency measurements of the motor and inverter were taken over the entire operation range of the motor. The efficiency contour map in Figure 9 represents the steady state efficiency characteristics of the motor for efficiencies above 60%. When compared to the efficiency map of the Prius, the advantages of the high-speed Camry rotor become apparent. The peak efficiency of 94% as well as efficiencies above 88% are spread out over a much larger area of the operation region. Additionally, for speeds below the base speed, the efficiencies of the Prius decrease much more quickly than they do for the Camry. Note

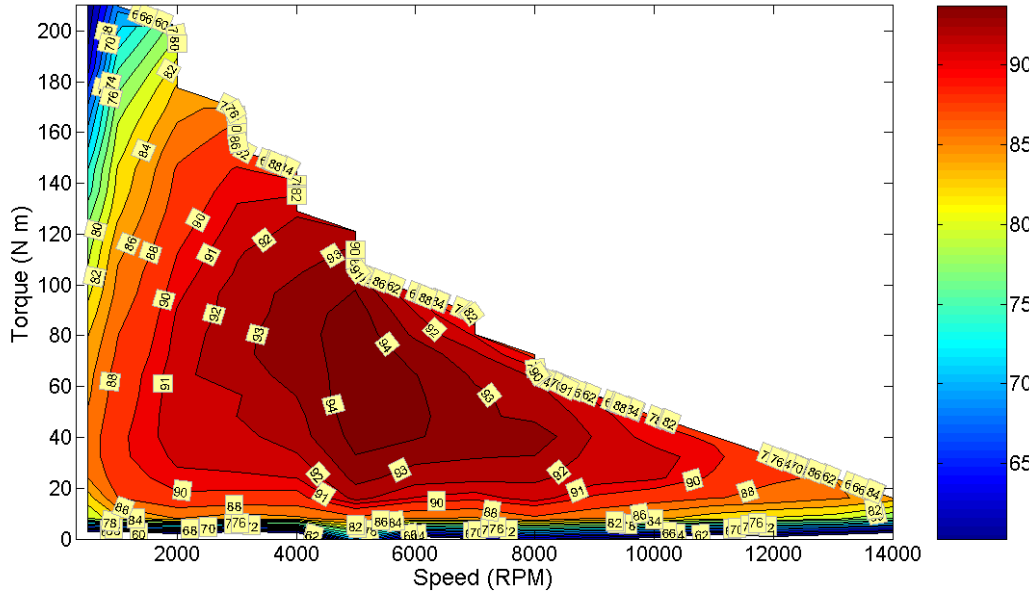


Figure 9. 2007 Camry motor efficiency map.

that only a peak power of nearly 70 kW was reached during these tests, as a voltage limit condition was encountered at high power levels. Interestingly, the peak power was not limited by thermal constraints. A dc voltage of 650 V was used throughout the tests, and rigorous efforts were made to ensure that the motor was being operated optimally because the peak power fell far short of the claimed rating. Simulations using parameters that account for nonlinear effects such as saturation also produce similar results. Efficiency maps are also available for the inverter and the motor and inverter combined. If the efficiency map is scaled using a gear ratio of 2.47, the resulting efficiency map is more comparable with the Prius in terms of the speed range.

Continuous tests were conducted at 25 kW, 33.5 kW, and 50 kW at 3,000 rpm, 5,000 rpm, and 7,000 rpm with coolant temperatures of 20°C, 25°C, 50°C, and 65°C. Stator, internal/external case, inverter, and coolant temperatures were measured throughout the tests. Shown in Figure 10 are the results

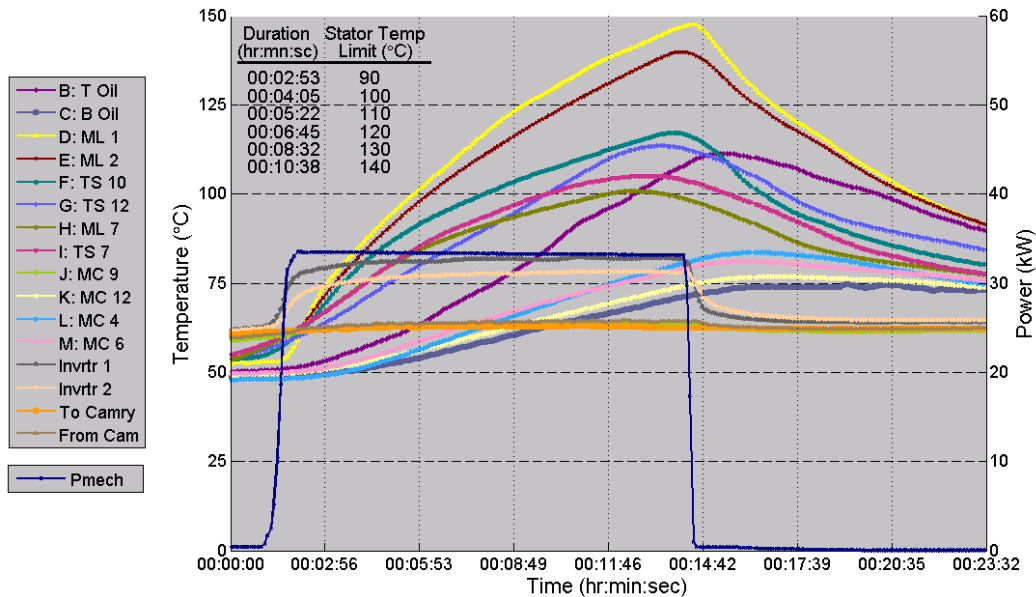


Figure 10. 2007 Camry continuous tests at 33.5 kW and 3,000 rpm with 65°C coolant.

from a test conducted at 33.5 kW at 3,000 rpm with 65°C coolant. The hottest location in the motor is near the upper portion of the stator, which is farthest away from the heat exchanger, as indicated by the yellow line. This particular test condition was maintained for about 11 min, at which time a stator temperature of 140°C was reached. For the same conditions, 33.5 kW was maintained at 5,000 rpm for about 30 min until a stator temperature of 140°C was reached. The duration of operation at a specific power level is affected by speed, coolant temperature, and temperature restraints placed on the stator. The service manual for the Camry indicates that the maximum stator temperature for normal operation is 90°C.

Conclusions

- The mass and volume of the PCU and transaxle were reduced significantly from the Prius design, even though the power capability has increased by at least 30%.
- The maximum speed of the primary motor has increased from 6,000 rpm to about 14,000 rpm.
- The motor lamination stack length has been reduced by about 0.85 in.
- Volumetric consumption associated with the primary motor was reduced 77% from the Prius design.
- Power densities for the Camry motor and inverter have been improved by 77% and 105%, respectively, when compared to the Prius motor and inverter.
- The specific power of the Camry motor and inverter has been improved by 53% and 63%, respectively.
- Benefits of moving to a high-speed motor are apparent through efficiency, performance, and continuous test results.
- Motor efficiencies are above 90% for a great portion of the operation range. Low-speed efficiencies of the Camry are much higher than those of the Prius, particularly when a gear ratio of 2.47 is used for speed reduction, in which the torque is increased significantly.
- The peak power of the primary Camry motor is about 70 kW at 5,000 rpm, which is much lower than the published rating of 105 kW. There are no specifications published for the generator, and the published power rating may be for both the motor and the generator. Simulations of this motor and a comparison of specific power characteristics with other high-speed motors also suggest that the power rating is near 70 kW.
- Continuous duration varies significantly with speed, specified stator temperature limit, and coolant temperature. A power level of 33.5 kW was maintained at 5,000 rpm for about 30 min with 65°C coolant, at which a stator temperature of 140°C was reached.

Publications

T. A. Burress, R. H. Staunton, and C. L. Coomer, *Evaluation of the 2007 Toyota Camry Hybrid Synergy Drive System*, ORNL/TM-2007/190, Oak Ridge National Laboratory, 2007.

This document highlights work sponsored by agencies of the U.S. Government. Neither the U.S. Government nor any agency thereof, nor any of their employees, makes any warranty, express or implied, or assumes any legal liability or responsibility for the accuracy, completeness, or usefulness of any information, apparatus, product, or process disclosed, or represents that its use would not infringe privately owned rights. Reference herein to any specific commercial product, process, or service by trade name, trademark, manufacturer, or otherwise does not necessarily constitute or imply its endorsement, recommendation, or favoring by the U.S. Government or any agency thereof. The views and opinions of authors expressed herein do not necessarily state or reflect those of the U.S. Government or any agency thereof.



A Strong Energy Portfolio for a Strong America

Energy efficiency and clean, renewable energy will mean a stronger economy, a cleaner environment, and greater energy independence for America. Working with a wide array of state, community, industry, and university partners, the U.S. Department of Energy's Office of Energy Efficiency and Renewable Energy invests in a diverse portfolio of energy technologies.

For more information contact:
EERE Information Center
1-877-EERE-INF (1-877-337-3463)
www.eere.energy.gov